Universität
Bremen

INSTITUT FÜR
BIOPHYSIK

Dissertation submitted towards the degree
Doctor of Natural Sciences
-Dr. rer. Nat.-

Dupuytren's disease investigation under 2D and 3D environment: Atomic Force Microscopy approach

Sandra Pérez Domínguez

Bremen, 02/05/2023

Referees: Prof. Dr. Manfred Radmacher
Prof. Dr. Daniel Navajas

A mi abuela Irma, que aunque no nos pudimos encontrar en este mundo siempre te he llevado, te llevo y te llevaré en mi mente y mi corazón.

A mi tío Óscar, al que extraño y recuerdo con una sonrisa plena en la cara, siempre conmigo.

Estoy más despistado que una cabra en un garaje

-Lorenzo Domínguez Manero-

Phys2BioMed project

This thesis has been carried out within the frame of a Marie Sklodowska-Curie Action entitled “Phys2BioMed” for “Biomechanics in health and disease: advanced physical tools for innovative early diagnosis. H2020-MSCA-ITN-2018 n.812772”.

The project involves fourteen ESR and eighteen partners working together to successfully perform exciting researches and training activities regarding the field of biophysics.

As ESR number 13, the main research activities were carried out at the University of Bremen (UB). In addition, thanks to the MSCA scholarship, three secondments were made in three different European institutions. CNRS-Lille (France), IBEC-Barcelona (Spain) and OSR-Milano (Italy) were the host institutions for the secondment periods.

This project allowed me to successfully carry out my PhD project together with the opportunity to visit cutting-edge laboratories and discuss and exchange ideas with really good scientists from all over the world.

Abstract

Atomic Force microscopy (AFM) is a powerful technique that serves to acquire topographical images of samples measuring the roughness of the superficial layer. In biology, this technique has gained popularity and has been used to image a large range of samples, from small molecules like DNA to micrometer dimension like cells and tissues. In addition, as the name indicates, allows applying small forces (pN, nN) to obtain diverse information about the sample. Cell mechanical properties, cell-cell interaction, single-molecule stretching, enzyme-substrate interactions are some of the AFM applications for biological samples. As above-mentioned, it is used to study cell mechanical properties at single cell level. This approach is especially interesting as a diagnostic tool to compare cancerous or pathological cells to healthy counterparts. It enables to decipher if there is any mechanical change within the cells that it may be relevant for the development of the disease.

Cells are the basic element of every living being and the human body is composed of infinite cell types, each one specialized in one or more functions within the organ. However, cells are far from being simple materials instead they are complex heterogeneous samples composed by many different structures such as biomolecules, organelles, nucleus, cytoskeleton network, plasma membrane, etc. This complexity makes them difficult to be described by simple mathematical and physical models. Fibroblasts are a type of cell present in the connective tissue whose mission is to synthesize extracellular matrix (ECM), especially collagen I and play a crucial role in wound healing process. Fibroblasts can differentiate into myofibroblasts (α-smooth muscle actin (SMA) positive fibroblasts) when changes in the tissue stiffness occurred or can also be stimulated by cytokines secreted by inflammatory cells. Changes in the surrounded ECM are transmitted to fibroblasts via focal adhesions, a group of proteins, such as integrins that connect the ECM with the actin-myosin network. Therefore, changes in the ECM are transmitted to fibroblasts, which react increasing or relaxing cell contraction. This mechanism produces a feedback loop reaction, in which cell-ECM communicate and respond to each other.

Dupuytren’s disease is a fibroproliferative disease of the palm that leads to the bending of one or more fingers and hand contraction. A common characteristic with other fibrotic diseases is the accumulation of myofibroblasts (in Dupuytren’s disease in the nodules and cords in the palmar fascia) and collagen in the ECM. In this project, three primary fibroblasts from the palm of a patient suffering from the disease were investigated using AFM. The different fibroblast samples were extracted from

different regions of the palm and were classified as healthy/control, scar and Dupuytren or pathological fibroblasts. AFM rheological experiments supported the idea of healthy fibroblasts presenting normal fibroblast phenotype and Dupuytren fibroblasts presenting myofibroblast phenotype. A more developed AFM scheme than typical force curves and employing Hertz model to analyze cell mechanical data was used, the so-called sweep frequency modulation scheme. It is based on applying a sinusoidal modulation with increasing frequency in contact with the sample and then using an appropriate model, in our case we employed the structural damping model, storage and loss modulus (representing the elastic and viscous properties) of the cells were obtained. This scheme enables to separate both cell responses and quantify them; in our experiments, Dupuytren fibroblasts presented the largest storage and loss moduli values.

In the literature the use of biomolecules to stimulate myofibroblast transition have been well studied. However, a more interesting approach is the assessment of compounds that targets a specific element of myofibroblasts, like α-SMA and could help in reverting myofibroblast differentiation. We used a myosin inhibitor (ML-7) that causes a decrease in cell contraction, more drastically affecting Dupuytren fibroblasts. 2D and 3D cell's environment was studied, first using circular micropatterns to assess how the different cells reacted to physical constraints and then using soft collagen gels seeding the cells on top and inside. Micropatterns serve to force cells to acquire a specific shape, usually similar shape as cell morphology in tissue. In our case, we used circular-shaped micropatterns to induce a "non-normal" condition and healthy fibroblasts seemed to react more than the other fibroblasts, presenting an increase in apparent Young's modulus and solid-like behavior with increasing the circular micropattern diameter. This behavior simulates myofibroblast differentiation, as the increased stiffness in healthy fibroblasts came together with an increase in actin fibers accumulation as well as organization. In contrast, when seeding the different fibroblasts on soft collagen gels and hard petri dishes, Dupuytren fibroblasts modulated its mechanical properties to those of the substrate and healthy and scar fibroblasts presented similar properties in soft collagen gels and in hard petri dishes. Here, cell-ECM interaction plays a crucial role in fibroblasts development. The use of artificial and natural hydrogels to resemble cell's environment is a promising approach to study cells' response closer to tissue-like conditions. 3D gels provide physical constraints and biochemical and mechanical stimuli similar to those in cell's natural environment. The three different fibroblasts were embedded in soft collagen gels and gels mechanical properties showed an increase in gel stiffness over time. Cell spreading and multiplication increased gels mechanical properties, being Dupuytren fibroblasts the ones that respond faster in spreading and multiplication at early states (2 days after incubation). At longer incubation periods, all fibroblast types behaved similarly, showing no big differences in gel's rheological properties among fibroblasts. The use of soft collagen gels restricted fibroblasts tensional properties and therefore, myofibroblast development.

In summary, understanding any disease leads to investigating all possible scenarios. The use of different approaches helps in deciphering new key cellular mechanisms for the development of the disease. Cell-cell and cell-ECM interaction strongly influence cell behavior, thus the lack of any of these elements would resolve in different cellular responses. In this way, 2D and 3D experiments are gaining space as it tries to resemble cell's natural environment simulating ECM's biochemical and mechanical properties. In our work, these two scenarios were assessed, evaluating cells response in 2D and 3D conditions. Differences in cells response in the two conditions come up with the general conclusion that cells not only react differently depending on the mechanical properties of the environment but also 3D environment is of truly importance due to the physical constraints cells encounter that leads to different cells responses as in 2D. Accordingly, each experiment provides useful and interesting data; however, it should be always mentioned and taken into account the environment and experimental conditions at which the experiments were done.

Table of contents

Acknowledgements

I would like to start truly thanking my family for all they have done during their whole life for me. Although I may not express it so often as it should be, I love you with all my heart. My parents worked so hard to give me all they could and more that I do not think I would be able to pay them back in hundred lives. They have been always by my side, helping me in the toughest moments and never giving up. My dear brother, César, such a good soul, he has always been with a smile in his face trying to comfort me and although we are extremely different, I love you and we both now that we are there any time for each other. This thesis is just for you to be proud of me. I would also like to thank Pablo; he has been a real support during these years and he has helped me to seed light in many scientific problems although it was not his field and I truly admire him so much for that.

When the time to decide what I wanted to study arrived, I had doubts about what to choose, although biology and chemistry were always my top subjects. I decided for chemistry thanks to my teacher, he was amazing and he knew how to make us enjoy it. Nevertheless, I had always loved biology, therefore, when I had the opportunity, I took as many subjects related to biology as possible. There are not boring or bad subject, it depends on the teacher and how they tell the story. For that, I thank all my teachers and professors who help me to be where I am. Besides, I would like to specially acknowledge Prof. Ramón Macias Maza and Dr. Anabel Gracia Lostao, my bachelor and master's thesis supervisors, respectively, who kindly taught me all they could and encouraged me to continue in this scientific path and helped me to grow as a scientist.

When I decided to enroll in a PhD program, I didn't know what to expect but I was feeling really excited to live abroad and with a lot of energy to learn new things and expand my knowledge. It was hard at the beginning, as I had to learn new scientific topics out of my comfort zone; however, thanks to my supervisor Prof. Manfred Radmacher and my former colleagues Dr. Carmela Rianna and Dr. Prem Kumar, I felt comfortable and enjoyed my work. My supervisor helped me to understand the physics behind my project, he gave me freedom to conduct my research as I wanted and thanks to that I learned a lot and encouraged me to become an independent researcher. Although they left soon after I started my PhD, Dr. Carmela Rianna and Dr. Prem Kumar always were available and open to help and taught me all the things in the lab. They were always kind and easy-going and I wish them all the best in their lives and future jobs. In addition, I would like to thank my lab member Shruti

Kulkarni, we started at the same time and faced the same issues and fortunately, we supported each other. I would like to thank her for her scientific support and her friendship.

Furthermore, I would like to thank Prof. Monika Fritz and Prof. Dorothea Brüggemann for all the comments and suggestions to improve my presentation skills. I would like to thank Prof. Dorothea Brüggemann for letting me use her lab facilities, especially the fluorescence microscope. Moreover, I thank Nina Messerschmidt for her work and help in cell culture. I am also very grateful to Prof. Dr. Ursula Mirastschijski for providing tissue samples and Prof. Gazanfer Belge for establishing cell lines.

I take this opportunity to thank the former members and members of the biophysics institute: Janka, Holger, Eva, Arundhati, Deepanjalee, Anja, Malte, Merthe, Meike, Thomas, Gaby for always being helpful.

Additionally, I would like to thank all the members of Phys2BioMed network for all the helpful inputs given on our meetings and the good moments we have shared during all these years. I am really grateful of having met many smart people and what is more important with good heart. Thanks to this project I can say that I have made good friends for life.

I would also like to thank my lifelong friends: Leyre, Lara, Sandra U., Sandra A., Sandra M., Laura and my beloved friend Eli, who is going through a bad time but she will recover stronger than ever.

Last but not least, I would like to thank my aunts Ana and Inma and my grandparents Matilde, José Luis and Lorenzo and especially my beloved uncle Javi, who always supported me and helped me to not giving up and going on.

I though this day will never arrive but here it is and I am really happy to see with my own eyes what I have achieved and have been able to complete this period of my life.

Chapter 1

Introduction

1.1 Atomic Force Microscopy

1.1.1 AFM basics

Scanning probe microscopy (SPM) is a family of microscopies that uses a sharp tip to scan the surface of a sample getting nano and atomic scale resolution. The first SPM invented was the scanning tunneling microscopy (STM), in 1981 by Binning and Rohrer (Binning *et al.*, 1982). Samples measured by STM have to be conductive or semi-conductive; therefore, these limitations prompted the invention of the atomic force microscopy (AFM).

In 1986, Binning et *al.* were able to record a tip-sample interaction using atomic forces with the AFM and unlike STM almost any type of surface can be imaged (Binning, Quate and Gerber, 1986). Some of the advantages brought by this technology are the different environments available to measure, like vacuum, air and liquid, from high to ultra-low temperatures. At the beginning, AFM was used to scan surfaces of hard samples; however, its application to biological systems and medical investigation has exponentially increased (Radmacher, 1997; Engel and Müller, 2000).

Moreover, AFM has also the advantage, over optical and electronic microscopes, of not requiring freezing, metal coating, vacuum or staining of the sample and thus it allows measuring samples in physiological conditions. This was something extremely important for biological samples, such as cells, because it allows measuring them in the same buffer, pH and temperature conditions as in physiological conditions. In addition, AFM provides high spatial resolution images applying really small forces (picoNewtons, (pN)) (Bian *et al.*, 2021).

The heart of the AFM is a cantilever that has a tip mounted at its very end. It will bend/deflect when interacting with the sample. AFM cantilevers are mostly made of silicon or silicon nitride and the back face is usually coated with a metallic compound, typically gold, to enhance its reflectivity. A piezo actuator allows the cantilever movement in xy direction to scan all sample surface, as well as in z direction to approach and retract the cantilever in and out of contact with the sample. A controller is implemented to collect and process the data and to drive the piezo. A laser beam is focused on the backside of the cantilever and reflected off towards a photodiode. Changes in cantilever deflection provide changes in the laser spot position on the photodiode (Fig. 1.1). The collected signal of the photodiode is processed and converted into a simple interface understandable to the user (Shao *et al.*, 1996). Nowadays, AFMs used for investigating cells are usually coupled with an optical microscope that allows following the cantilever position over the sample.

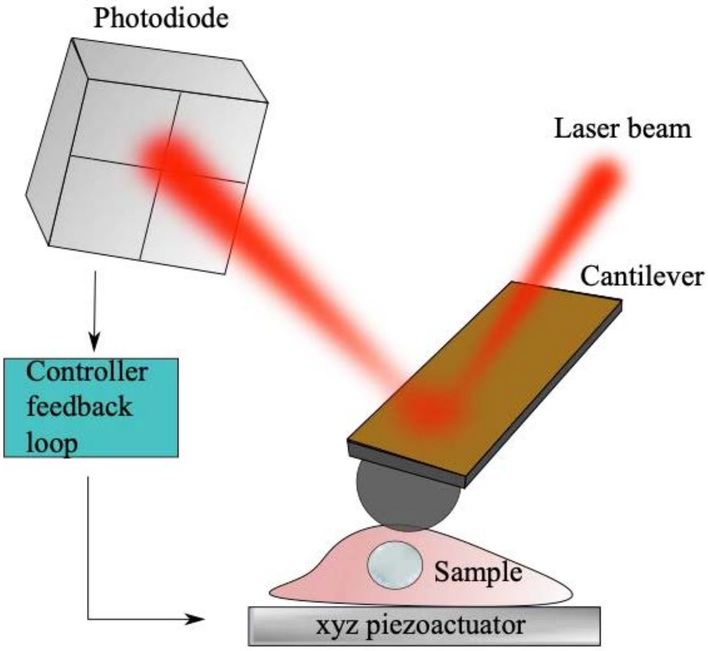

Figure 1.1 Scheme of the AFM components.

1.1.2 Types of experiments

AFM has been used for measuring hard and soft samples, such as scanning the roughness of new synthesized materials or biological samples. Its employment to decipher biological questions opened a new field in biophysics that is gaining more interest in the scientific community due to its wide versatility. From tissue to small molecules, like proteins, going through different levels of complexity, AFM is able to probe a broad range of elements (from mm to Å). Depending on the sample size and the biological question, different tip geometries and sizes can be used. Tipless cantilevers have been used as a support to attach different samples, like cells, extracellular matrix (ECM), proteins, etc., making them useful in providing custom cantilevers. Pyramidal and conical tips are sharp and have the advantage of displaying high lateral resolution and local indentations (Rico *et al.*, 2005; Carl and Schillers, 2008; Zemła *et al.*, 2020). Commercially available tips usually present small tip radius and opening angle, leading to high stresses when indenting the sample. Pyramidal and conical tips appear to procure ultra high pressure at the center (Fig. 1.2 cone and pyramidal); however, this is not real as the tip has a finite radius of curvature at the very end. Cylindrical tips have the advantage of procuring constant indented area when increasing the indentation depth; however, it generates high pressure at the edges (Fig. 1.2 cylindrical). Blunt tips, like spherical tips, sacrifice in resolution but allow probing large areas, and the pressure applied upon the sample is distributed over the entire indented surface; thereby the pressure in a local spot is reduced (Fig. 1.2 spherical). Procuring the same indentation as the previous tips (500 nm), the pressure upon a sample of 1 kPa stiffness is reduced being almost insignificant in comparison to sharp tips.

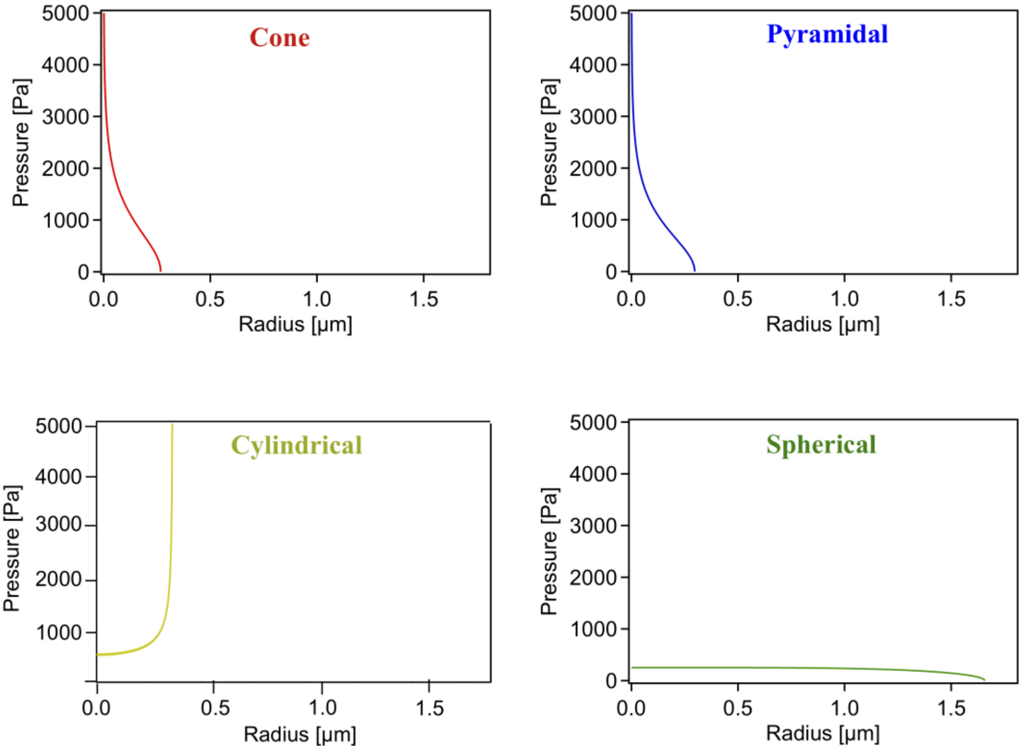

Figure 1.2 Simulated contact pressure versus radius from the center of conical, pyramidal, cylindrical and spherical tips at indentation 500 nm. Cone and pyramidal tips were assumed to have 40° opening angle and 35 nm tip radius, similar to commercially available MLCTs. Cylindrical tip was assumed to have 290 nm tip radius and spherical tip 5.5 µm, similar to MLCT-SPH-5UM cantilevers.

AFM can be used to obtain topographical images of the sample, for single-molecule force spectroscopy, cell and tissue mechanics, cell-cell interaction, and dynamic force spectroscopy among others. The two most used modes for obtaining the topography of a sample are categorized into contact and intermittent mode. Within the contact mode, there are two different modalities: “constant height” that is based on a direct interaction between tip-sample and scanning the sample holding the cantilever base height constant while the cantilever deflection is monitored. This mode is often used for hard and flat surfaces. In cells, the large differences in height will lead to large changes in cantilever deflection, thus in force that may cause damage in the cell. In “constant deflection mode”, as the name suggests, the cantilever deflection is kept constant, therefore if a sudden jump in sample height is encountered, the cantilever z-position with respect to the sample is changed in order to maintain the deflection signal constant (Fig. 1.3) (Radmacher, Tillmann and Gaub, 1993; Radmacher, 2002).

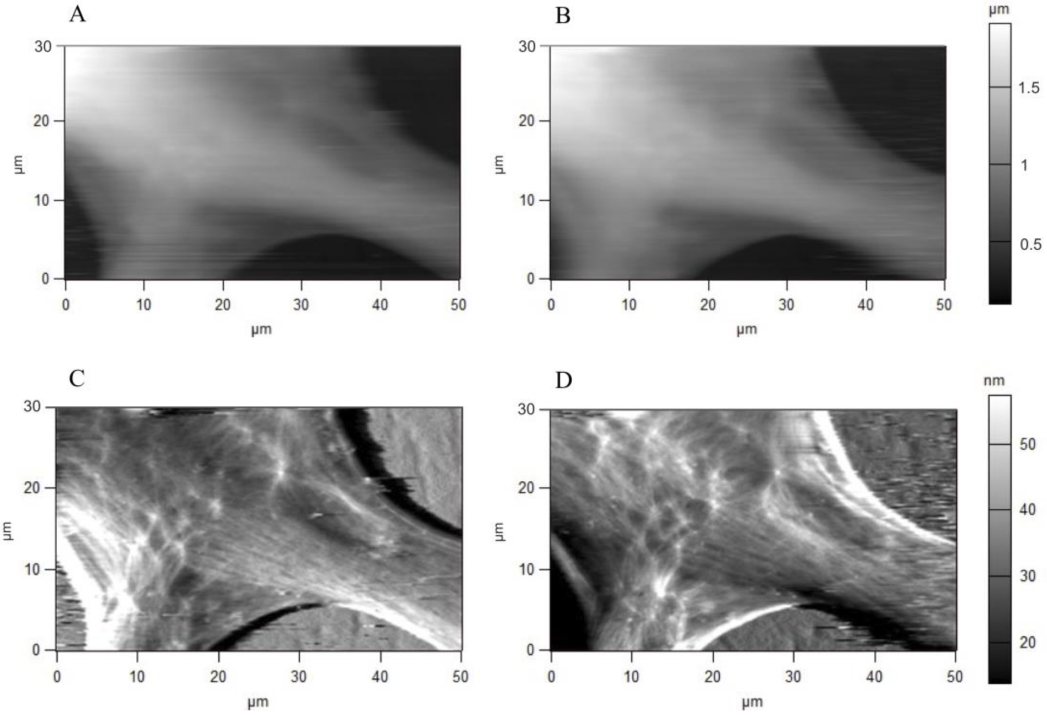

Figure 1.3 AFM image of a healthy fibroblast. A) Height trace and B) height retrace signal that corresponds to the output of the feedback circuit that tries to keep the deflection signal constant. C) Deflection trace and D) deflection retrace signal, which corresponds to the residual error due to the finite response time of the feedback circuit. Together, the overall topography of the cell with the height signal and the roughness with the deflection signal could be obtained.

The most popular “intermittent” mode is tapping mode. In this mode, the cantilever is oscillated at its resonance frequency and the amplitude of the oscillation is taken as the input signal of a feedback loop. During tip-sample interaction, the amplitude of the cantilever oscillation is reduced or even suppressed and it is recovered when the cantilever is retracted off the surface. This mode is often used for imaging single molecules, like proteins, DNA, etc.

In addition to imaging, AFM has been used to measure cell-cell interactions, folding/unfolding of proteins, substrate-enzyme interaction, etc. Cell-cell interaction experiments were developed to assess the strength of the bindings occurring between two cells of the same cell line or cells of different origin or pathological grade. The simplest way to perform this type of experiments requires attaching a cell to a tipless cantilever and then the cell cantilever is approached to a monolayer of cells. Having one monolayer of cells reduces the probability of partial or no interaction, as might occur when cells are dispersed. The cell attached to the cantilever is now the tip, and like any other cantilever, it has to be calibrated once the cell is attached (Puech *et al.*, 2006; Viji Babu *et al.*, 2021). Cadherins are part of the cell adhesion molecule (CAM) family that are important in the formation of adherent junctions and thus in the cell-cell adherence (Aberle, Schwartz and Kemler, 1996; Wheelock and Johnson, 2003; Hazan *et al.*, 2004). There are some cadherin types, classified in type I (E, N…) and type II (OB, VE…) (Yap and Kovacs, 2003). E-cadherin is presented in epithelial cells and N-cadherin is the most abundant in fibroblasts (Chu *et al.*, 2004; Borghi *et al.*, 2012). Fibroblast transition into myofibroblast results in an increase of OB-cadherin expression with respect to N-cadherin (Pittet *et al.*, 2008). Using AFM cell-cell interaction experiments, OB-cadherins homophilic interaction was found to be stronger than between N-cadherins (Viji Babu *et al.*, 2021).

Cell-ECM interaction is measured similarly to cell-cell interaction. The easiest way is to attach a cell to the cantilever and approach it to the ECM. However, new experiments doing the opposite, in which ECM squares (cutting ECM sections directly from decellularized tissue) are attached to the cantilever and then approached to a monolayer of cells. Cell-ECM interaction is basically carried out through integrins. Integrins are transmembrane proteins that connect the ECM to the cell's cytoskeleton (Hynes, 1992; Burridge and Chrzanowska-Wodnicka, 1996; Lehenkari and Horton, 1999). Cell attachment takes place through the formation of focal adhesion complexes that contain many cytoplasmic proteins, like vinculin, talin, paxillin and actinin, along with integrins (Goffin *et al.*, 2006). The investigation of cell-ECM interaction is really important to comprehend how cells react to biochemical and mechanical changes in ECM.

Single molecule force spectroscopy investigates individual protein interactions that typically require functionalizing the cantilever tip to make it accessible to the protein. The bond between the protein and the tip (functionalized tip) has to be stronger than the natural bond between the molecules under study (Ebner *et al.*, 2008; Alldritt *et al.*, 2022). Generally, the tip-protein functionalization is made through covalent bonds that are usually stronger than any other non-covalent bond. It allows measuring receptor/ligand interaction, substrate/enzyme and quantifying its binding strength (Rico *et al.*, 2019; Pérez-Domínguez, *et al.*, 2022). Furthermore, folding/unfolding AFM experiments can help to understand diseases related to the presence of unfolded/misfolded proteins and how this contributes to the pathology (Rico *et al.*, 2013; Sumbul, Marchesi and Rico, 2018; Ignatova and Gierasch, 2007).

In addition, cell and tissue mechanical properties can be investigated employing AFM as well (Hoffman and Crocker, 2009; Wu *et al.*, 2018; Pérez-Domínguez *et al.*, 2020). This type of experiments have gained interest in the last 20 years due to its ability to discriminate between normal and pathological cells and it is the main technique used during the presented research project. Cell mechanical experiments are based on applying small forces and recording cell response to this external force. This type of experiments can be performed by keeping the applied force or indentation in the sample constant. The cantilever is brought into contact with the sample and then keeps moving downwards until a preset force or sample indentation is reached. This process is recorded in deflection versus z-piezo curves that reflect the cell response to the applied force. The obtained data provides information about the stiffness of the sample, which can be compared with other cell types, other experimental conditions, etc. (Kirmizis and Logothetidis, 2010; Gavara, 2016; Rianna and Radmacher, 2016b).

1.1.3 Mechanical properties and techniques

The mechanical properties of a material is a term used to assess the suitability of that material for certain applications and they help to classify and identify the latter. Indeed, they are physical properties that materials exhibit reacting to an applied force. Some of them are the modulus of elasticity or Young's modulus, tensile strength, elongation, hardness and fatigue limit (Pelleg, 2013; Meyers *et al.*, 2008). All these properties can be identified in a stress-strain experiment, as depicted in figure 1.4. The first stage is the linear elastic region and the slope is the Young's modulus (Courtney, 2005; Jastrzebski, 1960). At the end of this stage, plastic deformation begins and the crossing point between elastic and plastic behavior is the yield strength. The second stage is the strain hardening, which is the strengthening of the material and third stage the necking that occurs with the formation of a cross-sectional area that is smaller than the rest of the material body. This stage finishes with the fracture of the material.

Stress is the applied force to a certain cross-sectional area of an object to deform it (Boyer, 1987). It can be described as follows:

$$\sigma = \frac{F}{A} \tag{Eq.1.1}$$

where σ is the stress, F the force and A the area of the object.

Strain is response of an object to the applied stress and can be quantified as the total deformation in the direction of the force divided by the initial length of the object.

$$\varepsilon = \frac{\Delta L}{L_0} \tag{Eq. 1.2}$$

where ε is the strain, ΔL is the total deformation and L_0 the initial length.

In a stress-strain plotting, the linear-elastic portion, in which stress is proportional to strain, is also denoted as the Young's modulus or modulus of elasticity. Young's modulus (E) quantifies a material's resistance to limited or elastic deformation. This parameter serves to describe linear elastic materials (Hearn, 1997).

$$\sigma = E\varepsilon \tag{Eq. 1.3}$$

Solid elastic materials deform immediately under mechanical stress but recover their original shape when the stress is removed. For measuring the mechanical properties of pure elastic materials, using oscillatory testing, stress and strain are said to be in phase. Some elastic materials are rubber or elastin, where a spring is considered to be representative of linear elastic solids (Malvern Instruments, 2016).

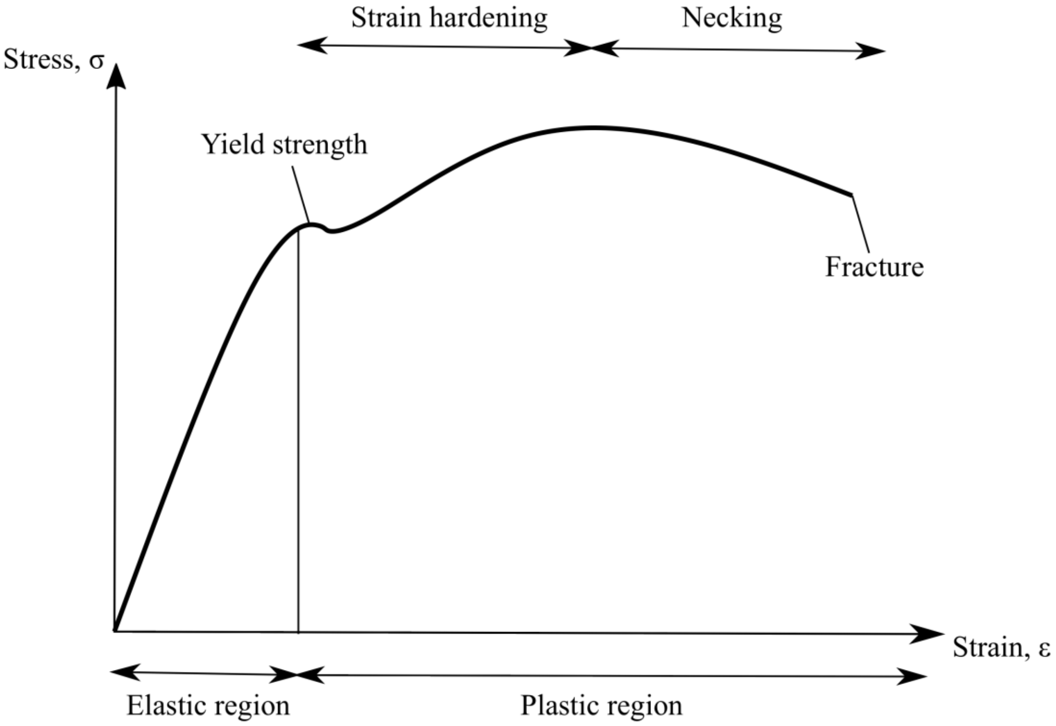

Figure 1.4 Typical stress-strain curve of a ductile material, like steel. Graph taken as a reference from the following page: https://www.cmrp.com/blog/faq/analysis-design/exploring-stress-strain-curve-mild-steel.html.

Viscous materials are represented by a dashpot; when a stress is applied, it starts to deform and continues deforming at a constant velocity flow until the stress is stopped. The energy invested in the deformation is dissipated (usually as heat) and the strain is permanent. The stress and strain are out of phase by 90° (Janmey and Schliwa, 2008; Murata, 2012). Nevertheless, many materials exhibit both elastic and viscous properties and are known as viscoelastic materials. Viscoelastic materials exhibit both solid- and liquid-like characteristics, and the phase difference between stress and strain in an oscillatory testing is somewhere between 0-90° (Ferry, 1980; Christensen, 1982). Cells are complex heterogeneous materials due to their crowded bodies, filled with a diverse number of elements presenting varied mechanical properties, like cytoskeleton network (stress fibers), organelles, nucleus, micro and macromolecules, etc. For that reason, cells are classified as viscoelastic materials presenting both elastic and viscous properties at different time scales (Kasza *et al.*, 2007).

Cells' mechanical properties are governed by many cellular structures and their contribution may distinguish between different cell types and pathological grades. Thereby, cell viscoelastic behavior varies depending on the origin (organ, tissue of provenance) and on the disease. Cells’ elasticity is said to be governed by the cytoskeleton network properties, especially the actin fibers. The number of stress fibers, rearrangements and number of crosslinks dictate cell's elasticity. The viscous contribution of cells is rather difficult to identify, but is simply attributed to cell's fluid cytosol and its friction with micro and macromolecules in the cell body. According to the technique employed or the part of the cell measured (cell membrane, glycocalyx, cell body, etc), cell's mechanical properties vary greatly as different cell components are taken into account. Fortunately, these cell properties can be investigated using different and very diverse techniques.

AFM is a versatile technique that apart from imaging purposes can work in multiple modes, like dynamic force spectroscopy and cell mechanics, where it compresses and indents the sample with a sharp tip to finally quantify the sample response to the external mechanical stimuli. It is able to detect small forces on the order of pico- to nano-Newtons, which is usually the observed range for cell mechanical response. One of the main advantages is the ability to measure samples with really different stiffnesses. This is feasible thanks to the wide availability of cantilevers encompassing a large range of force constants. Stiff cantilevers are able to probe hard samples like steel or bone; however, softer cantilevers may be used to probe soft samples like cells (Fig. 1.5) (Vinckier and Semenza, 1998; Khan, Wang and Fitzpatrick, 2016; Vlassov *et al.*, 2018).

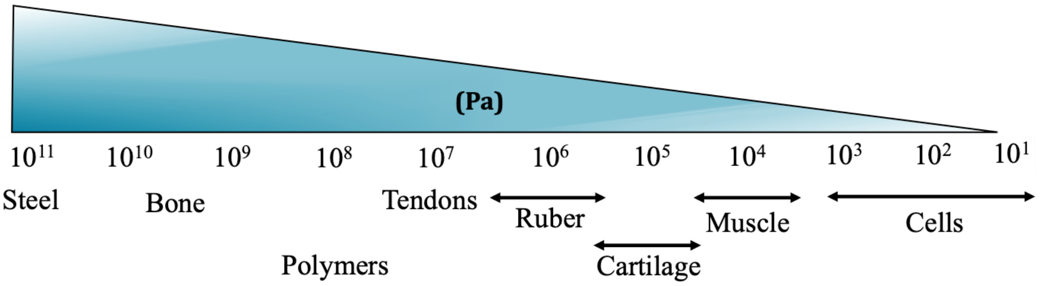

Figure 1.5 Mechanical properties of different materials (elasticity in Pascals (Pa)). Biological samples such as cells are soft in comparison to hard materials like bone.

In addition to AFM, there are many other techniques able to measure cell and tissue mechanics, such as optical tweezers, particle tracking microrheology, traction force microscopy, flow deformation cytometry, etc (Moeendarbary and Harris, 2014).

Optical tweezers rely on the concept that when light enters a medium with a refractive index, the light path changes. Optically, cells and beads can be trapped and manipulated with a collimated light source. It provides high sensitivity (pico-Newton resolution) and high spatio-temporal accuracy (Zhang and Liu, 2008). A bead can be attached to the cell membrane and, upon removal, measure the strength of adhesions and tether formation (Fig. 1.6). In addition, cells can be deformed by a bead that approaches and retracts, giving loading and unloading force curves (force-distance, F-d) similar to AFM measurements. Another approach consists in embedding a bead inside the cell or entrap an organelle and measure cell interior mechanics, which is the closest methodology to assess overall cell mechanics, as AFM technique only allows to probe the cell surface, providing a cell response that AFM users consider to be general cell mechanics. Nevertheless, this approach has many disadvantages, as it is first challenging to embed beads inside the cell body and then has a force limitation, that is sometimes not enough for indenting stiff cells; therefore, it is conventionally used for micro and macromolecule experiments, like DNA stretching (Hochmuth *et al.*, 1996; Guck *et al.*, 2001).

Particle tracking microrheology has the advantage of avoiding the application of external forces to track cell mechanical behavior. Small beads (nano- or micro-meter) in diameter are inserted into the cell body to follow its spontaneous motion with high spatial and temporal resolution. In a pure viscous environment, the beads move randomly in Brownian motion. In contrast, in a purely elastic environment, the beads are stuck and the thermal motion is not strong enough to induce random motion. Cells presenting viscoelastic behavior follow a complex mixture of both behaviors, showing a continuous motion over time due to thermal fluctuations and non-Brownian motion (Wirtz, 2009). Different viscoelastic responses of various cell types under pharmacological treatment and physiological conditions have been tracked (Hale, Sun and Wirtz, 2009).

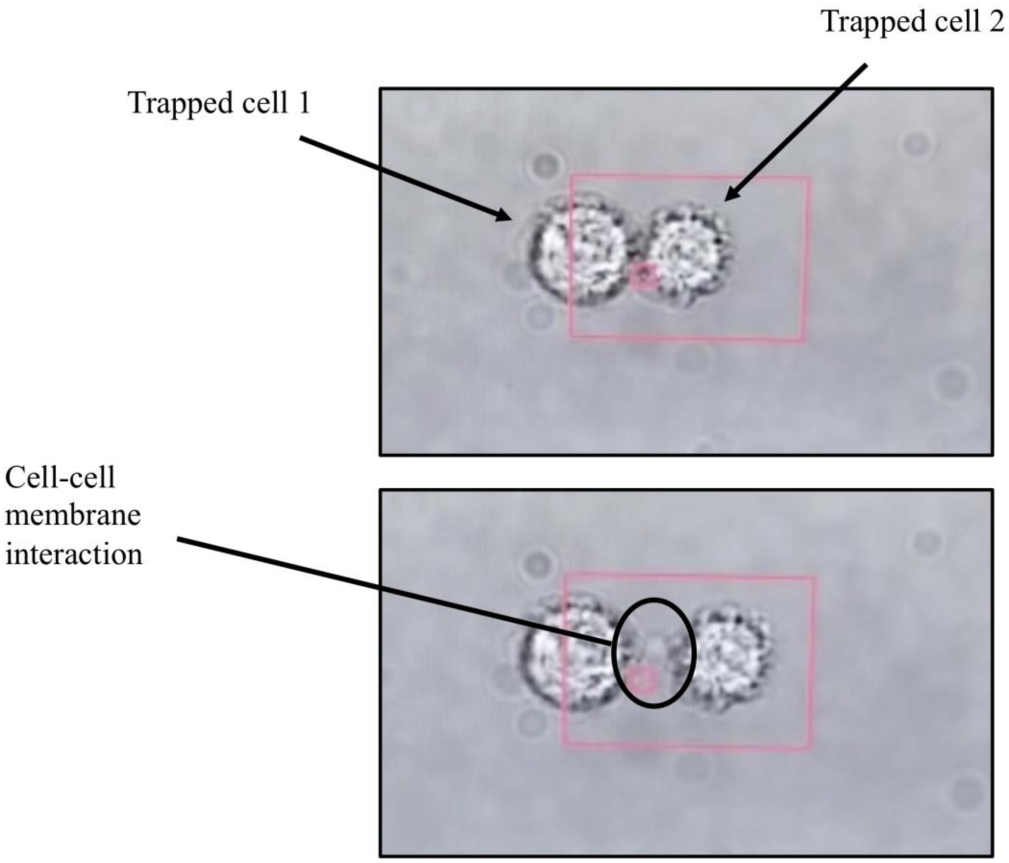

Figure 1.6 Optical tweezers: 2 suspended fibroblasts are trapped by a highly focused laser beam. Trapped cell 1 is kept still while the position of the optically trapped cell 2 can be controlled by the movement of the trap and small forces can be estimated from the changes in the displacement of the cell 2 from the center of the trap.

Traction force microscopy has a great potential in measuring the forces generated by the cell in the surrounding environment. The use of micropillars as well as beads embedded in compliant matrices can serve to detect the force exerted by the cell in a specific environment (Fu *et al.*, 2010; Kraning-Rush, Califano and Reinhart-King, 2012; Chan *et al.*, 2014). Flow deformation cytometry is a novel method to measure the mechanical properties of single cells based on the hydrodynamic deformation of the cell through a microfluidic channel (Gerum *et al.*, 2022). Hundreds of cells can be tracked in a second and differs from the other techniques in its use of suspended cells (Mietke *et al.*, 2015; Otto *et al.*, 2015; Rosendahl *et al.*, 2018).

As above mentioned, AFM is widely used for measuring cell and tissue mechanics. Cell elasticity is extracted by pressing a tip against the cell while the cell indentation and the applied force are monitored. Using the appropriate contact mechanics model considering the tip geometry, cell elasticity is obtained. It can be used for both suspended and adherent cells and allows controlling CO_2 and temperature levels. It is also possible to monitor changes in cell elasticity under pharmacological treatment and the piezo permits to design novel AFM methodologies to measure cell rheological properties (stress-relaxation, creep testing and oscillatory tests) (Fabry *et al.*, 2001; Alcaraz *et al.*, 2003; Darling *et al.*, 2007; Moreno-Flores *et al.*, 2010).

1.1.4 AFM rheological methodologies and theoretical models

Young's modulus is a mechanical parameter that describes the elastic behavior of materials; therefore, when using this parameter to describe cell's mechanical data, it only reflects the elastic properties of cells, which in fact, is far from the cell's real behavior. The cell's cytoplasm can be described as a viscoelastic material. Cells rheological properties can be measured by different techniques described in the previous section; nonetheless, we will focus our attention on the different AFM methodologies that can be employed to extract the cell's viscoelastic properties. Creep response, stress relaxation and oscillatory testing are some of the strategies developed to measure the viscoelasticity of living cells (Papanicolaou and Zaoutsos, 2010; Murata, 2012).

Creep is the tendency of a viscoelastic material to deform slowly but continuously under constant stress (Nwoke, Okokpujie and Ekenyem, 2017). In the case of a viscoelastic material, after stress removal, only the elastic deformation will recover and the viscous deformation will be permanent (Fig. 1.7A). Cells will deform under certain load and will continue deforming until a new equilibrium is reached, although they do not recover their original shape due to viscous deformation. Therefore, in AFM experiments, cell creep behavior can be investigated with the force clamp method (Hecht *et al.*, 2015; Flormann *et al.*, 2021).

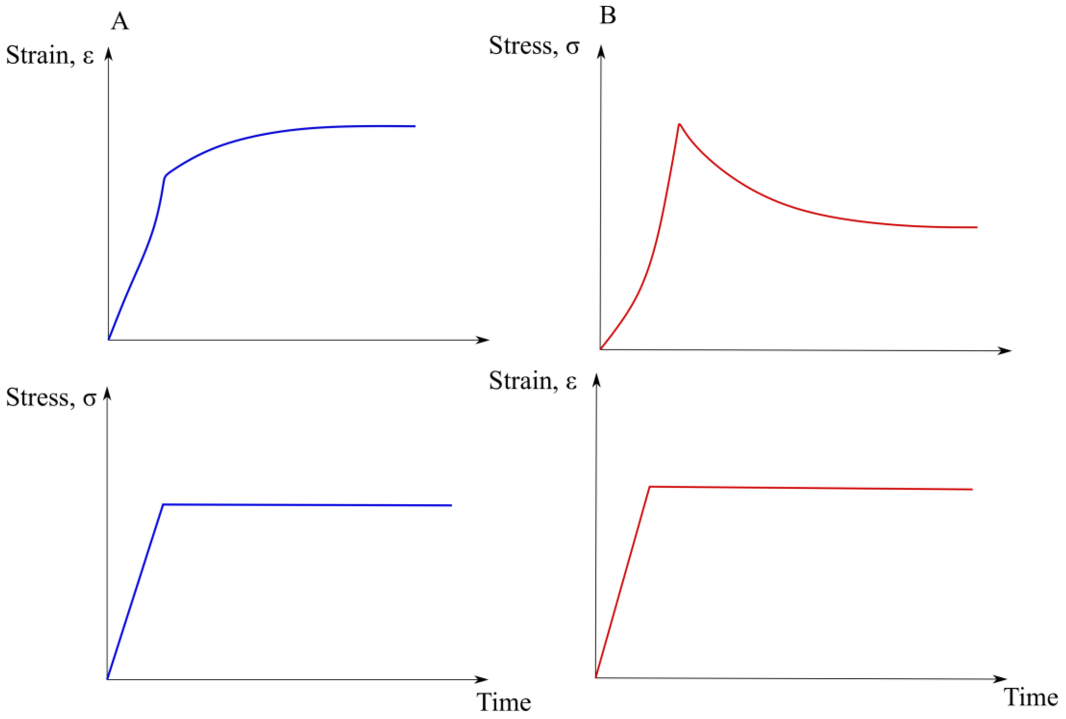

Figure 1.7 A) Creep test measuring the evolution of strain, top blue, under application of a constant stress, bottom blue. B) Stress relaxation scheme, measuring the evolution of stress, top red, over time under constant strain, bottom red.

Stress relaxation is the observed decrease in stress of a material under constant deformation (Fig. 1.7B) (Fancey, 2005). A pure elastic material does not relax over time as it requires constant stress to hold the position, while viscous materials relax instantaneously. The stress relaxation of cells can be investigated with the step response method (Yango *et al.*, 2016).

One of the most robust methods for measuring viscoelastic properties of samples is applying low amplitude oscillations over a wide frequency range to compute the complex elastic modulus E* (Fig. 1.8). For large samples like tissues or hydrogels, rheometers are used to measure the sample viscoelasticity, where the sample is loaded between two plates and the upper plate is oscillated back and forth at a given stress or strain amplitude, and frequency. Using the AFM for samples on the nano or micrometer scale, a similar procedure was developed, in which the cantilever is oscillated up and down at a given frequency or various frequencies and constant amplitude while indenting the sample (Mahaffy *et al.*, 2000; Fabry *et al.*, 2001; Alcaraz *et al.*, 2003; Rigato *et al.*, 2017).

In an oscillatory testing experiment, for a pure elastic material, both stress and strain are known to be in phase. Instead, for a pure viscous material, stress and strain are out of phase by 90°. As previously mentioned, in the case of a viscoelastic material, the phase difference between stress and strain is somewhere between 0-90°. The phase difference between stress and strain allows deciphering the total elastic and viscous contribution to the total material stiffness ($E*$) and specifically, the phase angle δ is a measure of the viscous and elastic properties of the material. This phase angle is often represented as the loss tangent (tan δ), which is a rheological parameter that quantifies the solid- or liquid-like behavior of the sample (Fig. 1.9).

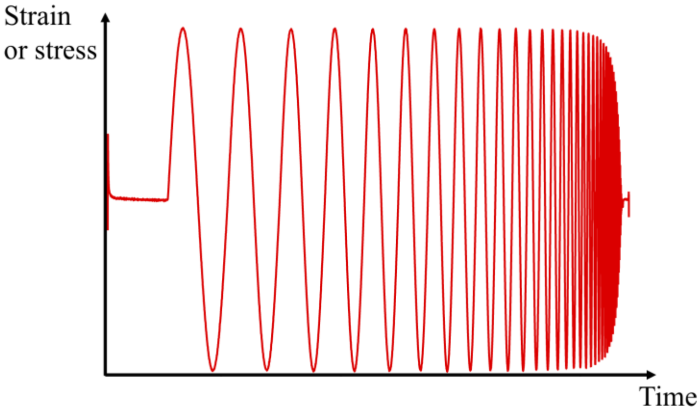

Figure 1.8 Sinusoidal modulation of the AFM z-piezo in an oscillatory test, in which a frequency sweep is applied (See Materials and Methodology section 2.2.2).

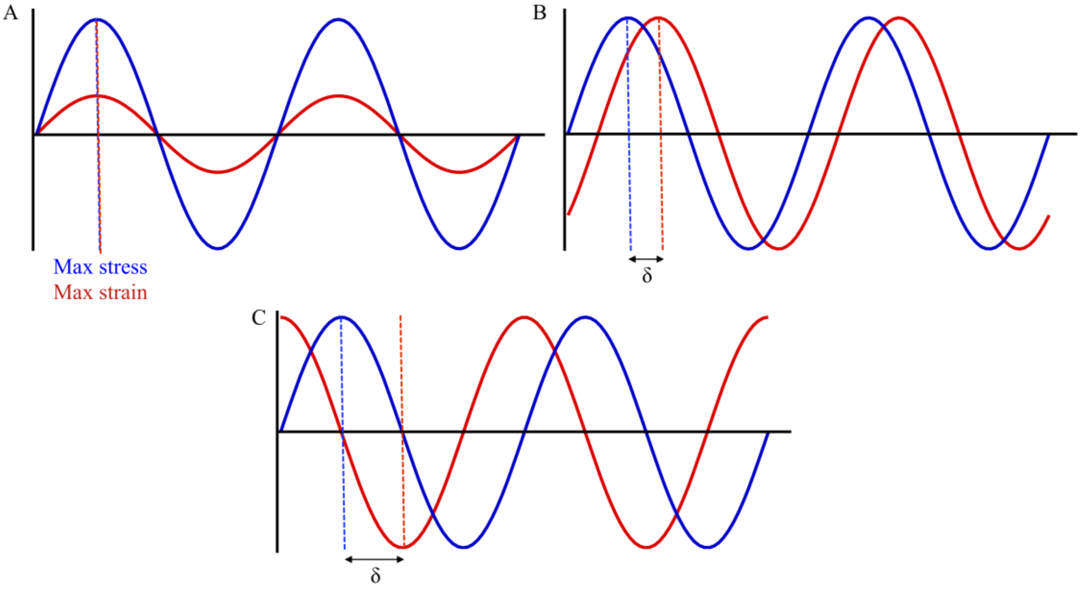

Figure 1.9 Stress and strain wave relation for a pure elastic material (A), viscoelastic material (B) and pure viscous material (C). The phase angle (δ) is 0 for the pure elastic material because both maximum stress and strain are in phase; 90° for the pure viscous because there is a 90° shift from one maximum to the other; and 0< δ< 90° for a viscoelastic material.

The complex elastic modulus or total stiffness ($E*$) can be separated into its real or imaginary components. The real part is known as the storage modulus (E') and represents the energy stored per oscillatory cycle; also depicts the elastic contribution of the sample. The imaginary part is known as the loss modulus (E'') and represents the energy lost per oscillatory cycle and the viscous contribution of the sample (Murata, 2012; Malvern Instruments, 2016).

The time dependence of E’ and E” can be tested by varying the frequency of the applied stress or strain, with high frequencies corresponding to short time scales and low frequencies to longer time scales.

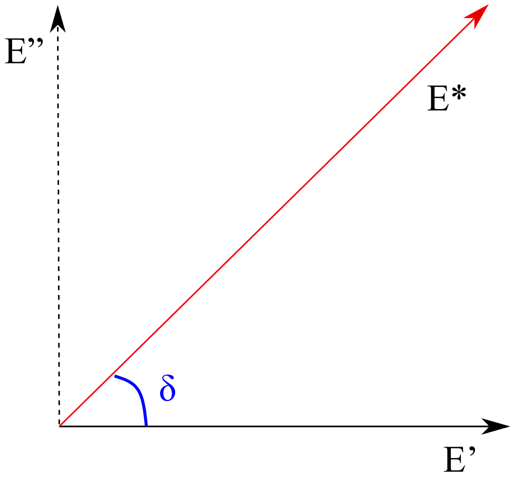

$E' = E^* \cos\delta$ (Eq.1.4)

$E'' = E^* \sin\delta$ (Eq. 1.5)

$E^* = \sqrt{E'^2 + E''^2}$ (Eq. 1.6)

$\tan\delta = \frac{E''}{E'}$ (Eq. 1.7)

Figure 1.10 Graphical relation of the complex modulus E* and its components: storage modulus E' and loss modulus E", which are the real and imaginary part of the complex modulus.

E' and E'' can be calculated from the trigonometric relationship between them and E^* (Fig. 1.10). The loss tangent ($\tan\delta$), also expressed as phase angle or hyteresivity, is the ratio between loss and storage modulus and describes the solid- or liquid-like behavior of the sample. Using an alternative mathematical representation, E^* can be represented as follows:

$$E^* = E' + iE'' \qquad \text{(Eq. 1.8)}$$

This expression makes use of the imaginary number i, differentiating between the real and imaginary parts, E' and E'', respectively.

The oscillatory testing method has been used in AFM measurements to assess rheological behavior of live cells applying oscillations on the cantilever at low amplitude (50 – 100 nm) and different frequencies.

AFM measurements in living cells allow experiments to be performed in liquid environments, using a cell culture medium whose composition is designed to resemble as closely as possible the cell's natural environment. AFM force measurements in liquid are subjected to hydrodynamic drag force artifact that is caused due to viscous friction of the cantilever dragged through the liquid. Therefore, viscoelastic properties measured by AFM taken in liquid at frequencies above 1 Hz can be overestimated if no correction is applied. This correction requires recording the drag factor of the cantilever, b(h), at different distances (h) from the sample while oscillating the cantilever over the sample with a sinusoidal modulation at different frequencies. By plotting the drag factor against the cantilever-sample distance (h) at which the drag factor was calculated, the hydrodynamic drag factor at contact, b(0), can be extrapolated. This parameter depends on the cantilever geometry and on the velocity of the cantilever's free end (Alcaraz *et al.*, 2002). The hydrodynamic drag force can be expressed as follows:

$$F_d = b(0)\nu \qquad \text{(Eq. 1.9)}$$

where F_d is the hydrodynamic drag force on the cantilever, ν is the velocity of the cantilever's free end and $b(0)$ the drag factor at contact. The contribution of hydrodynamic drag in the frequency domain is:

$$\frac{F_d(\omega)}{\delta\,(\omega)} = i\omega b(0) \qquad \text{(Eq. 1.10)}$$

where $i = \sqrt{-1}$ is the imaginary unit, ω is the angular frequency (ω $= 2\pi f$) and $F_d(\omega)$ and $\delta\,(\omega)$ are the Fourier transforms of the force and indentation, respectively.

To describe cell mechanics, the Hertzian contact model and its derivatives are used to extract the cell Young's modulus (Hertz, 1881). However, as above-mentioned, this parameter does not fully represent cell mechanics due to its viscoelastic behavior. For this reason, more developed models have been used to describe the mechanical behavior of cells, such as the linear viscoelasticity model, tensegrity and soft glassy rheology. It is worth mentioning that those models are able to explain certain aspects of cell mechanics, but none of them fully capture the cell mechanical behavior, but since Hertz model is used to calculate cells stiffness, these models are a good compromise to characterize cells mechanical properties.

The first type of models, linear viscoelasticity models, are based on the combination of springs and dashpots, which represent the elastic and viscous contributions, respectively. Some of the most well-known models are Maxwell, Kelvin-Voigt, Zener and Burgers models (Makris and Constantinou, 1991; Nguyen *et al.*, 2011; Jóźwiak, Orczykowska and Dziubiński, 2015). The Maxwell model consists of the combination of one spring and one dashpot in series. This model describes a viscoelastic response dominated by an elastic response at short times and viscous behavior prevailing at longer time periods. The Kelvin-Voigt model combines a spring and a dashpot in parallel. If a stress is applied to a sample that behaves like a Kelvin-Voigt viscoelastic material, it initially behaves like a viscous material due to the effect of the dashpot that retards the spring's behavior; and then behaves elastically over longer time periods. The Burger model describes the viscoelastic behavior of real samples a bit better, as it adds complexity to the model, being just the combination of Maxwell and Kelvin-Voigt models together. Zener model or standard linear solid (SLS) model is a bit more complex than Maxwell and Kelvin-Voigt and involves both springs and dashpots in series and in parallel. Zener model is simplest model that describes both creep and stress relaxation phenomena.

In an oscillatory test, when measuring the elastic and viscous properties (E' and E") of a viscoelastic material described by a Maxwell model at different time scales (sweep in frequency), it shows that E" is greater than E' at low frequencies (liquid-like behavior), whereas at higher frequencies E' is greater than E". This type of behavior is characteristic of viscoelastic liquid materials. When performing the same frequency sweep for a Kelvin-Voigt material, E' is constant and frequency independent, while E" increases with frequency and dominates at high frequencies. This behavior is characteristic of viscoelastic solid materials and tends to be seen in glass-like materials. Burgers model describes a typical viscoelastic spectrum of an entangled polymer system encompassing a wide frequency range. However, with standard techniques, like rheometer or AFM, it is only possible to observe a portion of the spectrum (Wu, Kuhn and Moy, 1998; Bausch *et al.*, 2001).

A more complex theoretical model is the tensegrity model that represents the cell as a mechanically stable structure, composed of struts and cables that endure compression and tension, respectively (Ingber, 1993). The cables create an initial stress, which is supported by the struts, in order to maintain mechanical equilibrium in the system. Extrapolating it to the cell model, microtubules, stress fibers, cell-cell and cell-ECM attachments are viewed as the struts, resisting compressive stress, whereas cables are represented by actin filaments and intermediate filaments, which bear tensional loads. This model identifies mechanical stress supported by the cytoskeleton as one of the most important mechanisms of shape stability within cells and tissues and also describes how cell-ECM interplay is decisive for various cellular functions. Although it realistically explains the structure and function of each cytoskeleton component in live cells, one of its weaknesses is that tensegrity is a static model that may hardly explain active cellular processes (actin polymerization, cytoskeleton rearrangements, cell contraction…). Many studies have used this model to describe strain hardening or prestress stiffening (Wendling, Oddou and Isabey, 1999; Stamenovic, Wang and Ingber, 2006; Benjamin, 2010; Rodriguez and Sniadecki, 2014).

The last model addressed in this section describes cells behavior in terms of the soft glassy rheology, which describes a diverse group of substances like foams, pastes, colloids, emulsions and slurries (Sollich *et al.*, 1997; Sollich, 1998). It is based on Bouchaud's glass model to develop a unified theory. It incorporates characteristics common of all soft glassy materials, such as structural disorder and metastability. This model describes each element of a matrix with an energy landscape presenting many wells of different depths. The well depth is such that it is very difficult for the elements to escape. However, when an external agitation (effective temperature or noise level, x) is applied, it may or may be not sufficient for the elements to hop randomly between wells. If the agitation is enough ($x > 1$), the system becomes disordered and can flow, behaving as a glassy material. Nevertheless, if x approaches to 1, the elements are trapped in the well since the agitation in the matrix is not sufficient to hop off. In this case, the system becomes stabilized and it behaves like an elastic material. The criteria that define soft glassy materials are:

- They have to be very soft
- Storage and loss modulus (E' and E") should increase with the same weak power law ($x - 1 = \alpha$) over frequency.
- Loss tangent ($\tan \delta = \eta$), which is the ratio of loss to storage modulus, is frequency independent and close to 0.1.
- Under certain conditions they display physical aging behavior.

It has been considered that due to the parallelism between live cells and soft glassy materials, the cytoskeleton behavior can be added to this group (Mandadapu, Govindjee and Mofrad, 2008). The complex elastic modulus for soft glassy materials has been described by the structural damping model (Hildebrandt, 1969; Fredberg and Stamenovic, 1989; Maksym *et al.*, 2000; Fabry *et al.*, 2001; Alcaraz *et al.*, 2003):

$$E^*(\omega) = E_0(1 + i\eta)\left(\frac{\omega}{\omega_0}\right)^{\alpha} + i\omega\mu \qquad \text{(Eq. 1.11)}$$

where E_0 and ω_0 are scaling factors for stiffness and frequency, respectively; ω is the frequency in radians, α is the power-law exponent, η is the hysteresivity or loss tangent; μ is the Newtonian viscous term and i the imaginary number (See Materials and Methodology section 2.2.2).

1.2 Cells and fibrotic diseases

1.2.1 Basics in cell mechanics

Cells are living samples and one of the basic structural and functional components of the human body. However, basic is not a representative word for these samples since they are really complex and heterogeneous materials. All eukaryotic cells are composed of plasma membrane, cytoplasm, nucleus and subcellular components. The cell membrane consists of a phospholipid bilayer, in which proteins are embedded. The cytoplasm is made up of the cytoskeleton and organelles (including nucleus) that are essential for basic cell functions, such as gene expression and protein synthesis. The cytoskeleton is mainly composed of three filamentous elements: actin-myosin fibers, intermediate filaments and microtubules (Jamora and Fuchs, 2002; Deng *et al.*, 2006; Fletcher and Mullins, 2010; Pegoraro, Janmey and Weitz, 2017). Cytoskeletal structure is constantly disassembled and remodeled, costing the cell some of its metabolic energy. For example, in the actin polymerization process cells spend one ATP/GTP molecule to connect two proteins to each other (Kollmannsberger and Fabry, 2011). Actin fibers are the cytoskeleton components that mainly govern cell mechanical behavior. Moreover, the rearrangement and number of fibers, as well as number of crosslinks, determine cell mechanics. Actin filaments (F-actin) are flexible helical polymers of G-actin (monomer) presenting a Young's modulus of 1-2 GPa and are an essential part of the cell contractile apparatus. It constitutes between 5-10% of total protein in eukaryotic cells and presents around 7 nm in diameter and several μm in length (Alberts *et al.,* 1994; Fudge *et al.*, 2003). They are commonly found underneath the plasma membrane and are typically assembled at the cell periphery providing mechanical support and determining cell shape, migration and division (Isambert and Maggs, 1996; Cooper, 2000).

The employment of cytoskeletal inhibitors helps to understand the contribution of individual elements to cell contractility, motion and cell shape maintenance.

Latrunculin A and cytochalasin D are inhibitors of actin assembly and polymerization (Coué *et al.*, 1987; Rotsch and Radmacher, 2000; Klymenko *et al.*, 2009). Instead, blebbistatin, ML-7, ML-9 and W-7 are inhibitors of different parts of the myosin network, myosin II, myosin light chain kinase (MLCK) and calmodulin antagonist, respectively (Isemura *et al.*, 1991; Kovács *et al.*, 2004; Sengupta *et al.*, 2007). Latrunculin and cytochalasin cause cell softening produced by the disassembly of stress fibers and reduced cell motion and contraction (Rotsch and Radmacher, 2000; Lekka, 2016). Myosin inhibitors also cause a decrease in cell elasticity due to a reduction in myosin activity leading to the loss of cytoskeletal tension (Rehfeldt *et al.*, 2007; Lu *et al.*, 2008; Martens and Radmacher, 2008). Therefore, actin and myosin need each other to preserve cell mechanical properties as well as cell motion and morphology. The malfunction of any of them, actin filaments or myosin motors, leads to cell disturbance that may be overcome depending on the drug concentration and the cell recovery system. Different drug concentrations produce distinct cell responses, which may also vary from one cell type to another.

1.2.2 Fibroblasts and myofibroblasts

Cells are the basic units of a living system. There are a large variety of cell types but they all have common characteristics. Cells can be sorted into prokaryotic and eukaryotic cells; the main difference between them is that prokaryotes have the genetic material in the cell cytosol while eukaryotes have a nucleus and other membrane-bound organelles. In addition, eukaryotic cells can also be distinguished between animal and plant cells. The human body is composed of multiple cell types that can be grouped by function, location, morphology, etc. Most of them are found in different organs/tissues or parts of the body, such as skin cells including melanocytes, keratinocytes; muscle cells: skeletal, cardiac and smooth muscle cells; blood cells: red and white; fat cells like adipocytes, stem cells, fibroblasts, etc.

Fibroblasts are most commonly found in connective tissue and are the most abundant cell type in the stroma. They have multiple functions, can interact with many other cell types and compose the basic framework for tissues and organs. Fibroblasts are of mesenchymal origin and usually present an elongated spindle-like shape (Plikus *et al.*, 2021; Dick, Miao and Limaiem, 2022). They play an active role in the maintenance and reorganization of the extracellular matrix (ECM) and secrete a diverse group of ECM proteins such as collagen type I, III and IV, fibronectin, laminin, proteoglycans, etc. They present a well-developed cytoskeletal network and are able to feel and respond to mechanical and chemical stimuli. Transmembrane proteins such as integrins and cadherins that connect cell actin-myosin network with the external environment (through focal adhesions and adherent junctions, respectively), make possible the interplay among neighboring cells or its environment that allows to react rapidly to sudden changes.

After the inflammatory phase in the wound formation process, blood-borne cells liberate cytokines and growth factors that are essential for granulation tissue formation (Gabbiani *et al.*, 1972; Desmoulière, Chaponnier and Gabbiani, 2005; Wynn and Ramalingam, 2012). These molecules, along with mechanical changes in the wound area (increase in stiffness), seem to stimulate fibroblast to myofibroblast transition. After the production of a wound, local fibroblasts from the dermis of the adjacent intact tissue start moving towards the wound position and develop bundles of microfilaments containing β- and γ-cytoplasmic actin. This process generates the so-called "proto-myofibroblasts" that evolve expressing α-smooth muscle actin (α-SMA) in the cell body, differentiating into a myofibroblast phenotype (Hinz *et al.*, 2001; Tomasek *et al.*, 2002; Bochaton-Piallat, Gabbiani and Hinz, 2016) (Fig. 1.11). Myofibroblasts are responsible for wound contraction and when the wound is closed, they should disappear through apoptosis or revert to the normal fibroblast phenotype; however, in some diseases, myofibroblasts do not die and stay permanently in the closed area, like many fibrotic diseases, such as scleroderma, liver, kidney and lung fibrosis, as well as infarction (Grinnell, 1994; Desmoulière and Gabbiani, 1995).

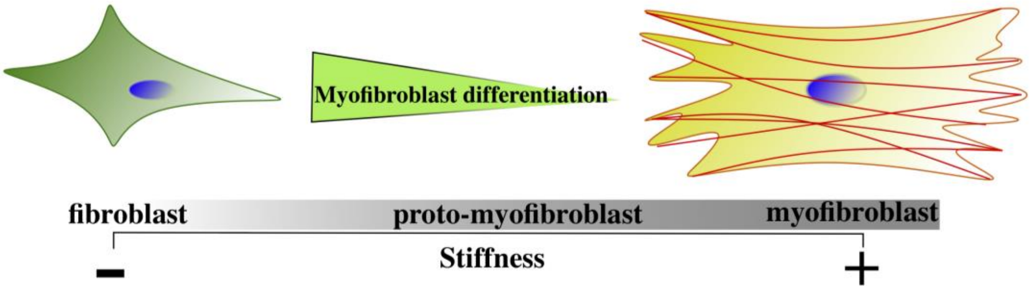

Figure 1.11 Fibroblast differentiation into myofibroblast phenotype, which involves an increase in cell stiffness to due to the formation of extra cytoskeletal filaments (α-SMA) that help in wound healing process.

In addition to α-SMA appearance and organization into stress fibers in the myofibroblast body, there are others myofibroblast biomarkers to distinguish it from any other cell type. In granulation tissue, myofibroblasts start to synthesize ECM components such as collagen I and III, as well as fibronectin splice variant ecto-domain A (Brown *et al.*, 1993; Serini *et al.*, 1998; Tomasek *et al.*, 2002; Singh *et al.*, 2004). The transforming growth factor (TGF)-β1 is essential for the development of α-SMA and is present in the ECM as a latent complex. The release and activation of the TGF-β1 molecule can be mediated through proteolytic enzymes as well as integrin-dependent mechanisms, in which the binding of the latent complex to αv integrin receptors (present only in differentiated myofibroblasts) connects ECM fibers to cell cytoskeleton. The stress generated by the cytoskeleton fibers is enough to liberate TGF-β1 and produce a persistent ECM tension and stiffening (Desmoulière *et al.*, 1993; Klingberg *et al.*, 2014; Hinz, 2015b). When TGF-β1 is liberated, it can bind to its binding site on the cell membrane, triggering a cascade of signaling events that lead to upregulation of α-SMA (Malmström *et al.*, 2004; Hinz, 2007). Integrins, together with other intracellular proteins, organize into focal adhesions that develop into mature focal adhesions on activated myofibroblasts. Mature focal adhesions are 3-4 times stronger and larger (10-30 μm long) than fibroblast focal adhesions (2-6 μm long) providing myofibroblasts with stronger adhesive properties ("more sticky") (Dugina *et al.*, 2001; Hinz *et al.*, 2003; Choi *et al.*, 2008). Some of the proteins that constitute focal adhesion complexes are talin, paxillin, vinculin, α-actinin, etc. These proteins gather at the cell membrane and connect the intracellular integrin domain to cytoskeleton actin-myosin fibers.

In addition to myofibroblasts, smooth muscle cells also express α-SMA that has given rise to question about the origin and function of myofibroblasts. Smooth muscle (SM) cells have been in the spotlight to understand myofibroblast origin; however, there are many features that differentiate them. SM cells express markers that are not present in myofibroblasts, such as SM myosin heavy chain, h-caldesmon and smoothelin (Arnoldi *et al.*, 2012). Moreover, SM cell contraction is rapid and short, whereas myofibroblast contraction is long and permanent, highlighting the different functional activities of the cells (Gabbiani *et al.*, 1972).

Many strategies have been developed to revert the myofibroblast phenotype, like downregulation of α-SMA using TGF-β1 antagonists and growth factors (interferons, interleukins, tumor necrosis factor (TNF)-α) (Siwik, Chang and Colucci, 2000; Lowin *et al.*, 2020). Interleukin-1 showed an influence on the expression of α-SMA in dermal fibroblasts (Shephard *et al.*, 2004; Kanangat *et al.*, 2006). Furthermore, interferon (IFN)-γ, a cytokine produced by T cells, was proposed to suppress α-SMA expression in myofibroblasts, although the results only suggested changes in α-SMA expression in TGF-β1-induced myofibroblasts but not in already differentiated myofibroblasts (Tanaka *et al.*, 2001, 2003, 2007; Gu *et al.*, 2004). IFN-γ seems to activate YB-1 repressor protein, which inhibits Smad3-enhanced gene transcription and upregulates the transcription of Smad-7 (inhibitor of Smad3) (Higashi *et al.*, 2003; Dooley *et al.*, 2006). New approaches focusing on the inhibition of myosin contraction have shown to disassemble α-SMA from stress fibers while β-cytoplasmic actin filaments persist intact (Goffin *et al.*, 2006).

Matrix compliance and cell-cell interactions are also mechanisms for myofibroblast de-differentiation. ECM softening is transmitted to cells via focal adhesions leading to cellular stress release; thus, inducing either myofibroblast apoptosis or myofibroblast de-differentiation. Cell-cell interplay in myofibroblasts takes place via OB-OB-cadherin junctions (which are only present in myofibroblasts) that may propagate a downstream signal that leads to a decrease in the α-SMA expression (Petridou *et al.*, 2000; Jamora and Fuchs, 2002; Yap and Kovacs, 2003).

1.2.3 Fibrosis

Around 45 % of the mortality in Western developed countries is caused by fibrotic diseases and almost every organ of the human body can be affected by fibrotic reactions (Wynn, 2008; Rosenbloom, Castro and Jimenez, 2010; Wynn and Ramalingam, 2012; Rockey, Bell and Hill, 2015). These fibrotic reactions cause multi-system diseases, such as system sclerosis as well as fibrotic disorders of individual organs like lung, kidney, liver, heart and bladder as well as Dupuytren's disease (Varga and Abraham, 2007; Gabrielli, Avvedimento and Krieg, 2009; Ho *et al.*, 2014). Fibrosis is also involved in chronic autoimmune diseases such as scleroderma, Crohn's disease, ulcerative colitis, rheumatoid arthritis, etc. It is also implicated in tumor invasion and metastasis. The causes of fibrosis are not well identified but can include a variety of stimuli including persistent infections, autoimmune reactions, allergic responses, chemical insults, radiation and tissue injury.

The appearance of fibrotic diseases is quite diverse, but they all share common alterations like uncontrolled accumulation of ECM and myofibroblasts. Myofibroblasts can originate from various cell types. The major contribution comes from fibroblasts originating from the local connective tissue. In the liver, apart from portal fibroblasts, hepatic stellate cells also can differentiate into myofibroblasts (Guyot *et al.*, 2006). Fibrocytes, circulating cells, have been shown to produce ECM and acquire a myofibroblastic phenotype, helping in the formation of hypertrophic scar. These cells have been seen in pulmonary fibrosis observed in asthma (Schmidt and Schmieder, 2003; Yang *et al.*, 2005) and renal fibrosis (Okada *et al.*, 2005). Mesenchymal stem cells, like bone marrow cells, have also been shown to contribute to the maintenance and regeneration of connective tissue (Pittenger *et al.*, 1999;

Forbes *et al.*, 2004). Pericytes were also found to differentiate into myofibroblasts and are one of the major contributors to liver and kidney fibrosis (Mederacke *et al.*, 2013). Moreover, endothelial and epithelial cells via endothelial- and epithelial-to-mesenchymal transition, a marker of cancer progression, have also been included in the list of myofibroblast precursors (Hinz, 2007; Arnoldi *et al.*, 2012).

Nowadays, there are many strategies to treat fibrosis, like specific drugs for each type of fibrosis, although in most cases they only serve as a palliative solution rather than curing the damage; and organ transplantation when there is no organ cure. Epigenetic modifications and miRNAs could serve as therapeutics targets; however, combined therapies that target many mechanisms will probably be the best option.

1.2.4 Dupuytren's disease

Dupuytren's disease is a benign fibrotic disease of the palm that results in the formation of nodules and cords in the palmar fascia. The prevalence of Dupuytren's disease in the world varies from one research source to another; however, it is low in comparison to many other diseases (1-8%). This percentage increases with patient's age, affecting 20% of the population above 65 years old. In the early days, it was erroneously called "*Viking disease*" because it was recorded more frequently in Nordic descendants, but far from the reality, since there is no clear evidence of higher prevalence in any continent or ethnicity (Hart and Hooper, 2005).

This disease was discovered by Felix Plotter in 1614 and named after Baron Guillaume Dupuytren, a French anatomist and surgeon who was the first to describe the underlying mechanism. Although he gained popularity for treating Napoleon Bonaparte's hemorrhoids, today he is known for being the first to operate a person who suffered from Dupuytren's disease in 1831 and published it in "*The Lancet*" in 1833 (Dupuytren, 1833).

The disease is more common in older man and environmental risk factors like alcohol abuse, smoking, hand injuries, aging, hypertension, diabetes as well as family history favor the appearance of the disease (Descatha *et al.*, 2012; Becker *et al.*, 2016; Morelli, Fraschini and Banfi, 2017; Broekstra *et al.*, 2018).

The existing treatments can be classified into invasive and non-invasive treatments. Some of the non-invasive options are needle aponeurotomy and collagenase injection. Needle aponeurotomy is a procedure that makes use of a sharp needle to make holes in the damaged tissue weakening it and helping to straighten bent fingers. This technique is used for mild cases; however, it has a recurrence rate of 60% (Badois et al., 1993; Foucher et al., 2001; van Rijssen *et al.*, 2006). Collagenase injection uses the combination of two *Clostridium histolyticum* collagenases for the treatment of adult patients. These enzymes hydrolyze type I and II collagen into small peptides, which facilitates its later degradation by endogenous human collagenases (Hurst *et al.*, 2009; Warwick, Thomas and Bayat, 2012). Although it seems to be useful in reducing nodule size and hardness, it is still unclear how effective this procedure is. Nowadays, the most used and efficient treatment is surgical removal of the damaged area. This procedure also allows researchers to have access to tissue samples directly from patients, providing exclusiveness.

Dupuytren's disease is a fibroproliferative disease of the hand and fingers, which begins with the formation of nodules in the palmar fascia and develops to the formation of cords, which eventually causes one or more fingers to bend and remain immobile (Fig. 1.12). It is not a malignant disease but it decreases quality of life and hampers people to carry out normal daily activities such as holding objects, stretching out hands or putting gloves. In the palmar and digital fascia of Dupuytren's disease patients was shown an accumulation of contractile fibroblasts "myofibroblasts" and enhanced synthesis of ECM proteins, like collagen type I and III and fibronectin.

Figure 1.12 Finger flexion progression in Dupuytren's disease.

It is widely accepted the classification of the disease in three stages:

1) Proliferative stage: proliferation of myofibroblasts and formation of nodules.
2) Involutional stage: myofibroblasts align along lines of tension.
3) Residual stage: tissue becomes acellular and devoid of myofibroblasts, only remaining thick fibers of collagen.

As explained in the section 1.2.3, one of the main characteristics of fibrosis is the permanency of myofibroblasts in the wounded area after healing. In Dupuytren's disease, accumulation of myofibroblasts also takes places, due to a deregulation in myofibroblasts death mechanisms (apoptosis) or the inability of returning to their original state. Myofibroblasts are α-SMA positive fibroblasts that present higher contractile abilities than normal fibroblasts, since they are involved in the wound healing process. The expression of α-SMA in myofibroblasts body increases their stiffness and contractile mechanisms. α-SMA expression can be stimulated by TGF-β1 activation that, as mentioned above, is released from its latent state with changes in ECM mechanical properties and cytokines expressed by blood-borne cells. Myofibroblasts are responsible for depositing large amounts of excess ECM and especially type III collagen deposition, leading to changes in the type I/III collagen ratio, alongside with fibronectin deposition. Moreover, an imbalance between metalloproteinases and tissue inhibitors of metalloproteinases has also been implicated on Dupuytren's disease, leading to excess collagen in tissue. Metalloproteinases are a group of enzymes that break down certain proteins such as collagen; therefore, their regular function and presence is essential for the regular secretion and decomposition mechanisms of the ECM.

Similar to other fibrotic diseases, myofibroblast differentiation in the damaged tissue comes accompanied by stiffening of the surrounding ECM. Cell-ECM interplay through integrin focal adhesions connects the cell cytoskeleton to ECM fibers; therefore, any change in myofibroblast contraction is transmitted to the ECM and vice versa. Previous studies have demonstrated that TGF-β1 increased the stiffness of differentiated myofibroblasts from Dupuytren's tissue (Viji Babu *et al.*, 2018). Hence, myofibroblasts sense and respond to biochemical, physical and mechanical stimuli from the ECM. Thus, myofibroblasts are capable of modulating their mechanical properties to the stiffness of the underlying substrate.

Dupuytren's fibroblasts have also been inserted into 3D matrices, especially made of collagen I, as it is the main component of connective tissue. The stiffness of the new synthesized ECM in wound healing presents values around 10-100 Pa (Grinnell, 2003; Carlson and Longaker, 2004; Kaufman *et al.*, 2005). The mechanical properties of fibroblasts seeded in the previous matrix did not present contractile fibers and presented dendritic extensions. When increasing the stiffness of the gels, fibroblasts tension increased and started to form stress fibers (Tamariz and Grinnell, 2002; Marenzana *et al.*, 2006). Thus, ECM stiffness drives myofibroblasts mechanical properties (Yeung *et al.*, 2005). Previous studies suggested that stress fibers formation in fibroblasts occurs when the surrounding environment presents around 3-6 kPa in stiffness and they differentiate into myofibroblasts on substrates of 20 kPa and more (Goffin *et al.*, 2006). All these findings suggest the importance of ECM stiffness in myofibroblasts differentiation and activation; therefore, in Dupuytren's disease progression. Dupuytren's fibroblasts in 3D collagen matrices seemed to be in a latent state, as they did not exert measurable ECM contraction, displaying contractile properties similar to those of normal fibroblasts.

The next chapters (3, 4 and 5) deal with individual research experiments, in which the acquisition of mechanical properties of cells in different environments was sought. The mechanical properties of three different primary fibroblasts, all-coming from the palm of the same patient were investigated (normal/healthy, scar and Dupuytren fibroblasts). Normal fibroblasts were extracted from the dermal region, scar from the wounded area and Dupuytren fibroblasts from the nodules of palmar fascia. In each chapter, different approaches were used and cells were exposed to different environments in order to extract different information that could help in the understanding of the disease and in future strategies for finding a cure.

1.3 Extracellular matrix (ECM) and cell-ECM interplay

1.3.1 ECM composition

The extracellular matrix (ECM) is the cell's surrounding environment and acts as a structural scaffold of cells. It is a dense mesh composed of a mixture of proteins, such as fibronectin, collagen and laminin; and acts as a reservoir for many signaling molecules that modulate several cellular functions, like the transforming growth factor (TGF) β-1 and the tumor necrosis factor (TNF)-α (Labat-Robert, Bihari-Varga and Robert, 1990; Aumailley and Gayraud, 1998a; Bosman and Stamenkovic, 2003). The ECM is a highly dynamic structure and it is crucial in determining many cellular behaviors, such as proliferation, adhesion, migration, polarity, differentiation and apoptosis (Lu et al, 2011; Mecham, 2012). The ECM is composed by proteins secreted by neighboring cells, giving rise to different ECMs in the human body that are different in composition, fibers organization and distribution, as well as in mechanical properties. Different cell types secrete distinct ECM proteins; for example, fibroblasts mainly synthesize types I and III collagen and minor amounts of other collagens, fibronectin, elastin and laminin (Camelliti, Borg and Kohl, 2005). Chondrocytes, at the proliferating stage, synthesize type II collagen and aggrecan that generate strong bonds with water molecules forming a stable matrix that resists compressive and tensile stress (Lane Smith et al., 2000; Erlebacher *et al.*, 1995).

Osteoblasts, derived from mesenchymal cells in the bone marrow, secrete a mixture of ECM proteins, with type I collagen being the most abundant. Therefore, the ECM surrounding the different cell types presents different mechanical properties owing to the matrix composition that is defined depending on the compressive and tensional forces to which they are subjected.

Collagen is the major component of the ECM, being observed at least 20 types. It is the most prevalent protein in mammals and constitutes one-third of all protein present in humans. All collagens exhibit a repeating Gly-X-Y motif (wherein X and Y may be substituted with any aminoacid, but most frequently with proline and 4-hydroxyproline, respectively). This repeated Gly-X-Y sequence allows the assembly of three left-handed polypeptide strands into a right-handed triple helical molecule, thereby forming the characteristic structural organization of collagen molecules (Fig. 1.13) (Lee, Singla and Lee, 2001; Shoulders and Raines, 2009). Collagen type I, II and III are the most abundant in the human body; collagen I is found in almost all tissues, while type II is mainly found in cartilage. Collagen III is usually seen together with collagen type I aggregated in fibers in tissues like tendons, ligaments, skin and blood vessels (Hulmes, 1992; Eyre, 2004). In addition to collagen, many adhesive proteins are also present in the ECM playing important tasks. Fibronectin is also abundant in the cell environment, especially fibroblasts, helping in cell-ECM interaction and cell motion and differentiation (Mostafavi-Pour *et al.*, 2003). Laminin and vitronectin are also involved in cell-ECM attachment while tenascin contributes to cell spreading and elastin to tissue fibers elasticity (Aumailley and Smyth, 1998b; Chowdhury *et al.*, 2003).

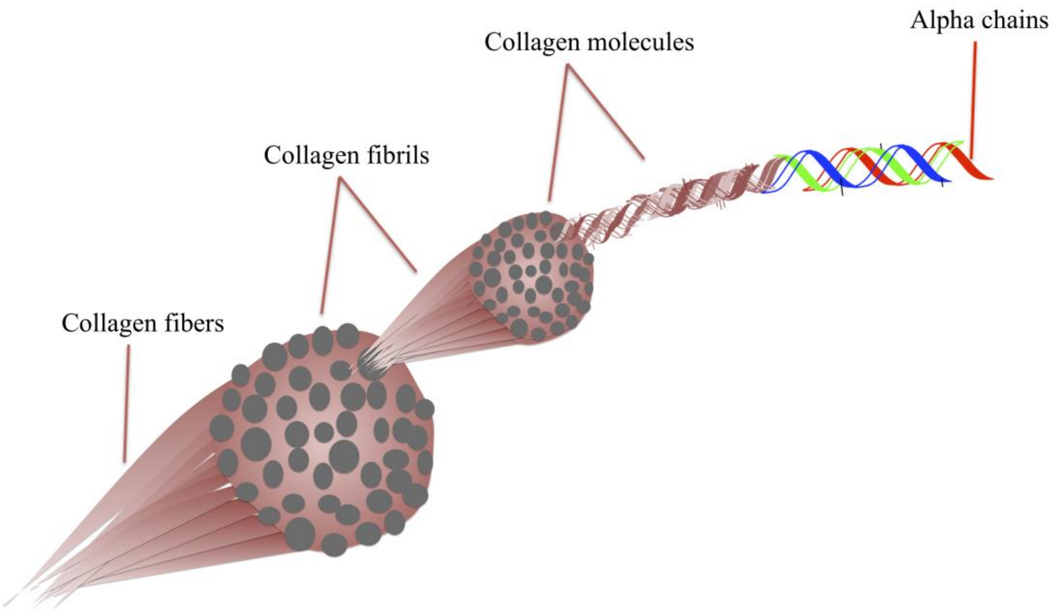

Figure 1.13 Scheme of a collagen fiber composition. From fiber to individual chains that composed the right-handed triple helical molecule.

1.3.2 Cell-ECM interplay

There are many ECM properties that play a critical role in its physical properties and in cell behavior, such as, stiffness, pore size, density and topography. The stiffness of the ECM is mainly determined by collagen fibers (arrangement and number of fibers and crosslinks) and is in the same order of the stiffness of the surrounding cells. The ECM serves as a scaffold for cells and cell-ECM interaction is performed through focal adhesion points, which are made of several membrane proteins, including integrins. As before mentioned, integrins are responsible of sensing changes in ECM mechanical properties, as they connect extracellular ECM to cell cytoskeleton network. Distinct ECM stiffnesses trigger different cellular responses. Stiff ECMs produce a chain reaction inside the cell body, leading to focal adhesion proteins clustering and activating cell proliferation and contractility. Furthermore, different ECMs stiffnesses could induce different cellular behaviors. Mesenchymal stem cells differentiate into neurons on soft ECMs but differentiate into osteoblasts on stiff ECMs (Engler et al., 2006). The area of these focal adhesions is in the order of 1-2 μm^2 and the size and strength depend on the mechanical properties and biochemical composition of the ECM. The combination of cells and its ECM constitutes a tissue, and cell-ECM interplay is crucial for tissue stabilization (Choquet, Felsenfeld and Sheetz, 1997; Gallant, Michael and García, 2005).

Cell-ECM interplay has a bidirectional response. Cells secrete and remodel ECM that leads to ECM modulation in terms of composition and physical properties. In return, ECM sends and transmits signals through the matrix to reach and influence cell behavior. Focusing in mechanical changes, cells sense external mechanical forces and react to them, transferring and converting them into cell biochemical signals that are still unknown. As already mentioned, cell-ECM interaction through integrins that activates a downstream response leading to a clustering of molecules inside the cell body that connect to the cell cytoskeleton is the most accepted hypothesis. These molecules, that are part of the focal adhesion complexes, are paxillin, talin, vinculin and filamin, gather and interact with integrins that present an ECM, cytoplasmic and transmembrane domains facilitating ECM-cytoskeleton connection (Jockusch *et al.*, 1995; Critchley, 2000; Wehrle-Haller, 2012). Therefore, changes in cytoskeleton strength are transmitted to the ECM and vice versa, ECM mechanical modulations are also transmitted to cells, which adapt their stiffness to that of the environment. Aside from variations in cells mechanical properties, changes in ECM stiffness also produce changes in the cell biochemical response. Alterations in the cell-ECM interaction are related to many diseases, leading to irregular ECM compositions, fibers orientation or abnormal cell behavior. All these anomalous situations can be measured with different techniques such as shear force rheometry, magnetic force spectroscopy, AFM, etc (Meyvis *et al.*, 2002; Passeri *et al.*, 2014; Mandal, 2020). These techniques are able to produce enough stress to deform the sample and measure its response using large probes encompassing large scan areas.

The individual cellular response to the matrix stiffness can be also assessed using traction force microscopy, optical and magnetic tweezers, AFM, among others (Neuman and Nagy, 2008; Zhang and Liu, 2008; Franck *et al.*, 2011; Kilinc and Lee, 2014; Style *et al.*, 2014).

The cell-ECM interplay governs many cellular activities; however, cell-cell interaction is also fundamental for regular cell behavior. Cell-cell interaction, as above-mentioned, takes place through cadherins, transmembrane receptors presenting extracellular regions, which makes possible cell-cell attachment. Similar to integrins, cadherins also form complexes bound to the cytoskeleton. Adherent junctions is the name given to the linkage between actin fibers and cadherin complexes, which are extremely important in cell mechanical response (Knust and Bossinger, 2002). For example, in vitro, as well as in vivo conditions, when cell population is getting crowded, cells communicate to each other to slow down the multiplication process and enter in a resting state. This communication takes place through cell-cell cadherins interaction. Accordingly, cell-cell and cell-ECM interaction are essential for normal cell functioning, tissue formation and organ function.

1.3.3 Modulation of ECM/hydrogels mechanics

Under natural conditions, cells are surrounded by neighboring cells and ECM. The 2D environment, in which cells are plated on ECM-like substrates, is very popular in research. Many studies have compared healthy cells and pathological counterparts behavior in matrices of different stiffness (Rianna and Radmacher, 2017a; 2017b; McKenzie *et al.*, 2018; Xie *et al.,* 2017). Many of these studies use synthetic polymers, such as polyacrylamide or PDMS, due to the ease of modulating their mechanical properties. The use of some ECM proteins, such as collagen and hyaluronic acid, are also popular as 2D scaffolds to assess cells behavior in compliant matrices. However, unfortunately matrices using these proteins are difficult to increase in stiffness. The employment of ECM from the cells' natural environment is the most complete environment to study cellular behavior under natural conditions, since both mechanical and biochemical composition are preserved. Nevertheless, obtaining tissue samples from which the real ECM can be extracted is not easy for research purposes. Therefore, the use of ECM proteins to generate matrices for research is the closest environment to natural ECM.

Collagen is one of the most widely used ECM proteins to make matrices/hydrogels due to its biocompatibility and similarity to the natural ECM. Hydrogels made only of collagen, have the problematic of presenting low mechanical properties. However, it exists many approaches to increase collagen hydrogels mechanical properties. Typically, one way to increase hydrogels stiffness is increasing the number of crosslinks, with physical and chemical crosslinking approaches being the most popular methods. Physical crosslinking methods encompass changes in pH and salt concentrations, collagen concentration, gelation temperature, fiber orientation and UV-crosslinking. Inside the chemical crosslinking agents include glutaraldehyde, isocyanates, carbodiimides, polyethylene glycol, genipin and molecules like glucose and ribose (glycation) (Sarrigiannidis *et al.,* 2021).

In collagen fibrillogenesis, pH is a critical parameter as it defines collagen fibrils dimensions and final gel mechanical properties. Collagen isoelectric point (pI) is 9.3; when the pH solution is equal or more basic than the collagen pI, the formed collagen gel shows thinner fibers but smaller pore size and stiffer mechanical properties (Wood and Keech, 1960; Silver, 1983; Li *et al.,* 2009). However, at acidic pHs, collagen fibers in the gels are shorter and thicker, but presents a larger pore size, leading to weaker strength and softer gels. Collagen gelation temperature also influences fibers properties. Many studies use 37°C to generate collagen hydrogels, which provides thinner, shorter and randomly distributed collagen fibrils. Instead, using low temperatures, such as 4°C, thicker, longer and well-aligned fibrils can be observed (McCoy *et al.,* 2016; Seo *et al.,* 2020). UV crosslinking requires UV light to activate a photoinitiator molecule that will trigger the binding between the crosslinking molecules, leading to collagen fibers crosslink. By exposing a photoinitiator to light of the appropriate wavelength, it generates free-radical reactive species. These radicals activate specific functional groups of the crosslinking molecules, making them accessible for chemical interaction. Methacrylate anhydride and methacrylic acid are some of the crosslinking molecules used for increasing collagen hydrogels crosslinking. Irgacure and LAP (lithium phenyl-2,4,6-trimethylbenzoylphosphinate) are some of the most common photoinitiators and can be activated by exposure to 365 and 405 nm UV light, respectively (Nichol *et al.,* 2010; Drzewiecki et al., 2014; Nguyen, Watkins and Kishore, 2019). In addition, there are molecules that do not need the help of a photoinitiator and react directly upon UV exposure as they already present photoreactive groups, such as aryl-azides, benzophenones, etc.

As before mentioned, many molecules have been used to increase collagen hydrogels crosslinking. Glutaraldehyde was one of the first used; however, nowadays, it is well known that it generates cytotoxic monomers over time (Cheung and Nimni, 1982; Sheu *et al.,* 2001). Isocyanates, carbodiimides and polyethylene glycol are good alternatives to glutaraldehyde, as they do not produce toxic by-products, are biocompatible and are under evaluation for biomedical applications (Weadock, Olson and Silver, 1983; Olde Damink et al., 1995; Zhu, 210).

Glucose or ribose have also been used to induce collagen crosslinking by glycation. This method has the advantage of employing non-toxic molecules (Francis-Sedlak *et al.,* 2009; Vicens-Zygmunt *et al.,* 2015). The use of natural-plant extracts like genipin has been also evaluated for increasing collagen crosslinking. Genipin is a natural compound extracted from *Gardenis jaminoides Ellis* fruits that, upon polymerization, releases blue pigments that cause collagen hydrogels to acquire a blue color. Its cytotoxicity is concentration-dependent, thus high concentrations could cause cell damage or death (Sundararaghavan *et al.,* 2008; Zhang *et al*., 2014; Kwon *et al.,* 2015).

All these physical and chemical crosslinking methods for collagen hydrogels can be used to tune 2D hydrogels, in which cells are seeded on top of the gel. However, when generating 3D hydrogels, in which cells are to be inside, some of the previously mentioned methods to increase collagen crosslinking are not available for all cell types due to their cytotoxicity (Fig. 1.14). 3D hydrogels provide cells of 3D spatial confinement (constraints) and biochemical and mechanical signals in all directions. 3D hydrogels resemble more tissue-like conditions; therefore, studying cells responses in environments close to their natural conditions is something that we, as scientist, should look for.

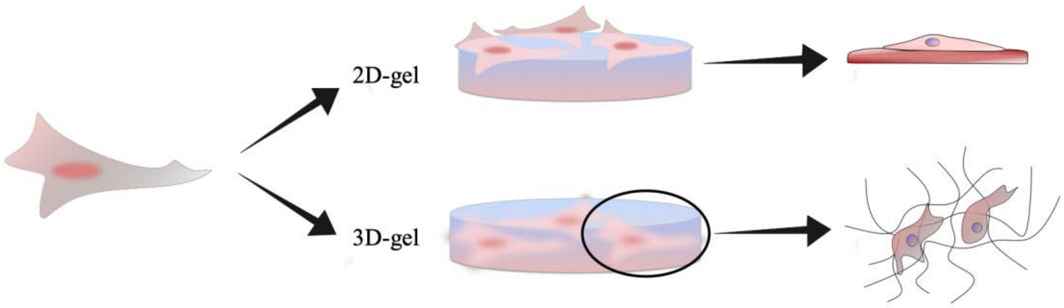

Figure 1.14 Drawing of cells in 2D and 3D hydrogels.

1.4 Enzymatic inhibition

Enzymes are molecules that reduce the required amount of energy (activation energy) needed to overcome the transition state of a chemical reaction and convert reactant molecules (substrates) into products. In other words, it helps the reaction to be faster (Illanes, 1999). Enzyme inhibitors are molecules that interact with the enzyme (temporary or permanently) causing a reduction or prevention of normal enzymatic catalytic activity. There are at least three types of inhibition: competitive, non-competitive and uncompetitive (Strelow *et al.*, 2012). In a competitive inhibition the inhibitor has similar shape to that of the substrate; therefore, it competes with the substrate for the active site of the enzyme. If the process is reversible, then the binding of the inhibitor is temporary, but it can also be permanent (irreversible), and the inhibitor binds covalently to the active site of the enzyme leading to a complete enzyme inhibition. If it is reversible, inhibitor-enzyme interaction will have a limited lifetime and after that the active site of the enzyme will again be available for the substrate. The Michaelis-Menten constant (k_M) is the concentration of substrate needed to achieve half of the maximum velocity (V_{max}), in other words, is a measure of the affinity of the enzyme for the substrate. The V_{max} is the maximum reaction rate or velocity of an enzymatically catalyzed reaction when the enzyme is saturated with its substrate and is determined from Lineweaver-Burk plot. In a competitive inhibition, k_M increases, which means that the affinity of the enzyme for its substrate decreases and V_{max} does not change. In a non-competitive inhibition, the inhibitor binds to the enzyme in another place different from the active site (Fig. 1.15). This binding produces changes in enzyme structure also leading to changes in the active site that make it difficult for the substrate to enter or the substrate can enter but the interaction is less efficient than under normal conditions. This type of inhibition is independent of the substrate concentration and in this case, V_{max} decreases but k_M remains constant (Fig. 1.16). The last case, uncompetitive inhibition, the inhibitor can only bind to the enzyme-substrate complex, turning into enzymatically inactive (Fig. 1.17) (Kuddus, 2019). For this type of inhibition, both k_M and V_{max} decrease, meaning that the affinity for the substrate increases but the rate of the reaction goes down.

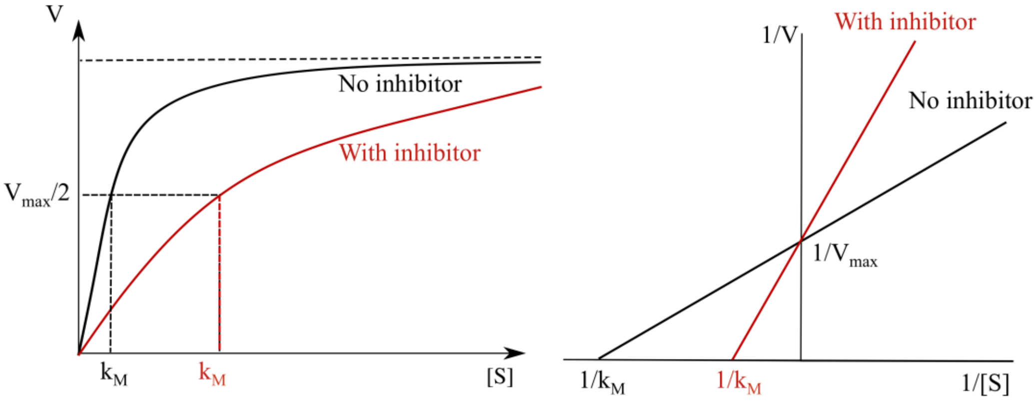

Figure 1.15 Competitive inhibition and Lineweaver-Burk plot.

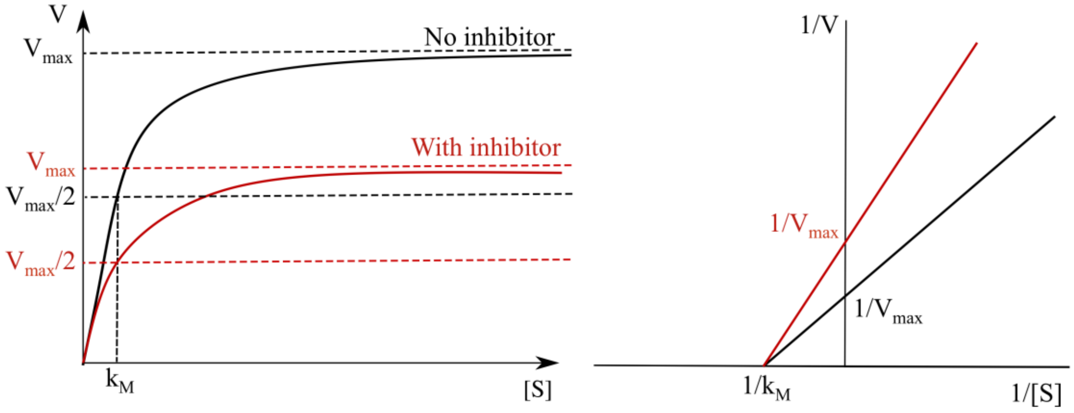

Figure 1.16 Non-competitive inhibition and Lineweaver-Burk plot.

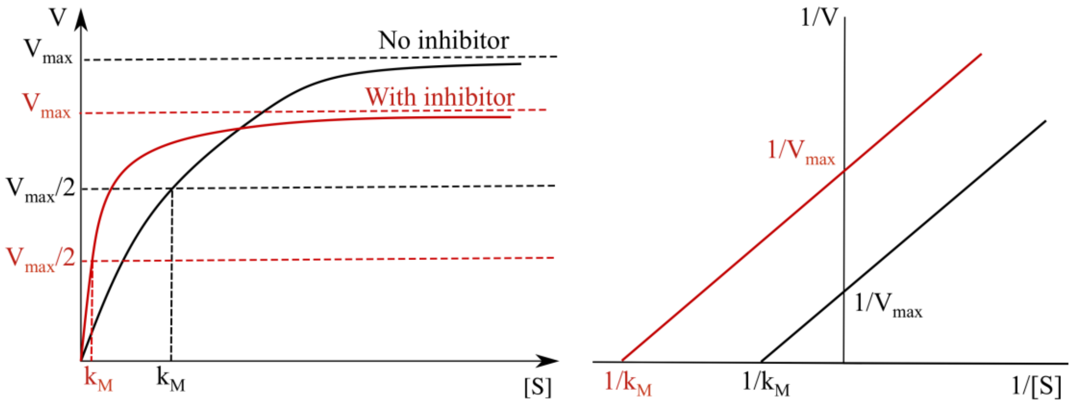

Figure 1.17 Uncompetitive inhibition and Lineweaver-Burk plot.

1.5 Micropatterning

Micropatterning is a technique based on the generation of adherent µm-sized features with specific geometries on a surface that serve to study the influence of the microenvironment on cell behavior. This technique allows limiting cell size, tuning cell shape, cell division, orientation and controlling the interaction with adjacent cells (Chen, 1997; Théry, 2010; Van Dongen *et al.,* 2013).

Micropatterning is a useful approach to control cell mechanical behaviour. Unlike cells seeded in infinite petri dishes, micropatterns provide limited space for the cell to spread; therefore, all cells present the same shape. In a well-defined environment, the cell body and cytoskeleton adapt to the geometrical constraint, exhibiting more consistent and reproducible cellular features than in unlimited spread spaces. Furthermore, micropatterns can be employed to mimic cells spatial constraints in tissue, providing greater resemblance to tissue-like conditions. The employment of a geometrical shape similar to that of the tissue environment best resembles cell's natural conditions; however, the use of pattern shapes far from cells' natural geometry could serve to induce pathological conditions. In addition, geometrical shapes far from cells' natural environment can be used to assess cells' cytoskeletal arrangements and correlate it with local mechanical properties (Young's modulus) (Rigato et al., 2015).

The patterned surface is coated with some ECM protein or synthetic polymer that enhances cell attachment. Some of the ECM proteins employed to increase cell adhesion are collagen I, II and IV, elastin, fibronectin, laminin and vitronectin (Kleinman, Klebe, Martin, 1981; Kleinman et al., 1987; Preissner, 1991). Moreover, some ECM proteins further enhance the adhesion of specific cell types, such as collagen I and fibronectin, which are used to ameliorate fibroblast attachment. In addition, poly-lysine and poly-L-ornithine are synthetic polymers that also facilitate cell attachment to bare surfaces (Mazia, Schatten and Sale, 1975). There are many micropatterning processes, such as photolithography, micro-contact printing, etc. Photolithography is a technique that makes use of light or deep UV-light and a photomask that contains the geometric design. Photomasks are typically made of fused silica or synthetic quartz covered with chromium or Fe_2O_3 that define the pattern geometry. The substrate to be patterned is usually coated with a photoresist or anti-fouling layer that is removed after light exposure, giving the geometric pattern of the photomask (Fig. 1.18) (Fink et al. 2007; Azioune et al., 2010; Yilbas, Al-Sharafi, Ali, 2019).

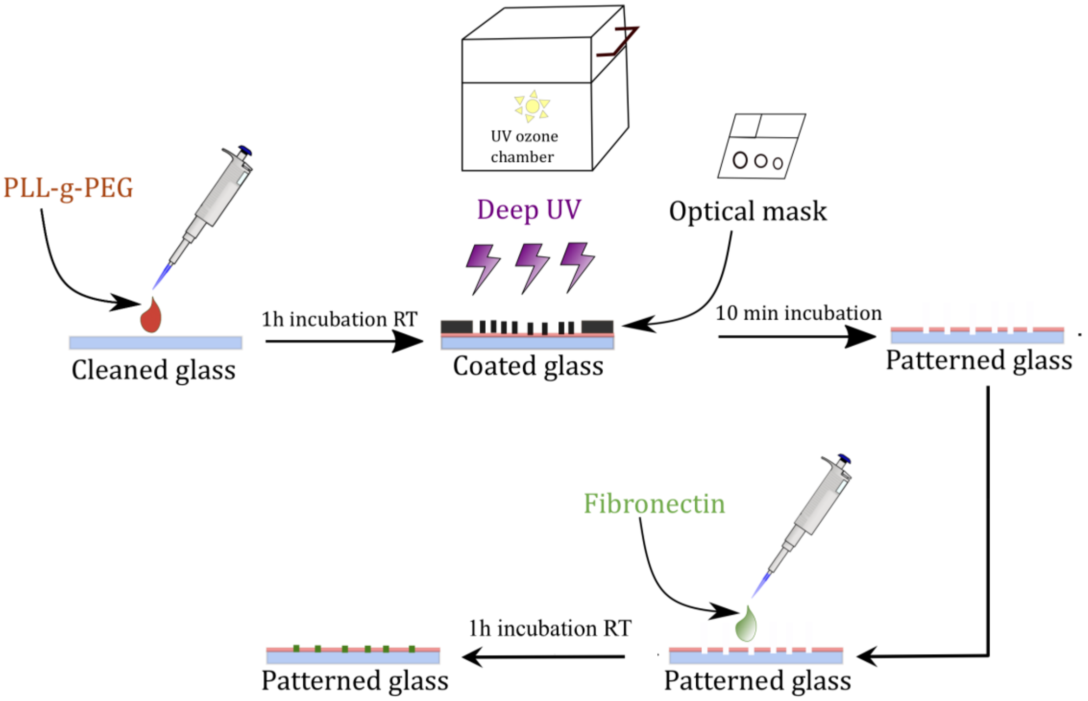

Figure 1.18 Micropatterning formation scheme using deep UV light and PLL-g-PEG and fibronectin as antifouling coating and ECM protein to enhance cell attachment, respectively.

Micro-contact printing is another micropatterning technique that requires the creation of a master/mold (typically made of PDMS) with the desired motif that is used to deposit molecules of interest onto the substrate (Mi et al., 2006; Rianna et al., 2016a).

Currently, in addition to photolithography techniques using a mask or a master, maskless photopatterning systems have been developed. This new technique allows any image to be drawn on the substrate, without the necessity of buying expensive masks with only one or two different pattern shapes. The user can design any image at will, making possible to plate cells in unusual geometrical shapes (Ma et al. 2018).

Micropatterning is also used to study the migration properties of cells, called "dynamic micropattern technique". Cells are seeded on a micropatterned substrate of specific geometry and the surrounded area is non-adherent; therefore, cells tend to remain in the adhesive region. However, the non-adherent region can become adherent ("switched on") at any time, allowing cells to leave the pattern and migrate.

A wide range of pattern shapes have been employed to investigate different cellular features. Circular, square, rectangular, triangle, Y and T may be the most used pattern shapes (Brock et al., 2003; James et al., 2008; Nakanishi et al., 2008). Triangular, Y and T patterned-shapes have been used together to compare local mechanical properties of cells with cytoskeleton distribution. Besides, the availability or dimension of the adhesive areas could also influence cell spreading, shape, adhesion points, as well as local Young's modulus and cytoskeleton distribution and development (Fig. 1.19) (Théry et al., 2006; Rigato et al., 2015).

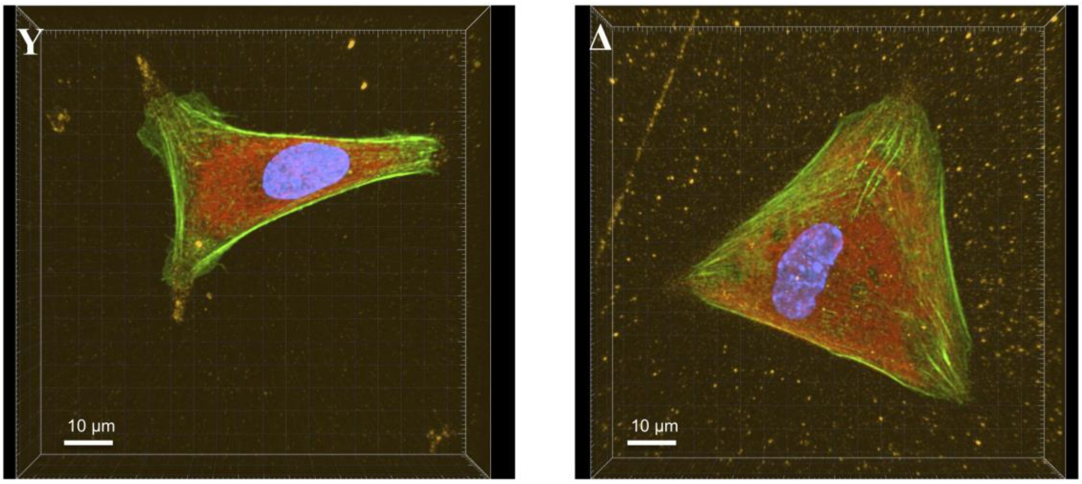

Figure 1.19 Dupuytren fibroblasts seeded on 60 µm Y and Δ-shaped micropatterns. Actin fibers labeled in green, vimentin in red and nucleus in blue.

1.6 Stimulated emission depletion (STED) microscopy

Confocal microscopy is a powerful technique for acquiring optical images, as it suppresses the light coming from adjacent focal planes, allowing reasonable 3D imaging. Although confocal microscopy provides good quality images, it has the obstacle of the effect of diffraction, which limits resolution to around half the wavelength of the light used. In the last decade, a variety of optical imaging techniques that overcome the resolution limit have been developed (super-resolution techniques).

Super-resolution techniques can be categorized in two groups:

1. Stochastic: photoactivation localization microscopy (PALM), stochastic optical reconstruction microscopy (STORM) and ground-state depletion followed by individual return (GSDIM).
2. Non-stochastic: structured illumination (SIM), reversible saturable optical fluorescence transitions (RESOLFT), ground state depletion (GSD) and stimulated emission depletion (STED).

Stochastic super-resolution microscopy is based on the use of single-molecule fluorescent emitters that present random switching on and off schemes allowing their position to be determined much more accurately. Only one molecule emits per area at a time, enabling for much more precise localization. Non-stochastic super-resolution microscopy is based on the use of fluorescent probes that can be reversibly switched between fluorescent “on” state and dark “off” state.

One of the most used super-resolution techniques is STED microscopy. STED is a super-resolution fluorescence microscopy technique that generates higher quality images than confocal as it overcomes the diffraction limit. It uses two synchronized lasers. The first laser “excitation laser” is employed to excite fluorescent molecules and then, a depletion laser is followed, which has a doughnut shape that quenches the fluorescence of molecules at the periphery of the excitation laser. In the center of the doughnut, the depletion laser intensity is zero, so only the fluorescence of molecules in this region is unaffected and detected. The fluorescent molecules in the doughnut area are first excited by the excitation laser and then return to the ground state by the depletion laser. This technique allows lateral resolution imaging in the 30 - 80 nm range and axial resolution of around 100 nm (Fig. 1.20-1.21) (Klar *et al.*, 2000; Dyba and Hell, 2003; Rittweger *et al.*, 2009; Müller, Schumann and Kraegeloh, 2012).

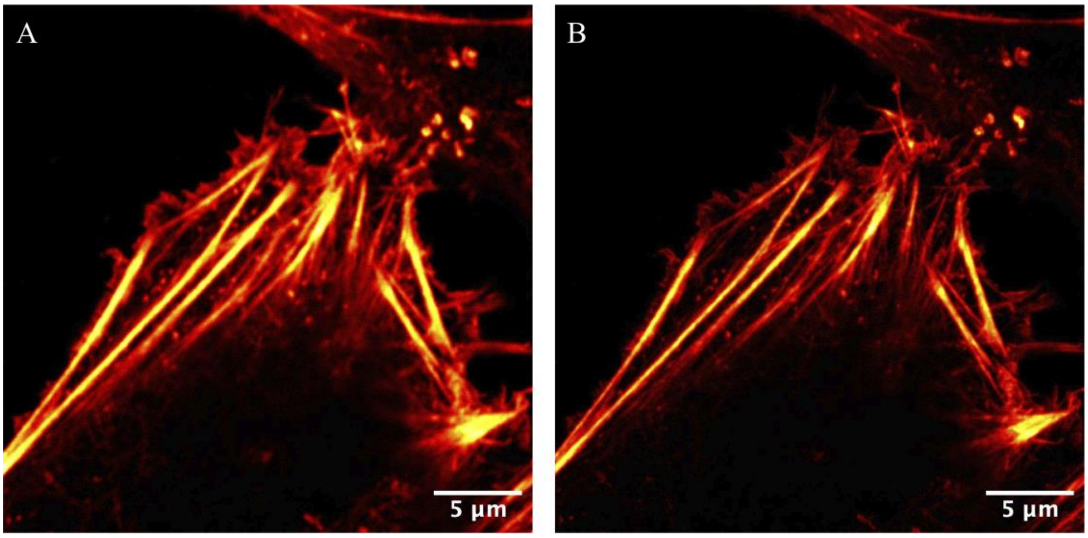

Figure 1.20 Optical images of a fixed Dupuytren fibroblast, A) Confocal image; B) STED image. Actin fibers labeled in red. The improvement in image resolution in the STED in comparison to confocal is clearly visible.

Nowadays, optical microscopy has been combined with other techniques, improving data acquisition quality and experiments interest. One example is the combination of STED microscopy with AFM (Fig. 1.22). This coupling allows measuring mechanical properties of living cells and correlating it with cell structural organization. Therefore, individual mechanical properties can be assigned to specific cytoskeleton structures. It exists a variety of dyes for staining cytoskeleton structures of living samples, like actin filaments, vimentin, tubulin, etc. These new products enable to label any cell cytoskeleton element without fixation that means maintaining cells alive in *in vitro* conditions.

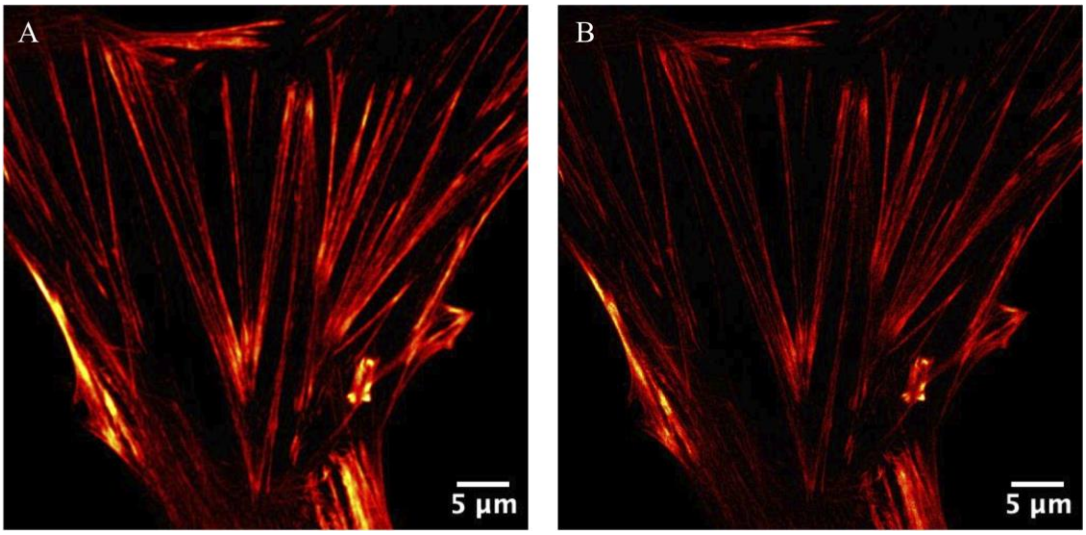

Figure 1.21 Optical images of a live Dupuytren fibroblast, A) Confocal image; B) STED image. Actin fibers labeled in red.

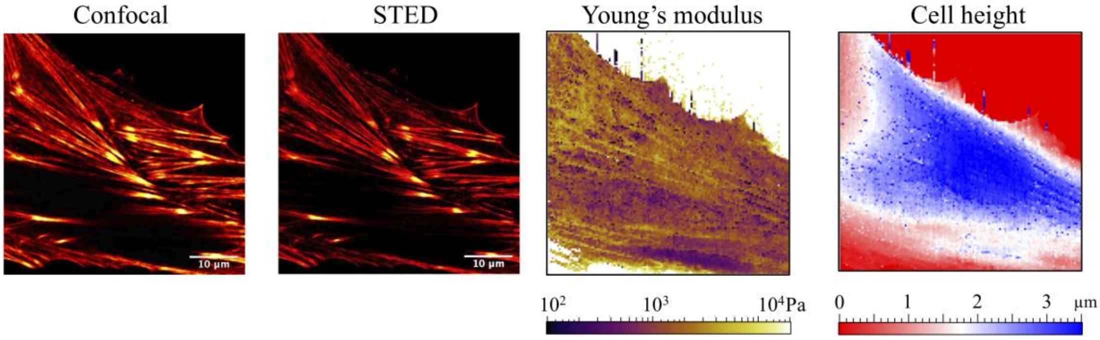

Figure 1.22 AFM-STED measurement of the same live cell.

Chapter 2

Materials and methodology

2.1 AFM and cantilever calibration

As it has been mentioned before, one of the main AFM components is the cantilever that - most times - carries a tip at the very end, which can be of different geometries (three or four pyramid, cylinder, cone, flat or sphere), resonance frequencies and spring constants. The resonant frequency of a cantilever is the oscillation at its natural or unforced resonance. Most systems, such as cantilevers, have one resonant frequency (fundamental) and multiple harmonic frequencies that progressively decrease in amplitude as they move away and are multiples of the fundamental frequency. The spring constant of a cantilever is a parameter to characterize its stiffness. It is an important parameter when measuring cell mechanics and for obtaining topographical images. The selection of a stiffer cantilever than the sample may lead to damage and the opposite (softer cantilever) may cause unreliable data or cause cantilever damage. Moreover, the nominal spring constant provided by cantilever manufacturers is often not accurate and provides a wide range of values. Manufacturers calculate the spring constant based on the length, width and thickness of the cantilever, using the following expression for a rectangular cantilever:

$$k = 0.25E\frac{wt^3}{l^3} \qquad \text{(Eq. 2.1)}$$

Where *E* is the Young's modulus, *w* the width, *t* the thickness and *l* the length. For other cantilever geometries, approximate relations are determined by finite element simulation.

From this equation we can figure out that slight changes in cantilever thickness will greatly vary its spring constant. Hence, the calculation of the cantilever spring constant has to be done for each individual cantilever and measurement. In addition, manufacturers compute the resonant frequency of the cantilever using the following expression (only valid for rectangular tipless cantilevers in vacuum):

$$f = \frac{1}{2\pi}\sqrt{\frac{k}{m_0}} \qquad \text{(Eq. 2.2)}$$

where f is the resonant frequency and m_0 is the mass of the cantilever. In liquid, the resonant frequency of a cantilever is reduced, and to estimate it, the fluid properties (viscosity), the added fluid mass per cantilever dimensions, the cantilever geometry and their interaction (damping coefficient of the fluid) have to be taken into account.

There are a few cantilever calibration methods, like the Sader method (Sader *et al.*, 1995), the Cleveland method (Cleveland *et al.*, 1993), the thermal fluctuations method (Butt and Jaschke, 1995), etc. Nowadays, most of the AFM instruments have already implemented the thermal fluctuations method. This method is based on the measurement of cantilever vibrations caused by a cantilever in thermal equilibrium. By means of the equipartition theorem, the spring constant of the cantilever can be estimated; which states that if a system is in thermal equilibrium, every degree of freedom will have an average energy equal to:

$$< E >= \frac{1}{2} k_B T \qquad \text{(Eq. 2.3)}$$

k_B is the Boltzmann constant and T is the absolute temperature. Assuming that the cantilever undergoes only bending vibrations at its resonant frequency, the spring constant of the cantilever can be estimated as:

$$< E >= \frac{1}{2} k < d^2 > \qquad \text{(Eq. 2.4)}$$

where $< d^2 >$ is the mean square deflection of the cantilever caused by thermal vibrations. Combining the two previous equations, the spring constant can be calculated:

$$k = \frac{k_B T}{< d^2 >} \qquad \text{(Eq. 2.5)}$$

This calibration protocol is performed with the cantilever far away from the sample. The thermal fluctuations of the cantilever are recorded and converted into power spectral density (PSD). The power spectrum as a function of frequency displays more than one peak, corresponding to the different resonant modes of the cantilever (Fig. 2.1). To obtain a more accurate spring constant value, just the first peak, which corresponds to the fundamental oscillation, is selected and fitted with an appropriate model function (Simple Harmonic Oscillator (SHO) or Lorentz). The integral under the peak (fundamental oscillation) is the mean square deflection.

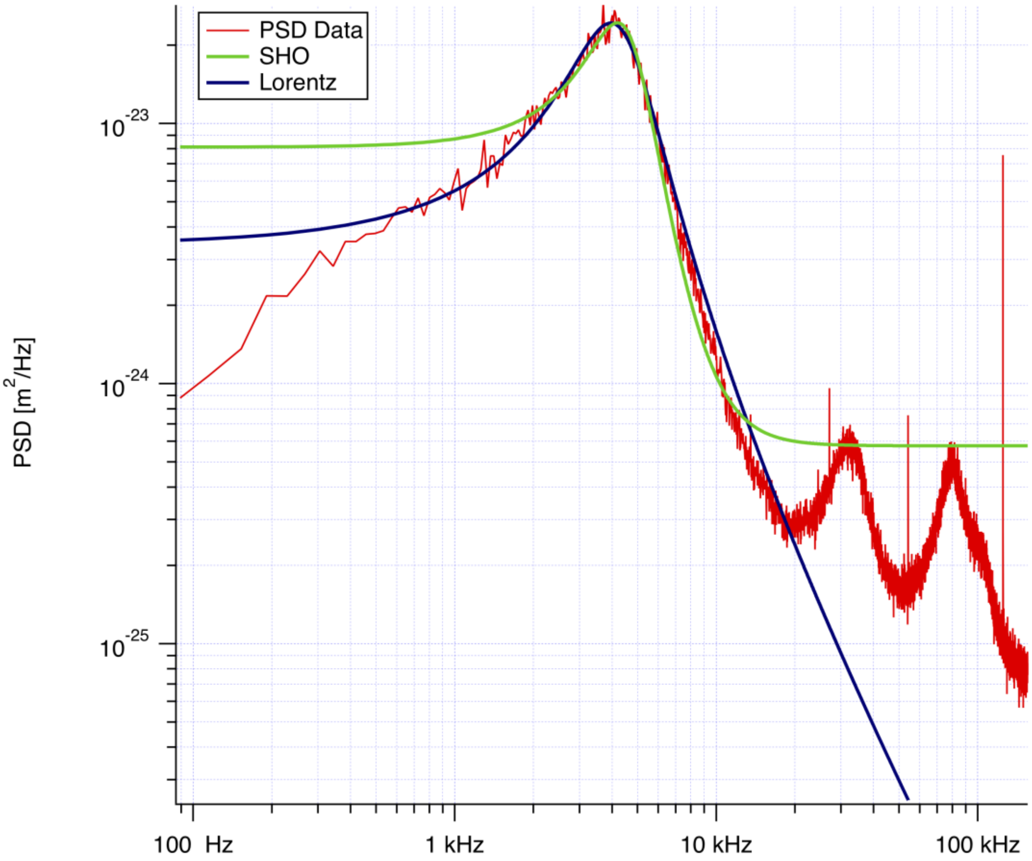

Figure 2.1 Power spectral density of the cantilever deflection signal as a function of frequency. The green and blue lines are the fitted model functions. The thermal data was recorded in liquid and the cantilever used was: MLCT-D, Bruker.

On many AFMs, the cantilever deflection is measured with the optical lever sensitivity (OLS) technique. The laser spot is focused onto the back of the cantilever and reflected off a photodiode. The total amount of reflected light reaching the photodiode is given in Volts (V) and the V average value given for a cantilever deflection depends on the specific location where the laser hits the cantilever. To calibrate the output signal of the photodiode, the deflection sensitivity is measured, that relates the reflected laser spot displacement to the cantilever deflection. This parameter is obtained by ramping the cantilever against a stiff support (petri plates or glass slides) and taking force-distance curves. The slope of the contact part of the force curve will be the inverse of the deflection sensitivity value (nm/V), since the additional downwards movement of the z-piezo, after overcoming the non-contact region and starting to touch the glass support, is equal to the cantilever bending (Fig. 2.2).

As a general summary: to start measuring and employing an AFM device, it is of fundamental importance to begin with two critical calibrations:

1. Calibration of the cantilever's spring constant
2. Calibration of the deflection sensitivity of the AFM

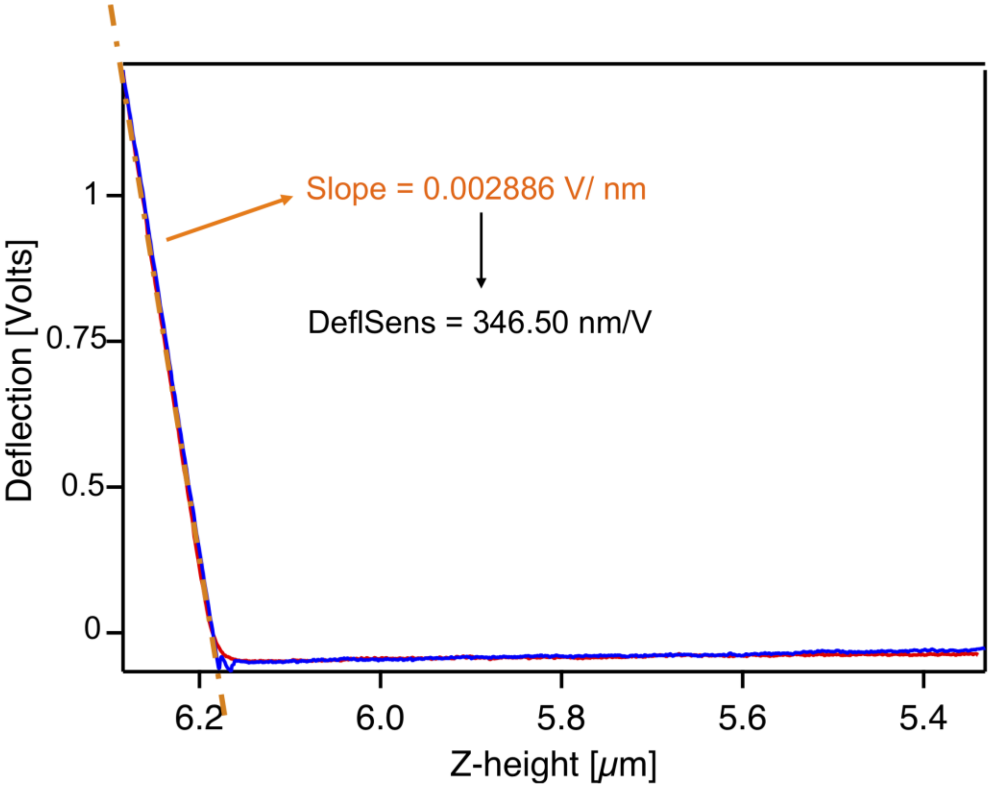

Figure 2.2 Calibration of the deflection sensitivity. The cantilever is moved towards a stiff surface. In the contact part (left part of the graph), the piezo motion will be equal to the cantilever deflection. The inverse of the slope (orange line) of the contact part of the force curve corresponds to the deflection sensitivity. The force curve was taken in a plastic petri plate in cell culture medium and the cantilever used was an MLCT-BIO-D (Bruker, 4-sided pyramid with an opening angle of 35° and tip radius of 40 nm. Nominal spring constant of 30 pN/nm and resonant frequency of 15 kHz in air).

2.2 AFM data (Force-distance curves) and analysis

AFM, studying biological samples, can serve to acquire topographical images, sample mechanics and single molecule force data. The fundamentals of AFM operation consist of approaching and retracting the cantilever in and out of contact of the sample -in our case, cells- recording tip-sample interaction. This cantilever movement is recorded in force-distance curves. Force-distance curves record the cantilever deflection versus the distance between the AFM tip and the sample surface. Force-distance curves can be described as follows: first, the cantilever is approached in the z-axis towards the sample with the help of the piezoelectric ceramic material. In this path called “non-contact part”, the cantilever does not deflect and is denoted as deflection offset (d_0). The piezo expands/retracts in response to an applied voltage that procure cantilever movement. The cantilever continues going down towards the sample until the tip touches for the first time the sample (contact point, z_0). Once the initial contact is overcome, the tip goes further into the sample, causing cantilever bending and sample indentation (δ). The AFM tip applies a force on the cell, generating a cell deformation in response to the applied force. Basically, the cantilever deflection is nothing but the cell response to an external force. After the tip-sample interaction, the tip is retracted off contact and in some cases, unspecific interactions between the tip and the sample can be observed, such as adhesion forces and stretched molecules between tip and the surface. In addition, some interactions can occur in the approaching process, like electrostatic forces, van der Waals and capillary forces (in air) among others (Fig. 2.3) (Meyer, 1992).

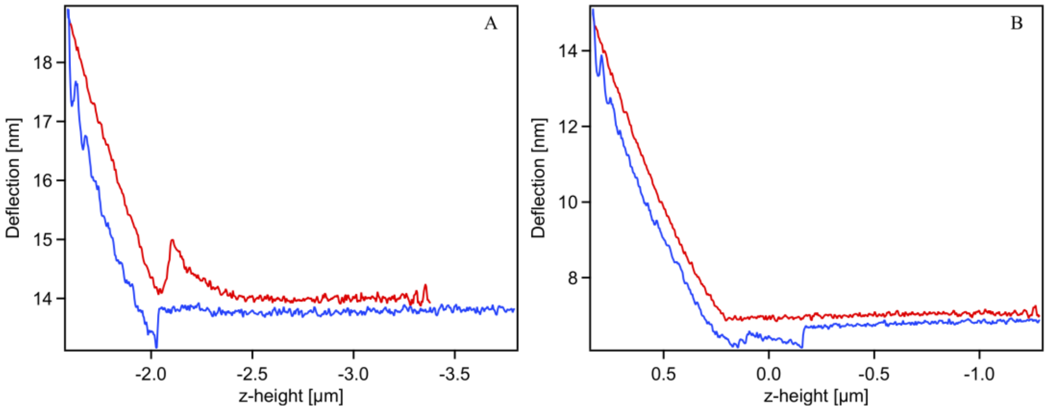

Figure 2.3 Example of a force curve that presents a) attraction forces in the approach curves (red) and b) adhesion forces in the retraction curve (blue). Force curves were taken in human fibroblasts using PFQNM cantilevers (Bruker, 3-sided pyramid and an opening angle of 20° and tip radius of 65-75 nm. Nominal spring constant of 100 pN/nm and resonant frequency of 45 kHz in air).

From the force distance curves, mechanical data of the sample of interest can be extracted. Original AFM data provides deflection versus z-piezo displacement ($d - z$) graphs (Fig. 2.3), both values dependent on time; however, to compute Young’s modulus, Hertzian models are predominantly used, which requires some conversions to obtain force-indentation (F-δ) curves.

The loading force (F) exerted by the cantilever upon the sample can be obtained from deflection values using Hooke's law, which states that the force applied to a spring (cantilever) to produce any deformation by some distance scales linearly to that distance, being true as long as the forces and deformations are small.

$$F = k \cdot (d - d_0) \qquad \text{(Eq. 2.6)}$$

Where k is the spring constant of the cantilever and d is the cantilever deflection and d_0 is the deflection offset.

The indentation (δ), which is the difference between the sample height and the cantilever deflection, is calculated from the following expression:

$$\delta = (z - z_0) - (d - d_0) \qquad \text{(Eq. 2.7)}$$

Precise identification of the contact point (z_0) is a critical process that can induce misleading values of the sample's Young's modulus, since it is needed to convert (d-z) to (F-δ) curves. In a hypothetical perfect experiment, the cantilever deflection (d_0) at the contact point (z_0) should be 0. One of the most used methodologies to identify z_0 is based on exanimating the force curve and considering each point as a potential contact point (Shoelson *et al.*, 2004; Hermanowicz *et al.*, 2014). For each potential z_0, the (d-z) curves are converted into (F-δ) curves and then fitted with the appropriate contact mechanics model depending on the cantilever-tip geometry. The z_0 with the highest r^2 is then selected as the final contact point.

To analyze the converted (F-δ) curves and extract the Young's modulus of the sample, the appropriate contact mechanics model is fitted, in our case, we employed Hertzian model for parabolic tips, which can be used for spherical tips if the indentation applied into the sample is smaller than $R/10$ (R being the radius of the spherical tip).

$$F = \frac{4}{3}\frac{E}{1-\nu^2}\delta^{\frac{3}{2}}\sqrt{R} \qquad \text{(Eq. 2.8)}$$

where the ν is the Poisson's ratio (which is considered 0.5 for cells).

Nevertheless, different formulas have been derived for each specific tip geometry.

$F = \frac{2}{\pi}\frac{E}{1-\nu^2}\delta^2 \tan\theta$ for conical tips (Sneddon, 1965) (Eq. 2.9)

$F = \frac{1}{\sqrt{2}}\frac{E}{1-\nu^2}\delta^2 \tan\theta$ for four-sided pyramids (Bilodeau, 1992) (Eq. 2.10)

$F = 2\frac{E}{1-\nu^2}a\delta$ for flat cylindrical tips (Sneddon, 1965) (Eq. 2.11)

where θ is the half-opening angle and a the radius of the flat cylindrical tip.

Hertz contact model for pyramidal and conical tips assumes that these cantilever tip geometries have an infinitely sharp apex; however, they actually have a bluntness or sphere of finite radius at the apex. Rico et *al*. developed a more precise contact model for blunted pyramidal AFM tips taking into account the real shape of the tip (Rico *et al.*, 2005). AFM simulations for a 1 kPa material reaching a maximum indentation of 1 µm for a blunted 3-sided pyramid and blunted 4-sided pyramid using Rico's blunted contact model gives information about the tip geometrical transition (from sphere to pyramid) and at what indentation depth the transition point takes place (Fig. 2.4-2.5). This information helps in selecting a specific contact model for each tip depending on the indentation depth applied.

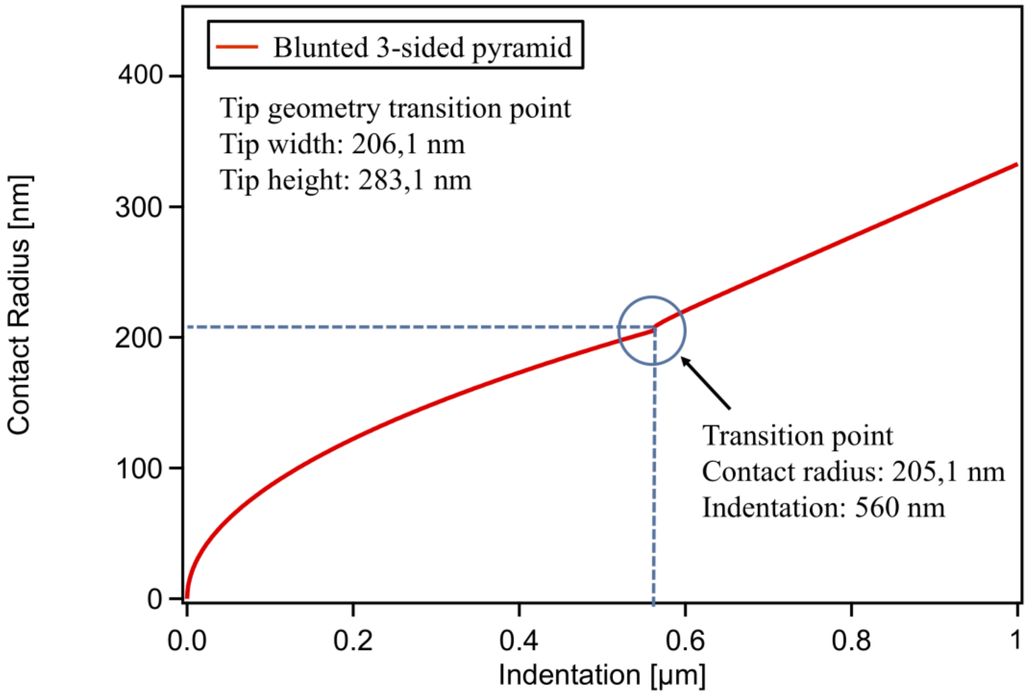

Figure 2.4 Contact radius versus indentation graph for a blunted 3-sided pyramid tip, like PFQNM cantilevers. The blue circle indicates the transition point from sphere to 3-sided pyramid tip geometry.

In the case of a blunted 3-sided pyramid, like PFQNM, the transition from spherical apex to pyramidal tip takes place at 283.1 nm tip height, which corresponds to a sample indentation of 560 nm. Therefore, after 560 nm sample indentation the pyramid takes over the spherical cap, thus when employing indentations lower or equal to 560 nm, the spherical contact model can be used for these type of tips (Fig. 2.4). For a blunted 4-sided pyramid, like MLCT-Bio, the transition from spherical cap to pyramidal tip takes place at 40.8 nm tip height, which corresponds to a sample indentation of 54.8 nm. Accordingly, from indentations greater than 54.8 nm, the pyramid takes over the sphere and the pyramidal contact model should be used. Since the transition from sphere to pyramid occurs at really small indentations, there are no large variations in Young's modulus results when employing the pyramidal or blunted 4-sided pyramidal contact model, thus, enabling the use of the Hertzian pyramidal contact model for simplicity (Fig. 2.5).

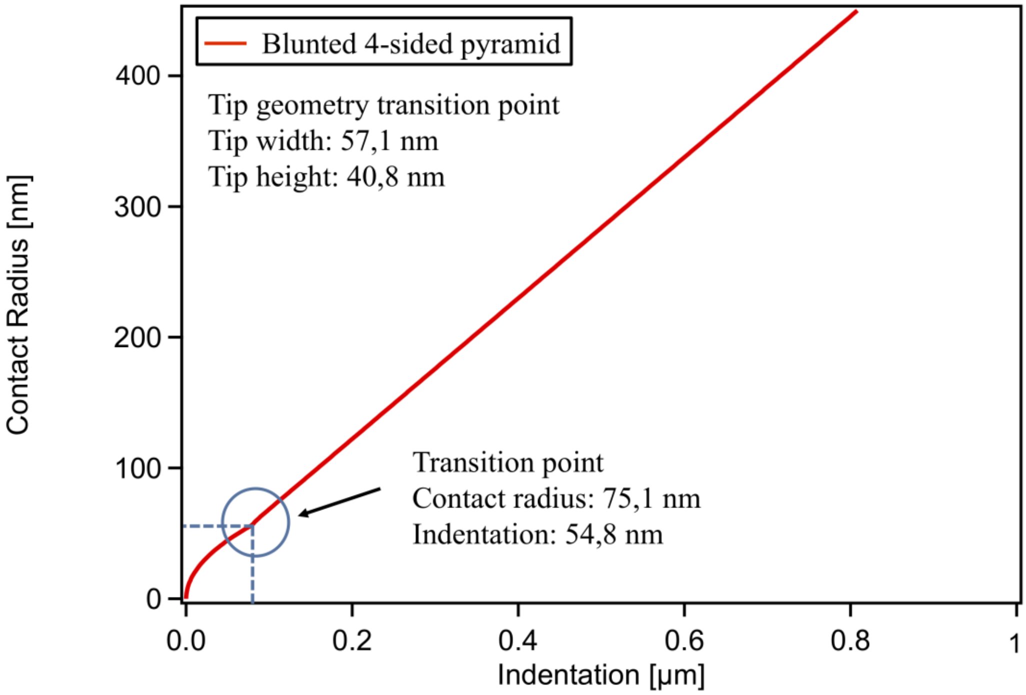

Figure 2.5 Contact radius versus indentation graph for a blunted 4-sided pyramid tip, like MLCT-BIO cantilevers. The blue circle indicates the transition point from sphere to 4-sided pyramid tip geometry.

2.2.1 Young's modulus and limitations

In cell mechanics, Young's modulus parameter is used to describe cell's elastic response to an external force. Young's modulus or elastic modulus is a mechanical property that measures the uniaxial stretching of a solid material when a normal stress is applied in the linear elastic region of the material.

$$E = \frac{\sigma}{\varepsilon} \qquad \text{(Eq. 2.12)}$$

Being σ the stress (force per area) and ε the strain (deformation). The forces employed in our experiments are small (approx. 1 nN) in an attempt to remain in the linear elastic response of cells behavior; therefore, when using the Young's modulus to describe cells' mechanical properties, they are considered to be elastic materials.

The most widely used model to describe cells mechanical properties is Hertzian model and its derivatives for the different tip geometries (Hertz, 1881). Heinrich Hertz was the first to solve the contact problem of two elastic spheres of different radii. Moreover, when using Hertz contact models to describe cells mechanical properties, several assumptions are taken:

1. Cells are linear elastic materials
2. Cells are isotropic, homogeneous and infinitely thick.

Although Hertz's contact mechanics models describe the mechanical data of cells surprisingly well -that is why it is widely used-, none of these assumptions are fulfilled by cells, especially because they are not pure elastic but rather viscoelastic materials. The Young's modulus extracted from the approach force curves of cells gathers both elastic and viscous contributions, thus we call it apparent Young's modulus to differentiate it from the true Young's modulus. For a pure elastic material, the approach and retraction traces on a force curve should follow the same path; however, as seen in figure 2.3, the approach and retract curves taken in cells present a mismatch, hysteresis in the contact part, which is attributed to the energy dissipated as heat, thus, the viscous contribution.

In biophysics, the elastic properties of cells are attributed to the cytoskeleton network, especially to actin fibers where the density and rearrangement of filaments and the number of crosslinks will affect the elastic properties. The viscous properties of cells are difficult to define, but lately it has been related to the internal friction between micro and macromolecules inside the cell body and the cell fluid cytosol. Cells present different viscoelastic properties and vary depending on their origin (organ, tissue) and it has been shown that cells from the same organ but presenting different pathological grades can also display distinct cell mechanical properties (Lekka *et al.*, 1999; Rianna and Radmacher, 2017a; Brás *et al.*, 2022).

As has been mentioned above, Young's modulus is a suitable mechanical parameter to describe elastic materials behavior. However, being cells complex heterogeneous viscoelastic materials, new strategies need to be searched to properly describe cell mechanics.

2.2.2 AFM methodologies (Sweep frequency)

There are some AFM schemes in the literature that serve to differentiate between the elastic and viscous contribution of cells. Step response (Yango *et al.*, 2016), force clamp (Hecht *et al.*, 2015), magnetic force modulation (Rebêlo *et al.*, 2014), double power law relaxation (de Sousa *et al.*, 2020) and oscillatory models (Fabry *et al.*, 2001; Alcaraz *et al.*, 2003; Rigato *et al.*, 2017) are some of the most employed AFM strategies to characterize cells rheological properties.

Sweep frequency modulation is an AFM scheme used to probe viscoelastic materials, that afterwards elastic and viscous properties of viscoelastic samples like cells can be obtaining using the appropriate model. It is similar to previous oscillatory models seen in the literature but has a few different methodological sections. Basically, it consists of adding a dwell time to the regular force curve, in which an oscillatory modulation with increasing frequency is applied. From the beginning, after approaching the cantilever towards the sample up to a deflection value defined by the trigger threshold, z-piezo motion is stopped for 1 second (dwell time). Typically, the dwell time lasts 8.7 seconds, where during the first second no modulation is applied since the cell creeps substantially. Then, the sweep frequency scheme is applied, that consists of applying a sinusoidal modulation increasing the frequency. The frequency is swept from 1Hz to 1kHz, where for each frequency only one cycle is applied. The frequency series is designed as a geometric series, so in each decade we use the same number of frequencies. Typically, the frequency increases by a factor of 1.15 from cycle to cycle, which results in 17 frequency values per decade, which are equally spaced on a logarithmic scale. The amplitude is set to be 50 nm. Finally, once the dwell time is finished, the cantilever is retracted off contact (Fig. 2.6).

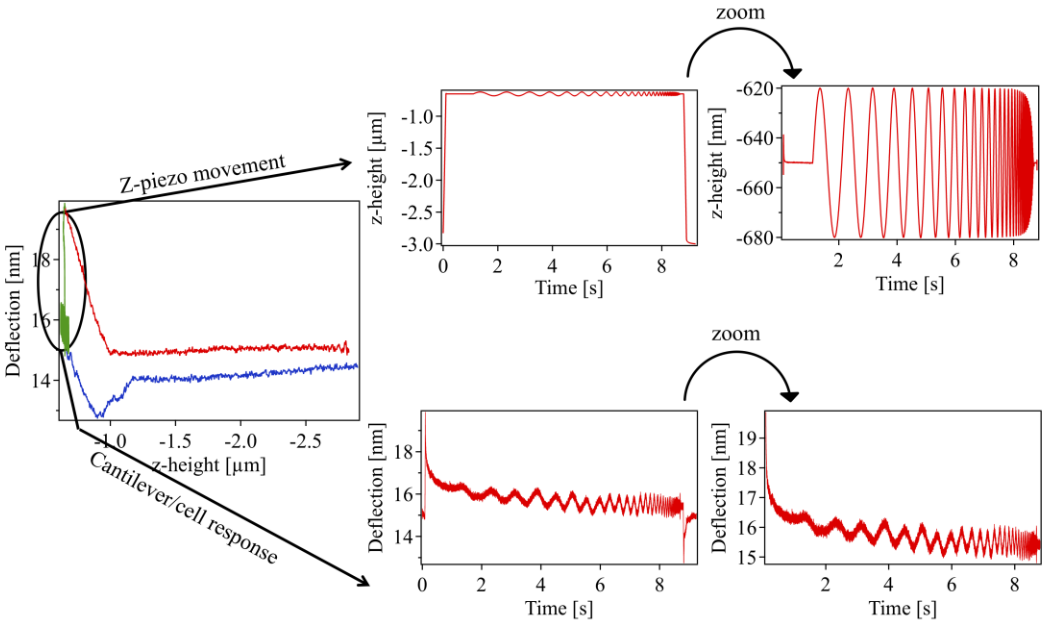

Figure 2.6 Deflection versus z-height of a sweep frequency force curve (approach curve in red, retraction curve in blue and dwell time in green -sweep modulation frequency-); z-height (piezo movement) versus time of a sweep frequency force curve and deflection versus time of a sweep frequency curve (cantilever/cell motion).

The resulting data should be analyzed with an appropriate model. Although most of the existing models do not fully describe cells behavior (see Introduction section 1.1.5), many of them describe individual cell's properties surprisingly well. The power-law structural damping model has been widely used to describe microrheological properties of cells, due to the similarities between cytoskeleton properties and soft glassy materials.

The power law structural damping model formula is as follows:

$$E^*_{(\omega)} = E_0 * (1 + i\eta) * \left(\frac{\omega}{\omega_0}\right)^{\alpha} + i\mu\,\frac{\omega}{\omega_0} \qquad \text{(Eq. 2.13)}$$

where E* is the complex elastic modulus; E_0 is the scale factor of the storage and loss moduli; i the imaginary unit; η the loss tangent; ω_0 in the frequency scale (in our case 1 Hz); α the power law exponent of the sample and μ the Newtonian viscous term, which will depend on the shape of the cantilever and the viscosity of the medium. The storage modulus (E') corresponds to the real part and increases for all frequencies (ω) according to a power law exponent α. The loss modulus (E'') corresponds to the imaginary part and includes a fraction η of the storage modulus and a Newtonian viscous term μ.

Results and Discussions

Chapter 3

This is a verbatim copy of an article that has been published in a peer reviewed journal: Pérez-Domínguez S., López-Alonso J., Lafont F., Radmacher M. Comparison of rheological properties of healthy versus Dupuytren fibroblasts when treated with a cell contraction inhibitor by Atomic Force Microscope. *International Journal of Molecular Sciences*, 24:2043 (**2023**). doi:10.3390/ijms24032043

Comparison of rheological properties of healthy versus Dupuytren fibroblasts when treated with a cell contraction inhibitor by Atomic Force Microscope

Sandra Pérez-Domínguez[1], Javier López-Alonso[2], Frank Lafont[2], Manfred Radmacher[1*]

[1]Institute of Biophysics, University of Bremen, Bremen, 28359, Germany.
[2]University of Lille, CNRS, INSERM, CHU Lille, Institute Pasteur Lille, U1019-UMR 9017 –CIIL- Center for Infection and Immunity of Lille, 59021 Lille, France.
* Correspondence: radmacher@uni-bremen.de

3.1 Abstract

Mechanical properties of healthy and Dupuytren fibroblasts were investigated by atomic force microscopy (AFM). In addition to standard force curves, rheological properties were assessed using an oscillatory testing methodology, in which the frequency was swept from 1 Hz to 1 kHz, and data were analyzed using the structural damping model. Dupuytren fibroblasts showed larger apparent Young's modulus values than healthy ones, which is in agreement with previous results. Moreover, cell mechanics were compared before and after ML-7 treatment, which is a myosin light chain kinase inhibitor (MLCK) that reduces myosin activity and hence cell contraction. We employed two different concentrations of ML-7 inhibitor and could observe distinct cell reactions. At 1 µM, healthy and scar fibroblasts did not show measurable changes in stiffness, but Dupuytren fibroblasts displayed a softening and recovery after some time. When increasing ML-7 concentration (3 µM), the majority of cells reacted, Dupuytren fibroblasts were the most susceptible, not being able to recover from the drug and dying. These results suggested that ML-7 is a potent inhibitor for MLCK and that myosin II is essential for cytoskeleton stabilization and cell survival.

Keywords: Dupuytren's disease, fibroblast, Atomic Force Microscopy, rheology, ML-7, inhibition.

3.2 Introduction

Dupuytren's disease is a fibromatosis of the connective tissue of the palm, which—in the worst case—leads to bending of the hand and/or one or more fingers hampering regular hand activities. Few non-invasive strategies have been used to release tension, such as needle acupuncture and collagenase injection (van Rijssen *et al.*, 2006; Abdelrahman *et al.*, 2020); however, in most cases, the contraction recurs. In the case of advanced stages of the disease, surgery is the most common solution (Desai and Hentz, 2011). In patients who suffer from Dupuytren's disease, the formation of nodules and cords in the palmar fascia is observed, which is caused by aggregation of proliferated fibroblasts that adhere to fibrin. The palmar fascia is made of bands of connective tissue that are mainly composed of type I collagen. Between the collagen fibers, rows of fibroblasts can be found, which secrete and deposit extracellular matrix (ECM) components. In wound healing, healthy fibroblasts undergo a phenotypic change into myofibroblasts expressing α-smooth muscle actin (α-SMA). The expression of α-SMA along with fibronectin ectodomain A is activated by the latent transforming growth factor β-1 protein (TGFβ-1) that is present in the ECM. Furthermore, in the palmar fascia of patients with Dupuytren's disease, an increase in collagen III/I ratio was found together with an increased differentiation of myofibroblasts leading to an increment of hand contraction (Baum and Duffy, 2011; Hinz, 2015a; Bochaton-Piallat, Gabbiani and Hinz, 2016). Similarities between myofibroblasts and smooth muscle (SM) cells were suggested in initial studies. Although both cell types present α-SMA, SM cells contraction is rapid and short in duration, while myofibroblast contraction is rather long-lasting and results in permanent contraction (Bochaton-Piallat, Gabbiani and Hinz, 2016). In wound healing, a few cytokines and growth factors (interleukins, TGFβ-1, etc) are released that have been involved in the stimulation of myofibroblast transition. Previous experiments suggested that exposing healthy fibroblasts to TGFβ-1 leads to differentiation into a myofibroblast phenotype (Kloen *et al.*, 1995; Bisson *et al.*, 2009; Viji Babu *et al.*, 2018). Moreover, lately a comparison between healthy and Dupuytren fibroblasts exposed to TGFβ-1 showed an increase in α-SMA expression in the case of Dupuytren fibroblasts but not in healthy fibroblasts, which corroborates the myofibroblast phenotype assignment to Dupuytren cells (Viji Babu *et al.*, 2018).

Many studies have tried to develop a strategy to revert myofibroblast to fibroblast differentiation. Unfortunately, not many have been successful. Interferon-γ (IFN-γ) has been reported as a possible therapeutic agent for contractile diseases in clinical trials and in vitro studies (Tanaka *et al.*, 2001; Gu *et al.*, 2004; Lowin *et al.*, 2020). However, late results suggested that IFN-γ inhibits myofibroblast generation and downregulates α-SMA production in TGFβ-1-induced myofibroblasts, but it does not produce the same effect on well-differentiated myofibroblasts (Tanaka *et al.*, 2003, 2007).

ML-7 is a specific inhibitor of myosin light chain kinase (MLCK), a Ca2+/calmodulin- dependent enzyme that is essential for the activation of myosin II and cell contraction (Cooper, 2000). ML-7 reduces the phosphorylation of the myosin light chain (regulatory chain), resulting in the inability of the myosin head to change to the optimal conformation to bind to actin filaments, thus reducing actin–myosin interaction and contraction (Tan and Leung, 2009). ML-7 is a reversible ATP-competitive inhibitor of MLCK that has been assessed as a potential chemotherapeutic drug for many diseases, such as prostate and mammary cancer (Gu *et al.*, 2006; Cheng *et al.*, 2015), atherosclerosis (Ding *et al.*, 2020), etc. A competitive inhibition occurs when the inhibitor molecule binds to the enzyme and blocks its activity. The inhibitor can bind either to the enzyme's active site (competing with the enzyme-substrate natural binding) or to another site on the enzyme such that the enzyme's activity is modified. However, as the inhibition is reversible, the inhibitor-enzyme interaction has a limited time life; therefore, the inhibitor will leave the enzyme allowing it to resume its regular enzymatic activity. In many diseases, such as pancreatitis, respiratory, cardiovascular and inflammatory bowel diseases, an abnormal expression of MLCK has been observed. Some works used ML-7 and analogs to study its potential beneficial effects on the previously mentioned disorders (Xiong *et al.*, 2017). A high concentration of ML-7 produced a rounding up of Panc1 cells and a marked reduction in the number of stress fiber (Kaneko *et al.*, 2002). In total, 10 μM ML-7 was added to 3T3 and NRK cells, and they stopped migration, retracted their lamellipodia and softened by a factor of 3 in peripheral and nuclear regions. Besides, a concentration-dependent effect on the cells was observed (Schäfer and Radmacher, 2005).

In this study, AFM rheological experiments were designed to assess cell behavior. Rheology is the study of the flow and deformation of matter and takes into account the interplay between force, deformation and time. In rheology, often using oscillatory testing, the elastic modulus is represented as the storage modulus (E') that refers to the stored energy in each oscillatory cycle and the viscous modulus, the loss modulus (E”) that measures the energy dissipated during one cycle as heat. The loss tangent (the ratio between loss and storage modulus) is taken as an indicator of the degree of solid- or liquid-like behavior. It can also be visualized as the tangent of the phase angle (δ) between the excitation (applied oscillatory force) and the response of the sample (indentation). The phase angle is the phase difference between stress and strain, and it will have a value equal to 0º for a pure elastic, 90º for a pure viscous and somewhat in the middle for viscoelastic materials.

AFM was initially developed as an imaging technique for hard samples; Lekka et al. were the first to employ the AFM as a diagnostic tool to discriminate between healthy and cancerous cells (Lekka *et al.*, 1999). Nowadays, the use of AFM for measuring biological samples is widely spread; in particular, cell mechanics has become a promising approach to assess diseases at single-cell and tissue levels. Our AFM experimental setup for measuring cell rheological properties is based on oscillatory testing methodology, in which the cantilever is oscillated at constant amplitude, varying the frequency up to 1 kHz. Thanks to this AFM scheme called “sweep frequency”, storage and loss modulus, as well as loss tangent, could be computed.

This study sought the following two aims: (1) investigate and evaluate the rheological properties of three human primary cell types from Dupuytren's disease. Due to the different phenotypes expressed by the cells, distinct rheological behaviors were expected. (2) Assess the effect of ML-7 as a cell contraction inhibitor and potential drug for reverting myofibroblast transition, tracking cell mechanical properties over time. We used 2 different concentrations (1 and 3 μM) in order to produce a significant effect while at the same time allowing the cells to recover.

3.3 Results

3.3.1 Rheological characterization

In this work, three different types of fibroblasts from the palm of the same patient were investigated. We measured the rheological properties of healthy, scar and Dupuytren fibroblasts and searched for differences in cell behavior after the addition of a MLCK inhibitor. By using AFM conventional force curves and sweep frequency data (Figures S3.1–S3.3), we studied the viscoelastic response of the above-mentioned cells before and after ML-7 inhibitor addition in order to follow the cell mechanical changes over time. Firstly, the mechanical properties of these cells seeded on bare plastic Petri dishes were investigated using PFQNM-LC-A-CAL cantilevers. These cantilevers are useful for this type of experi- ments because although they are stiffer than cantilevers usually used for cell mechanics, such as MLCTs, they have a fairly large tip height and a large resonance frequency that makes them suitable for oscillatory measurements at high frequencies.

The 3D images of the three fibroblast types can be seen in Figure S3.4. Dupuytren fibrob- lasts showed larger apparent Young's modulus values in comparison to scar and healthy fibroblasts. Moreover, scar fibroblasts presented slightly larger values than their healthy counterparts (Figure 3.1). A Wilcoxon signed-rank test and Cohen's d statistical analysis were performed on apparent Young's modulus, and statistically significant differences between healthy and Dupuytren and between scar and Dupuytren fibroblasts were found. Cohen's d test suggested a medium-size effect between scar and Dupuytren fibroblasts and a large-size effect between healthy and Dupuytren fibroblasts.

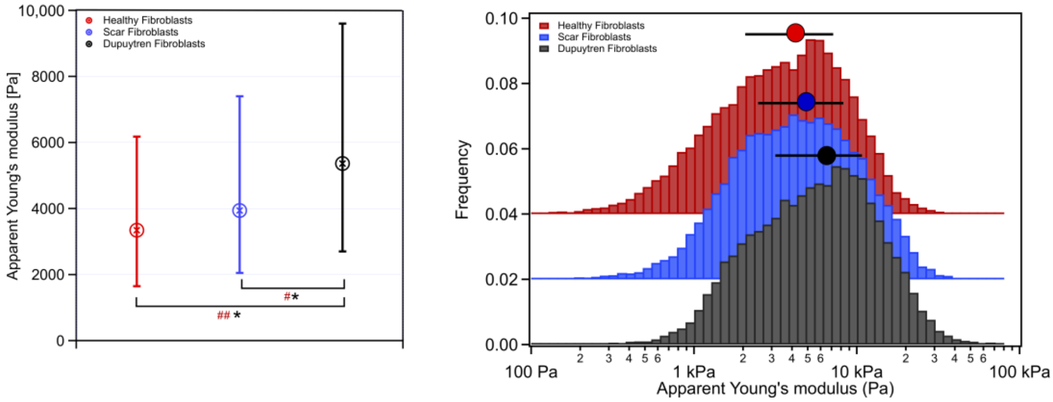

(a) **(b)**

Figure 3.1 (a) Box plot of apparent Young's modulus with the median and 25/75 percentiles for each fibroblast with Wilcoxon signed rank test significant difference:

* indicating $p < 0.01$ and Cohen's d test with # indicating $0.2 < d < 0.5$ and ## indicating $0.5 < d < 1.0$. **(b)** Histogram distribution of the apparent Young's modulus for each fibroblast together with the median and 25/75 percentiles above each histogram ($n = 90$). Healthy fibroblasts are displayed in red, scar in blue and Dupuytren fibroblasts in black.

Note that a hysteresis between approach and retract force curves was visible due to cell viscosity (Figure S3.1). Accordingly, the values of the elastic modulus extracted from the approach and the retract curves using Hertz models differ significantly when investigating cells. Hence, this is clear evidence of how important the viscous contribution of cells, which cannot be easily separated from the elastic one in conventional force curves, is. To solve this issue, we used the sweep frequency methodology to measure the elastic and viscous response of the cell samples. Briefly, after approaching the tip towards the cell up to a deflection value defined by the trigger threshold, the z-piezo motion was stopped for 1 s. During this time, the stress applied during the approach ramp of the cell relaxed, and we applied a sinusoidal modulation with increasing frequency while still in contact with the cell. The frequency was swept from 1 Hz to 1 kHz, although the later analysis was performed only from 1 Hz up to 100 Hz due to piezo response limitations. When the modulation finished, the cantilever was retracted as in a conventional force curve (Figures S3.2 and S3.3). We used the power-law structural damping model to analyze the elastic and viscous contribution of cells separately. The storage modulus E' of healthy fibroblasts was 3.26 kPa at the lowest frequency applied (1 Hz) and increased linearly on a log-log scale (Figure 3.2), i.e., it actually followed a power law. The loss modulus E" was approximately 6-fold smaller than E': 0.47 kPa. Both storage and loss moduli displayed similar frequency dependence up to 10 Hz. Nevertheless, E" showed a more marked frequency dependence at higher frequencies, which is to a large extent due to the hydrodynamic interaction of the cantilever with the liquid medium (Alcaraz *et al.*, 2002) (Figure 3.2). For this reason, a viscous drag correction was applied, subtracting cantilever-medium viscous contribution. Scar and Dupuytren fibroblasts showed a similar trend of storage and loss moduli over frequency (Figure 3.2).

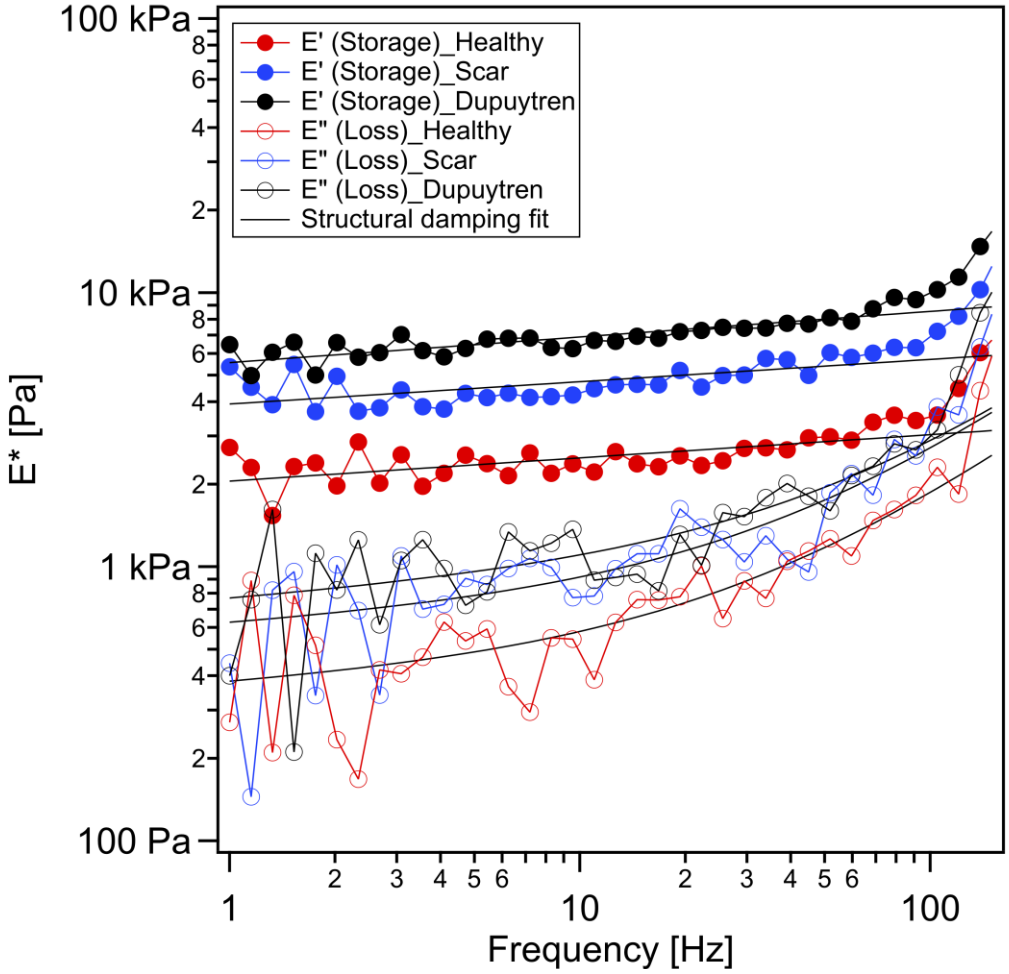

Figure 3.2 Frequency dependence of the storage (filled symbols) and loss moduli (open symbols) of healthy fibroblasts (red), scar fibroblasts (blue) and Dupuytren fibroblasts (black). Solid black lines are the fit of the power-law structural damping model ($n = 90$). Data shown are corrected for the viscous drag.

Dupuytren fibroblasts displayed the highest values in almost all moduli (Table 3.1). The loss tangent and the power-law exponent of the three cell types presented very close values to each other. Significant differences among all cell types were found for all rheological parameters (Figures 3.3 and 3.4). Both storage and loss moduli showed a similar trend as the apparent Young's modulus, which could also be seen in the respective histograms (Figures 3.1b and 3.3). The loss tangent at 1 Hz presented a barely significant difference among the cell types, the same as the power-law exponent (Figure 3.4). E_0, which is a scale factor for the storage and loss moduli, varied depending on the cell type. Healthy and scar fibroblasts presented similar values (healthy: 3308 Pa and scar: 3077 Pa); nevertheless, Dupuytren fibroblasts showed an increase going up to 4259 Pa. The Newtonian viscous term (μ) was rather small, and it increased from healthy to Dupuytren fibroblasts (7 to 13 Pa·s, respectively).

Table 3.1 Apparent Young's modulus, storage and loss modulus at 1 Hz, loss tangent at 1 Hz and power-law exponent median values for each cell type ($n = 90$).

	Apparent Young's modulus (Pa)	**Storage modulus (Pa)**	**Loss modulus (Pa)**	**Loss tangent**	**Power law exponent**
Healthy Fib.	3345	3260	473	0.18	0.11
Scar Fib.	3940	3024	576	0.19	0.13
Dupuytren Fib.	5364	4260	742	0.18	0.12

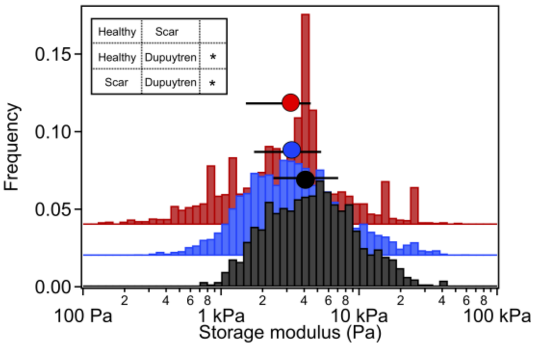

(a) **(b)**

Figure 3.3 Histogram representation of the **(a)** storage and **(b)** loss modulus at 1 Hz for each fibroblast type together with the median and 25/75 percentiles above each histogram distribution. Healthy fibroblasts are in red, scar fibroblasts in blue and Dupuytren fibroblasts in black. Wilcoxon signed- rank test showing significant differences among all cell types are indicated in the table (*; $p < 0.01$) and Cohen's d test with # indicating $0.2 < d < 0.5$ ($n = 90$).

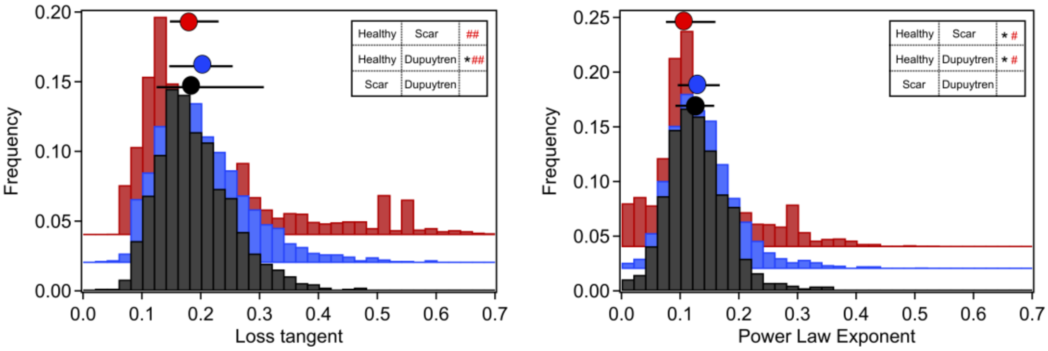

(a) **(b)**

Figure 3.4 Histogram representation of the **(a)** loss tangent at 1 Hz and **(b)** power-law exponent for each fibroblast type together with the median and 25/75 percentiles above each histogram distribution. Healthy fibroblasts are in red, scar fibroblasts in blue and Dupuytren fibroblasts in black. Wilcoxon signed-rank test showing significant differences among all cell types are indicated in the table (*; $p < 0.01$) and Cohen's d test with # indicating $0.2 < d < 0.5$ and ## indicating $0.5 < d < 1.0$ ($n = 90$).

3.3.2 Cytoskeleton inhibition

The effect of ML-7 on the three different cell types was observed by video microscopy over a period of 2–3 h. Different concentrations of the inhibitor were added to the cells to decide which concentration was optimal to produce a significant change in cell mechanics but, at the same time, let the cells recover again.

With the help of time-lapse videos, the optimal concentration of ML-7 to observe a sufficient cell mechanical change was determined. In total, 1 and 3 μM ML-7 were sufficient to produce visual effects on the cells showing contraction and changes in morphology (Figure 3.5 and videos in Supplementary Materials). Mechanical properties of the three cell types were measured using the AFM before and after the addition of the inhibitor. We selected 5–6 cells in each experiment and focused on tracking the changes in stiffness over time in these 5–6 cells. Cell mechanics were probed twice before and 4–5 times after adding ML-7 inhibitor, spending a maximum time of 2–3 h per experiment. Consecutive measurements were performed every 15 or 30 min.

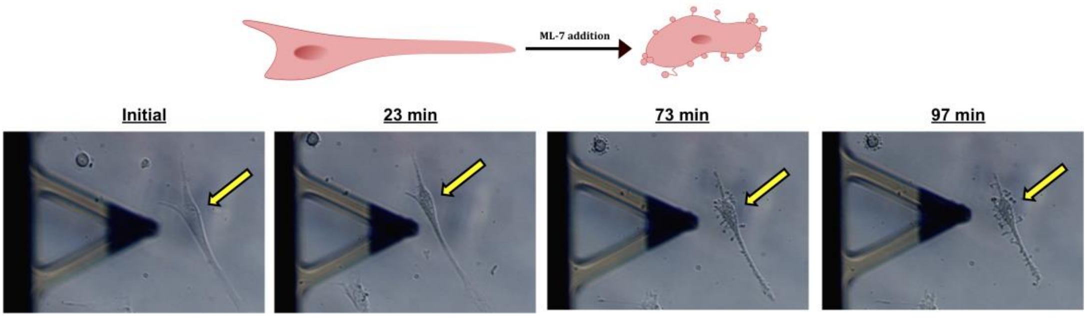

Figure 3.5 Effect of ML-7 addition on fibroblast morphology. Example of a scar fibroblast before and after the addition of 3 μM ML-7. Yellow arrow shows cell position. Cell contraction as well as bleb formation are visible.

After adding 1 or 3 µM ML-7, we observed differences in cell mechanical behavior. Healthy and scar fibroblasts did not show a clear response after adding 1 µM; however, Dupuytren fibroblasts seemed to be more sensitive to the drug and experienced a decrease in apparent Young's modulus right after the ML-7 addition (from 2 kPa to 0.2 kPa); after a while, they started to recover showing a slight increase in apparent Young's modulus values (from 0.2 kPa up to 0.5 kPa) (Figure S3.5).

We also recorded the rheological parameters during these experiments, and the storage and loss moduli over the frequency of each fibroblast can be seen in Figure S3.6. Initial E* values (cell before ML-7 treatment), together with two intermediate times after a 1 µM ML-7 addition, were plotted. Healthy and scar fibroblasts did not show E* changes over frequency after inhibition; however, Dupuytren fibroblasts displayed a decrease in both moduli after ML-7 addition. A scatterplot of the loss tangent versus storage modulus at 1 Hz can be seen in Figures 3.6 and 3.7. Each colored dot represents one cell measurement at a specific time point where the change towards lighter colors (from light blue-initial-, to yellow-last measurement-) corresponds to the time course during the experiment. In Figure 3.6 (Dupuytren fibroblast), the storage modulus followed the same trend as the apparent Young's modulus (Figure S3.5), it decreased after ML-7 addition and it developed towards slightly higher values over time. The opposite trend was observed for the loss tangent, which increased after ML-7 addition. These results can be understood as a decrease in the elastic over the viscous elements due to the disruption of the cytoskeleton network caused by the inhibitor. Otherwise, when exposing the cells to 3 µM of ML-7, they showed larger changes (Figure 3.7). A good percentage of healthy and scar fibroblasts still did not show any visible effect (Table 3.2); however, others reacted to the inhibitor with a decrease in stiffness and either recovered over time or died (Figure S3.7).

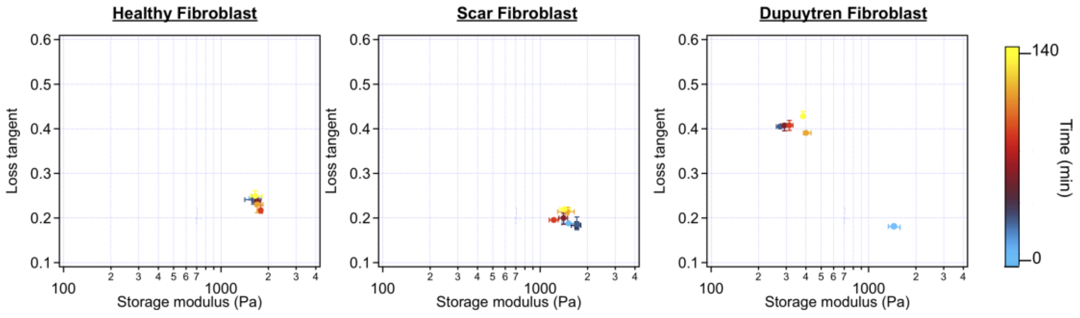

Figure 3.6 Scatterplot of the loss tangent versus storage modulus at 1 Hz before and after 1 µM ML-7 addition. The color bar indicates the time after addition (*n* = 15).

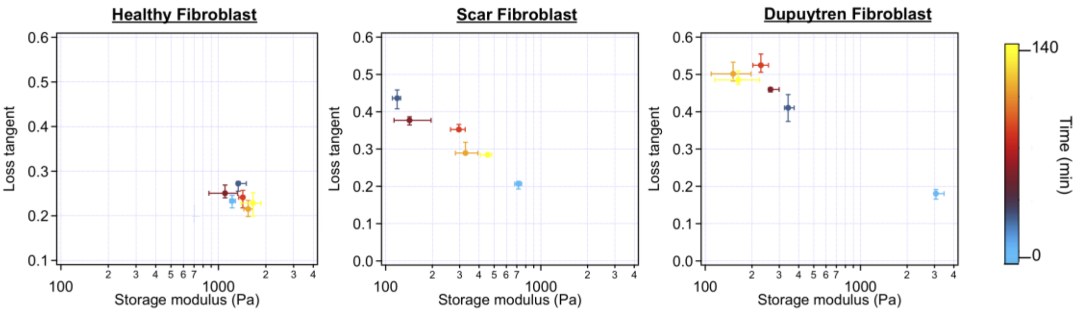

Figure 3.7 Scatterplot of the loss tangent versus storage modulus at 1 Hz before and after 3 µM ML-7 addition. The color bar indicates the time after addition (*n* = 20).

Table 3.2 Percentage of fibroblasts that die, recover or experience no change after addition of 1 or 3 µM of ML-7 inhibitor.

	Healthy Fibroblasts	**Scar Fibroblasts**	**Dupuytren Fibroblasts**
1 µM ML-7 (*n* = 15)	Dead: 20% Recovery: 20% No change: 60%	Dead: 0% Recovery: 20% No change: 80%	Dead: 13% Recovery: 47% No change: 40%
3 µM ML-7 (*n* = 20)	Dead: 39% Recovery: 34% No change: 27%	Dead: 39% Recovery: 25% No change: 36%	Dead: 60% Recovery: 10% No change: 30%

An example of a force curve demonstrating the change in mechanics (slope) after 3 µM ML-7 can be found in Figure S3.8. In panel B, which is an example of a scar fibroblast, a decrease in slope was visible after 36 min of 3 µM ML-7 addition, which increased again after 118 min thanks to cell recovery. It can be noted how the hysteresis between approach and retract curves also increased over time in panel C owing to a decrease in cell elasticity. The frequency dependence of storage and loss moduli was shown for the three cell types after 3 µM ML-7 (Figure S3.9). The example of healthy fibroblasts did not present changes in E* after inhibitor addition; however, scar fibroblasts presented a decrease in both storage and loss moduli immediately after ML-7 addition but recovered after about 120 min. Dupuytren fibroblasts E* over frequency displayed a continuous decrease over time after ML-7 addition. Dupuytren fibroblasts, as already seen at lower ML-7 concentrations, either reacted more drastically to the drug, and many cells died or responded with a contraction and decrease in elastic modulus with recovery over time (Figure 3.7).

Although the most representable data were shown in Figures 3.6 and 3.7, not all fibroblasts from the same cell type reacted similarly. There was always a percentage of cells that died, recovered or did not respond to the ML-7 inhibitor regardless of cell type and inhibitor concentration (Table 3.2). Note that all rheological parameters of each fibroblast when treated with 1 and 3 µM ML-7 can be found in Figures S3.10–S3.15.

To disentangle what happened to the cells in terms of the cytoskeleton network, actin fibers of the three cell types were labeled in all conditions (with and without ML-7 addition) (Figure 3.8). Cells affected by the inhibitor changed their shape (from elongated to more roundish due to a reduction in contractility) as well as actin fibers broke. In Figure 3.8F (Dupuytren fibroblasts treated with ML-7), some cells formed green dots in their interior along with blebs in the cell membrane, which could be due to cytoskeleton disruption (actin fibers break in small pieces) and cortex rupture. The bleb formation is an indicator of apoptosis initiation.

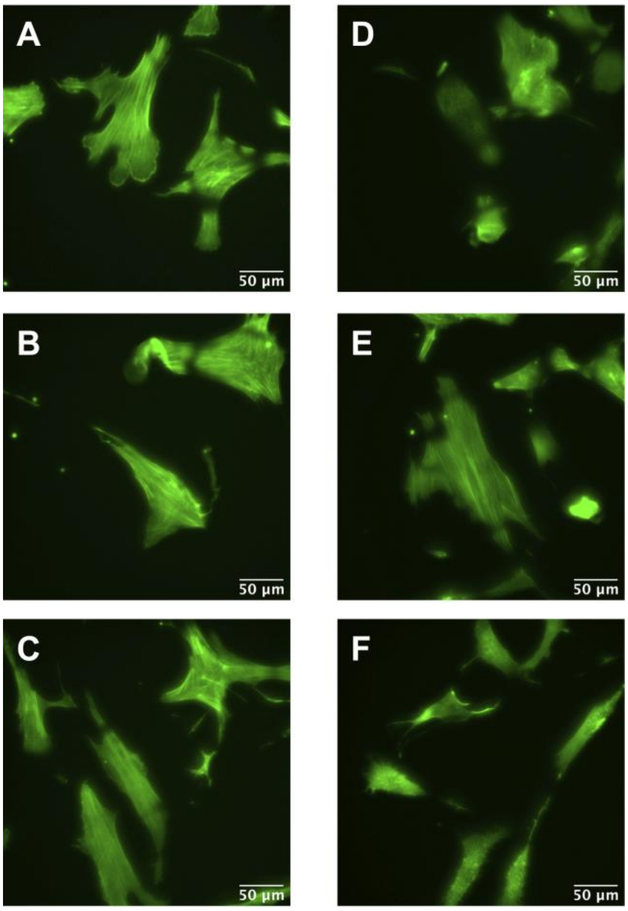

Figure 3.8 Fluorescence images of **(A)** healthy, **(B)** scar and **(C)** Dupuytren fibroblasts in normal conditions (no inhibitor); **(D)** healthy, **(E)** scar and **(F)** Dupuytren fibroblasts 20 min after the addition of 3 µM ML-7. Actin fibers are labeled in green. Control measurements adding DMSO at the same contraction as

ML-7 can be found in Figures S3.16–S3.17. AFM measurements of Dupuytren fibroblasts over time without drug treatment can be observed in Figure S3.18.

3.4 Discussion

3.4.1 Mechanical and rheological properties

Cells are living samples that are complicated to study and characterize. In most (AFM) cell mechanical studies, force curves are usually analyzed only in terms of Young’s modulus, which describes the mechanical behavior of elastic samples. More precisely, the widely used Hertz model quantifies the relationship between stress and strain only in the linear elastic regime of a material. Cells are much more complex materials: they are viscoelastic materials, i.e., they combine properties of viscous liquids and elastic solids. Purely elastic solids obey Hooke’s law, and when a stress is applied, an instantaneous strain appears, and on the removal of the stress, the strain reverts to zero. Viscous liquids are described to have a constant velocity flow and energy dissipation while a constant shear force is applied. In biophysics cell elasticity is understood in terms of cytoskeleton dynamics, where the number of crosslinks, rearrangements and deformation and stress (contractile forces) will affect the elastic properties of cells. The viscosity of cells is much more complicated to attribute, but it can be understood as the internal friction that occurs when all components in a flowing liquid are forced to slide along each other. For acquiring cells’ elastic and viscous properties, the AFM sweep frequency scheme was employed, which allows the separation of elastic and viscous components using an appropriate model. In the above graphs, the apparent Young’s modulus and the storage modulus displayed similar distributions, in which healthy fibroblasts presented the lowest values and Dupuytren fibroblasts the highest, which can be attributed to the changes in cytoskeleton organization and accumulation (Figure 3.1), being Dupuytren fibroblasts the ones showing thicker and more accumulation of actin fibers in the cell body (Figure 3.8C). This cytoskeleton organization of Dupuytren fibroblasts is related to myofibroblast phenotype, which are differentiated fibroblasts found in wound healing and present an increased contractile activity. Many cell types can differentiate into myofibroblasts, such as smooth-muscle cells, cardiomyocytes, bone marrow cells, etc. Nevertheless, the vast majority of myofibroblasts come from neighboring fibroblasts. The mechanical properties of these fibroblasts had already been measured in a previous study (Viji Babu *et al.*, 2018); however, they used non-calibrated cantilevers (MLCTs), where (unavoidable) errors in the cantilever calibration could induce misleading values. Therefore, in this study, we used PFQNM cantilevers, which are pre-calibrated, to minimize errors. Besides, they calculated the elastic modulus and dynamic viscosity using a stress relaxation methodology, but here we employed oscillatory testing, which is a more robust approach to determine the viscoelastic properties of cells. We measured the complex elastic modulus (E*) using AFM over three frequency decades (1–1000 Hz); however, analyses were performed only from 1 Hz to 100 Hz due to the limited response time of the z-piezo. The E' data at 1 Hz were around 3 kPa for healthy and scar fibroblasts, and 4 kPa for Dupuytren fibroblasts (Table 3.1) and all of them showed the same tendency: they increased weakly with frequency following a power law with an exponent around 0.1. The loss modulus E" was around 1/6 of the storage modulus E' in all cell types and increased similarly up to 10 Hz, but it presented a greater frequency dependence at higher frequencies (Figure 3.2). After viscous drag correction (cantilever-liquid hydrodynamics) (Alcaraz *et al.*, 2003), the loss modulus still presented a more marked frequency dependence, which is intrinsic to cell viscoelastic behavior (Figure S3.19). The hydrodynamic correction factor b(0) obtained for the PFQNM cantilever is relatively small in comparison to other cantilevers due to their small dimensions and large stiffness (Alcaraz *et al.*, 2002). The values of the loss tangent are close to 0.2, and power-law exponents are around 0.1 (Table 3.1), which is in agreement with previous works found in the literature (Fabry *et al.*, 2001; Rico *et al.*, 2005; Hecht *et al.*, 2015). Larger differences in cell's loss tangent could have been expected due to the different cytoskeleton organization; however, as fibroblasts do have already a well-developed cytoskeleton network, especially on hard substrates such as Petri dishes, the formation of few extra fibers in Dupuytren fibroblasts' cytoskeleton does not result in measurable changes in loss tangent. The loss tangent is rather a useful rheological parameter for measuring cytoskeleton changes after drug treatment or distinguishing between different cell lines.

Over the last couple of years, evidence has accumulated that proposes the existence of 1 or 2 power-law regimes of cytoskeleton dynamics at high frequencies (Rigato *et al.*, 2017; de Sousa *et al.*, 2020). In the early days, most of the rheological measurements on cells were performed up to a limited oscillatory frequency of 100–200 Hz (Fabry *et al.*, 2001; Alcaraz *et al.*, 2003). Active and passive microrheology have shown that E' and E" are coupled following a weak power-law with an exponent around 0.05–0.35 (Fabry *et al.*, 2001; Rebêlo *et al.*, 2014). This behavior was interpreted in terms of soft glassy rheology theory (SGR) and suggested that cells with an exponent near zero resembled a soft glassy material close to the glass transition, which is also the case for the three fibroblasts studied in this work (Sollich, 1998). Exponent values of 0.1 suggest that the three measured fibroblast types resemble a soft glassy material close to the glass transition. Recently, cell rheological experiments increasing the frequency regime over 5–6 decades from 0.01 Hz to 1 kHz have been performed. In these measurements, a second regime at higher frequencies (100 Hz–1 kHz) is visualized with a second power-law exponent around 0.3–1 attributed to single filaments dynamics (Isambert and Maggs, 1996; Rigato *et al.*, 2017). Our AFM rheological experiments cover only frequencies up to 100 Hz; thus, we are not able to observe the second regime because of frequency limitations. Rigato et al. used the high-speed AFM to study the rheological behavior of different cell types under cytoskeletal drug treatments spanning a high-frequency range (1 Hz–100 kHz). They saw two dynamic regimes, one at low frequencies (1 Hz–1 kHz) and another at high frequencies (1 kHz–100 kHz) (Rigato *et al.*, 2017). Our experimental design reached frequencies up to 1 kHz; however, due to the limited response of the piezo, data were just analyzed until 100 Hz, showing only one power-law exponent. Therefore, future experiments employing faster AFMs encompassing higher frequency ranges would provide data on cell behavior at shorter time scales.

3.4.2 ML-7 effect on cell mechanics

The organization of actin and myosin II mediates many cellular processes, such as cell migration, division, adhesion, etc. (Fletcher and Mullins, 2010; Tojkander, Gateva and Lappalainen, 2012). Cell contraction requires actin–myosin binding and sliding along actin filaments that depends on the phosphorylation of the myosin regulatory light chain (MRLC). The phosphorylation of myosin II at its regulatory light chain is mediated through the MLCK enzyme, which is a Ca2+/calmodulin-dependent enzyme (Tan and Leung, 2009). The activation of MRLC facilitates actin (β-actin and α-actin in myofibroblasts) and non-muscle myosin binding. Non-muscle myosin is believed to be a key protein for cell contraction and a regulator in wound and scar contraction (Tomasek and Rayan, 1995). When intracellular calcium increases, calcium interacts with calmodulin, which at the same time binds to MLCK. This calcium-calmodulin-MLCK complex formation activates MLCK enzymatic activity. MLCK activity is inhibited by drugs such as naphthalene sulfonamide derivatives. ML-7 is a member of naphthalene sulfonamide derivatives that acts by binding directly to MLCK on its active site (Figure 3.9). It is a reversible ATP-competitive inhibitor, and when ML-7 binds to MLCK, it blocks for a limited time the binding of ATP to the enzyme's active site, therefore preventing the phosphorylation of myosin RLC, non-muscle myosin activation, which leads to inhibition of actin–myosin binding and cell contraction. It has been found that ML-7 induces apoptosis in mammary and prostate cancer cells in vitro and also stimulates the ability of a chemotherapeutic drug to prevent the growth of mammary and prostate tumors in vivo (Gu *et al.*, 2006). Pancreatic cancerous cells were also treated with

ML-7 producing a rounding up and reduction of the number of stress fibers in the cell body (Kaneko *et al.*, 2002).

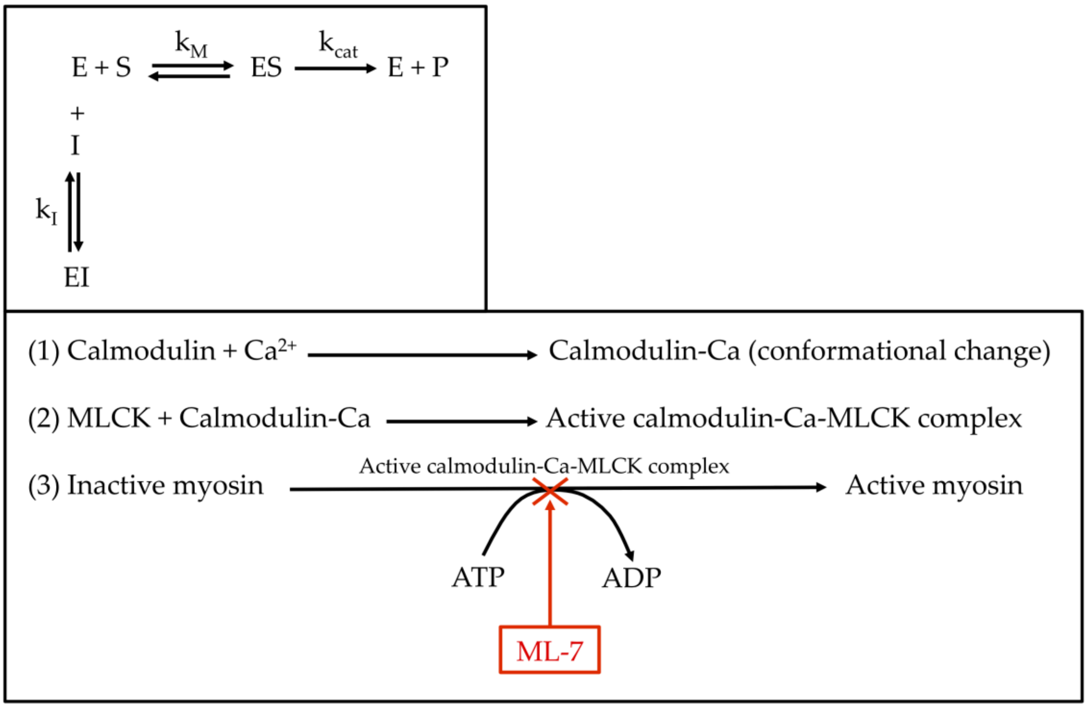

Figure 3.9 Schematic mechanism of a competitive inhibition and ML-7 place of action.

Although it is not clear if MLCK is overexpressed in myofibroblasts, an increase of MLCK expression has been observed in myofibroblasts obtained from the nodules of the palm of Dupuytren's patients in comparison to normal and cords fibroblasts (Hadeed *et al.*, 2011; Sayadi *et al.*, 2019). With these findings, we propose that the inhibition of MLCK by ML-7 is a potential target to reduce myofibroblasts contractility.

ML-7 effect is dose-dependent, from provoking no reaction at low concentrations to cell death at higher doses (Schäfer and Radmacher, 2005). 3T3 and NRK cells subjected to ML-7 exhibited a retraction of lamellipodia and softening of the cells; however, in some cases cell recovery was seen over an hour.

In this study, we treated the three fibroblast types with two different concentrations of ML-7. We used 1 and 3 µM as intermediate concentrations to assess differences in cell behavior among the cell types. Dupuytren fibroblasts differ from their healthy counterparts as they contain extra actin fibers, α-SMA, that result in a more-developed cytoskeleton network. This is translated into more elastic filaments in the cell body, more cortical tension and higher stiffness. This is in agreement with the data shown in Figure 3.1. Our data showed that Dupuytren fibroblasts present a more drastic reaction to the drug, and when treated with 1 μM of the inhibitor, ML-7 inhibits MLCK activity, thus resulting in disruption of the cytoskeleton network and reduction in stress fiber strength that is at the same time translated into a decrease in storage modulus and an increase in loss tangent as the cell becomes more liquid-like (Figure 3.6). In the case of healthy and scar fibroblasts at the same ML-7 dose, there were no visible changes in elasticity after adding the inhibitor. The different behavior of the three fibroblasts to the drug demonstrates the different nature of the cells and their different susceptibility towards MLCK inhibition. Lyapunova et al. found that the ML-7 effect on cancerous thyroid cells was less notorious than healthy counterparts (Lyapunova *et al.*, 2016). In the literature, compounds from the ML-7 family, such as ML-9, have also been tested as MLCK inhibitors. Both ML-9 and ML-7 are naphthalene sulfonamide derivatives, but ML-7 inhibition is more than 30-fold more potent than that ML-9 (Shi *et al.*, 2007; Xiong *et al.*, 2017). These inhibitors were also used on mouse lung carcinoma cells to study their effect on the cell attachment to fibronectin substrates (Isemura *et al.*, 1991). They suggested that MLCK phosphorylation is involved in cytoskeleton rearrangements required for the cell surface fibronectin receptor to cluster in order to achieve cell attachment to fibronectin substrates.

Myofibroblasts develop very mature focal adhesion complexes that connect the cell to the ECM and thus allow the propagation of mechanical stimuli. Focal adhesion complexes are composed of many intracellular proteins that connect the cell actin–myosin network to the ECM via integrins. Integrins are provided by extracellular, transmembrane and intracellular domains that enable the cell-ECM interplay. Changes in actin–myosin strength, such as cytoskeleton disruption through MLCK inhibition, have been seen to disentangle focal adhesion complexes leading to cell-ECM attachment interruption (Burridge and Chrzanowska-Wodnicka, 1996). Our study is in agreement with the previous idea, in which MLCK-inhibited fibroblasts lose their attachment to the substrate and start floating. Therefore, it seems likely that MLCK reduces actin–myosin contraction provoking a downstream signaling pathway in which focal adhesion complexes are also inhibited, weakening cell-ECM interaction.

An increased ML-7 concentration produces a stronger effect on the mechanical proper- ties of all cell types. Nonetheless, healthy and scar fibroblasts still showed less effect than Dupuytren fibroblasts. If cells did not present any shape or mechanical change, this does not necessarily imply that the cells have not reacted to the inhibitor in a biochemical way. The concentrations of the inhibitor used may produce effects that we are not able to pick up with the methods employed in this study. Another possible explanation is that cells in different stages of the cell cycle may show different susceptibility to the drug. Besides, since ML-7 is a reversible inhibitor, it may also happen that when the ATP concentration is greater than ML-7, ATP will preferentially bind to the enzyme restoring MLCK enzyme catalytic activity. As a matter of fact, we hypothesize that this may happen when fibroblasts start recovering their mechanical properties after cell softening. When cells experience a drastic change in shape and mechanical properties, it is often difficult to overcome the inhibition process and they end up dying. Cells experiencing death, in addition to cell shrinkage (acquiring a rounded shape), the formation of blebs and protrusions in the cell membrane, as well as fragmentation, is observed, where all these processes can be seen at different stages of apoptosis.

Our data support the notion that MLCK inhibition plays a role in fibroblasts and especially in myofibroblasts contraction. The more drastic effect of Dupuytren fibroblasts on ML-7 treatment supports its myofibroblasts phenotype and the potential use of ML-7 as a therapeutic treatment for Dupuytren's disease. Although our data show promising results, future studies are needed to corroborate our findings and to encompass different approaches, for example, looking at calcium-independent pathways (Rho-kinase), which are also known to play an important role in myofibroblasts contraction.

3.5. Materials and Methods

3.5.1 General materials

ML-7 inhibitor was purchased from Merck (Sigma-Aldrich, St. Louis, MO, USA, Merck, Rahway, NJ, USA, 475880). A 50 µM stock solution was prepared in DMSO. Further dilutions were made in complete cell culture medium.

3.5.2 Cell isolation and cell culture

Primary fibroblasts were isolated from 3 surgically removed skin tissues of a 55-year-old female patient's left-hand palmar fascia regions. Scar fibroblasts were extracted from the dermal scar excision and healthy fibroblasts from the adjacent skin tissue.

Dupuytren fibroblasts were isolated from nodules on the palmar fascia. The protocol to isolate the three cell types has been described previously (Viji Babu *et al.*, 2018). All fibroblasts were cultured with DMEM (Sigma-Aldrich, FG0435) medium supplemented with 10% fetal bovine serum (Sigma- Aldrich, F7524) and 2% penicillin-streptomycin (Sigma-Aldrich, P0781) and incubated at 37 ◦C in a 5 % CO2 humidified chamber. Cells were seeded in Petri dishes 48 h prior to AFM experiments. Passages from 4 to 10 were used for the measurements.

3.5.3 AFM experiments

AFM measurements were performed with an MFP3D AFM (Asylum Research, Santa Barbara, CA, USA) combined with an optical microscope (Zeiss Axiovert 135, Zeiss, Oberkochen, Germany) to be able to control tips and samples. Petri dishes, containing samples, were fixed to an aluminum holder with vacuum grease and mounted on the AFM stage with two magnets. The entire set-up was enclosed in a home-built polymethyl-methacrylate (PMMA) box in order to inject and maintain 5% CO2 during experiments. Fibroblasts were probed 48 h after seeding and data were collected on the nuclear region.

In this work, two types of experiments were carried out. Firstly, rheological properties of the cells were measured. For such purpose, PFQNM-LC-A-CAL cantilevers were employed (Bruker, Karlsruhe, Germany, pre-calibrated spring constant around 100 pN/nm and 45 kHz resonance frequency in air), which have a three-sided pyramidal tip (15–25° opening angle) with a protrusion of 75 nm tip radius and 0.8–1 µm length at its end. Around 90 cells of each type were probed and the apparent Young's modulus values were extracted from regular approach curves. In addition, sweep frequency force curves were employed to obtain individually the elastic and viscous properties. Shortly, in sweep frequency curves a sinusoidal modulation in z-height with increasing frequency (from 1 Hz to 1 kHz) is applied for 8.7 s after the trigger threshold was achieved. After 1 s, the sinusoidal modulation was started while still in contact with the cell and after an extra 1 s this step was reversed (Figures S3.1–S3.3). From these experiments, storage and loss modulus, loss tangent and power-law exponent parameters were acquired. Each force map was spaced 5 × 5 µm and composed of 16 or 256 force curves (4 × 4 or 16 × 16 lines per frame). Typically, force curves were recorded at a scan rate of 2 Hz, corresponding to a maximum velocity of 20 µm/s.

For the second set of experiments, cells' mechanical properties were assessed before and after ML-7 addition for each fibroblast. Pre-calibrated cantilevers (MLCT-SPH-

DC-E, Bruker, nominal spring constant 150 pN/nm and 17 kHz resonance frequency in air) with a semi-spherical tip of 5.5-µm radius were used to assess cell properties. At least 20 fibroblasts were measured for each cell type. Concentrations of 1 and 3 µM ML-7 were used in order to assess differences in cell behavior. Each force map was spaced 5 × 5 µm and composed of 4 or 36 force curves (2 × 2 or 6 × 6 lines per frame). Force curves were recorded at a scan rate of 1.3 Hz, corresponding to a maximum velocity of 10.4 µm/s. Indentation depths were always greater than 500 nm in order to average the stiffness over a large contact area, which gives values that do not depend on local variations of the cytoskeleton structure.

3.5.4 AFM data analysis

The data analysis software IGOR 7 (Wavemetrics, Lake Oswego, OR, USA) was used to evaluate the mechanical properties of cells in terms of Young's or elastic modulus (E). The Hertzian model for spherical/parabolic tips was used to calculate the apparent Young's modulus for each force curve within a force map. The logarithmic histogram and median with 25/75 percentiles of Young's modulus were considered representative modulus of each force map. Sweep frequency data were fitted with the power-law structural damping model (Alcaraz *et al.*, 2003). E* data are separated into real (in phase) and imaginary (out of phase) parts. The real part represents the storage modulus, and it is a measure of the elastic energy stored and recovered per cycle of oscillation. The imaginary part depicts the loss modulus, and it accounts for the energy dissipated per cycle of sinusoidal deformation. We also calculate the loss tangent, which is an index of the solid-like (<1) or the liquid-like (>1) behavior of the cell. This model assumes a storage modulus that increases with the frequency following a power law with exponent α and a loss modulus that includes a term that is a fraction η of the storage modulus and a Newtonian viscous term (Supplementary, sweep frequency).

3.5.5 Immunostaining

Forty-eight hours after seeding of cells on Petri dishes, cells were fixed with 4% paraformaldehyde for 15 min and permeabilized with 0.1% Triton ×100 for 5 min. Samples were washed with PBS after each step and then incubated with ActinGreen 488 ReadyProbes Reagent (Invitrogen, ThermoFisher, Waltham, MA, USA, R37110) (2 drops in 1 mL PBS) for F-actin staining for 30 min at room temperature. Finally, cells were stored in PBS at 4 ◦C prior to image acquisition. Nikon Eclipse Ti inverted epi-fluorescence microscope (Nikon Instruments Inc., Melville, NY, USA) with 40× objective lens was used to observe cells and collect fluorescent images.

3.5.6 Statistical analysis

Differences between apparent Young's modulus values obtained for each cell type were checked for statistical significance with the Wilcoxon signed-rank test and for effect size with Cohen's d test using IGOR. For each force volume the median of E values was calculated. The effect size (Cohen's d) between the means of E and the significance of difference (Wilcoxon signed-rank) between the medians of the E for each type of cell was tested. For p-values obtained from the Wilcoxon signed-rank test, * indicating $p < 0.01$ and Cohen's d test with # indicating $0.2 < d < 0.5$ and ## indicating $0.5 < d < 1.0$.

3.6 Conclusions

We have assessed the rheological properties of three primary fibroblasts, all established from the palm of the same patient. Dupuytren fibroblasts, expressing a myofibroblast phenotype, presented larger apparent Young's modulus values than healthy or scar fibroblasts, which is attributed to extra actin fibers. We have also determined the effect of myosin II function on the stiffness of fibroblasts. ML-7, an MLCK inhibitor, was used to deactivate myosin II in these three fibroblast types. The changes in rheological properties were measured by AFM employing oscillatory testing as a methodology to extract separately elastic and viscous contributions. In summary, it was shown that myosin activation is a key element for cell contractility, and ML-7 reduces fibroblasts and myofibroblasts contractility through the inhibition of MLCK, especially Dupuytren fibroblasts, which were the most susceptible. ML-7 effect suggests its potential use as a pharmacological treatment for Dupuytren's disease.

3.7 Author Contributions

S.P.-D. performed AFM experiments, fluorescence experiments, data analysis, and manuscript preparation. J.L.-A. helped in JPK AFM data acquisition used for 3D-images representation of the cells. F.L. helped in JPK AFM data acquisition used for 3D-images representation of the cells. M.R. helped in the design of the experimental scheme and was involved in data analysis and preparation of the manuscript. All authors have read and agreed to the published version of the manuscript.

3.8 Acknowledgments

We thank Ursula Mirastschijski for kindly providing tissue samples and Gazanfer Belge for establishing cell lines from primary cells. We would like to thank Dorothea Brüggemann for kindly providing access to the flourescence microscope and Deepanjalee Dutta and Arundhati Joshi for sharing their knowledge. We would also like to thank Nina Messerschmidt for kindly helping in cell culture.

3.9 Funding

This project was funded by the H2020 European Research and Innovation Programme under the Marie Skłodowska-Curie grant agreement "Phys2BioMed" contract no. 812772.

3.10 Institutional Review Board Statement

The study was conducted in accordance with the Declaration of Helsinki, and approved by the local Ethics Committee (Ärztekammer Bremen, #336/2012).

3.11 Informed Consent Statement

Patient was informed pre-operatively and had given its informed consent to anonymous tissue donation.

3.12 Supporting information

Data Availability Statement: Part of the data generated and/or analyzed during the current study is available in zenodo (https://doi.org/10.5281/zenodo.7376914).

AFM original data are obtained as follows, deflection versus z-piezo movement (d-z):

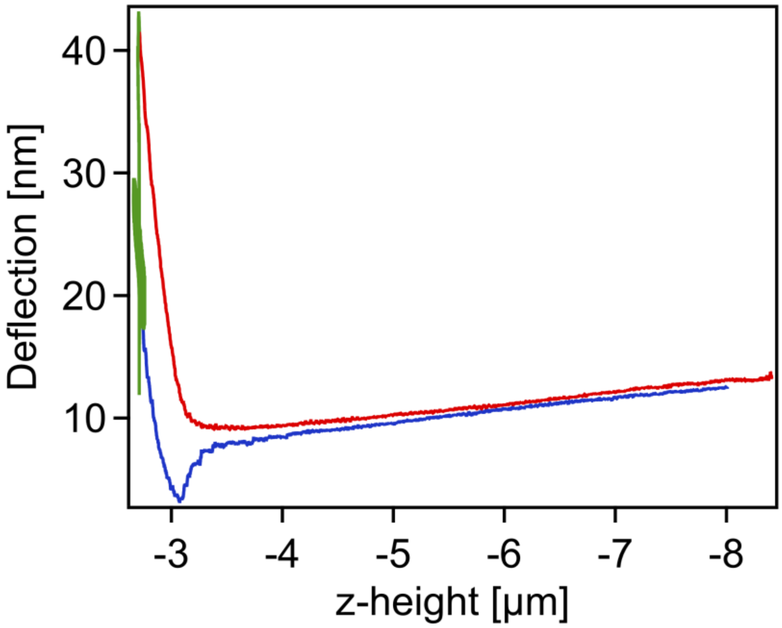

Figure S3.1 Example of a sweep modulation force curve. Deflection versus z-height display. The approach curve is in red, the retract curve in blue and the dwell in green (sweep modulation). The hysteresis between approach and retract curve is due to the cell's viscous contribution and adhesion.

However, to compute Young's modulus E, which is a measure of the sample's elasticity, force curves need to be converted into force versus indentation (F- δ) data. For that, the total force applied to the sample can be calculated using Hooke's law:

$$F = k \cdot (d - d_0) \qquad \text{(Eq. 3.1)}$$

where k is the spring constant of the cantilever and d the cantilever deflection.
Indentation data can be derived from the following expression:

$$\delta = (z - z_0) - (d - d_0) \qquad \text{(Eq. 3.2)}$$

where z_0 is the cantilever displacement at the tip-sample contact point and d_0 is the deflection offset. To obtain E, (F- δ) curves are analyzed with the appropriate contact model. In our experiments we used Hertz's model for spherical tips (more exactly: for parabolic tips, which are a good approximation and commonly used for spherical tips):

$$F = \frac{4}{3}\frac{E}{(1-\nu^2)}\sqrt{R}\delta^{3/2} \quad \text{(Eq. 3.3)}$$

where R is the radius of curvature in spherical/paraboilic probes and ν is the Poisson's ratio (is assumed to be 0.5).

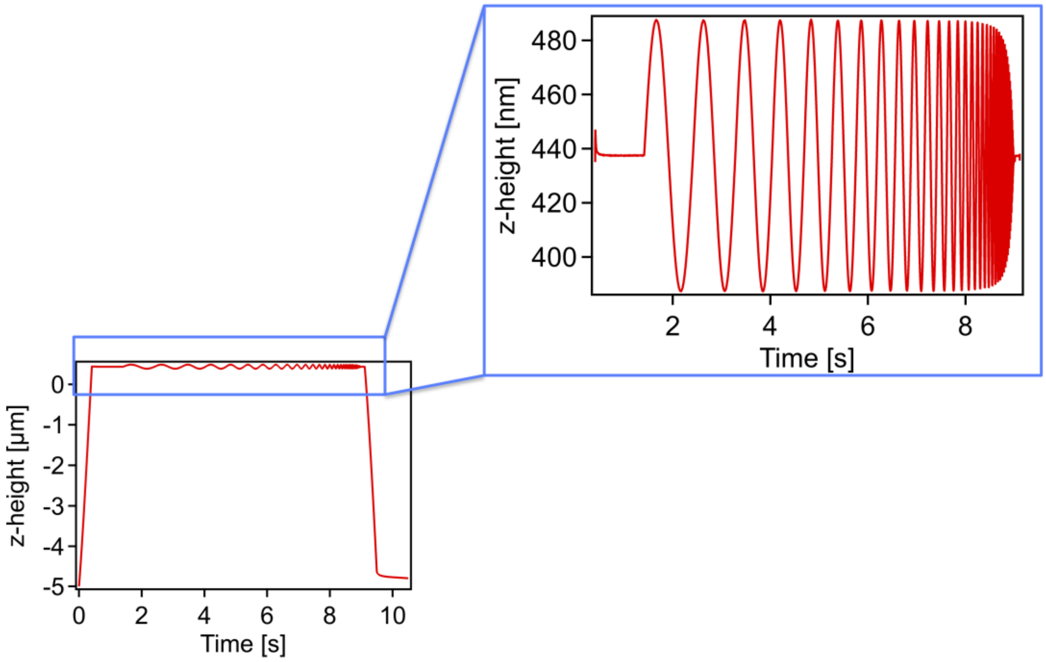

Figure S3.2 Z-height versus time in sweep modulation. The z-height reflects the piezo movement in z direction over time while the sweep modulation is taking place. The blue box zooms in the sweep modulation part.

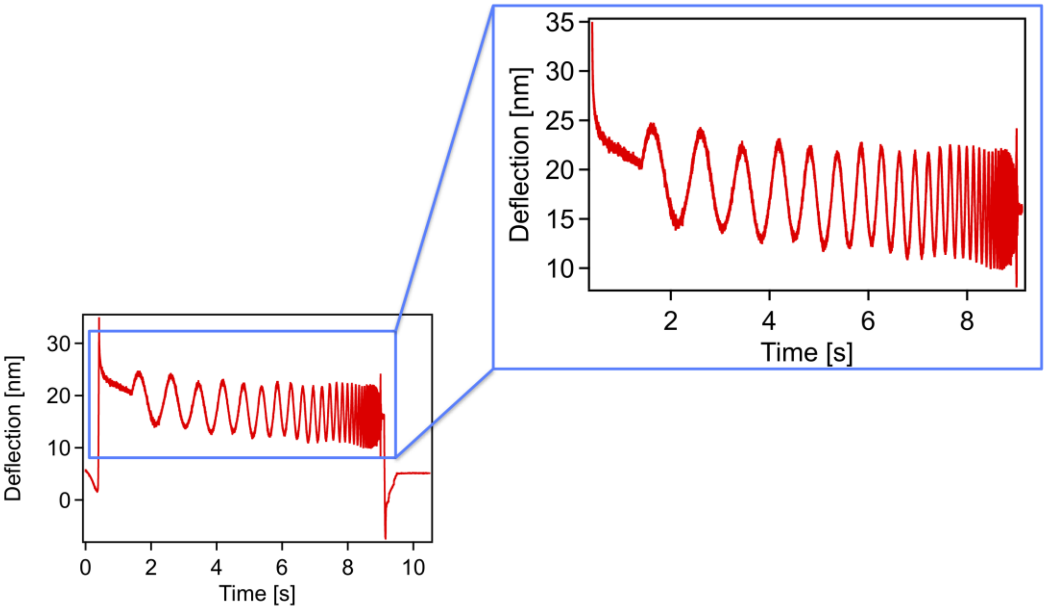

Figure S3.3 Deflection versus time display during sweep modulation. The deflection reflects the cantilever movement over time while the sweep modulation is taking place in a force curve. The blue box zooms in the sweep modulation part.

In sweep modulation methodology a sinusoidal modulation with increasing frequency is added to the z-piezo while the tip is in contact. Typically, we use a dwell time of 8.7 seconds, where during the first second no modulation is applied since the cell creeps substantially. Then, the modulation starts and the frequency is swept from 1Hz to 1kHz, where for each frequency only one cycle is applied. The frequency series is designed as a geometric series, so that in each decade we use the same number of frequencies. Typically, the frequency increases by a factor of 1.15 from cycle to cycle, which results in 17 frequency values per decade, which are equally spaced on a logarithmic scale.

We employed the power law structural damping model as has been introduced to AFM rheology by (Alcaraz *et al.*, 2003). Here, the complex modulus G^* is written as:

$$G^*_{(\omega)} = G_0 * (1 + i\eta) * \left(\frac{\omega}{\omega_0}\right)^{\alpha} + i\,\mu\,\frac{\omega}{\omega_0} \qquad \text{(Eq. 3.4)}$$

where G_0 is the absolute value of the moduli, i is the imaginary unit, η is the ratio between loss modulus and storage modulus (often called the loss tangent), ω_0 is the frequency scale (in our case we use 1 Hz), α is the power law exponent of the sample, and μ is the strength of the hydrodynamic damping, which will depend on the shape of the cantilever and the viscosity of the medium. The real part represents the storage modulus and the imaginary part corresponds to the apparent loss modulus, which has two contributions; (1) from the sample, which scales with the same power law exponent as the storage modulus, and the hydrodynamics, which is directly proportional to the frequency. Thus, we can first obtain the power law exponent by fitting the storage modulus as a function of frequency, and then in a second step obtain the loss tangent η and the strength of the hydrodynamic damping of the cantilever μ.

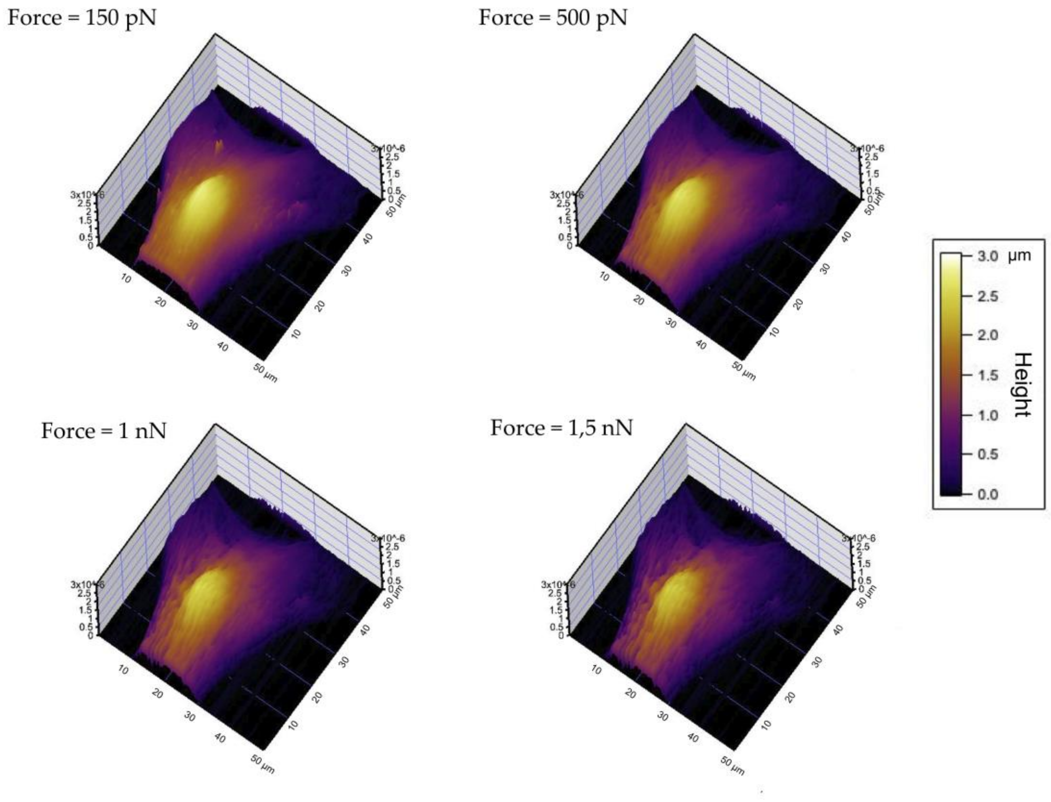

(a)

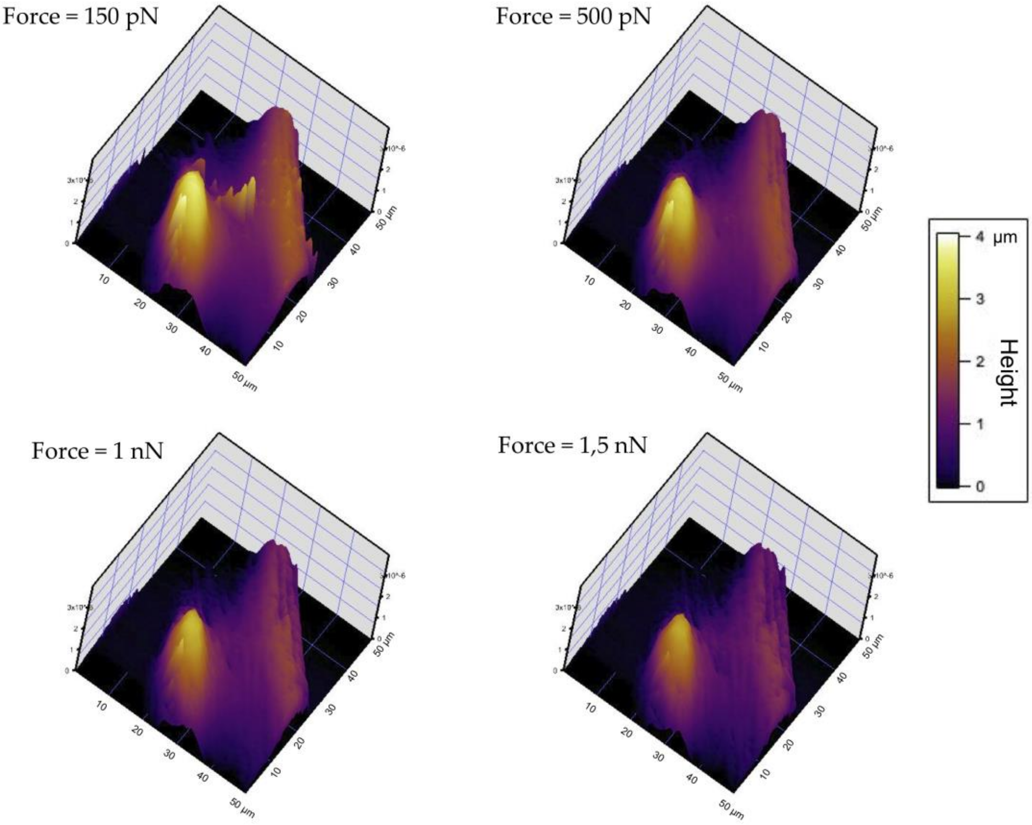
Force = 150 pN
Force = 500 pN
Force = 1 nN
Force = 1,5 nN
3x10^-6
10^-6
50 µm
10
20
30
40
4 µm
3
2
1
0
Height

(b)

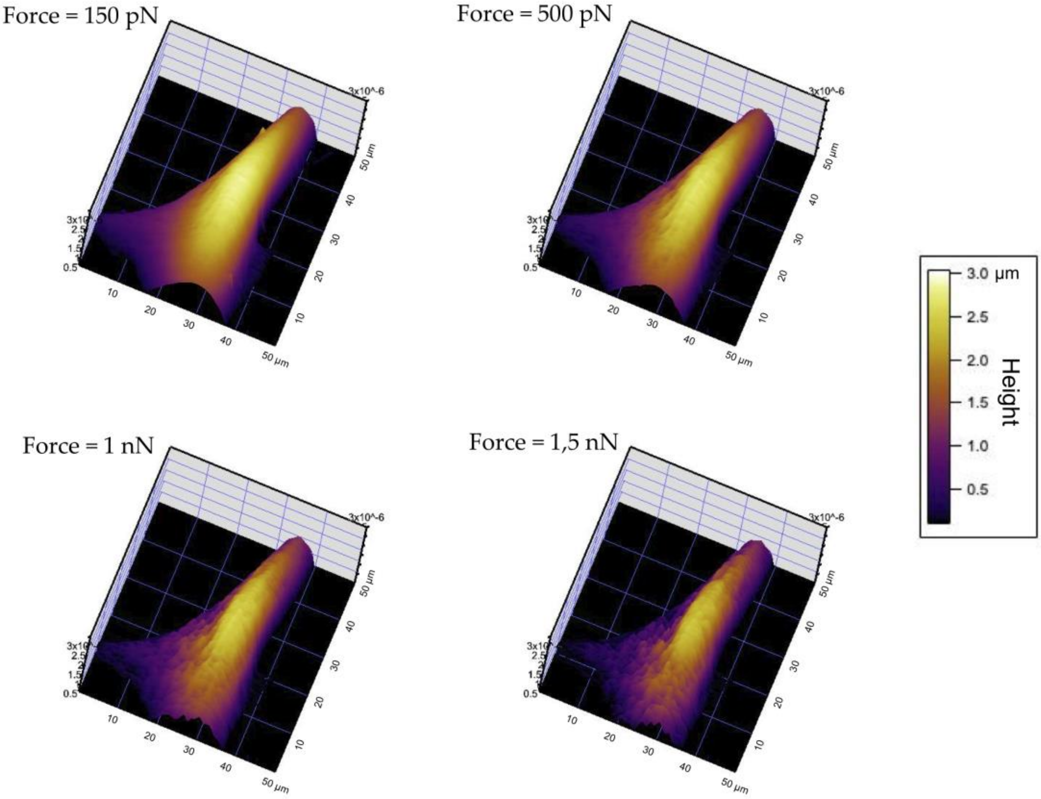
Force = 150 pN
Force = 500 pN
Force = 1 nN
Force = 1,5 nN
3x10^-6
50 µm
10
20
30
40
3.0 µm
2.5
2.0
1.5
1.0
0.5
Height

(c)

Figure S3.4 3D-images representation of a) Healthy, b) scar and c) Dupuytren fibroblasts obtained from high-resolution JPK force maps. Forces maps of 50x50 µm with pixel resolution of 135x135. The color bar indicates the cell height.

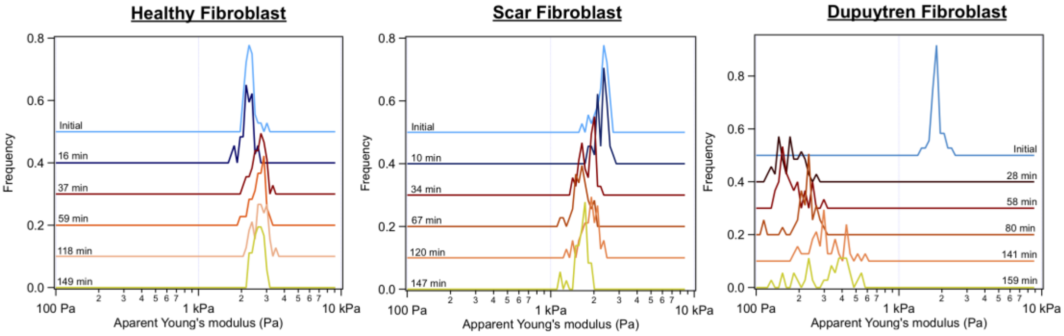

Figure S3.5 Histogram distribution of the Apparent Young’s modulus of each fibroblast before and after 1 µM ML-7 addition (*n* = 15).

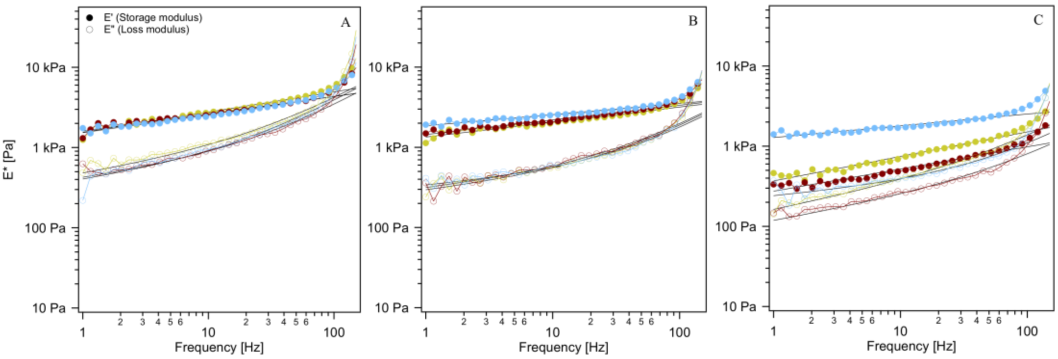

Figure S3.6 Frequency dependence of the storage (filled symbols) and loss modulus (open symbols) before and after addition of 1 µM ML-7 in a) healthy fibroblast (blue: initial; red: 37 min after ML-7; yellow: 149 min after ML-7), b) scar fibroblast (blue: initial; red: 34 min after ML-7; yellow: 147 min after ML-7) and c) Dupuytren fibroblast (blue: initial; red: 58 min after ML-7; yellow: 159 min after ML-7). Solid black lines are the fit of the power law structural damping model. ML-7 produces a drop in storage and loss modulus in C (*n* = 15).

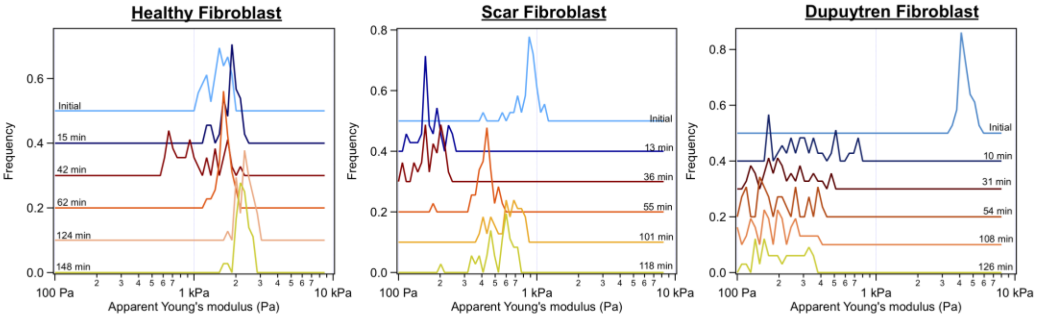

Figure S3.7 Histogram distribution of the Apparent Young’s modulus of each fibroblast before and after 3 µM ML-7 addition (*n* = 20).

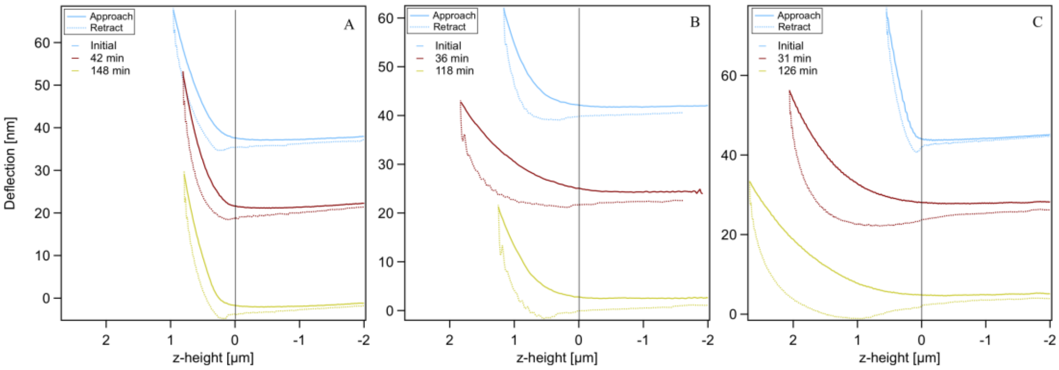

Figure S3.8 Example of a regular force curve of A) healthy, B) scar and C) Dupuytren fibroblast before and after 3 µM of ML-7 addition. Solid line is the approach curve and the dashed line retract curve. The effect of ML-7 in the cell is visible in B and C panels with a decrease in the slope and an increase in the hysteresis between the approach and retract curve. The increment in the hysteresis reflects an increase in the viscosity of the cell due to cell cytoskeleton disruption. The B panel also reflects a cell recovery after 118 minutes of ML-7 addition, the slope of the curve (yellow) increases with respect to the red curve.

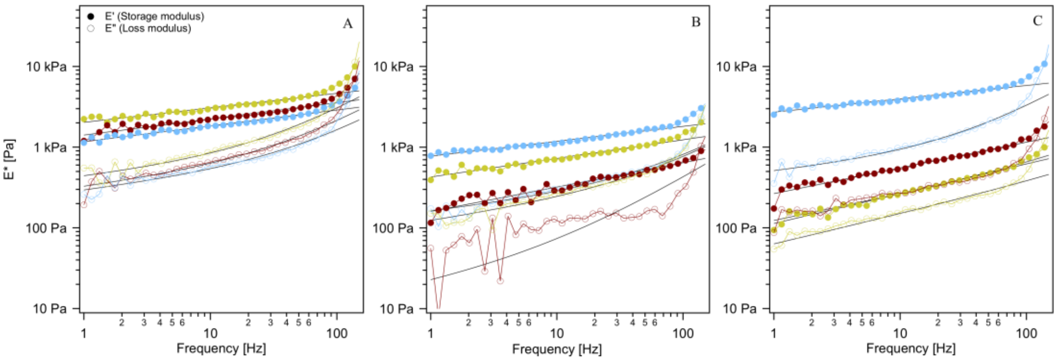

Figure S3.9 Frequency dependence of the storage (filled symbols) and loss modulus (open symbols) before and after addition of 3 µM ML-7 in a) healthy fibroblast (blue: initial; red: 42 min after ML-7; yellow: 148 min after ML-7), b) scar fibroblast (blue: initial; red: 36 min after ML-7; yellow: 118 min after ML-7) and c) Dupuytren fibroblast (blue: initial; red: 31 min after ML-7; yellow: 126 min after ML-7). Solid black lines are the fit of the power law structural damping model. ML-7 produces a drop in storage and loss modulus in B and C panels ($n = 20$).

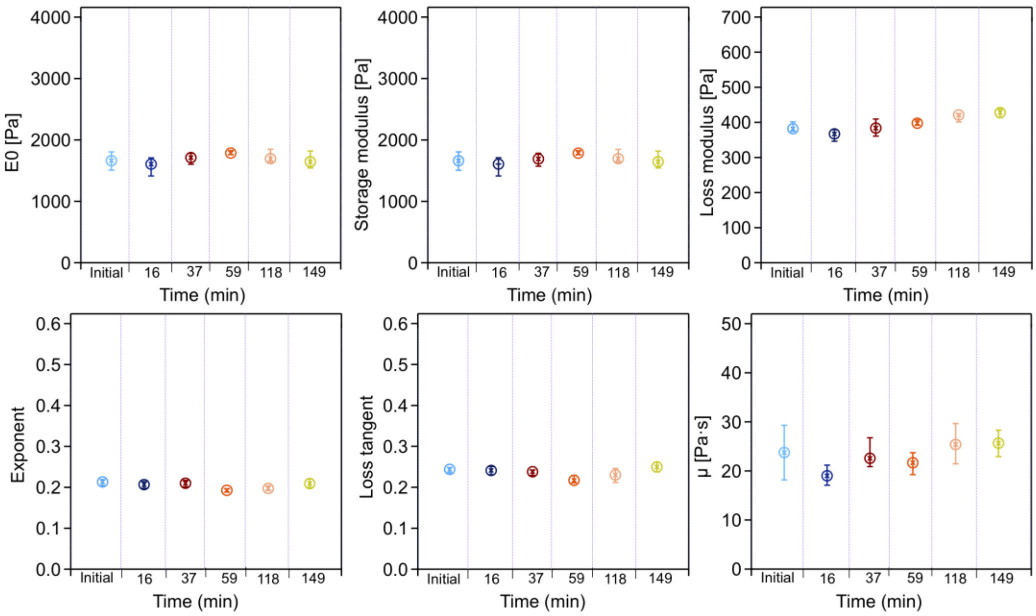

Figure S3.10 Median with 25/75 percentiles representation of rheological properties of a healthy fibroblast before and after 1 μM ML-7 addition. From left to right: scale factor for storage and loss moduli, storage modulus, loss modulus, power law exponent, loss tangent and Newtonian viscous term (*n* = 15).

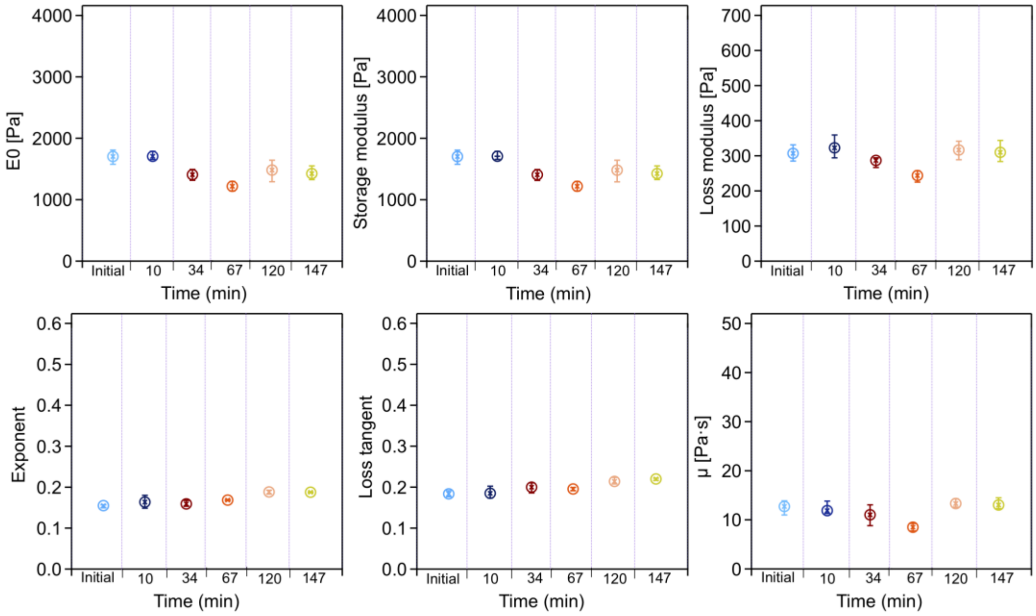

Figure S3.11 Median with 25/75 percentiles representation of rheological properties of a scar fibroblast before and after 1 μM ML-7 addition. From left to right: From left to right: scale factor for storage and loss moduli, storage modulus, loss modulus, power law exponent, loss tangent and Newtonian viscous term (*n* = 15).

.

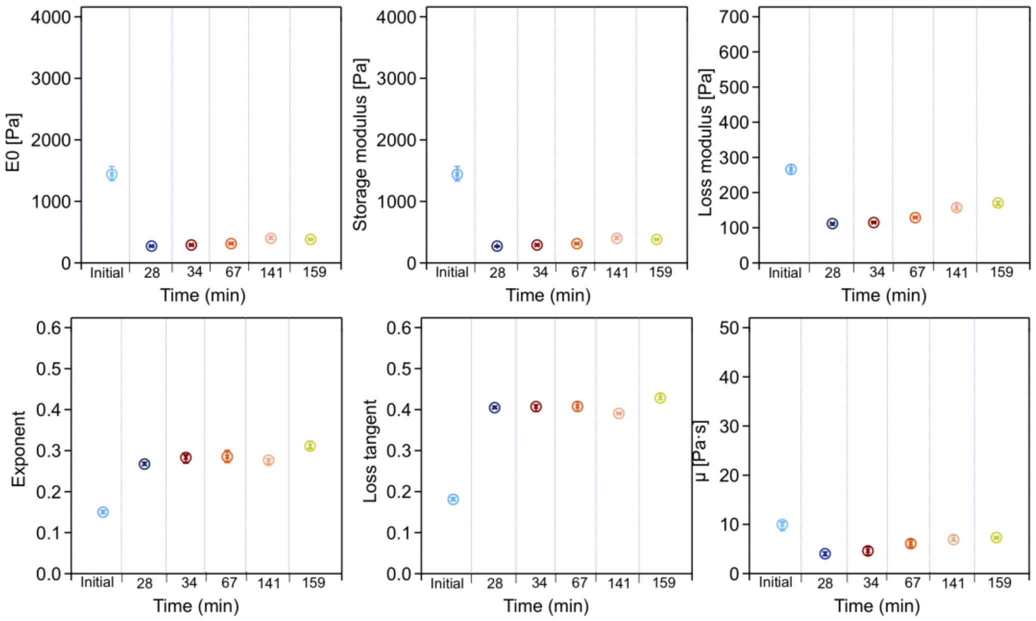

Figure S3.12 Median with 25/75 percentiles representation of rheological properties of a Dupuytren fibroblast before and after 1 μM ML-7 addition. From left to right: From left to right: scale factor for storage and loss moduli, storage modulus, loss modulus, power law exponent, loss tangent and Newtonian viscous term (*n* = 15).

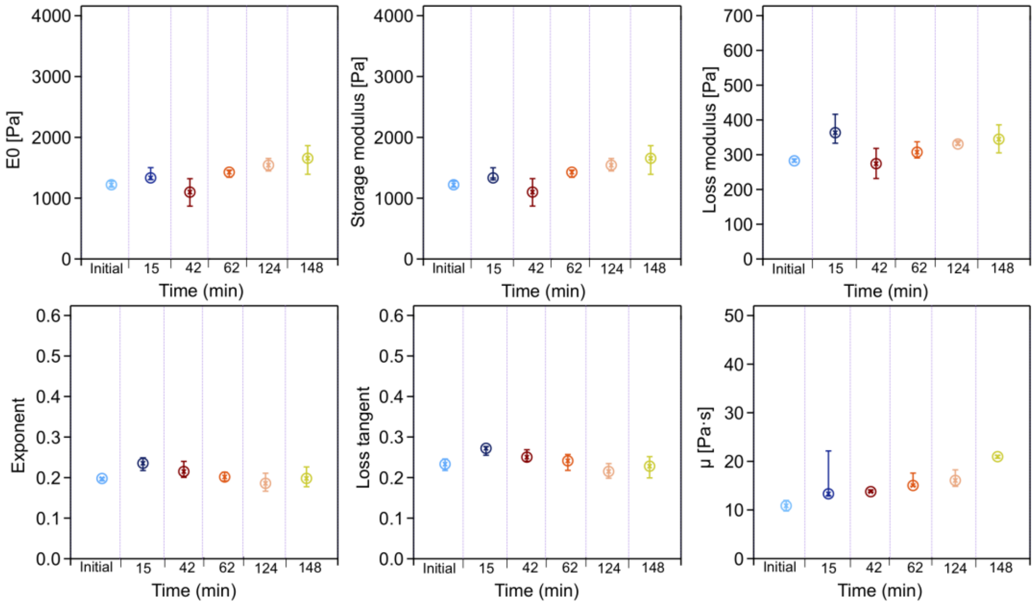

Figure S3.13 Median with 25/75 percentiles representation of rheological properties of a healthy fibroblast before and after 3 μM ML-7 addition. From left to right: From left to right: scale factor for storage and loss moduli, storage modulus, loss modulus, power law exponent, loss tangent and Newtonian viscous term (*n* = 20).

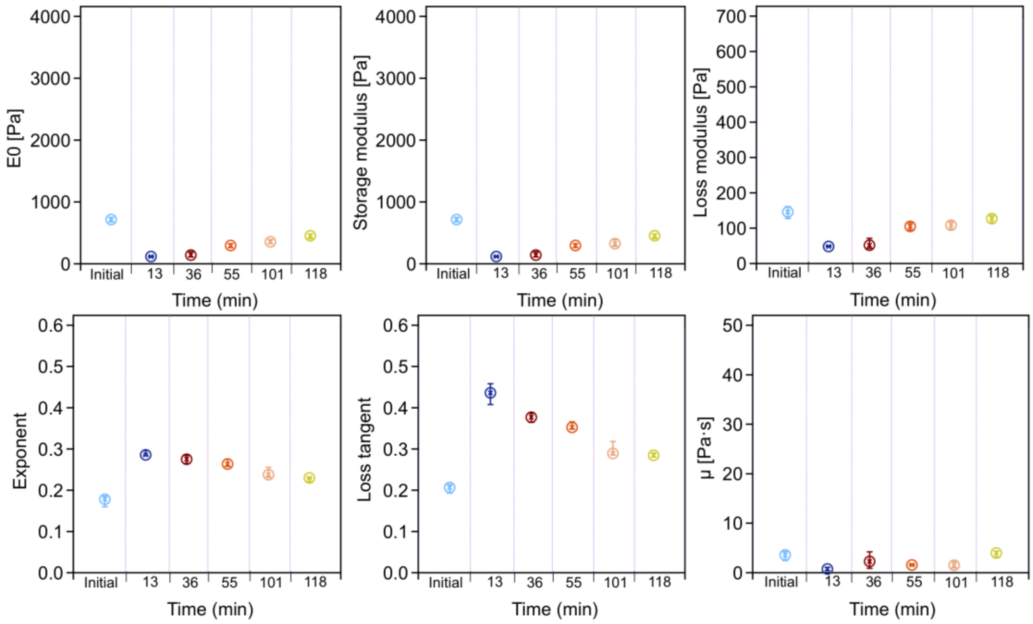

Figure S3.14 Median with 25/75 percentiles representation of rheological properties of a scar fibroblast before and after 3 μM ML-7 addition. From left to right: From left to right: scale factor for storage and loss moduli, storage modulus, loss modulus, power law exponent, loss tangent and Newtonian viscous term ($n = 20$).

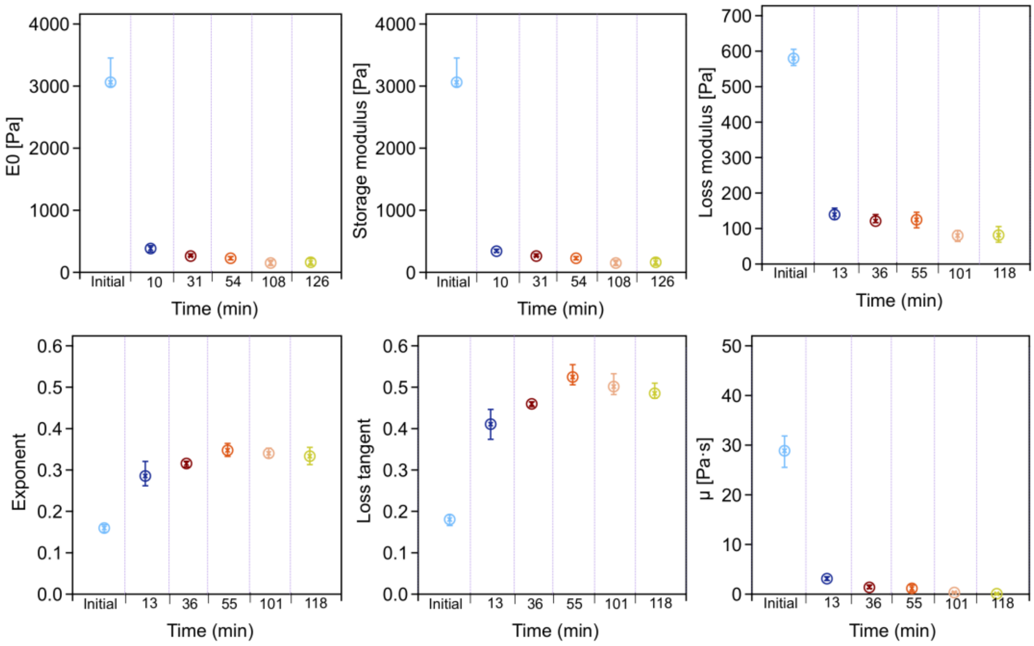

Figure S3.15 Median with 25/75 percentiles representation of rheological properties of Dupuytren fibroblast before and after 3 μM ML-7 addition. From left to right: From left to right: scale factor for storage and loss moduli, storage modulus, loss modulus, power law exponent, loss tangent and Newtonian viscous term ($n = 20$).

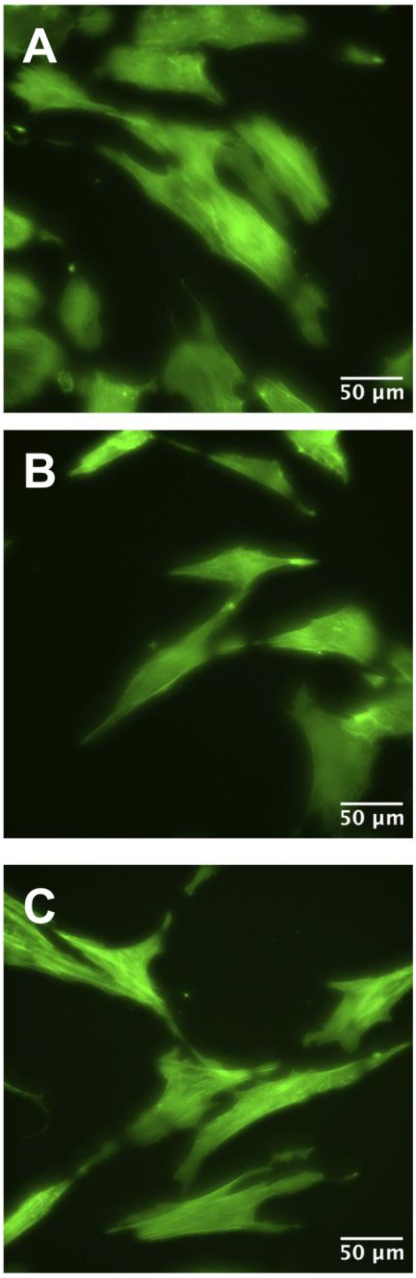

Figure S3.16 Actin fibers staining after DMSO addition, same concentration as ML-7 experiments. A) Healthy, B) Scar and C) Dupuytren fibroblasts. Experiments suggest that cell mechanics changes are due to ML-7 effect and not DMSO or time effect.

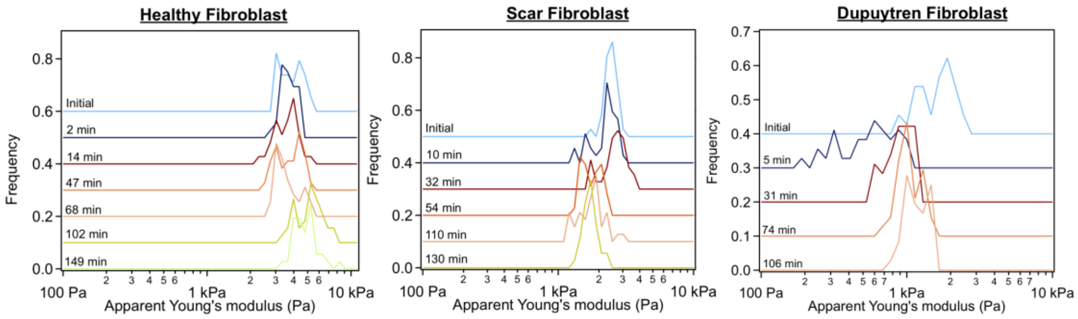

Figure S3.17 Histogram distribution of the Young's modulus of each type of fibroblasts with DMSO at the same concentration as ML-7 experiments. Cells were followed the same way as ML-7 experiments to verify if changes in cell stiffness were due to ML-7 or DMSO effect. Cells maintained their stiffness along the entire experiment; therefore, cell mechanical changes after ML-7 addition were due to the inhibition effect on the cell ($n = 5$).

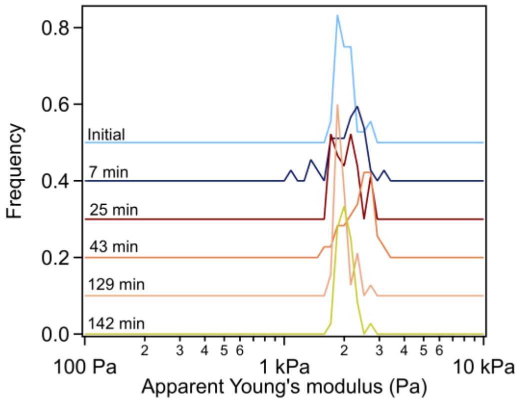

Figure S3.18 Histogram distribution of the Young's modulus of Dupuytren fibroblasts without ML-7 addition. Cells were followed the same way as ML-7 experiments to verify if changes in cell stiffness were due to ML-7 effect or just cell cytoskeletal changes over time. Cells maintained their stiffness along the entire experiment ($n = 5$).

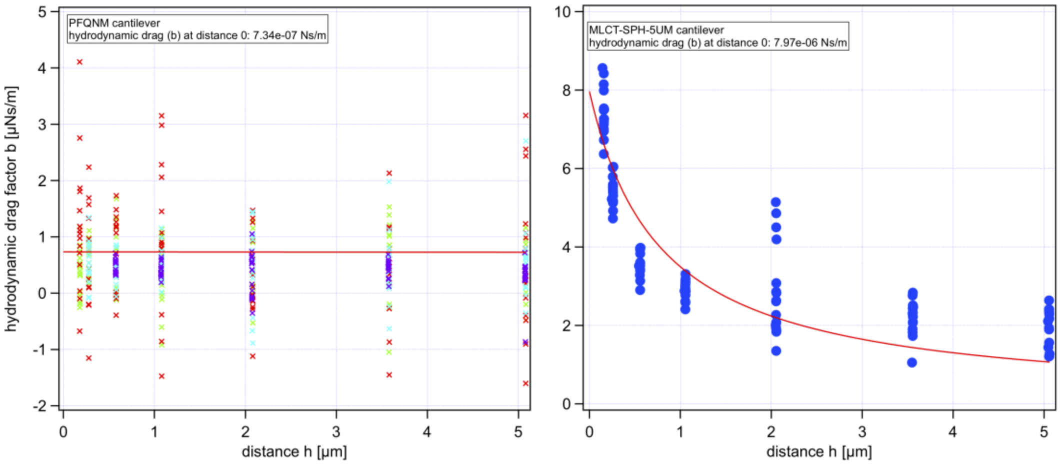

Figure S3.19 Drag factor at contact for PFQNM and MCLT-SPH-5UM cantilevers. PFQNM could be considered of having rectangular shape and MLCT-SPH-5UM V-shape. The b(0) was calculated measuring the drag factor at different distances from the sample as previously described (Alcaraz *et al.,* 2002). The color code represents different cantilever amplitudes used (50, 100, 200, 500 nm) and the cantilever was subjected to sinusoidal modulation sweeping the frequency from 1 Hz to 100 Hz.

Chapter 4

This is a verbatim copy of an article that has been published in a peer reviewed journal: Pérez-Domínguez S., Werkmeister E., Marini M. L., Dupres V., Janel S., Lafont F., Radmacher M. Rheological comparison between control and Dupuytren fibroblasts when plated in circular micropatterns using atomic force microscopy. *Frontiers in Physics,* 10:1052203 (**2022**) doi:10.3389/fphy.2022.1052203. 'Corrigendum: doi.org/10.3389/fphy.2023.1289123'.

Rheological comparison between control versus Dupuytren fibroblasts when plated in circular micropatterns using Atomic Force Microscopy

Sandra Pérez-Domínguez[1], Elisabeth Werkmeister[2], Maria Luisa Marini[2], Vincent Dupres[2], Sébastien Janel[2], Frank Lafont[2], Manfred Radmacher[1*].

[1]Institute for Biophysics, University of Bremen, Bremen, Germany.
[2]University of Lille, CNRS, INSERM, CHU Lille, Institute Pasteur Lille, U1019 - UMR 9017 - CIIL - Center for Infection and Immunity of Lille, Lille, France.

4.1 Abstract

In tissue, cells are obliged to confine and adapt to a specific geometric shape due to the surrounding environmental constraints. Under healthy conditions, fibroblasts present an elongated shape; however, changes in biochemical and physical properties of the extracellular matrix could distort the cell shape, inducing a pathological state. We have studied fibroblasts' mechanical behavior under circular geometrical constraints. Circular micropatterns force fibroblasts to acquire a different shape from that of a healthy tissue, inducing a possible pathological condition. In total, three different fibroblast types from Dupuytren's disorder, all obtained from the same patient, were confined in circular-shaped micropatterns of three different diameters

(25, 35, and 45 μm), and mechanical properties were evaluated using an atomic force microscope (AFM). We found that control fibroblast mechanics (apparent Young's modulus) increases with the increasing pattern diameter and comes together with a decrease in cell height and in loss tangent, translated into a more solid-like behavior. We hypothesize that these results resemble the transition toward the myofibroblast phenotype, ameliorating cytoskeleton formation and organization and enhancing cell contraction. Scar and Dupuytren fibroblasts did not display major changes in cell mechanics and cell height when changing the pattern diameter, suggesting that they are less affected by physical changes in the environment as they can adapt their shape to the geometrical dimensions. Therefore, our findings demonstrate that combining micropatterning and AFM measurements provides a powerful tool to study cell mechanics inducing constraints onto the cell, thus mimicking certain aspects of the tissue environment in both healthy and pathological states.

Keywords: AFM, Dupuytren's disease, micropatterning, viscoelasticity, fibroblast.

4.2 Introduction

Dupuytren's disease (DD) is a fibroproliferative disease that affects the palmar hand, causing progressive and permanent bending of the digits. The disease may cause hand contraction, hampering hand normal function and diminishing the patient's quality of life. The palm of patients who suffer from the disease shows high numbers of fibroblasts, increased deposition of collagen, and the presence of myofibroblasts (differentiated fibroblasts that present α- smooth muscle actin (SMA)), which are involved in wound healing. In wound healing, fibroblasts from the surrounding area migrate to the damage area and experience a transdifferentiation into myofibroblasts that increase mechanical stress on the extracellular matrix (ECM) and help in tissue remodeling. The differentiation into the myofibroblast phenotype depends on the activation of transforming growth factor β-1 (TGFβ-1) that lives in the ECM and stimulates α-SMA expression that leads to an increase in cell contraction. Myofibroblast contraction is transmitted to the ECM, also provoking changes in ECM stiffness due to fiber rearrangements and protein deposition, such as collagen. Non-invasive treatments, such as needle fasciotomy and collagenase injection, have been used to treat the disease; however, in the vast majority of the cases, it recurs. Open surgery for removing the affected area is normally used in later stages of the disease.

Cell mechanics is a useful approach to study cell viscoelastic behavior at a single-cell level and is mainly governed by a cytoskeletal network, especially by actin fibers that are also responsible for cell contractility. The cytoskeleton network is important to maintain cell shape and mechanics, playing a role in many cellular processes, such as migration and contraction (Deng *et al.*, 2006; Yamaguchi and Condeelis, 2007). The cell–cell interplay, cell–ECM as well as matrix stiffness, and composition have been shown to modify cell mechanics dictating cell cytoskeletal network organization, cell shape, and polarity (Fletcher and Mullins, 2010). Many techniques have been used to assess cell mechanical behavior, like optical and magnetic tweezers, micropipette aspiration, and atomic force microscopy (AFM), among others. Atomic force microscopy (AFM) is one of the most established and leading techniques to measure cell mechanics under physiological conditions. It allows applying a well-defined force and provides both topographical and mechanical characterization of living cells (Radmacher, 1997).

In the last decade, the interest in studying mechanical properties of cancer cells in comparison to healthy counterparts using AFM has grown due to its ability to discriminate one from the other (Lekka *et al.*, 1999). The majority of these studies were performed in hard cell culture dishes, whose stiffness is far from the natural tissue mechanics. Recently, soft artificial hydrogels, such as polyacrylamide (PA) and hydrogels employing abundant ECM proteins, like collagen, have been used to mimic cell's environment stiffness. For example, changes in thyroid cells when plated in PA gels of different stiffness have been reported (Rianna and Radmacher, 2017a). Lately, experiments trying to resemble cell's environment are gaining importance, either biochemically or biophysically. The biochemical and biophysical composition of this environment governs many cellular processes, such as cell differentiation, growth, division, and even cell death (Bohnet *et al.*, 2006; McKenzie *et al.*, 2018). In general, it is not easy to get access to tissue samples, especially from humans, which is the closest biological organization to cell's natural conditions; therefore, different strategies have been devised to resemble cell's natural environment. In tissue, cells are not isolated; instead, they are surrounded by a large number of neighboring cells and the extracellular matrix (ECM). This natural environment provides cells with geometrical constraints that not only influence cell morphology and mechanics but also polarity and function. In research, photolithography techniques generating reusable masks with specific geometries, as well as protein micropatterning, are considered a good compromise to resemble cell constraints in tissue. AFM experiments using cell culture dishes lead to continuous cell structural and morphological rearrangement; however, the use of micropatterns of different geometries and dimensions is an interesting approach to limit cell spreading in a defined space (Rigato *et al.*, 2015). Regular pattern shapes mimicking tissue constraints drive cells to adapt their morphology and cytoskeletal architecture. One of the main advantages of systematizing a regular shape is the reduction in heterogeneity and variation due to constant and reproducible cell features. Many studies used PDMS-based lithography to confine cells in limited spaces, creating different geometries in which cells could adapt (Mi *et al.*, 2006; Rianna, Radmacher and Kumar, 2020). The ECM environment has a strong influence on actin cytoskeleton localization inside the cells that contributes to cell polarity establishment; hence, it was shown that convex micropattern features promoted the assembly of lamellipodia and concave features promoted the assembly of stress filaments (Théry *et al.*, 2006; James *et al.*, 2008). Cell's spreading direction - lamellipodia protrusions- differs depending on micropattern geometry (Parker *et al.*, 2002; Brock *et al.*, 2003). Patterned cells in square or triangular shapes preferentially extended the lamellipodia at the corner; however, cells adherent to circular shapes formed lamellipodia at all regions of the perimeter. Several studies evaluated the directionality and speed of cell migration using switchable surfaces, whose adhesiveness can be turned on and off when desired (Liu *et al.*, 2005; Nakanishi *et al.*, 2008). In addition, micropatterning can be used to study cell's focal adhesion points using different geometries that provide similar cell morphology but different cytoskeleton distributions (Rigato *et al.*, 2015). Therefore, the use of micropatterns could help resemble cell's constraints under healthy tissue conditions, but it could also serve to study cell adaptability to new environments, forcing them to acquire a different geometrical constraint to healthy conditions.

In this study, we prepared circular micropatterns on glass coverslips using UV photolithography with a chrome photomask. The micropatterned surfaces were used to culture three different fibroblasts from Dupuytren's disorder (control and pathological fibroblasts) on circular areas of different diameters (25, 35, and 45 μm in diameter), and cell mechanics was assessed employing AFM. Under healthy tissue conditions, fibroblasts possess an elongated shape; however, in the pathological state, physical and biochemical changes in the environment can modify fibroblast morphology; therefore, we employed circular-shaped patterns to force cells to develop in a non-natural state. Circular-shaped fibronectin micropatterns could enable us to induce or simulate a disorder typical of a pathological state and therefore compare the behavior of fibroblasts presenting different pathological states. Moreover, using the AFM sweep modulation scheme and analyzing the data using the structural damping model, we could extract viscous and elastic properties of the cells.

4.3 Results

4.3.1 Adhesive protein selection

Two different ECM proteins were tested in order to optimize the highest efficiency in cell patterning. We compared fibronectin versus collagen I as adhesive proteins, both present in fibroblast’s natural environment. The fibronectin-coated micropatterns provided much higher cell patterning and attachment success than collagen (Fig. 4.1). The number of patterned cells in circular patterns with respect to the number of attached cells is similar in both cases, reaching around 50–60%. The rate of success, referring to the number of patterned cells with respect to the number of circular patterns, in the case of collagen micropatterns was around 20%; however, the fibronectin covering reached around 50% cell patterning.

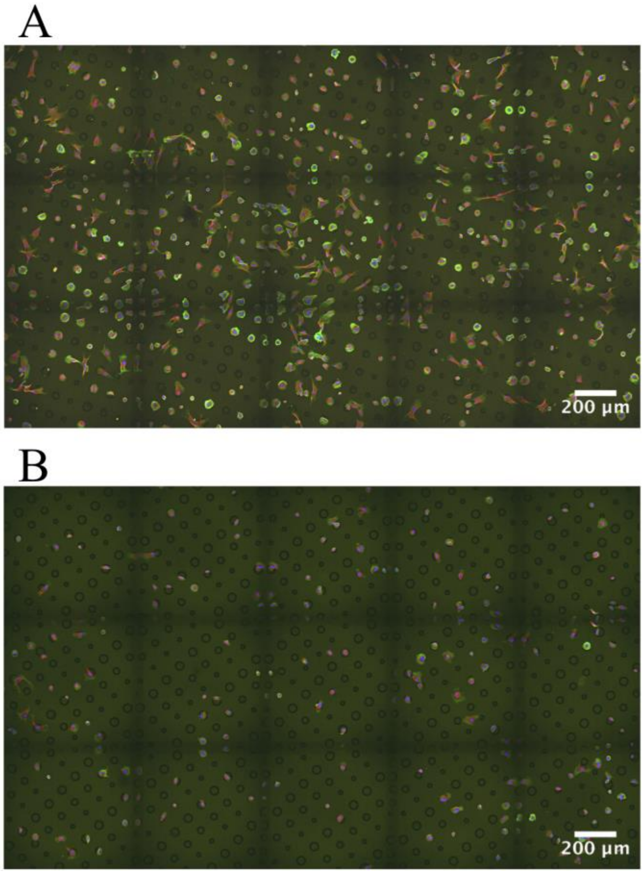

Figure 4.1 Dupuytren fibroblasts plated on the three circular micropatterns of different diameters. Adhesive proteins (A) fibronectin and (B) collagen I. Fibroblast labeling: actin in green, vimentin in red, and nuclei in blue. Supplementary Figures S4.9, S4.10: control and scar fibroblasts plated on the three circular micropatterns of different diameters (fibronectin coating).

4.3.2 Cell confinement

We plated all fibroblast types in circular micropatterns, and figure 4.2 shows an example of each fibroblast under all conditions. We could observe how actin filament distribution was significantly influenced by the pattern diameter. Thanks to the z-stack images taken along the entire cell height, from the bottom to the top layer, we could generate 3D view representation of the cells under all conditions (Supplementary Videos, Supplementary Material). This 3D view allowed us to assess if there was any correlation between cell height, pattern diameter, and fibroblast type (Table 4.1). Three-dimensional videos showed cells in which actin, vimentin, and nucleus were stained, giving interesting information about cell cytoskeleton organization. As actin fibers are one of the main cytoskeleton components that dictate the cell mechanical behavior, z- and orthogonal projections of scar fibroblasts - showing just actin fibers- patterned in the three circular-shaped patterns were generated (Figure 4.3).

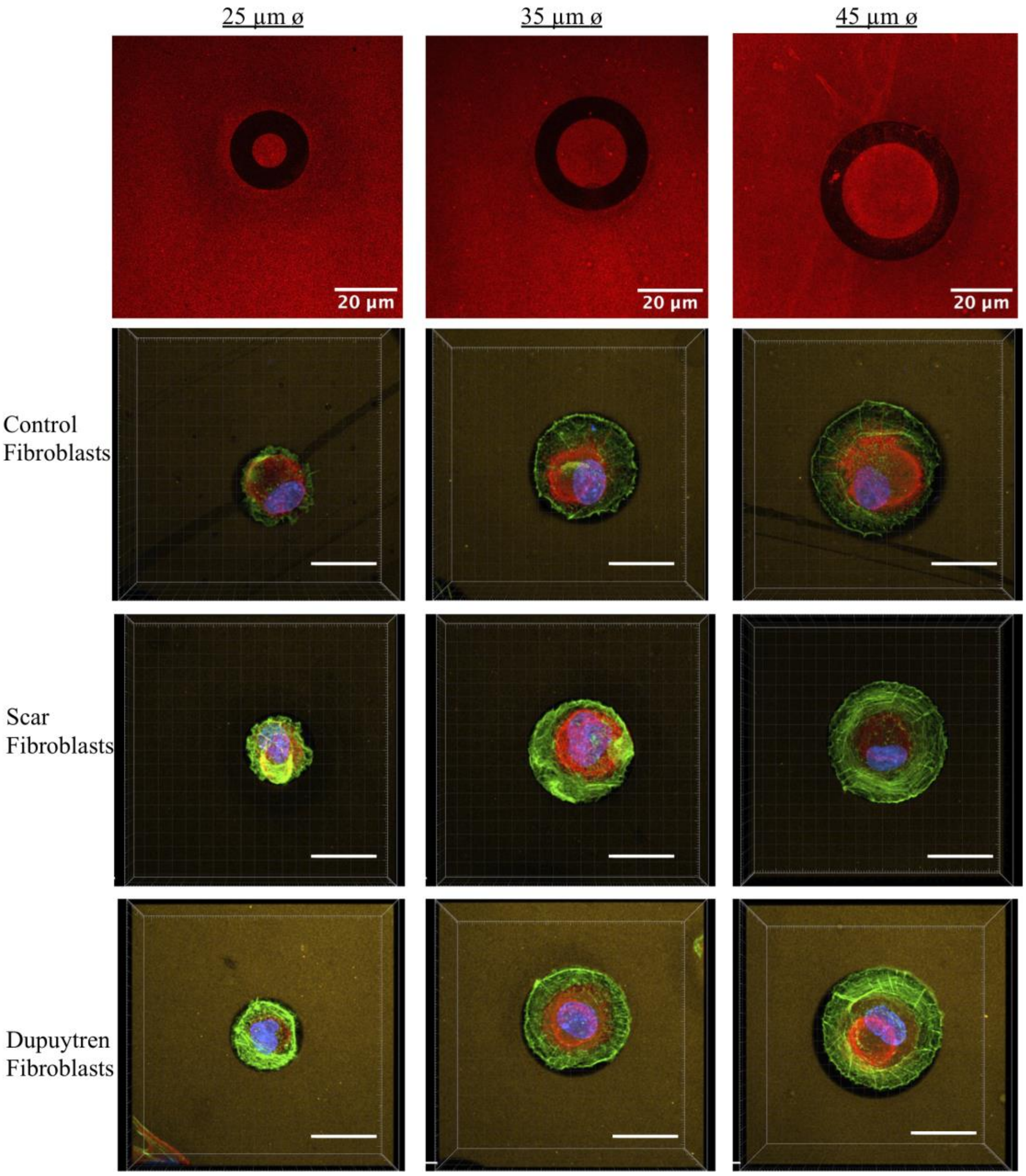

Figure 4.2 Examples of individual fibroblasts plated on 25-, 35-, and 45-µm-diameter circular micropatterns (left to right). The first row represents fibronectin circular-shaped micropatterns in black. The following rows represent fluorescence microscopy images of each type of fibroblasts in which the actin fibers are labeled in green, vimentin in red, and nuclei in blue. Three-dimensional view videos are available in the Supplementary Material.

The z-projection accumulates all images taken alongside the cell body, from the bottom to the upper layer, and it shows how actin fibers organize within the cell when patterned on the circles of different diameters. In particular, in Figures 4.3B,C, the actin fibers follow the circular pattern that corresponds to the lamellipodia (concentric fibers) and in the cell body, which is sitting in the non-adherent area, filaments are less concentrated and organized. In the case of control fibroblasts, there is a decrease in cell height when the pattern diameter increases; however, scar and Dupuytren's fibroblasts did not present the same behavior, showing a more constant cell height regardless of the pattern dimension (Figure 4.4 and Table 4.1).

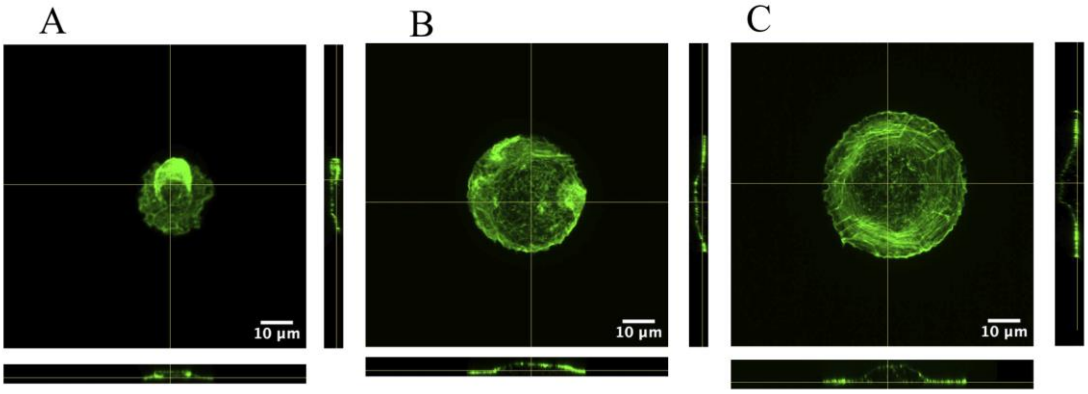

Figure 4.3 Z and orthogonal projections of scar fibroblasts patterned in (A) 25-µm circle, (B) 35-µm circle, and (C) 45-µm circle. Actin fibers labeled in green. (Supplementary Figures S4.11, S4.12: control and Dupuytren fibroblasts projections).

Moreover, from the xz projections, we estimated a relative volume of the cells; in all cases, fibroblasts increase their volume with the increasing pattern diameter (Supplementary Figure S4.13). Control fibroblasts appear to present less actin filaments than the pathological counterparts (Figure 4.2).

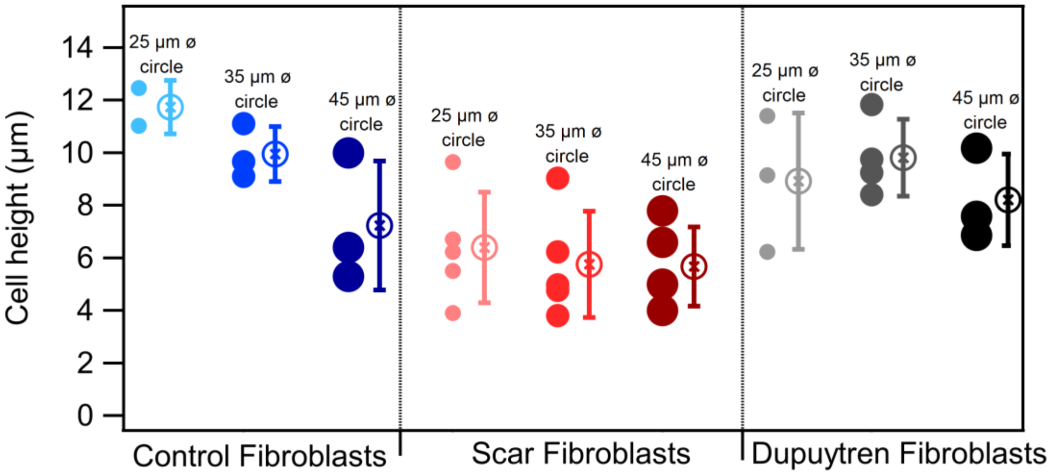

Figure 4.4 Mean and standard deviation representation of the cell height obtained from the xz projections (N = 4). The circles next to each mean value correspond to the individual measurements.

Table 4.1 Cell height when patterned in the different circular-shaped diameters. *Three to five cells for each condition from confocal images were analyzed to obtain cell height.

Height*	25 µm diameter	35 µm diameter	45 µm diameter
Control Fibroblasts	11 µm	9 µm	6 µm
Scar Fibroblasts	6 µm	5 µm	5 µm
Dupuytren Fibroblasts	9 µm	10 µm	8 µm

A similar cell behavior was shown in flat rigid cell culture dishes. Control fibroblasts presented less and randomly distributed actin fibers in contrast to scar and Dupuytren fibroblasts, which displayed aligned and thick actin fibers (Viji Babu *et al.*, 2018b; Sayadi *et al.*, 2019) (Figure 4.5).

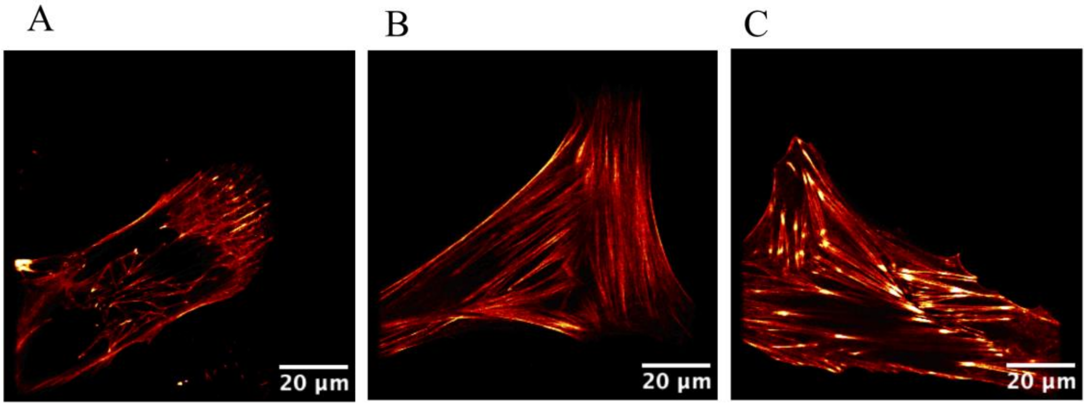

Figure 4.5 STED images of live single cells plated on cell culture dishes. (A) Control fibroblasts, (B) Scar fibroblasts, (C) Dupuytren fibroblasts. Actin fibers were labeled in red. Scale bar: 20 µm.

4.3.3 AFM measurements

Mechanical and rheological properties of patterned cells were evaluated using AFM. The number of cells scanned in each circular-shaped pattern was arbitrary, since the pattern size at which the cells were adhered was analyzed after AFM measurements. Measurements were performed on the nuclear region to avoid artifacts of feeling the underlying support; but in some cases, the elasticity of the whole cell could be scanned (Figure 4.6A). We found that the softest area of the cell correlates with the tallest part that corresponds to the cell body (Figure 4.6B).

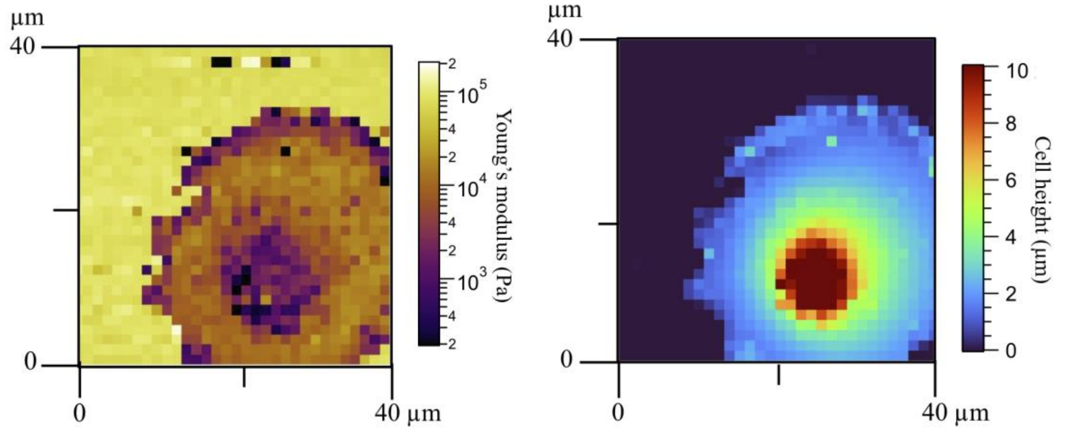

Figure 4.6 (A) Apparent Young's modulus of a Dupuytren fibroblast patterned in a 35-µm-diameter circle and (B) cell height.

The cell lamellipodia is thinner and stiffer due to the bottom effect and accumulation of actin filaments, as shown in the fluorescent images (Figure 4.2). Our AFM results corroborate the different behaviors of the three fibroblast types. The apparent Young's modulus was extracted from the approach part of the force curves using the Hertzian model for parabolic tips. The apparent Young's modulus of control fibroblasts increases with increasing pattern diameter (1.02, 1.39, and 2.12 kPa for 25-, 35-, and 45-µm-diameter circular constraints, respectively); however, this behavior is not followed by the other two cell types (Figure 4.7).

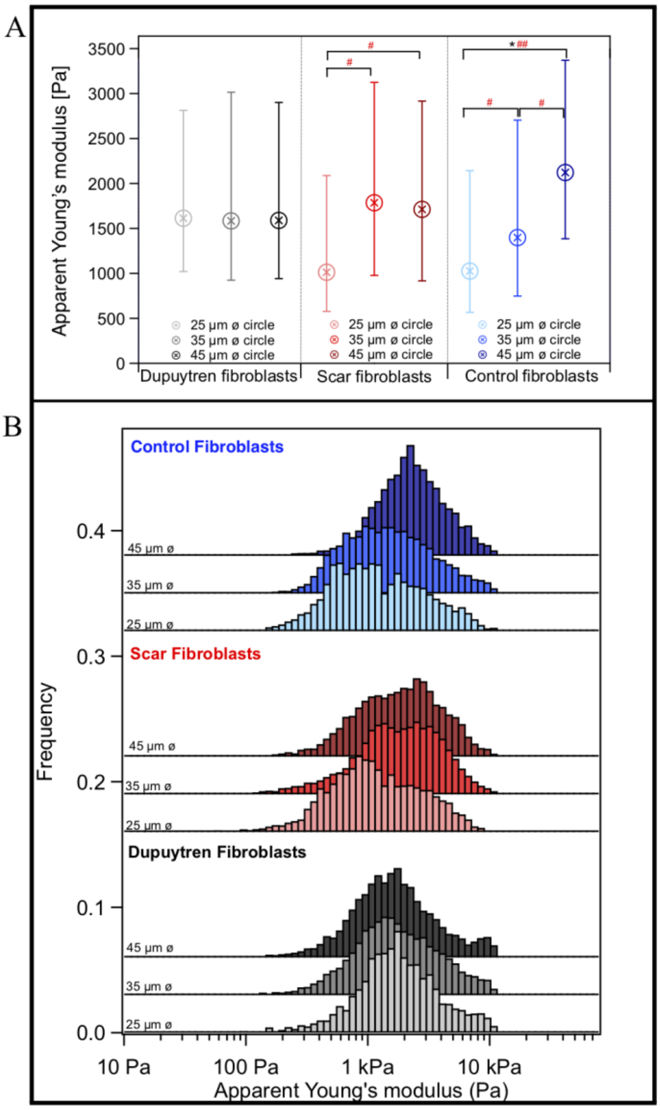

Figure 4.7 (A) Box plot of the apparent Young's modulus with the median and the 25/75 percentiles and (B) histogram distribution. Data shows information about different cells. Each color represents one type of fibroblast, Dupuytren, scar, and control were labeled in black, red, and blue, respectively. In addition, within each group, the color gradient shows the cells patterned in each circular size, from the lightest to the darkest, goes from 25 to 45 µm ø circular sizes, respectively. Statistical analysis: Wilcoxon signed-rank test significant difference: * indicating $p < 0.01$ and Cohen's d test with # indicating an effect size of $0.2 < d < 0.5$ and ## indicating $d > 0.5$. ø= diameter (N = 15).

Interestingly, Dupuytren fibroblasts maintain their mechanical properties regardless of the circle diameter (1.61, 1.58, and 1.59 kPa for 25-, 35-, and 45-µm-diameter circle constraints, respectively). In addition, scar fibroblasts appear to mix both behaviors, similar to control fibroblasts at a lower pattern diameter and closer to the pathological fibroblasts when the constraint diameter increases (1.02, 1.78, and 1.71

kPa for 25-, 35-, and 45-µm-diameter circle constraints, respectively). The Wilcoxon signed-rank test and Cohen's d statistical analysis were used to evaluate statistical significance of apparent Young's modulus between different cell types and pattern dimensions. Highly significant differences were found within control fibroblasts patterned on 25-µm and 45-µm-diameter circles. Cohen's d-test suggested a medium size effect between control fibroblasts patterned on 25 and 35 µm circles; and also, between 35- and 45-µm-diameter circles. Moreover, a medium size effect was seen between scar fibroblasts patterned on 25-µm circles and the two larger patterns (scar fibroblasts on 35- and 45-µm- diameter circles). A large effect of the pattern size was also seen in control fibroblasts patterned between 25- and 45-µm- diameter circles (Figure 4.7). As it has been mentioned in previous studies (Rianna and Radmacher, 2017a), Young's modulus is a parameter that describes the elastic response of an object when deformed by an external force. However, cells are complex and heterogeneous materials that present elastic and viscous responses. According to that, apparent Young's modulus parameter (which is the Young's modulus determined from the approach curve) gathers both elastic and viscous contributions and it is not able to distinguish between them. To overcome this issue, there are few AFM strategies that allow describing cells' mechanical properties separating both elastic and viscous contributions. In this work, we employed the so-called sweep frequency, already described in previous studies (Hiratsuka *et al.*, 2009; Rother *et al.*, 2014). Briefly, after approaching the tip to the sample as in a regular force curve, a sinusoidal modulation with increasing frequency (1 Hz–1 kHz) is applied, while the tip is still in contact with the cell. When this step is finished, the tip is fully retracted out of contact (Supplementary Figures S4.2, S4.3). The cantilever is oscillated applying a low amplitude of 50 nm. To analyze the data, the power law structural damping model is used, and viscous drag of the cantilever has been corrected (Supplementary Figure S4.5). This model provides information about the elasticity and viscosity of the cells separately. Frequency dependence of the storage and loss modulus measured on the different fibroblasts in all circular patterns can be seen in Supplementary Figure S4.4. Both moduli displayed a similar trend up to 10 Hz; however, the loss modulus showed increased frequency dependence at higher frequencies. We observed that control fibroblasts displayed a decrease in the loss tangent at 1 Hz with increasing pattern diameter, whereas Dupuytren and scar fibroblasts did not show major changes (Dupuytren: 0.24 in all cases; scar: 0.36, 0.27, and 0.32 from 25- to 45-µm-diameter circles) (Figure 4.8). Statistical analysis suggests a significant difference between control fibroblasts patterned on 25- and 45-µm-diameter circles and a medium size effect between Dupuytren fibroblasts patterned on 25 µm and the other two bigger circular patterns, as well as a medium size effect between control fibroblasts on 25 µm versus 35 µm and 35- versus 45-µm-diameter circles. Finally, a large size effect is observed between control fibroblasts patterned on 25- and 45-µm-diameter circle. Therefore, in the case of control fibroblasts, we saw that an increase in the Young's modulus with increasing the pattern diameter comes together with a decrease in loss tangent, which can be related with an increase in the elastic over the viscous properties, corresponding to a more solid-like behavior. The power law exponent is associated with cell's dynamic structural elements at the mesoscale and present similar values for all cases, presenting values around 0.15 and 0.2 for Dupuytren and scar fibroblasts, respectively, except for control fibroblasts, which decreases with increasing pattern diameter (going from 0.23 to 0.13, from 25 to 45 µm diameter) (Figure 4.8).

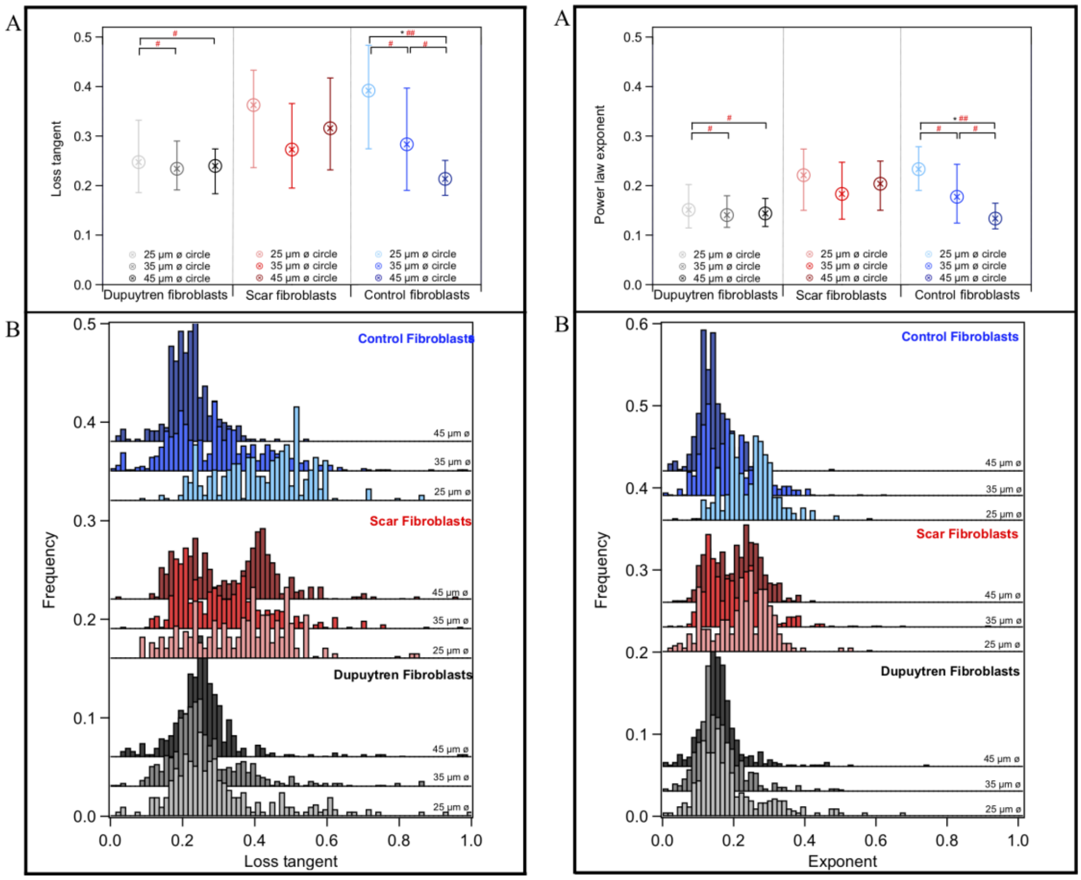

Figure 4.8 (A) Box blot with the median and the 25/75 percentiles and (B) histogram distribution of the loss tangent at 1 Hz and power law exponent for each fibroblast, left and right graphs, respectively. Data shows information about different cells. Each color represents one type of fibroblast, Dupuytren, scar, and control in black, red, and blue, respectively. In addition, within each group, the color gradient shows the cells patterned in each circular size, from the lightest to the darkest, goes from the 25 to the 45 µm ø circular sizes, respectively (E_0, μ, and storage and loss moduli graphs are given in Supplementary Figures S4.6–S4.8) (N = 15).

Statistical analysis for power-law exponent results displays same significant differences and size effect as the loss tangent. E_0, which is the scale factor of storage and loss modulus, varies depending on the cell type and pattern diameter. Dupuytren and scar fibroblasts seem to be independent on the pattern diameter (Dupuytren: 1,500 to 1,400 Pa, from 25 µm to 45 µm diameter; and scar: 900–1,000 Pa, from 25 µm to 45 µm diameter). Nevertheless, control fibroblasts show an increase going from 500 to 2,300 Pa (Supplementary Figure S4.6). The statistical analysis showed significant differences between control fibroblasts patterned on 25- and 45-µm- diameter circles; Cohen's d size effect displayed a medium size effect between control fibroblasts on 25 µm and the bigger circles; also, all patterned scar fibroblasts within each other and Dupuytren fibroblasts patterned on the 45-µm-diameter circle and the two smaller circles. The Newtonian viscous term (μ) is rather small and constant for Dupuytren and scar fibroblasts regardless of the pattern diameter (10 Pa·s), and it increases for control fibroblasts with increasing pattern diameter (6–10 Pa·s) (Supplementary Figure S4.7).

4.4 Discussion

In this study, we plated fibroblasts in circular-shaped patterns of different diameters. Fibronectin and collagen I used for surface coating differently affect the efficiency of cell patterning. Both proteins are commonly used to ameliorate cell adhesion in cell culture dishes, and they are both abundant in the fibroblast environment; however, the suitability of one over the other may vary on the cell type (Lacouture, Schaffer and Klickstein, 2002; Colombo *et al.*, 2013). Fibroblasts are a cell type that synthesizes ECM and collagen; therefore, it would have been expected to have a better affinity to collagen coating. In addition, collagen deposition by fibroblasts takes place with the help of fibronectin. Fibronectin was also observed to be associated with the deposition of new collagen fibrils. Therefore, it appears that fibronectin promotes cell attachment to collagen filaments, supporting the idea that fibroblasts have a higher affinity for fibronectin than for collagen coatings. Accordingly, if we compare the pattern efficiency between both proteins, fibroblasts presented better predilection to adhere to fibronectin than collagen. Another possible explanation could be that animal origin of the proteins may also influence cell attachment. We used bovine fibronectin and rat collagen I; therefore, the animal origin of the proteins may decant and influence the adherence of the fibroblasts, in our case preferring bovine fibronectin to collagen. Mechanical and rheological properties of cells under the different conditions were correlated with fluorescent images, in which actin fibers, vimentin, and nucleus were stained. Control fibroblasts displayed an increase in elasticity with increasing circle diameter. This behavior was linked to an increase in actin filament formation and a change in organization, since they presented better-developed actin filaments at the maximum circle diameter (45 µm) (Figure 4.2). It is visible how actin filaments accumulate in the outer circle that is the fibronectin-coated area, which seems to stimulate actin fiber formation. Interestingly, control fibroblasts showed a branching actin meshwork, randomly distributed alongside the cell body without any orientation at the smallest circular-shaped pattern. Nevertheless, actin filaments in both radial and concentric directions started to appear at the intermediate and larger patterns (35 and 45 µm in diameter). These filaments mimic the circumference of the pattern, and radial filaments connect the cell periphery with the cell body cytoskeleton. Song *et al.* reported similar results in mesenchymal stem cells (MSCs), suggesting that cell spreading is a significant parameter in cytoskeleton development and therefore in a cell mechanical state (Song, Kawazoe and Chen, 2011; Wang *et al.*, 2016). Variations in mechanical properties and cytoskeleton organization and distribution were followed with changes in cell height. We observed a decrease in cell height with increasing pattern diameter. In flat cell culture dishes, control fibroblasts were seen to be smaller in spreading than pathological fibroblasts; therefore, the decrease in height with the increase in the circle diameter may suggest an attempt to cover the entire area but sacrificing cell thickness. This behavior of control fibroblasts might simulate a transition toward a myofibroblast phenotype, similar to the wound closure process. Cell spreading increases cytoskeletal contractility that may activate fibroblast to myofibroblast differentiation due to the changes in force/tension in the cell interior. Additionally, the crowding of thicker actin filaments at the edge is a phenomenon that occurs when cells are maximizing their spreading. Myofibroblasts are differentiated fibroblasts that help in wound closure. When a wound appears, fibroblasts from the vicinity move to the affected area and acquire bundles of microfilaments formed by β- and γ-cytoplasmic actin; these cells are named proto-myofibroblasts. The latter evolve into α-smooth muscle actin (SMA)-positive fibroblasts called differentiated myofibroblasts that are responsible for wound contraction. The activation of the myofibroblast phenotype is diverse, but one of the most common mechanisms is through the activation of latent transforming growth factor (TGF) β-1. The force exerted by this extra actin fibers can be transmitted to the ECM via integrins that activates TGFβ-1 leading to an ECM straining that produces a feedback mechanism, preserving cell–ECM contraction (Hinz, 2010; Bochaton-Piallat, Gabbiani and Hinz, 2016). We suggest that a similar mechanism may be occurring to control fibroblasts when decreasing cell constraint. Fibroblasts try to adapt their shape to the geometric size, developing extra cytoskeletal fibers to reach the new spreading area, leading to an increasing cell contraction. Control fibroblasts may feel a similar situation to that in wound closure. There is a gap that they need to fill and close -increased circle dimensions- thus they might need to ameliorate their cytoskeleton, increasing cell contraction. Hence, not only biochemical changes regulate cell fate, but also physical changes modulate cell behavior. Similar results were found in MSC patterned on different circular-shaped patterns. An increase in the spreading area -circle diameter- favored osteogenic differentiation due to an increase in cytoskeletal contractility (Song, Kawazoe and Chen, 2011). Scar and Dupuytren cells did not experience the same behavior as control fibroblasts when increasing the pattern diameter. Dupuytren fibroblasts did not change either their stiffness or height, which may denote that they are less affected by physical changes in the surrounding environment than control counterparts. They expressed a bunch of thick actin fibers regardless of the circular-shaped constraints, showing an accumulation of actin filaments at the lowest spreading area that they dispersed, reorganized, and even developed at a higher circle diameter. Scar fibroblasts presented an intermediate behavior between the other two cell types. Low accumulation and organization of actin filaments can be seen in the cell body when plated in the smallest circular pattern (25 μm in diameter), which is close in relation to control fibroblast behavior. These observations bring together values of apparent Young's modulus similar to control fibroblasts seeded in 25-μm circles. Scar fibroblasts are an interesting cell type having intermediate characteristics between control and pathological fibroblasts and can be a key point to understand fibroblast-to-myofibroblast transition and Dupuytren's disorder. However, as the pattern diameter increases, scar fibroblast behavior leans toward more pathological phenotype, displaying constant mechanical properties at the intermediate and big circle pattern. A huge bunch of actin filaments fills cell body, accumulating more fibers in the lamellipodia and increasing cytoskeleton fiber organization as the spreading area increases. We have seen that control fibroblasts reduce their height with increasing pattern diameter; however, scar and Dupuytren fibroblasts conserve their height regardless of the circle diameter. From the xz projection images, we estimated a relative number for cell volume, leading to an increase in cell volume with increasing circle diameter regardless of the cell type (Supplementary Figure S4.13). The volume increase in scar and Dupuytren fibroblasts could be understood as maintaining the height with increasing spreading area, and this could lead to an increase in cell volume. Nevertheless, control fibroblasts also experienced an increase in volume. We attribute these findings to a more homogeneous cell covering of the pattern, also reaching constant height overall pattern (Supplementary Figure S4.14). An increase in cell volume with an increase in the spreading area may be linked to migration and invasion processes. Similar results were found in single monitored glioma cells, in which changes in cell volume were connected to invasiveness and migration properties (Watkins and Sontheimer, 2011). Rheological properties of the cells were extracted from the sweep frequency data, and the power law structural damping model was used to analyze it. We measured the complex elastic modulus using AFM over three frequency decades (1 Hz–1 kHz); however, the data were analyzed until 130 Hz due to piezo limitation ofour instrument. The cell culture medium exhibits a pure viscous behavior; therefore, the hydrodynamic viscous drag force on the cantilever overestimates the loss modulus. For that reason, viscous drag was corrected calculating the b factor at a distance zero (b (0)) from the sample. The estimation of b (0) was performed following the Alcaraz *et al.* 2002 procedure (Alcaraz *et al.*, 2002). The cantilever was oscillated at low amplitude (50 nm) at different frequencies (1 Hz–1 kHz) and at different tip-sample distances (0–5 µm). Frequency dependence of storage and loss moduli showed an increase in the storage modulus over frequency in all cases (Supplementary Figure S4.4); the loss modulus also increased over frequency, even after viscous drag correction; nonetheless, it increases with a more marked frequency dependence at higher frequencies. This loss modulus increase over frequency may be linked with micro- and macromolecule friction differences with cell's cytosol. The exponent and loss tangent are related parameters; therefore, similar values and distribution are expected. The decrease in the exponent and loss tangent with increasing pattern diameter in control fibroblasts is understood in terms of cytoskeleton development, which provides the cell with more elastic components (actin filaments), which is known as an increase in the solid-like behavior. Experiments exposing cells upon cytoskeleton disruption, like lantrunculin-A and blebbistatin, showed an increase in the exponent and loss tangent, together with a decrease in the storage modulus and increase in the loss modulus, corroborating the cytoskeleton contribution to cell elasticity (Rigato *et al.*, 2017). The exponent values of Dupuytren and scar fibroblasts (0.15 and 0.2, respectively) are in agreement with previous studies on human alveolar and bronchial epithelial cells, as well as 3T3 fibroblasts (Alcaraz *et al.*, 2003; Rigato *et al.*, 2017). Similar experiments using oscillatory modulation schemes have reported the appearance of two power law exponents instead of one. Those experiments used a higher frequency range than that in our experimental setup, ranging from 1 Hz to 100 kHz. Thanks to this frequency widening, data suggested the existence of two regimes: one at low frequencies with a weak power law and the second at high frequencies with stronger power laws. This methodology may provide extra information about cell's dynamics and single filament dynamics; however, we were limited by our piezo response and cantilever resonance frequency, reaching frequencies up to 100 Hz. In addition, there are many others models, instead of the structural damping model, to analyze viscoelastic behavior of samples. Those models consist of a combination of springs and dashpots in such a way to describe real viscoelastic behavior. A viscoelastic liquid can be represented by Maxwell model, which consists of a spring and dashpot connected in series. This model predicts that storage and loss moduli vary with frequency and at higher frequencies the storage modulus is larger than the loss modulus; therefore, solid- like behavior predominates, while at lower frequencies the situation is opposite. This model does not fit our data; therefore, it is not a suitable model to describe our samples. The Kelvin–Voigt model, suggested for viscoelastic solids, is a combination of a spring and dashpot but connected in parallel. In this case, the storage modulus is frequency-independent and constant, and the loss modulus increases linearly with frequency. None of these statements are followed in our samples, in which both storage and loss moduli are frequency-dependent and the loss modulus does not increase linearly with frequency. Single power law fit to storage and loss moduli was used to validate structural damping model employment (Supplementary Figure S4.15). We obtained one different exponent for each modulus (storage exponent: 0.115 and loss exponent: 0.224); nevertheless, it is clearly visible that the loss modulus does not follow a single power law; in any case, multiple power law fits may better describe loss modulus behavior over frequency. However, we have seen that the structural damping model fits our data appropriately and suggests a storage modulus that increases for all frequencies according to a power law exponent and a loss modulus that includes a component of the storage modulus (loss tangent) and scale with the same power law (Fabry *et al.*, 2001, 2003). Another interesting model used to describe viscoelastic behavior is the Burgers model, which is basically a Maxwell and Kelvin–Voigt model connected in series. This model provides a viscoelastic spectrum for an entangled polymer system over a wide frequency range, but in some cases, it is not possible to observe a part of the spectrum depending on the instrumentation limitations. In our case, again AFM piezo and cantilever response limit the employment of this model (Malvern Instruments, 2016; Pajic-Lijakovic and Milivojevic, 2019, 2022).

Previous studies, in which circular-shaped patterns were utilized, all circle interior was covered with some adherent protein favoring cell attachment (Song *et al.*, 2011). In our work, we discussed circular patterns; however, a better description would be a ring-shaped pattern because only a ring profile is filled with fibronectin and the center of the circle is coated with the antifouling PLL-PEG. Thanks to this shape, we have seen that cells tended to touch only the fibronectin area, leading to an interesting actin filament distribution and organization. In particular, in cells patterned in the 35- and 45-µm-diameter circles, concentric and radial actin filaments are visible mimicking the ring-shaped, otherwise the cell body seemed to be detached or not interacting with the centric area, leading to a weak distribution of actin filaments with no specific orientation and organization. Accordingly, pattern coating with an optimal selection of an ECM protein appears to be indispensable for optimizing cell patterning as well as for driving cell cytoskeleton organization and thus cell mechanical properties.

4.5 Materials and Methods

4.5.1 Cell culture

Primary fibroblasts were isolated from three surgically removed skin tissues of left-hand palmar fascia regions of a 55-year-old female patient. Scar fibroblasts were derived from cutaneous scar excision and control from adjacent skin tissue. Dupuytren fibroblasts were isolated from the nodules in the palmar fascia. Cells were incubated in Dulbecco's modified Eagle medium (DMEM, containing 3.7 g/L NaHCO3 and 4.5 g/L D-glucose, FG0435, Sigma) supplemented with 10% fetal bovine serum (F7524, Sigma) and 2% streptomycin–penicillin (P0781, Sigma). Approximately 30,000 cells were added onto patterned coverslips and incubated for 5–6h at 37 °C and 5% CO2.Then, the patterned coverslips were washed with a complete medium twice to remove non-adherent cells. Fibroblasts between passages 8–10 were used, where cells proliferate consistently.

4.5.2 Micro-patterns formation

Here, 22-mm-diameter round glass coverslips were sonicated with acetone for 2 min followed by water sonication for 2 min. The coverslips were then washed with ethanol for 1 minute and dried. Once the coverslips were completely dried, they were incubated in a UV ozone chamber (UVO Cleaner 30–220, Jelight Company Inc., USA) for 5 minutes to activate the surface. The surface of the coverslips must be coated with an antifouling polymer that prevents adhesion of molecules and cells. The activated surface of the coverslip was incubated with the antifouling PLL (20)-g [3.5]-PEG (2) solution (SuSoS AG, Switzerland) at a concentration of 0.1 mg/ml for 1 hour at room temperature in a wet chamber. After 1 hour of incubation, the coverslips were rinsed with PBS once and milli-Q water four times. To generate patterns, we used a chromate synthetic quartz mask that has the circles drawn on it (Delta Mask B.V., Netherlands) (circular-shaped micropatterns used have dimensions of 25, 35, and 45 µm diameter and illuminating a ring of 7 µm width). The coverslips were attached onto the mask with a small water drop and exposed to UV for 5 minutes. The UV oxidizes the PLL-PEG layer generating a chemically structured surface on the coverslip. After that step, the coverslips can be stored at 4°C for 1 month. Before usage, the coverslips need to be hydrated for 30 min with PBS and incubated with 25 µg/ml fibronectin—5 µg/ml fibrinogen (Sigma) for 1 hour at room temperature. The fibronectin–fibrinogen solution is prepared in 100 mM NaHCO3 (pH = 8.6), and the fibrinogen is labeled using an Alexa Flour 488 dye to allow checking pattern formation. The fibronectin should attach to the bare glass, that is, the areas where the PLL-PEG was removed by UV irradiation (Azioune *et al.*, 2010).

4.5.3 AFM experiments

Approximately 10 cells of each type of fibroblasts were measured in 25-µm-diameter circles, 20 cells in 35-µm- diameter circles, and 15 cells of each fibroblast type in 45-µm-diameter circles. AFM measurements were performed using an MFP3D AFM (Asylum Research, Santa Barbara, California, USA) combined with an optical microscope (Zeiss Axiovert 135, Zeiss, Oberkochen) to control tip and sample positioning. Coverslips were glued onto cell culture dishes with superglue (UHU) to avoid detachment, and the medium was just added over the coverslip to avoid contamination with the glue. Cell culture dishes, containing samples, were fixed to an aluminum holder with vacuum grease (Merck, silicone high-vacuum grease) and mounted on the AFM stage with two magnets. The entire setup was enclosed in a home-built polymethylmethacrylate (PMMA) box in order to inject and maintain 5% CO2 during experiments. Patterned fibroblasts were probed on the nuclear region. PFQNM-LC-A-CAL cantilevers were used (Bruker, pre-calibrated spring constant around 100 pN/nm and resonance frequency of 45 kHz in air), which are three- sided pyramid cantilevers (opening angle 15–25°) with a sausage-like protrusion at the very end that has a length of 0.8–1 µm and a radius of curvature of 75 nm. Apparent Young's modulus values were extracted from regular force curves, and the sweep frequency method was used to obtain cell rheological properties (Hecht *et al.*, 2015; Instruments, 2016). The force map scan size was 5 µm and composed of 16 or 256 force curves (4×4or 16×16 lines per frame). Typically, the force curves were recorded at a scan rate of 2 Hz, corresponding to a maximum velocity of 20 µm/s.

4.5.4 AFM data analysis

Data analysis software IGOR (WaveMetrics, Lake Oswego, OR, USA) was used to evaluate the mechanical properties of cells in terms of apparent Young's modulus (E). The Hertzian model for parabolic tips was used to calculate apparent Young's modulus for each force curve within a force map (Hertz, 1881). The median and 25/75 percentiles and logarithmic histogram of apparent Young's modulus were considered representative modulus of each force map. Sweep frequency data were fitted with the power law structural damping model (Hildebrandt, 1969; Fabry *et al.*, 2001) and corrected for the hydrodynamic viscous drag (Alcaraz *et al.*, 2002). E* data are separated into real (in phase) and imaginary (out of phase) parts. The real part represents the storage modulus, and it is a measure of the elastic energy stored and recovered per cycle of oscillation. The imaginary part depicts the loss modulus, and it accounts for the energy dissipated per cycle of sinusoidal deformation. We also calculate the power law exponent and loss tangent, which is an index of the solid-like (<1) or the liquid-like (>1) behavior of the cell. This model assumes a storage modulus that increases with frequency following a power law with the exponent α and a loss modulus that includes a term that is a fraction η of the storage modulus and a Newtonian viscous term, μ (Alcaraz *et al.*, 2003; Malvern Instruments, 2016).

4.5.5 Immunostaining

After 5 to 6 hours of cell seeding on coverslips, cells were fixed with 4% paraformaldehyde for 10 min and permeabilized with 0.2% Triton X-100 for 5 min. The samples were washed with PBS after each step and then incubated with 10% FBS along with the primary antibody against vimentin (rabbit anti- vimentin 1:200) (Abcam, ab92547) for 30 min at room temperature. The secondary antibody (goat anti-rabbit 1: 200, Atto647N) and Alexa Flour 488 phalloidin for actin fibers (1:200) (Thermo Fisher Scientific, A12379) were then incubated for 45 min at room temperature. DAPI (1:5,000) was added for 10 min, while the incubation of the secondary antibody was still running. Finally, cells were stored in PBS at 4 °C prior to image acquisition. An inverted spinning-disk microscope equipped with a Live SR module (LNSB2, Nikon TI-2, Yokogawa CSU-W1-T2, Gataca Systems) with the ×63 objective lens (Plan Apo, NA 1.4 Oil) was used to observe cells and collect fluorescent images (Photometrics Prime95B Scientific CMOS Camera) through appropriate filters (emission: 450/50; 525/50; 595/50; and 700/75). Three-dimensional-view representation videos were created using IMARIS software (Bitplane, Oxford Instruments).

The super-resolution images were taken using a stimulated emission depletion (STED) microscope (Abberior Instruments GmbH, Germany) with the ×100 objective lens (Plan Apo, NA 1.4 Oil), with an excitation at 640 nm followed by a depletion at 775 nm. SiR-actin (Cytoskeleton, Inc., 1:1,000) was used to label F-actin in live cells. The cell culture medium was replaced, and SiR-actin was directly added to the cells. The cells were then placed in the incubator at 37°C and 5% CO2 for 1–2 h prior to image acquisition.

4.5.6 Cell height and volume

Cell height and volume were calculated using Fiji software. From the orthogonal projections of the cell, the cell height was obtained, and the cell volume was estimated from the area of the orthogonal projections.

4.5.7 Statistical analysis

Differences between the apparent Young's modulus of different cells or different patterns were determined using the Wilcoxon signed-rank test and Cohen's d-test using IGOR. For each force volume, E's median was calculated. The effect size (Cohen's d) between the mean of E and the significance of difference (Wilcoxon signed-rank) between the E for each type of patterned fibroblasts was tested. *p*-values were obtained using the Wilcoxon signed-rank test, where * indicates $p < 0.01$, and Cohen's d-test, where # indicates $0.2 < d < 0.5$ and ## indicates $d > 0.5$.

4.6 Conclusions

In this work, fibroblasts from the Dupuytren'sdisorderwere confined in circular-shaped patterns of three different sizes (25, 35 and 45 µm diameter). We compared mechanical properties of control fibroblasts, scar fibroblasts from a wounded area and pathological fibroblasts, and Dupuytren fibroblasts, using the AFM. PFQNM cantilevers probed the cells over the nucleus area, and the apparent Young's modulus from the approach curve showed that control fibroblasts stiffen when increasing the pattern diameter. This behavior may simulate a fibroblast transition toward the myofibroblast phenotype, owing to an increase in cortical tension inside the cell body. Rheological properties, represented as the loss tangent and power law exponent parameters, corroborated an increase in solid-like behavior as the pattern dimension increases. Scar and Dupuytren fibroblasts maintain their stiffness regardless of the pattern diameter, suggesting that they appear to be less affected in cell rheological properties by changes in adhesive contact areas in the environment, adapting their body to the patterns' geometry. The fibronectin-coated area supported cell adhesion to the substrate and cytoskeleton formation; however, the central area of the circle, which was covered with PLL-PEG, forbade cell attachment and cytoskeleton development. These experiments suggest that micropatterning is a valuable approach to study cell mechanics, as it diminishes cell morphology variability and limits cells' free spreading as well as allows combination with other methodologies, such as AFM measurements.

4.7 Acknowledgements

We thank Prof. Dr. Ursula Mirastschijski for kindly providing tissue samples and Prof. Dr. Gazanfer Belge for establishing cell lines from primary cells. We thank the members of the Institute Pasteur Lille for making their facilities available and for their help and support during the visit. We thank Dr. Lorena Redondo, Dr. Fabio Perissinotto and Javier Lopez-Alonso for their help and support.

4.8 Funding

This project was funded by the H2020 European Research and Innovation Programme under the Marie Skłodowska-Curie grant agreement “Phys2BioMed” contract no. 812772.

4.9 Institutional Review Board Statement

The study was conducted in accordance with the Declaration of Helsinki, and approved by the local Ethics Committee (Ärztekammer Bremen, #336/2012).

4.10 Informed Consent Statement

Patient was informed pre-operatively and had given its informed consent to anonymous tissue donation.

4.11 Supporting information

Data processing

To extract the Young’s modulus from the obtained curves (d-z), we used the following approach based on Hertz’s model. Firstly, to compute the force (F) applied by the cantilever, the following relation is employed:

$$F = k \cdot (d - d_0) \qquad \text{(Eq. 4.1)}$$

and the indentation (δ) is calculated:

$$\delta = (z - z_0) - (d - d_0) \qquad \text{(Eq. 4.2)}$$

where d_0 is the deflection offset and z_0 the cantilever displacement at the tip-sample contact point. To analyze the F-δ curves, Hertz’s model for spherical indenters is used:

$$F = \frac{4}{3}\sqrt{R}\frac{E}{1-\nu^2}\delta^{3/2} \qquad \text{(Eq. 4.3)}$$

where R is the radius of the curvature in spherical or parabolic probes, ν is the Poisson's ratio (which is considered 0.5 for cells) and E is the elastic or Young's modulus of the sample.
Contact point determination is based on the inspection of the force curve, where each point is considered as a potential contact point. For each potential contact point, the d-z curve is converted into F-δ and then fitted with the appropriate contact mechanics model, in our case Hertz fit for spherical indenters.

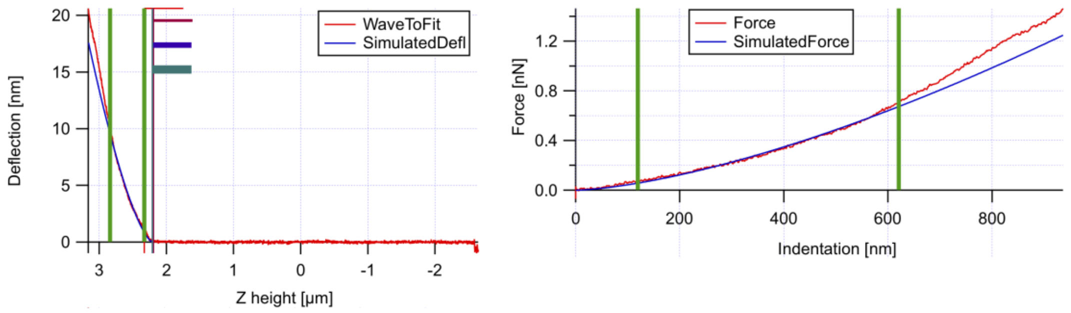

Figure 4.1 Approach force curve in red with the Hertz fit in blue. Vertical green lines limit the analysis range of the curve and green, blue and red flags represent the

estimations of the contact point (left). Force versus indentation display after contact point determination, original data are in red, blue curve is Hertz fit and the vertical green lines delimit the analysis range (right).

Sweep modulation

In sweep modulation a sinusoidal modulation with increasing frequency is applied to the z-piezo while the tip is in contact. Typically, we use a dwell time of 8.7 seconds, where during the first second no modulation is applied since the cell creeps substantially. Then the frequency is swept from 1Hz to 1kHz, where for each frequency only one cycle is applied. The frequency series is designed as a geometric series, so that in each decade we use the same number of frequencies. Typically, the frequency increases by a factor of 1.15 from cycle to cycle, which results in 17 frequency values per decade, which are equally spaced on a logarithmic scale.

The elastic and viscous modulus, denoted here as loss and the storage modulus, are a function of frequency and in the simplest case we expect a power law behavior. However, in our case at frequencies beyond 10 Hz (depending on experimental parameters especially dimension of the cantilever) hydrodynamic drag of the cantilever will become very prominent. Thus, we employ the structural damping model as has been introduced to AFM rheology by Alcaraz *et al.* (Alcaraz *et al.*, 2003). Here, the complex modulus G^* is written as:

$$E^*_{(\omega)} = E_0 * (1 + i\eta) * \left(\frac{\omega}{\omega_0}\right)^{\alpha} + i\,\mu\,\frac{\omega}{\omega_0} \qquad \text{(Eq. 4.4)}$$

where E^* is the complex elastic modulus; E_0 is the scale factor of the storage and loss moduli; i the imaginary unit; η the loss tangent; ω_0 in the frequency scale (in our case 1 Hz); α the power law exponent of the sample and μ the Newtonian viscous term, which will depend on the shape of the cantilever and the viscosity of the medium. The real part represents the storage modulus and the imaginary part corresponds to apparent loss modulus, which has two contributions; (1) from the sample, which scales with the same power law exponent as the storage modulus, and the hydrodynamics, which is directly proportional to the frequency. Thus, we can first obtain the power law exponent by fitting the storage modulus as a function of frequency, and then in a second step obtain the loss tangent η and the strength of the hydrodynamic damping of the cantilever μ.

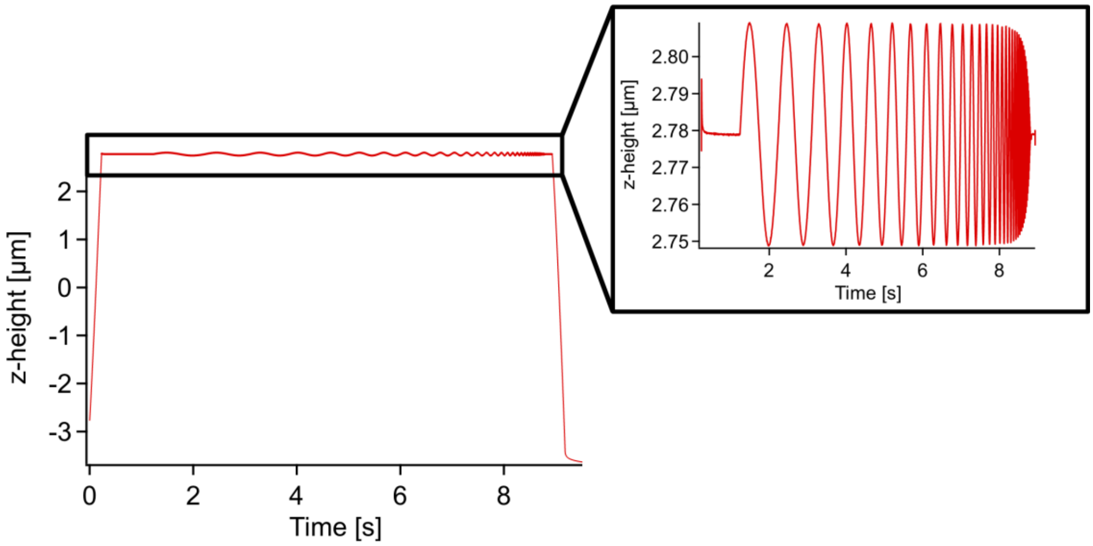

Figure 4.2 Sweep modulation AFM methodology. Representation of the piezo movement in z direction versus time.

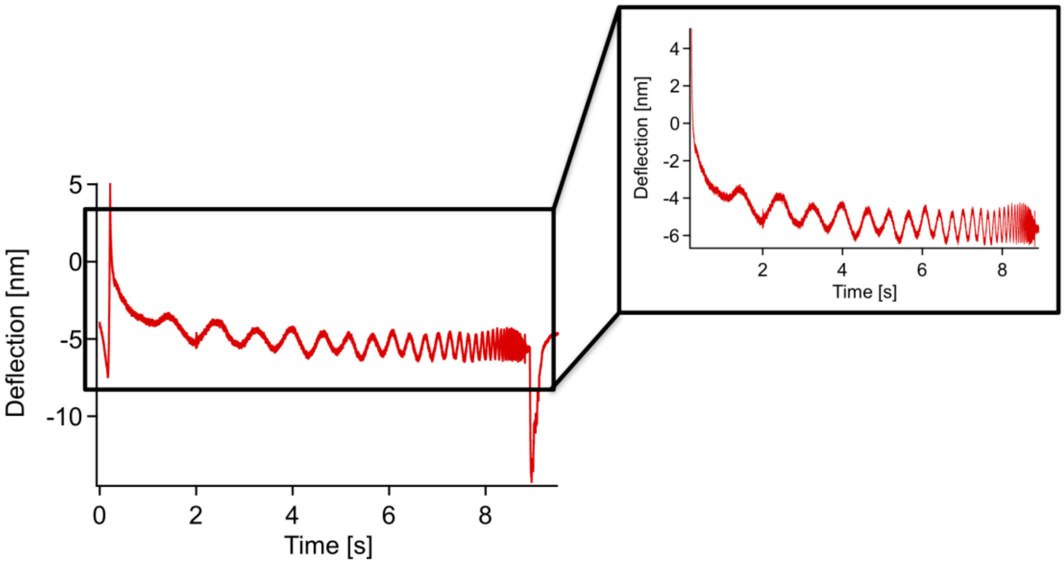

Figure 4.3 Sweep modulation AFM methodology. Deflection versus time. The deflection is the cantilever bending and it can be extrapolated to cell response. The highlighted area in the black box is the zoom of the sweep step. Deflection reflects cantilever movement over time.

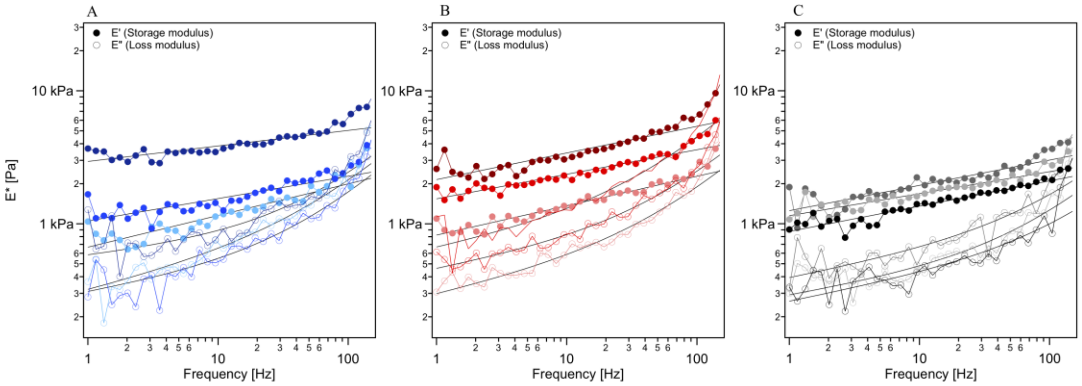

Figure 4.4 Frequency-dependent of complex elastic moduli of the A) control fibroblasts, B) scar fibroblasts and C) Dupuytren fibroblasts. Close and open circles represent the storage (E') and loss modulus (E"), respectively. From lightest to darkest color display the modulus from the cells patterned in the 25, 35 and 45 µm diameter circle patterns, respectively (N = 15). Data shown after viscous drag correction.

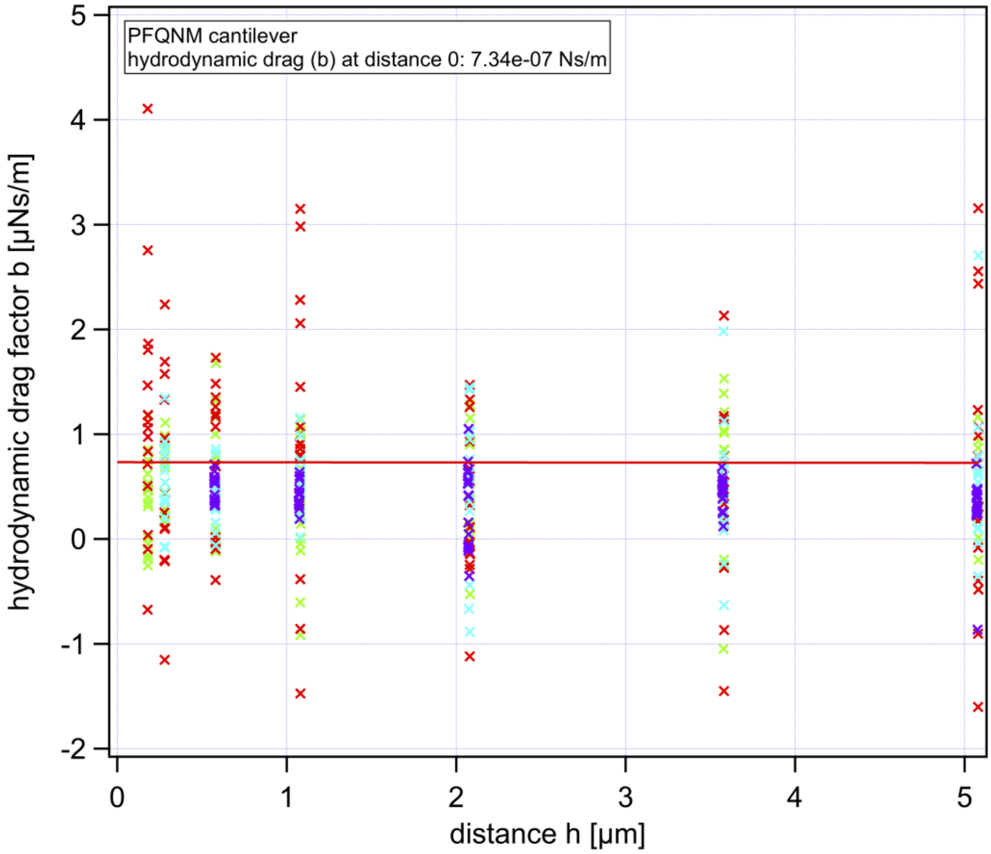

Figure 4.5 Hydrodynamic drag factor b(h) at different tip-substrate distances (h) for PFQNM cantilevers above glass. The value of b(0) is so small for this cantilever that the correction is almost negligible (Alcaraz *et al.*, 2002).

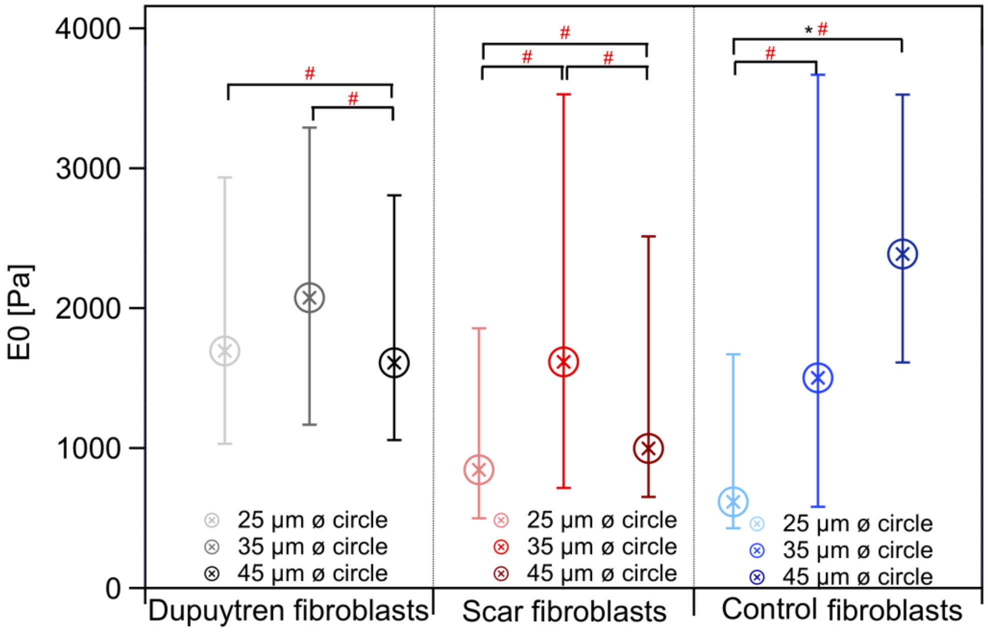

Figure 4.6 E_0, scale factor of the storage and loss moduli. Box plot of E_0 with the median and 25/75 percentiles. Data shows information from different cells. Each colour represents one type of fibroblast, Dupuytren, scar and control in black, red and blue, respectively. Besides, within each group the colour gradient shows the cells patterned in each circular diameter, from the lightest to the darkest, goes from the 25 to the 45 µm circular diameter, respectively. Statistical analysis: Wilcoxon signed-rank test, * indicating $p < 0.01$ and Cohen's d test with # indicating an effect size of $0.2 < d < 0.5$ and ## indicating $d > 0.5$. ø = diameter. (N = 15).

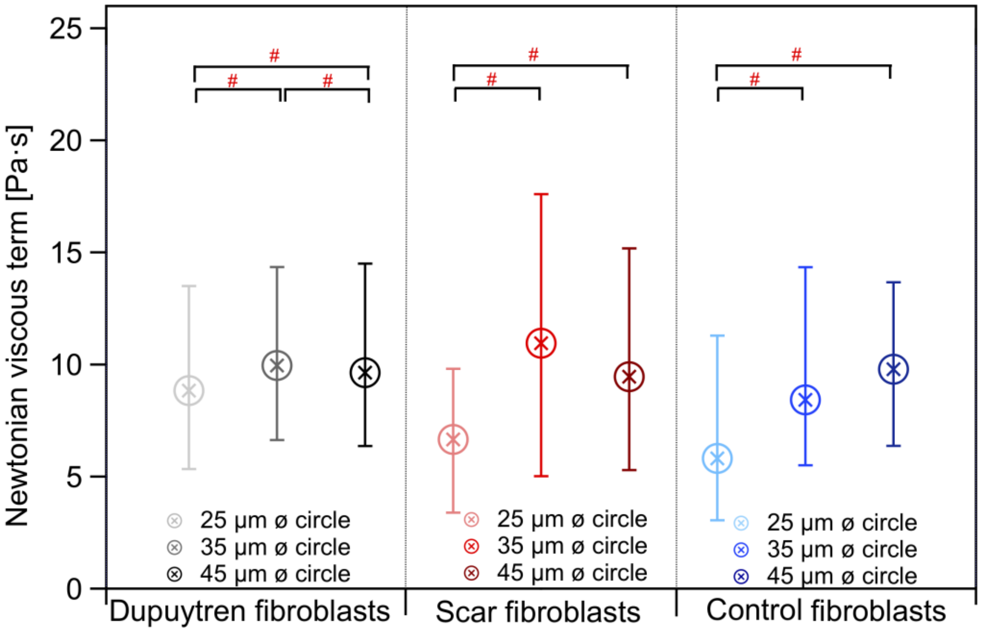

Figure 4.7 Box plot of μ (Newtonian viscous term) with the median and 25/75 percentiles. Data shows information from different cells. Each colour represents one type of fibroblast, Dupuytren, scar and control in black, red and blue, respectively. Besides, within each group the colour gradient shows the cells patterned in each circular diameter, from the lightest to the darkest, goes from the 25 to the 45 μm ø circular diameter, respectively. Statistical analysis: Cohen's d test with # indicating an effect size of $0.2 < d < 0.5$ and ## indicating $d > 0.5$. ø = diameter. Wilcoxon signed rank test was performed and showed no significant differences between any circular pattern diameter within each type of fibroblast (N = 15).

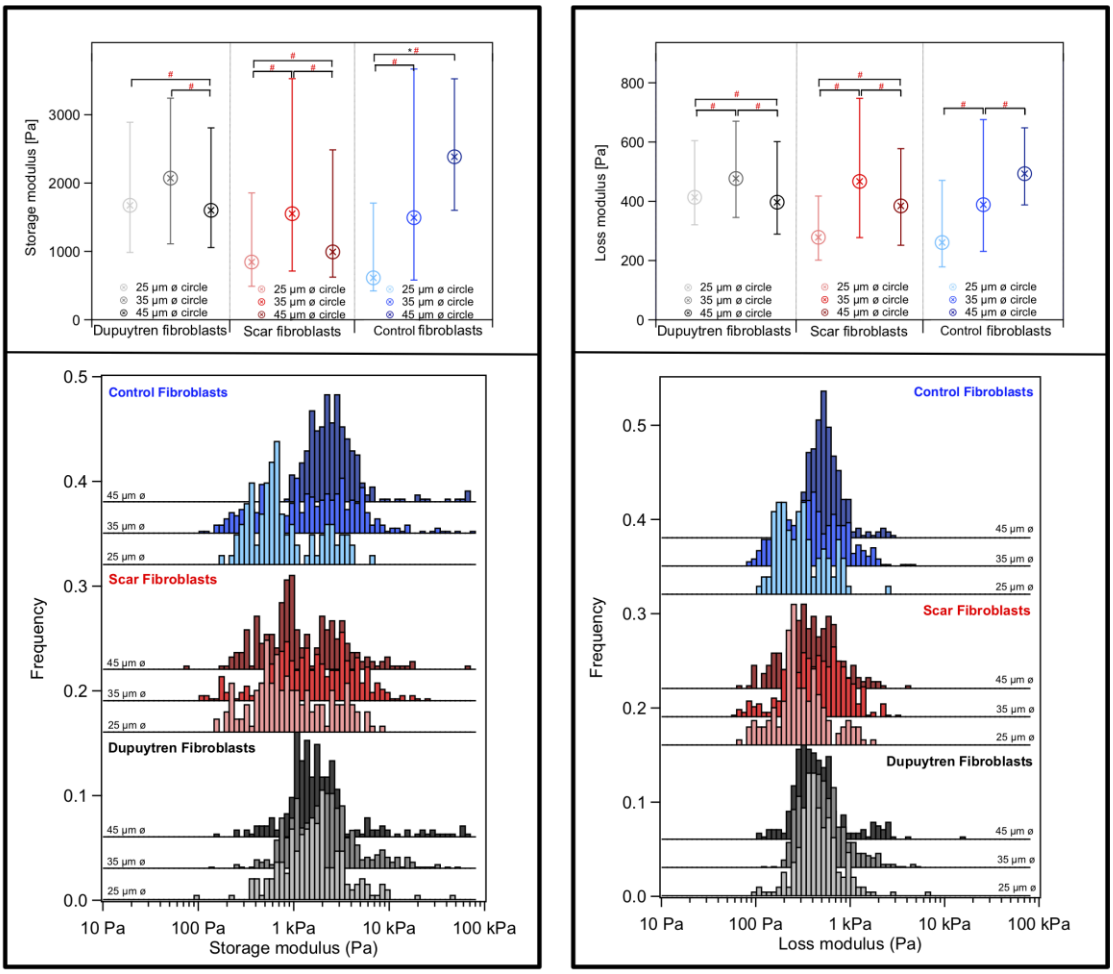

Figure 4.8 Median with 25/75 percentiles (above) and histogram display (below) of the storage and loss modulus at 1 Hz, left and right, respectively, of each fibroblasts type. Data shows information from different cells. Dupuytren fibroblasts are presented in black, scar fibroblasts in red and control in blue. Within each type of fibroblast there is a gradient in color, from lightest to darkest represents the patterned cells in 25 µm diameter circles, 35 µm diameter circles and 45 µm diameter circles, respectively. Statistical analysis: Wilcoxon signed-rank test, * indicating $p < 0.01$ and Cohen's d test with # indicating an effect size of $0.2 < d < 0.5$ and ## indicating $d > 0.5$. ø = diameter (N = 15).

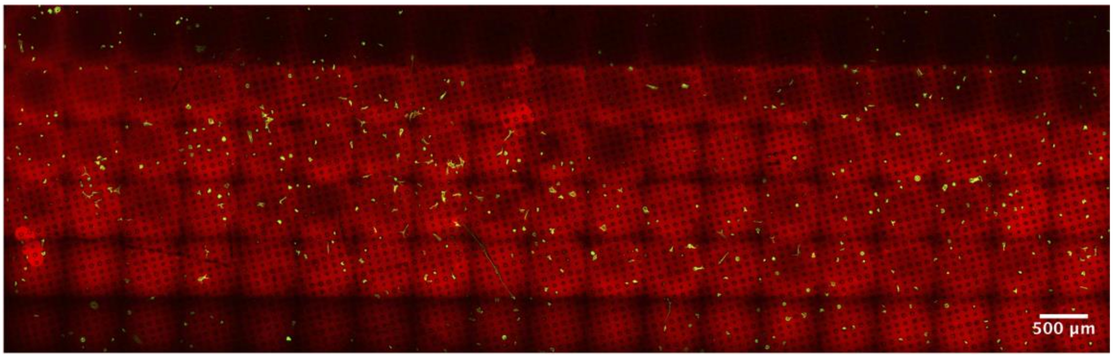

Figure 4.9 Scar fibroblasts patterned in fibronectin-coated circles. Actin fibers labeled in green, PLL-PEG layer in red.

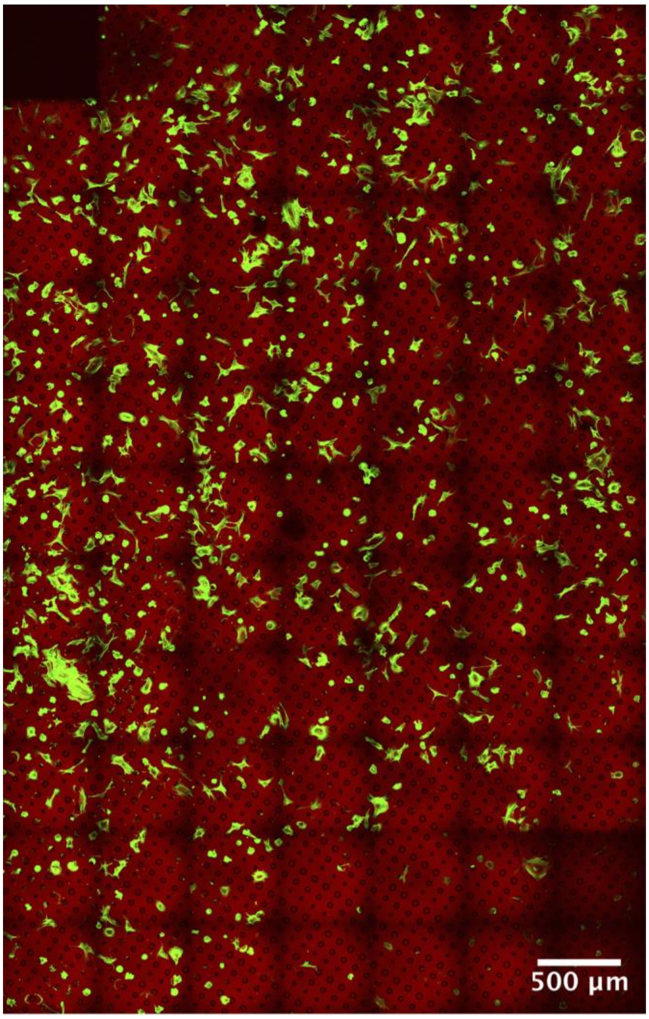

Figure 4.10 Control fibroblasts patterned in fibronectin-coated circles. Actin fibers labeled in green, PLL-PEG layer in red.

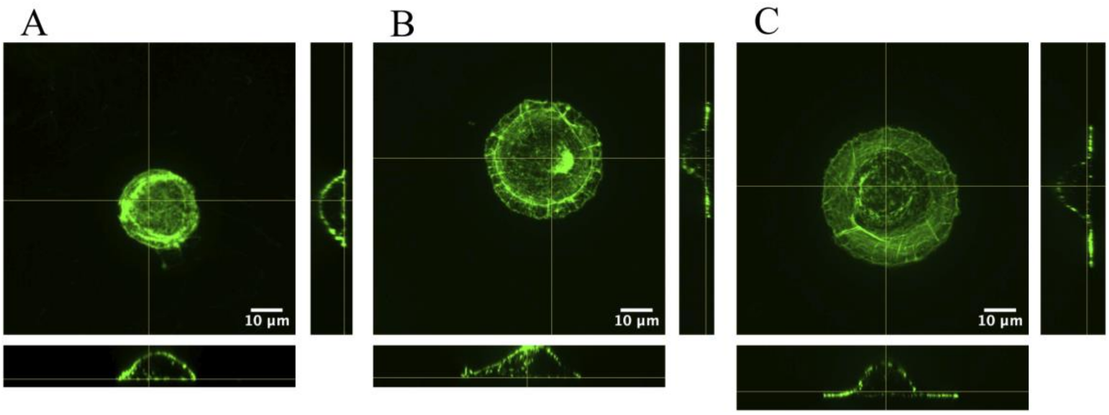

Figure 4.11 Z- and orthogonal projections of Dupuytren fibroblasts patterned in: A) 25-µm, B) 35-µm and C) 45-µm ø circles. Actin fibers labeled in green (N = 4).

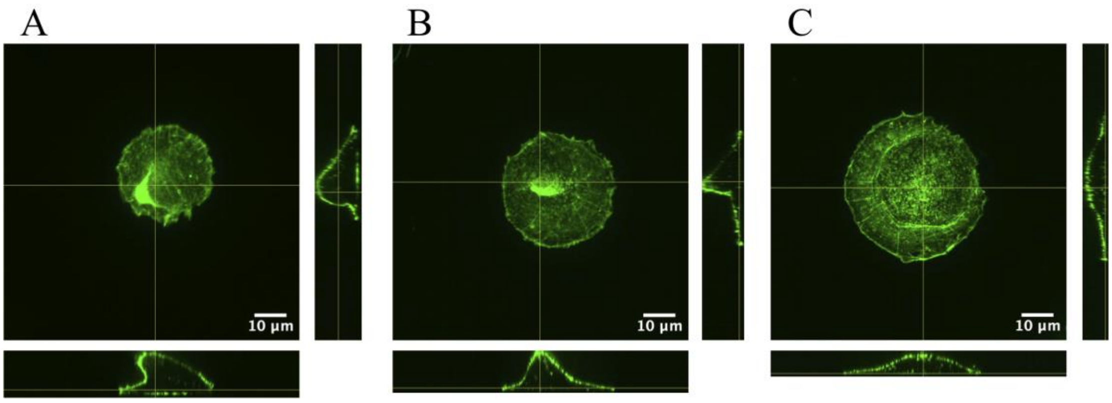

Figure 4.12 Z- and orthogonal projections of control fibroblasts patterned in: A) 25-µm, B) 35-µm and C) 45-µm ø circles. Actin fibers labeled in green (N = 4).

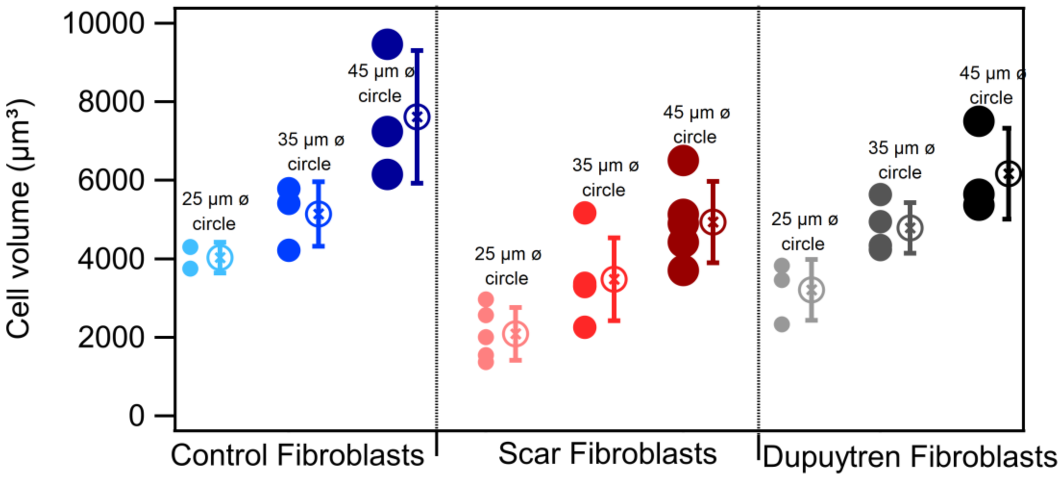

Figure 4.13 Estimation of relative cells volume from the xz projections from the fluorescent images. The dots represent the mean with the standard deviation (N = 4). The circles next to each mean value correspond to the individual measurements.

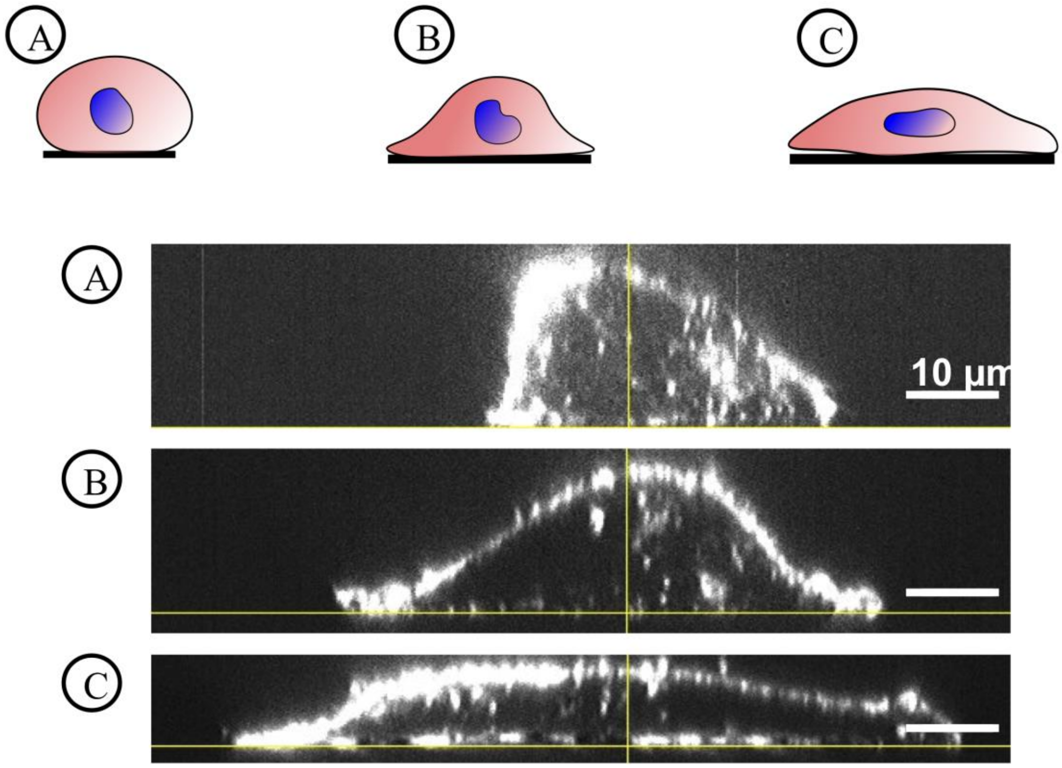

Figure 4.14 Control fibroblast xz projections when patterned in A) 25 µm diameter, B) 35 µm diameter and C) 45 µm diameter circles. We propose a possible explanation to the changes in cell height when increasing circle diameter but cells increase their volume. Control fibroblasts decrease their height but increase their volume with increasing pattern diameter. We suggest that the increase in volume may be because they spread more homogeneous through the pattern, reducing the height but gaining volume in the lamelipodia protrusions.

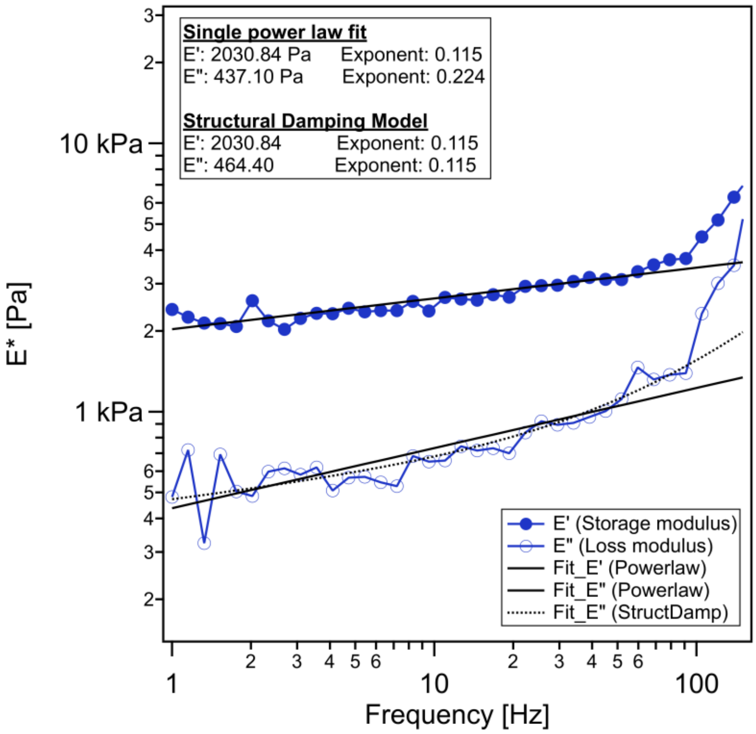

Figure 4.15 Frequency-dependent of complex elastic moduli of a control fibroblast pattern in a 45 µm circle. Close and open circles represent the storage (E') and loss modulus (E"), respectively. Continuous line represents a single power law fit to the storage and loss modulus and dashed line represents power law structural damping fit. Single power law fit gives different exponents for storage and loss modulus due to the different frequency dependence and the structural damping provides one power law, which is the same for the storage and loss modulus. Data shown after viscous drag correction.

Chapter 5

This is a verbatim copy of an article publishing in the preprint “bioRxiv”: Pérez-Domínguez S., Sanz-Fraile H., Martínez-Vidal L., Alfano M., Otero J. & Radmacher M. Characterizing the viscoelastic properties of different fibroblasts in 2D and 3D collagen gels, (**2023**). doi:10.1101/2023.12.15.571880

Characterizing the viscoelastic properties of different fibroblasts in 2D and 3D collagen gels

Sandra Pérez-Domínguez[1], Héctor Sanz-Fraile[2], Laura Martínez-Vidal[3,4], Massimo Alfano[4], Jorge Otero[2], Manfred Radmacher[1*]

[1] Institute for Biophysics, University of Bremen, Bremen, Germany
[2] Unit of Biophysics and Bioengineering, University of Barcelona, Cellular and respiratory biomechanics, Institute for Bioengineering of Catalonia, CIBER Respiratory diseases, Barcelona, Spain.
[3] Vita-Salute San Raffaele University, Milan, Italy
[4] Division of Experimental Oncology/Unit of Urology, URI, IRCCS, Ospedale San Raffaele, Milan, Italy

***corresponding author**: radmacher@uni-bremen.de

Keywords: Dupuytren’s disease, collagen matrix, fibroblast, rheology, viscoelasticity.

5.1 Abstract

We assessed cell mechanical properties in both 2D and 3D environments employing compliant type I collagen matrices. Firstly, collagen gels of varying stiffness were prepared using a photocrosslinker to increase gel stiffness. Using methacrylic anhydride and UV light, a 10-fold increase in apparent Young’s modulus with respect to the soft collagen gel was achieved (0.2 kPa to 2 kPa). In addition, cells were plated onto the different collagen gels and hard Petri dishes (as a super stiff substrate) and their mechanical properties were evaluated. An increase in apparent Young's modulus was observed in Dupuytren fibroblasts behavior when increasing substrate stiffness, supporting its myofibroblast phenotype (3.8 kPa to 5.2 kPa from soft collagen gels to hard Petri dishes). Secondly, gel's mechanics, in which fibroblasts were embedded, were evaluated over time to assess cells contraction properties. Gel's apparent Young's modulus increased over time regardless of fibroblasts type and cells presented dendritic protrusions. Rheological properties of both cells and gels were extracted using AFM sweep frequency scheme and power law structural damping model for data analysis. As a summary, we have found that fibroblasts contractile properties, related to myofibroblast differentiation and development are highly influenced on the mechanical properties of the surrounding environment, being stiffer environments those that favor the increase in fibroblast mechanical tension.

5.2 Introduction

Tissue is the biological organization of structurally and functionally similar cells and their extracellular matrix (ECM) (Bosman and Stamenkovic, 2003). In disease, it is important to study both cellular and ECM alterations to reach a better understanding of disease's origin and progression (Choquet, Felsenfeld and Sheetz, 1997; Trappmann and Chen, 2013; Matte *et al.*, 2019). In biophysics, studies at single cell level are commonly employed to assess cell mechanical changes, among other changes like adhesion or biochemical variations, in disease. AFM has been used to compare mechanical alterations between healthy and cancerous or pathological cells (Lekka *et al.*, 1999), opening a new window supporting the potential of studying cell mechanics with AFM as a diagnostic marker. However, it is well known that cells react and respond to their surrounding environment; therefore, it is important to specify in which conditions measurements were performed. Several progresses in the topic showed that cancerous cells being softer than healthy cells could not be taken as a general statement. Healthy cells were found to modify its stiffness to the stiffness of the support in contrast to cancerous cells, which appear to be less sensitive to changes in substrate mechanical properties (Rianna and Radmacher, 2017b). Currently, artificial and natural hydrogels are becoming popular as 2D scaffolds to plate cells and assess cell behavior under specific conditions. Polyacrylamide (PA) gels are widely used due to their capacity of being modulated to achieve large range variability in stiffness (Witkowska-Zimny *et al.*, 2013; Abidine *et al.*, 2018; Viji Babu *et al.*, 2018). Artificial hydrogels made of natural polymers such as collagen, gelatin, hyaluronic acid, alginate, and dextrin are also employed to measure cell mechanics on and in compliant substrates. These hydrogels are often ultra soft (few hundreds of Pa) and certain chemical or physical agents are needed to increase the number of crosslinks and thus to raise gel's stiffness. Glutaraldehyde, genipin and ribose are some of the compounds used to increase collagen gel's strength (Sheu *et al.*, 2001; Sundararaghavan *et al.*, 2008; Zhang *et al.*, 2014; Vicens-Zygmunt *et al.*, 2015). Methacrylic anhydride along with a photoinitiator has also been employed as a crosslinker to modify collagen gel's stiffness. The exposure of methacrylated collagen under UV light of a certain wavelength favors the linkage between methacrylated collagen fibers (Gaudet and Shreiber, 2012; Drzewiecki *et al.*, 2014; Nguyen, Watkins and Kishore, 2019). Thanks to the use of the above-mentioned techniques, collagen gels reaching a few kPa can be successfully made. The seeding of cells on top of compliant hydrogels, which present similar mechanical properties to cells, resembles more tissue-like environments; however, 3D dimensionality is still lacking (Duval *et al.*, 2017; Jensen and Teng, 2020). For that reason, hydrogels made of some ECM proteins, such as collagen, are gaining importance to be used as scaffolds to culture cells (Rhee and Grinnell, 2007; Nichol *et al.*, 2010; Duval *et al.*, 2017; Xie *et al.*, 2017; Court, Malier and Millet, 2019; Vaughan *et al.*, 2019). Type I collagen is the most abundant protein in connective tissue that provides mechanical stability and strength and fibroblasts are responsible for its synthesis (Fratzl, 2008); thus, its use resembling ECM properties is increasing.

Cells, in tissues, are surrounded by neighboring cells and ECM, which together provide different stresses and biochemical cues as in a 2D environment. Tissue availability is limited for research purposes, which is the closest biological organization to cells' natural environment; therefore, other strategies are needed to provide tissue-like conditions. In disease, cells can experience changes in biochemical and biomechanical composition that may be transmitted to the ECM, procuring ECM composition and stiffness alterations as well (Janmey and Miller, 2011). Accordingly, both cells and ECM variations may generate feedback loop responses, in which cell-ECM interplay is essential. Hence, cell-to-cell interaction as well as with its surrounding is vital for cell mechanical properties development. Cell behavior assessment surrounded by its natural ECM is desirable; otherwise artificial hydrogels mimicking ECM composition and mechanics offer a good compromise (Heffernan *et al.*, 2015; Link *et al.*, 2017; Court, Malier and Millet, 2019; Vogel *et al.*, 2020). 3D hydrogels provide physical constraints forcing the cells to adapt morphologically as well as chemically and biologically to an environment similar to that in tissue. There are several models to study fibroblasts contractile activity; free-floating matrix contraction and anchored matrix contraction are the most employed. In the method first the gel is detached from the substrate right away after gelation and is based on measuring the reduction in matrix's diameter and the tension is distributed isotropically; however, the anchored model maintains the gel attach to the substrate for some time and after a certain time period, the gel is detached and measures changes in matrix height and the tension is distributed anisotropically. Many studies used the free-floating model because it is easier to measure; nevertheless, it was shown that fibroblasts do not proliferate in compliant matrices; they become arrested in cell phase G0 (Sarber *et al.*, 1981; Kono *et al.*, 1990). Therefore, mechanical stress in the anchored matrix due to the attached surface seems to simulate better fibroblasts' environment and more specifically wound healing process.

Cell and tissue mechanics have been investigated using several techniques, such as optical and magnetic tweezers, flow cytometer and atomic force microscopy (AFM) (Zhang and Liu, 2008; Kirmizis and Logothetidis, 2010; Kilinc and Lee, 2014; Otto *et al.*, 2015; Rosendahl *et al.*, 2018). This latter technique has gained importance over the last twenty years, due to its ability to be used as a diagnostic tool as above mentioned. By applying an appropriate AFM methodology and contact model to analyze it, the sample's mechanical response can be well described. AFM piezo-based nanopositioning provides the user flexibility to design any useful scheme to get the desired sample response. Step response (Yango *et al.*, 2016), force clamp (Hecht *et al.*, 2015) and sweep modulation (Alcaraz *et al.*, 2003) are some of the employed AFM methodologies to differentiate between elastic and viscous properties of cells. Fractional models, such as Kelvin-Voigt, and damping models based on exponential and power law's cell response can be used to analyze AFM data (Alcaraz *et al.*, 2003; Jóźwiak, Orczykowska and Dziubiński, 2015; Pajic-Lijakovic and Milivojevic, 2019; Bonfanti *et al.*, 2020).

In this study fibroblasts from a patient suffering Dupuytren's disease were used. Dupuytren's disease is a fibromatosis of the connective tissue of the palm that generates nodules and cord in the palmar fascia leading to finger flexion and hand contraction (Bayat *et al.*, 2002; Shaw *et al.*, 2007; Warwick, Thomas and Bayat, 2012; Morelli, Fraschini and Banfi, 2017). Fibroblasts differentiation into myofibroblast phenotype (α-smooth muscle actin positive fibroblasts) is one of the disease's characteristics that bring together changes in the ECM that enhances fibroblasts stress and thus hand contraction (Grinnell, 1994; Baum and Duffy, 2011b; Hinz, 2015a; Bochaton-Piallat, Gabbiani and Hinz, 2016). We dispose of three fibroblast types from different tissue samples from the palm of the same patient; healthy from dermal region, scar fibroblasts from the scar excision and Dupuytren fibroblasts from the nodules of the palmar fascia, presenting a myofibroblast phenotype (Viji Babu *et al.*, 2018).

The aim of this project is to assess cells mechanical behavior with increasing substrate stiffness and cells contractile ability when embedded in collagen gels. For this purpose, firstly cells were seeded in collagen gels of different stiffness (0.2 to 2 kPa) and petri dishes as a hard substrate for comparison. Secondly, to provide 3D dimensionality, fibroblasts were embedded in soft collagen gels and gels' stiffness were evaluated after different culture times.

5.3 Results

Collagen from rat-tail was used to prepare collagen gels of two different stiffnesses. We used the same collagen concentration in both gels (5.5 mg/ml); however, to increase gel stiffness we employed a crosslinking molecule (methacrylic anhydride) to induce an increase in collagen fibers crosslinks. The free amino groups on the lysine residues of the collagen fibers undergo nucleophilic substitution with methacrylic anhydride. A photoinitiator, in our case Irgacure, when exposed to UV light (365 nm) generates radicals that are transmitted to methacrylate groups favoring the linkage between them in different collagen fibers increasing the number of crosslinks and therefore leading to stiffening of the gel (Fig. 5.1).

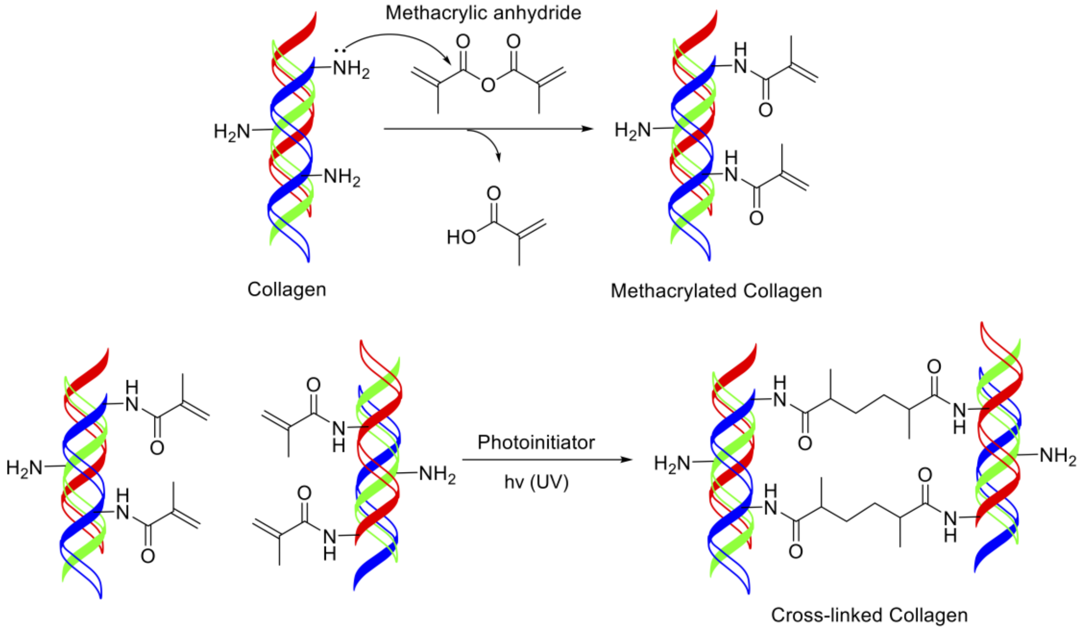

Figure 5.1 Synthesis of methacrylated collagen.

We performed AFM experiments to evaluate gel stiffness and we obtained an increase in stiffness of 10-fold of the methacrylated collagen with respect to the soft collagen (soft collagen: 0.2-0.3 kPa; methacrylated: 2-3 kPa) (Fig. 5.2).

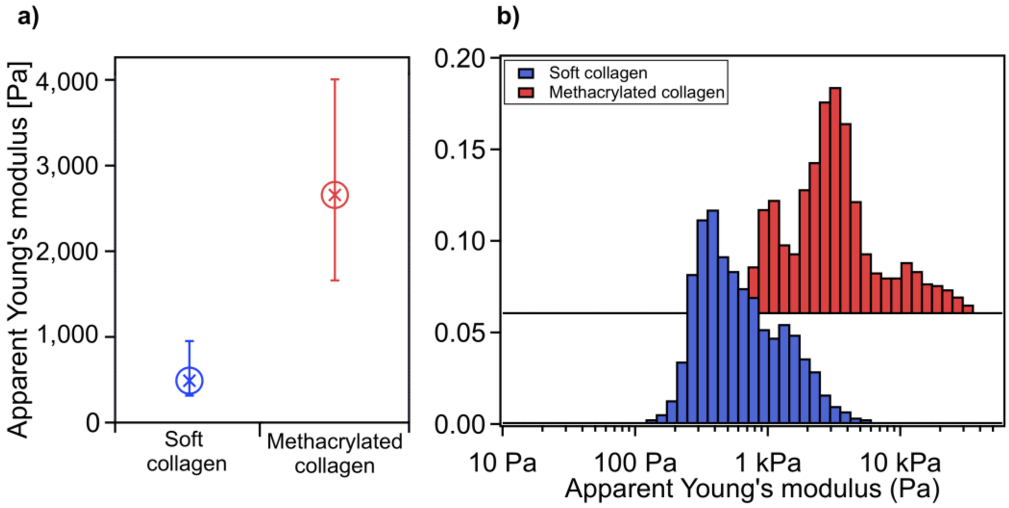

Figure 5.2 A) Box plot (median with 25/75 percentiles) of collagen gels stiffness (*n* = 7) and B) logarithmic histogram representation of apparent Young's modulus. Data were extracted from AFM measurements on bare gels incubated the same time as cells.

We seeded three different fibroblast types on the two different collagen gels and used petri dishes as a hard substrate for comparison. Thanks to the collagen gels' stiffness obtained and the petri dishes, we assessed cell mechanical behavior in substrates with really different stiffness, thus allowing us to encompass cell response in different environments. Cells data on hard petri dishes are used as a reference and were described in the previous work (Pérez-Domínguez *et al.,* 2023).

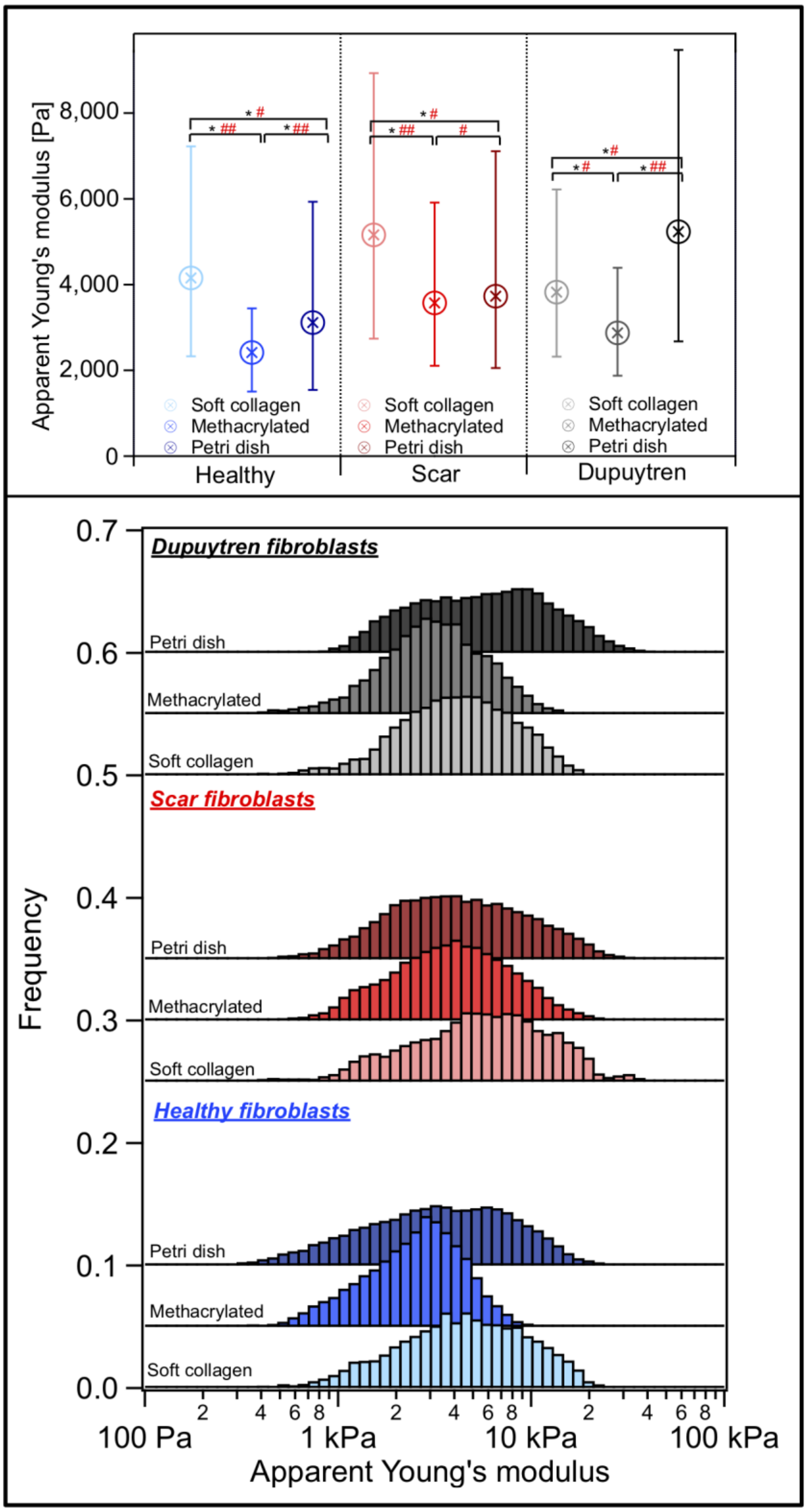

Figure 5.3 Box plot (median with 25/75 percentiles) and histogram distribution of the Apparent Young's modulus from approach curves of the three different fibroblasts seeded on soft collagen gel, methacrylated collagen gel and petri dish ($n = 30$). Data are sorted by cell type and within each group; from lightest to darkest color represents the softest to the stiffest substrate where the cells were seeded.

Table 5.1 Numerical results of apparent Young's modulus of fibroblasts, presented in Fig. 5.3 (median).

Apparent Young's modulus	Control collagen	Methacrylated collagen	Petri dish
Healthy Fib.	4156 Pa	2419 Pa	3115 Pa
Scar Fib.	5161 Pa	3575 Pa	3732 Pa
Dupuytren Fib.	3826 Pa	2876 Pa	5236 Pa

As a comparative parameter, the apparent Young's modulus from the approach curve was computed and the Hertz model for spherical indenters was used (Fig. 5.3). All cell types showed a decrease in apparent Young's modulus when seeded in methacrylated collagen in comparison to soft collagen gels. Nevertheless, healthy and scar fibroblasts presented a slightly increase in apparent Young's modulus when seeded on petri dishes with respect to methacrylated collagen, but Dupuytren fibroblasts showed a large increase in apparent Young's modulus even surpassing apparent Young's modulus values of the cells when seeded on soft collagen gels (Fig. 5.3 and Table 5.1). Statistical analysis showed significant differences among healthy fibroblasts seeded on the different substrates. Scar fibroblasts seeded on soft collagen and methacrylated collagen showed significant differences, as well as scar fibroblasts plated on soft collagen and petri dishes. Additionally, significant differences among Dupuytren fibroblasts seeded on the three different substrates were observed. Cohen's d test was calculated to complement Wilcoxon test and large size effect was observed between healthy fibroblasts seeded on soft and methacrylated collagen as well as methacrylated and petri dish. Medium size effect was found between healthy fibroblasts seeded on soft collagen and petri dish. Moreover, medium size effect could be seen between scar fibroblasts seeded on soft collagen and petri dish, as well as when seeded on methacrylated collagen and petri dish. Scar fibroblasts seeded on soft and methacrylated collagen showed large size effect. Same size effect results as healthy fibroblasts were observed for Dupuytren fibroblasts, except when comparing Dupuytren fibroblasts seeded on soft and methacrylated collagen, in which medium size effect was obtained.

The hysteresis between approach and retract curves is due to cell viscosity, which cannot be quantified and separated from the elastic response in conventional force curves. To measure the elastic and viscous response of the cell samples, we used the sweep frequency scheme, previously described (Pérez-Domínguez *et al.*, 2022). In figure S5.1 comparison between viscoelastic properties of the three different fibroblasts obtained from the sweep frequency data as a function of substrate were shown. In healthy and scar fibroblasts, the measured storage modulus at 1 Hz seemed independent on the substrate stiffness (healthy fibroblasts: 3150 Pa to 2500 Pa, from soft collagen to Petri dish; scar fibroblasts: 4050 Pa to 3050 Pa, from soft collagen to Petri dish), while Dupuytren fibroblasts showed an increase in storage modulus going from 3202 Pa (soft collagen) to 4322 Pa (Petri dish). The loss modulus at 1 Hz showed similar results as the storage modulus, in which healthy and scar fibroblasts slightly varied (healthy: 615 to 495 Pa, from soft collagen to Petri dish; and scar: 675 to 581 Pa, from soft collagen to Petri dish), whereas Dupuytren fibroblasts displayed an increase from 599 to 737 Pa (Fig. S5.1). Both moduli (storage and loss) displayed similar frequency dependence up to 10 Hz. However, loss modulus showed more marked frequency dependence at higher frequencies due to in a large extent the hydrodynamic drag of the cantilever in contact with the liquid (Fig. S5.2). Healthy and scar fibroblasts E* vs. frequency results almost overlapped each other, suggesting similar behavior regardless substrate stiffness. The representation of E* over frequency before and after viscous drag correction could be seen in figure S5.3. The three fibroblast types showed similar power law exponent in the different substrates, presenting values around 0.11, and loss tangent values were around 0.2 at 1 Hz (Fig. 5.4). E_0 values varied depending on cell type and substrate and presented similar results as the storage modulus (Fig. S5.4) and the Newtonian viscous term (μ) was rather constant for Dupuytren fibroblasts regardless substrate stiffness (15 Pa·s) (Fig. S5.5).

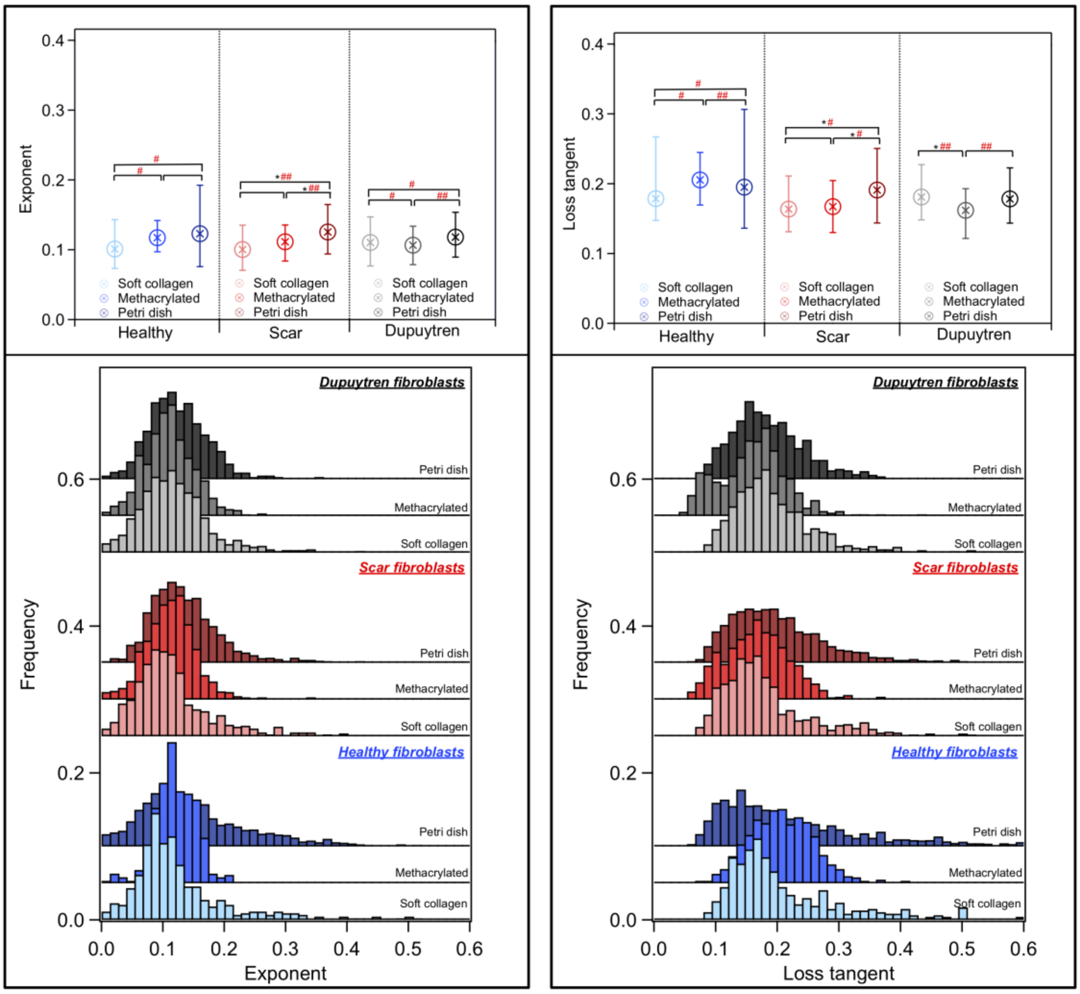

Figure 5.4 Box plot (median with 25/75 percentiles) and histogram distribution of the power law exponent and loss tangent at 1 Hz (left and right) ($n = 30$). Data are sorted by cell type and within each group; from lightest to darkest color represents the softest to the stiffest substrate where the cells were seeded.

Cytoskeleton organization in the cells seeded on the different substrates was evaluated labeling actin fibers. Scar and Dupuytren fibroblasts presented elongated shape and seemed to be aligned when seeded on soft collagen (Figure 5.5 d,g) while they displayed more spread body and randomly dispersed when seeded on methacrylated collagen (Figure 5.5 e,h) and petri dishes (Figure 5.5 f,i). Healthy fibroblasts seemed to follow the same trend; however, due to the low number of cells found in the images, big statements cannot be made (Figure 5.5 a,b,c). Differences in cell morphology were also corroborated with the quantification of cell eccentricity and fibroblasts showed a decrease in eccentricity when seeded on petri dish with respect to soft collagen gel substrate (Fig. S5.6).

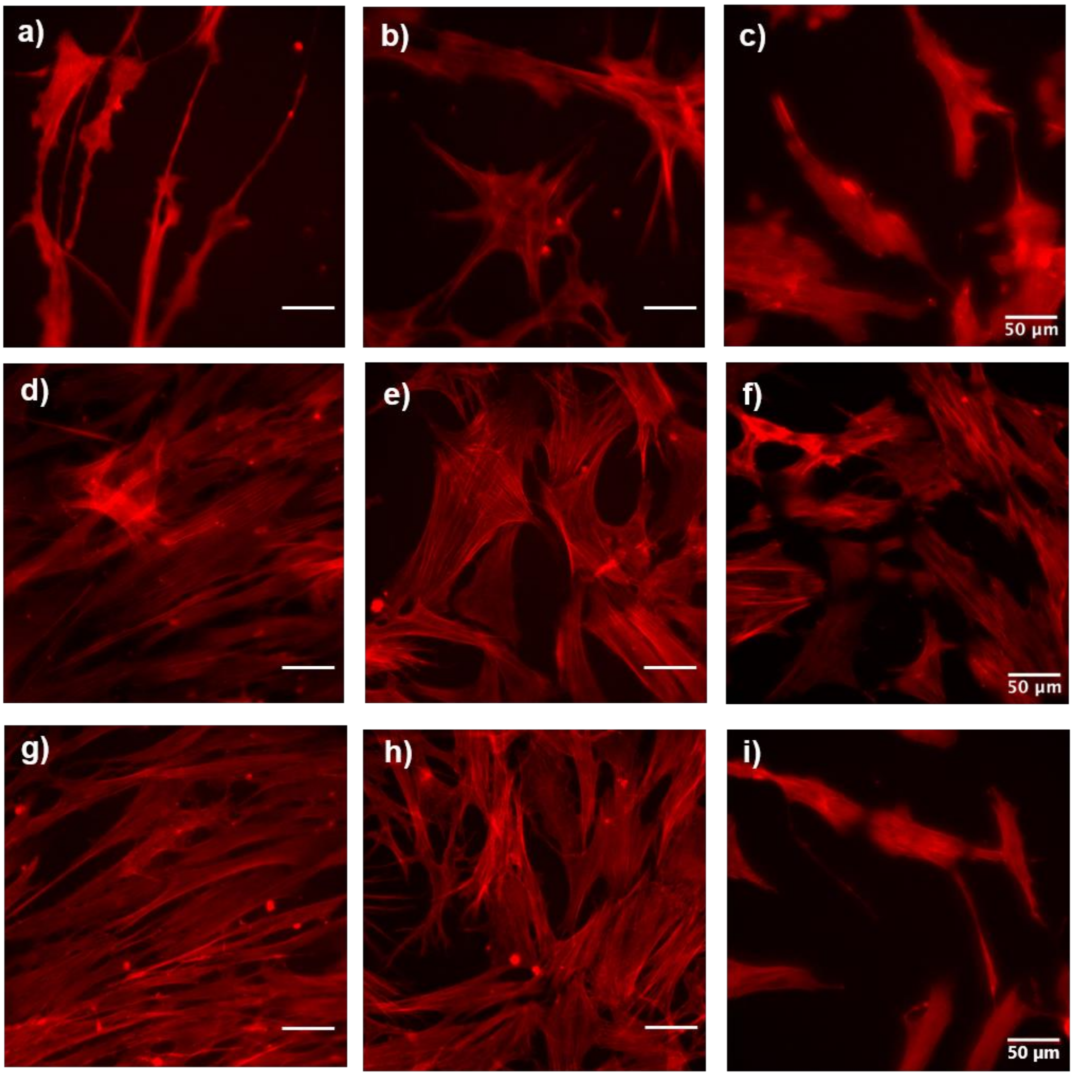

Figure 5.5 Fluorescence images of healthy, scar and Dupuytren fibroblasts labeled with rhodamine phalloidin (actin cytoskeleton). The upper panels show healthy fibroblasts seeded on soft collagen (a), methacrylated collagen (b) and Petri dish (c). The middle panels show scar fibroblasts, seeded on soft collagen (d), methacrylated collagen (e) and Petri dish (f). The lower panels show Dupuytren fibroblasts, seeded on soft collagen (g), methacrylated collagen (h) and Petri dish (i). Scale bars are 50 µm.

In an attempt to better resemble the cells' environment in tissue, fibroblasts were embedded in soft collagen gels generating 3D structures. We measured 3D gels stiffness after three different incubation times: 2 days, 1 week and 2 weeks. Conventional force curves of the gels after the different incubation times were presented in figure 5.6. Note that there was an increase of the slope with increasing the incubation time in all gels regardless of fibroblasts type. This slope increment was observed in an increase in gel stiffness over time (Fig. 5.7).

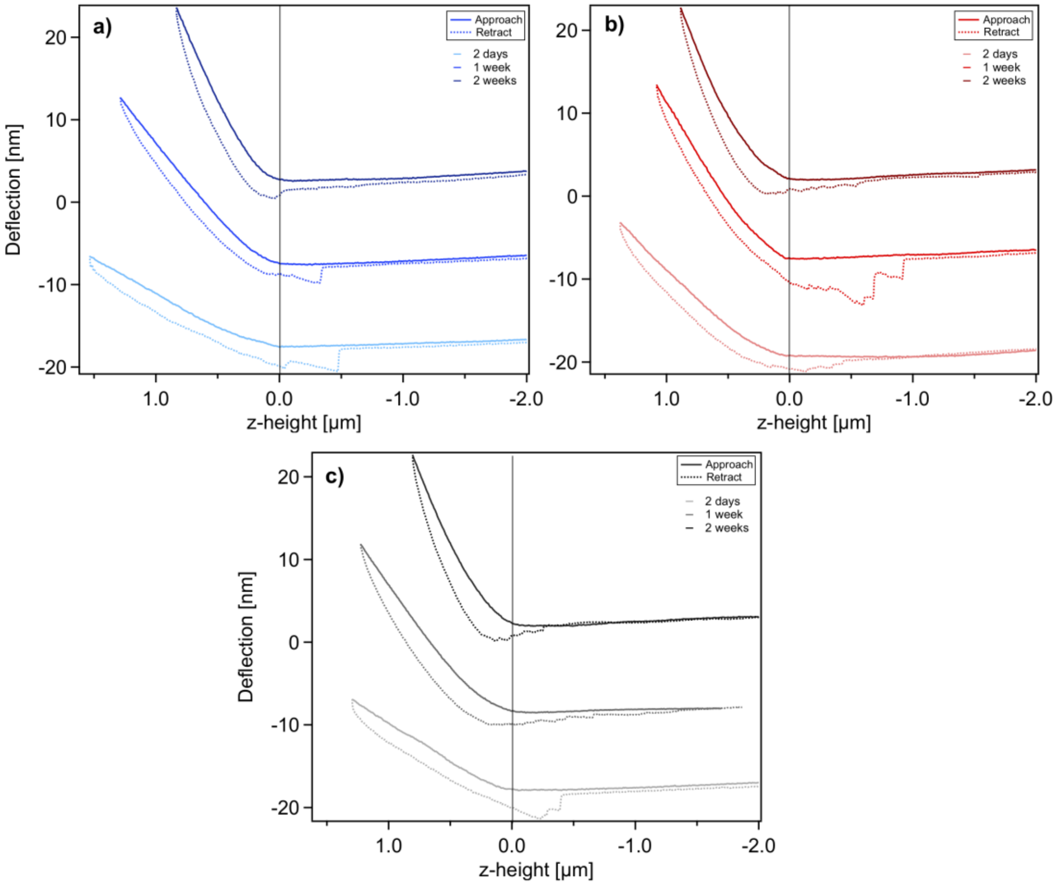

Figure 5.6 Representative force curves of gels where healthy (a), scar (b) and Dupuytren (c) were embedded. From lightest to darkest color in each graph represents gels measured after 2 days, 1 week and 2 weeks incubation time, respectively. Solid and dashed lines represent approach and retract curves, respectively.

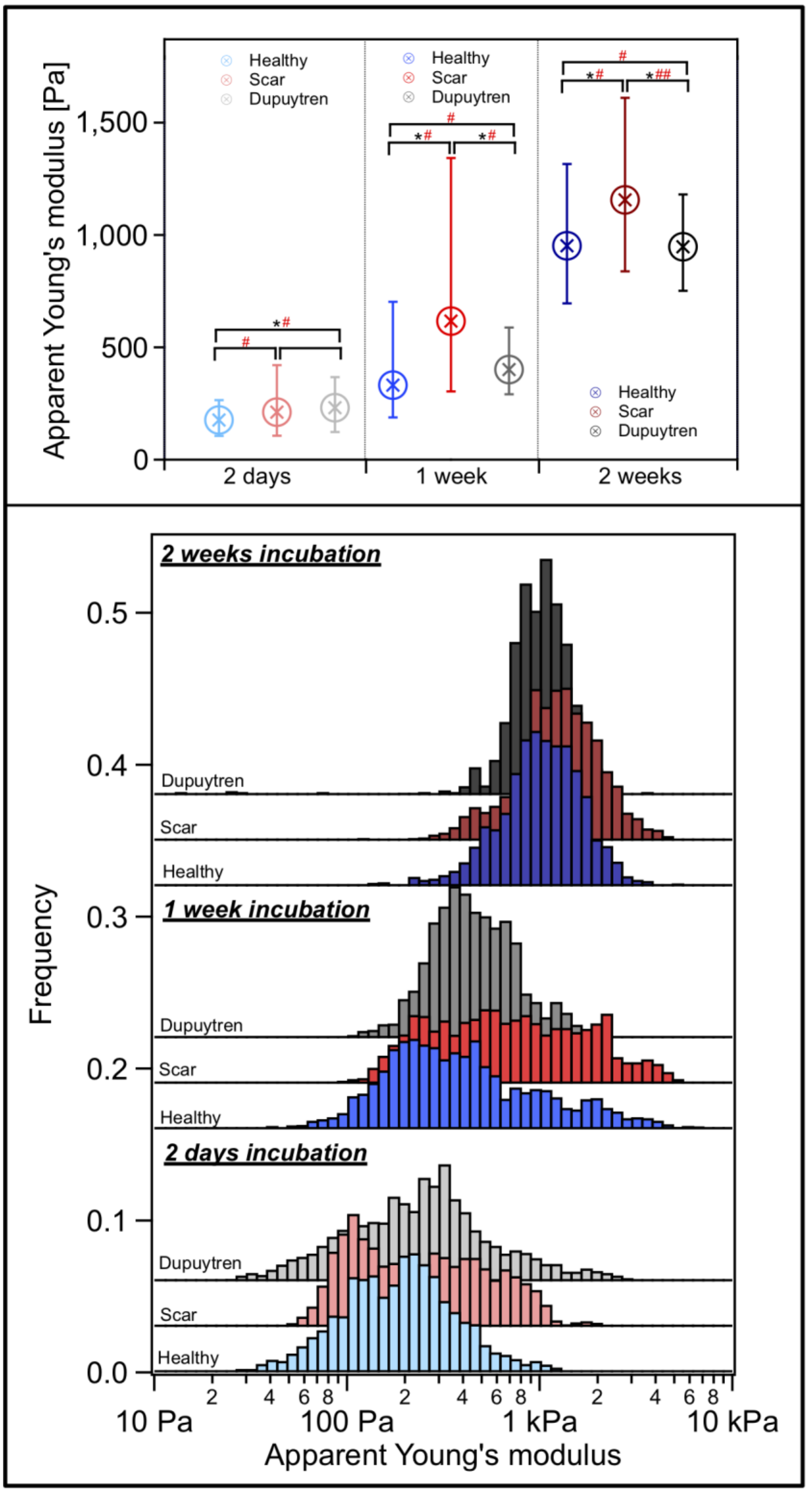

Figure 5.7 Box plot (median with 25/75 percentiles) and histogram distribution of the Apparent Young's modulus from approach curves of gels (n = 30). Data sorted by incubation time. Within each group (incubation time) each color represents one type of fibroblast embedded in the gel (blue: healthy, red: scar and black: Dupuytren fibroblasts).

The measured apparent Young's modulus of the gels went from 177 Pa (2 days) to 952 Pa (2 weeks) when healthy fibroblasts were embedded; 212 Pa (2 days) to 1156 Pa (2 weeks) for scar fibroblasts and 231 Pa (2 days) to 948 Pa (2 weeks) having Dupuytren fibroblasts embedded. Significant differences between healthy and Dupuytren gels after 2 days incubation could be seen in figure 5.7. In addition, healthy versus scar and scar versus Dupuytren gels after 1 week incubation also showed significant differences; these differences were also visible after 2 weeks of incubation. Cohen's d analysis suggested medium size effect between healthy and scar; and healthy and Dupuytren gels after 2 days of incubation. A similar medium size effect could be observed among all gels after 1 week of incubation and healthy versus scar and healthy versus Dupuytren gels after 2 weeks of incubation. Finally, scar and Dupuytren gels after 2 weeks of incubation presented a large size effect.

We used sweep frequency data to obtain the viscoelastic response of the gels in the different conditions. Frequency dependence of storage and loss moduli are displayed in figure 5.8. We could see how storage and loss modulus almost follow the same trend over all frequency range after viscous drag correction (Fig. 5.8).

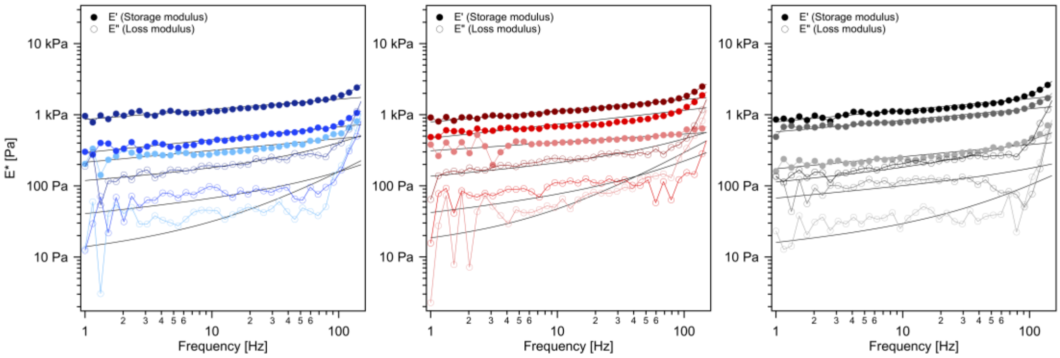

Figure 5.8 Frequency dependence of the storage modulus (filled symbols) and the loss modulus (open symbols) measured on gels in which healthy (blue), scar (red) and Dupuytren (black) fibroblasts (*n* = 30) were embedded at different oscillation frequencies (median). From the lightest to the darkest colors in each graph represents more to less incubation time (from 2 days to 2 weeks). Solid lines are the fit of the power-law structural damping model.

Storage modulus at 1 Hz versus power law exponent plot for all gels was presented in figure 5.9. We saw a tendency towards larger storage modulus values and slightly decrease in power law exponent, from 0.16 (2 days incubation) to 0.14 (2 weeks incubation) with increasing incubation time (Fig. S5.10).

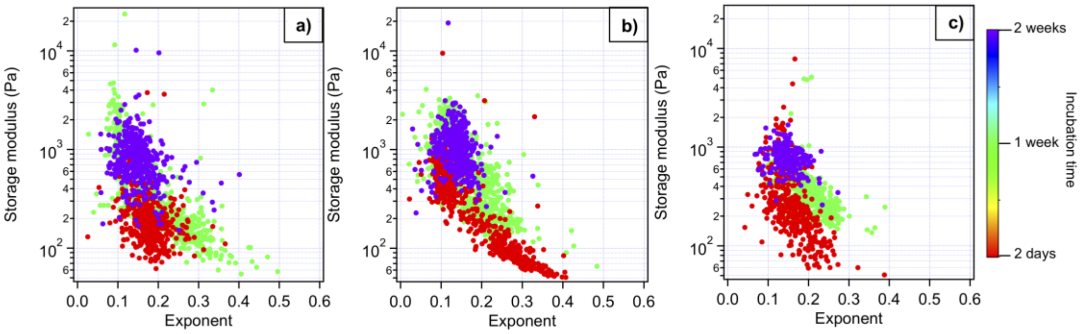

Figure 5.9 Scatterplot of storage modulus at 1 Hz versus power law exponent. Each dot corresponds to an individual force curve. a) Gels with healthy fibroblasts; b) gels with scar fibroblasts and c) gels with Dupuytren fibroblasts. Colors present gel data at different incubation times (*n* =30). Rheological properties of the gels can be seen in figures S5.7-S5.12.

There were no significant differences between gels in loss tangent parameter, presenting values close to 0.1. From less to more incubation time there was a small increase in loss tangent, related to an increase in gel viscosity (Fig. S5.9). E_0 and Newtonian viscous term (μ) values were calculated and can be seen in figure S5.11-S5.12.

Live/dead staining of cells inside the collagen gels was performed in order to evaluate cell survival inside artificial hydrogels, showing the three fibroblasts a good viability when embedded in collagen gels (Fig. S5.13). Moreover, to assess how the cell's cytoskeleton reacted to a soft 3D environment, actin fibers and nucleus were labeled (Fig. 5.10). We saw how Dupuytren fibroblasts spread faster than the other two cell types after 2 days of incubation (Figure 5.10 a,b,c); however, after 1 week and longer time periods, the three cell types seemed to stabilize, showing similar cell morphology and actin fibers distribution (Figure 5.10 d-i). Cell morphology was corroborated quantifying cell eccentricity, showing an increase in healthy and scar fibroblasts' eccentricity over time but Dupuytren fibroblasts maintained similar values throughout the incubation period (Fig. S5.14).

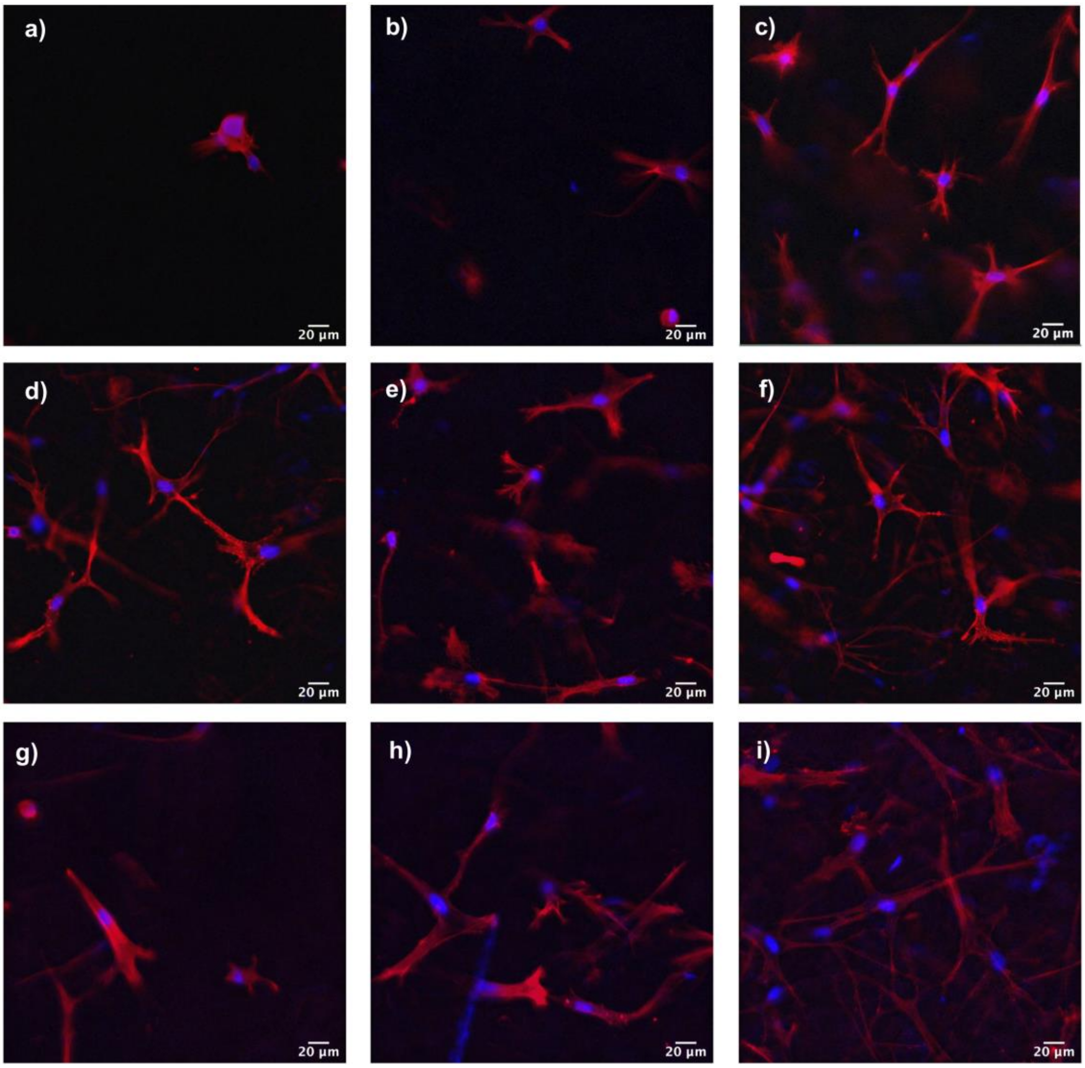

Figure 5.10 Fluorescence images of cells in 3D-collagen matrices. 2 days incubation: a) healthy, b) scar and c) Dupuytren fibroblasts; 1 week incubation: d) healthy, e) scar and f) Dupuytren fibroblasts and 2 weeks incubation: g) healthy, h) scar and i) Dupuytren fibroblasts. Actin fibers labeled in red and nucleus in blue. Scale bar: 20 µm.

We calculated the number of cells per cm^3 inside each gel to verify how cells respond to the collagen 3D environment (Table 5.2). The number of healthy fibroblasts in the gel from 2 days to 1 week increased 3-fold and continued increasing constantly, 3-fold, from 1 week to 2 weeks incubation. Scar fibroblasts duplicated faster, increasing the number of cells 5-fold after 1 week. However, this rate decreased to 3-fold from 1 week to 2 weeks incubation. Dupuytren fibroblasts duplicated a bit faster than healthy from 2 days to 1 week (4-fold) and rose from 1 week to 2 weeks (4.5-fold).

Table 5.2 Number of cells per cm^3 for each gel condition.

Incubation time	Healthy Fibroblasts	Scar Fibroblasts	Dupuytren Fibroblasts
2 days	$1.9\cdot10^6$ cells/cm^3	$2\cdot10^6$ cells/cm^3	$2.9\cdot10^6$ cells/cm^3
1 week	$6.2\cdot10^6$ cells/cm^3	$1.1\cdot10^7$ cells/cm^3	$1.1\cdot10^7$ cells/cm^3
2 weeks	$2\cdot10^7$ cells/cm^3	$3.2\cdot10^7$ cells/cm^3	$4.9\cdot10^7$ cells/cm^3

Immunostaining of the gels for fibronectin, collagen I and III was performed in combination to AFM measurements. Collagen I and III were not visible in any gel regardless of cell type and incubation time; however, differences in fibronectin secretion were observed. All cell types increased the secretion of fibronectin over time, presenting 2 weeks incubation the strongest signal (Fig. 5.11). 2 weeks incubation gels, in which Dupuytren fibroblasts were embedded, presented a slightly increase in fibronectin signal intensity. Besides, fibronectin signal was stronger on the upper layer of the gels, probably due to the impediments of the antibodies to diffuse within the gel.

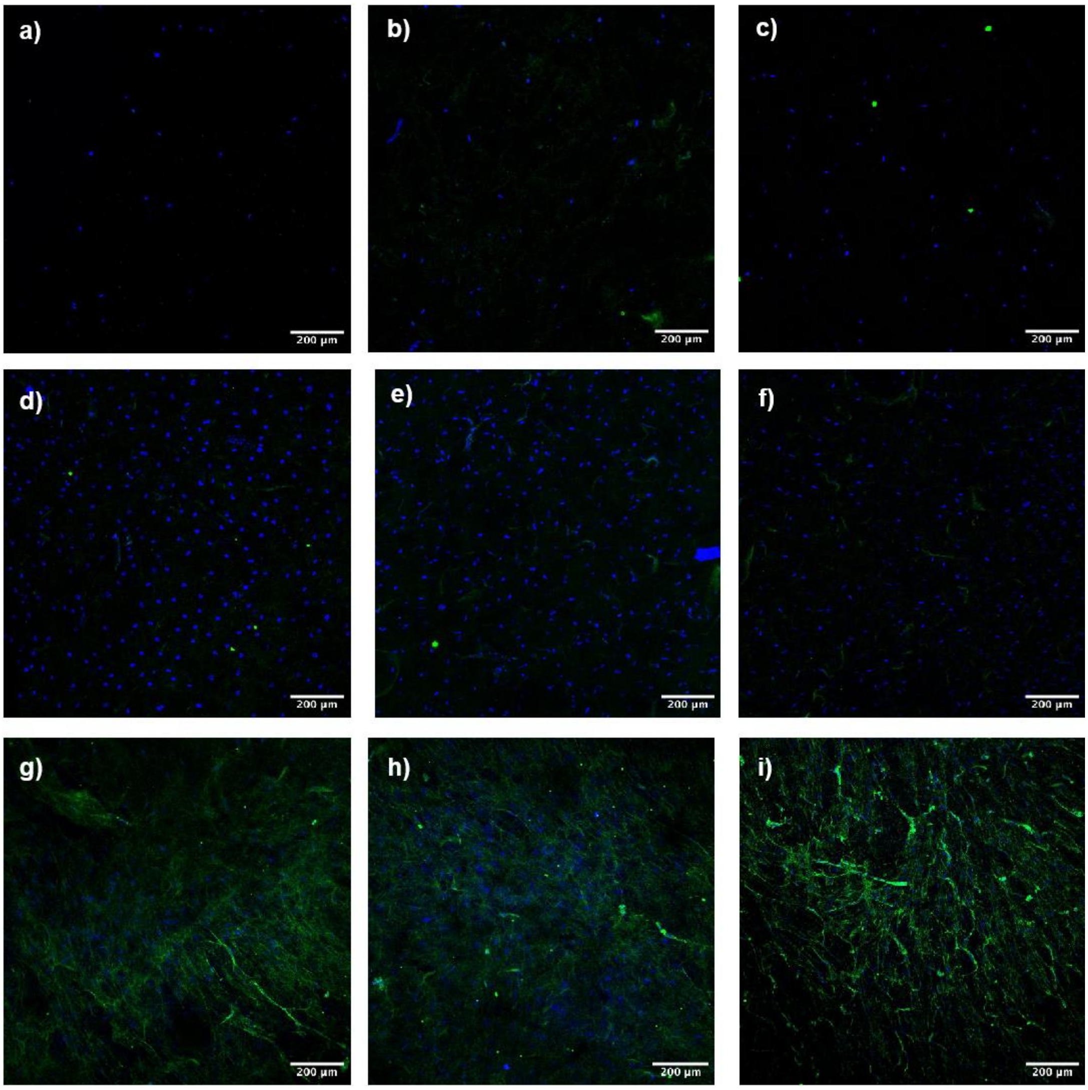

Figure 5.11 Fluorescence images of the 3D-collagen gels presenting fibronectin labeling in green and cell's nucleus in blue (scale bar: 200 µm). 2 days incubation: a) healthy, b) scar and c) Dupuytren fibroblasts; 1 week incubation: d) healthy, e) scar and f) Dupuytren fibroblasts and 2 weeks incubation: g) healthy, h) scar and i) Dupuytren fibroblasts.

5.4 Discussion

Collagen is the most abundant structural protein in the ECM and it is found in connective tissue such as cartilage, tendons, ligaments and skin. Fibroblasts are responsible of producing and remodeling collagen that is secreted to the ECM via exocytosis. It has been observed that artificial collagen gels use to be much softer than tissues or cells, and it may be due to lower amount of crosslinking between filaments in these artificial gels and the absence of a mixture of proteins that provide distinct strength. Different approaches were used to increase collagen gels stiffness - apart from increasing the concentration - and the most employed one is to use a photocrosslinker that increment the number of crosslinks between collagen fibers, leading to a certain increase in gel stiffness. We used methacrylic anhydride and Irgacure and reached a 10-fold increase in apparent Young's modulus with respect to the untreated collagen gel (soft collagen). How ECM mechanics and biochemical composition influences the cell's mechanics is an important issue; therefore, the substrates used in this work can span a broad fibroblasts response due the different mechanical and biochemical composition.

In our experiments, we varied two experimental parameters: cell type and substrate stiffness, which resulted in a highly complex and interesting research project; therefore, it is possible to discuss it in two different ways. By focusing on individual fibroblast types seeded in different substrates, we saw that healthy and scar fibroblasts presented a similar response when changing the stiffness of the underlying support; showing slightly higher apparent Young's modulus when seeded on soft collagen but they stayed almost unaltered when cultured in the methacrylated collagen and petri dish. These results may suggest that healthy and scar fibroblast present a similar phenotype and they react similarly to changes in substrate stiffness. This is an interesting finding, since it is unclear if scar fibroblasts resemble more healthy-like or pathological-like fibroblasts's behavior. However, although Dupuytren fibroblasts also presented larger apparent Young's modulus when seeded on soft collagen gels with respect to methacrylated collagen gels, its mechanical properties in hard petri dishes surpassed the rest, which corroborate their myofibroblast phenotype. Myofibroblasts are contractile fibroblasts developed in wound healing and facilitate wound closure (Hinz, 2007, 2016; Baum and Duffy, 2011); thus, Dupuytren fibroblasts' response to substrate stiffness is linked to the wound healing process. It may be noted that soft and methacrylated collagen gels present not only differences in stiffness but also in biochemical composition, therefore, changes in fibroblasts' mechanics may not only depend on the stiffness of the underlying support but also on the biochemical composition. In fact, all fibroblasts displayed a decrease in stiffness when plated on methacrylated collagen, which may be due to the toxicity of methacrylate groups, to which cells were exposed. Previously, physiological matrices with different protein content as well as different stiffness were used to study fibroblasts response (Viji Babu *et al.*, 2019). Pathological fibroblasts remodeled the ECM, leading to a stiffening of the matrix but healthy fibroblasts softened it. The matrices employed in the latter work presented more than one ECM protein; however, in our case, collagen I was the only ECM protein employed. We believe that our experimental setup provides clearer results regarding cell response to ECM stiffness because only one parameter is being investigated at the same time, which is ECM stiffness and the biochemical composition is not different enough to play a key role in our experiments. By looking at cells' responses to the same substrate, curious results were obtained. In both collagen gels, fibroblasts followed the same distribution, in which all fibroblasts presented close values in terms of apparent Young’s modulus. Nonetheless, when cells were plated on hard petri dishes, an increased tendency towards larger apparent Young’s modulus values from healthy to Dupuytren fibroblasts were observed. The mechanical stress of a matrix is transmitted to the cell through integrins that connect the ECM to the cell actomyosin network via focal adhesion complexes (Lehenkari and Horton, 1999; Critchley, 2000; Wehrle-Haller, 2012). Myofibroblasts present mature focal adhesion complexes that connect the cell cytoskeleton to the ECM and are essential for cell attachment; thus, they are more sensible to changes in ECM stiffness. The tendency towards larger apparent Young’s modulus values in fibroblasts seeded in hard petri dishes is related to the myofibroblast phenotype expressed by Dupuytren fibroblasts that adapt to variations in the mechanical properties of the surrounded environment. These results are consistent with previous findings, in which Dupuytren fibroblasts modified their mechanics according to the stiffness of PA gels (Viji Babu *et al.*, 2018).

Frequency dependence of storage and loss modulus of all fibroblasts in all substrates present the same distribution, storage and loss modulus showing the same frequency dependence up to ≈ 10 Hz; however, loss modulus present a more marked frequency dependence at higher frequencies. Hydrodynamic viscous drag was corrected; therefore, the more marked increase in loss modulus over frequency is an intrinsic behavior of cells. Cell viscosity is governed by internal friction of micro- and macromolecules sliding in the cytosol. Molecules of different dimensions contribute differently to the viscous response, being largest molecules the ones that contribute most (Kalwarczyk *et al.*, 2011). Surprisingly, power law exponent and loss tangent values were constant across all cells and substrates. Fibroblasts solid-like behavior does not vary depending on the substrate stiffness, displaying close loss tangent values on soft collagen gels and hard petri dishes. These values corroborate the altered cell behavior in soft collagen gels that is similar to that in hard petri dishes, suggesting that substrate stiffness is not the only parameter governing cell mechanics, but that other hidden mechanisms are probably at play.

It is often possible to correlate cell mechanics to cell morphological changes; e.g. cells presenting elongated and spread shapes usually display higher apparent Young’s modulus that is related to the cytoskeleton development. It was known that cells increase their spreading with increasing the stiffness of the support, expecting to see higher cell spreading in petri dish substrates (Chopra *et al.*, 2011). Cells plated in soft ECM functionalized PA gels (few hundreds of Pa), remain little spread with a rounded shape (Yeung *et al.*, 2005; Ulrich, De Juan Pardo and Kumar, 2009). The three fibroblasts investigated in this work presented similar morphology and cytoskeleton organization in the different substrates regardless substrate stiffness. Although cells displayed a more orientated/aligned shape on soft collagen gels, cell spreading did not differ substantially among the different substrates. Cell eccentricity was calculated and surprisingly, the larger values were displayed by fibroblasts seeded on soft collagen gels. This cell behavior on soft collagen gels was also shown in 3T3 and MKF fibroblasts that presented similar morphological properties in compliant collagen gels and rigid glass substrates (Ali, Chuang and Saif, 2014).

Cell's natural environment provides of 3D dimensionality as they are wrapped in ECM that restricts cell mobility and spreading, and causing a downstream signaling pathway within the cells that activates biochemical and biophysical cues that may lead to a cell response and therefore changes in cell mechanics. Changes in cell mechanics are also transmitted to the ECM, generating ECM release/contraction or changes in ECM composition and/or organization. To provide the cells of these 3D environmental stimuli, fibroblasts were embedded in soft collagen gels. Gels were anchored to coverslips since gelation was performed directly on them, thus subjecting them to an additional tension. Our experimental setup resembles to the anchored matrix contraction model, in which 3D collagen gels are attached to a surface for up to a certain time period allowing possible myofibroblast generation and then the gel is released from the surface. This model is needed when myofibroblast differentiation wants to be study. The free-floating model does not provide sufficient tension to stimulate myofibroblast differentiation; thus, it is really important to choose the appropriate model for the desired results. Matrix dimensional changes to assess fibroblasts tension generation have been studied using light microscopy or optical coherence tomography (OCT) and anchored collagen matrix model (Vaughan *et al.*, 2019). In our experimental work, changes in gels mechanical properties were assessed using the AFM. AFM allows us to obtain a quantitative measure of gel's tensional variations rather than changes in matrix's dimensions. Gel contraction occurs as a consequence of motile activity by cells trying to migrate through the matrix, termed tractional remodeling. Moreover, gel contraction also occurs as fibroblasts spread, duplicate and elongate, as they first organize proximal collagen fibrils and subsequently these tractional forces are propagated throughout the entire collagen fibril network, resulting in the whole matrix contraction (Grinnell, 1994; Rhee and Grinnell, 2007; Vaughan *et al.*, 2019). Changes in gel stiffness over time were expected; however, surprisingly, there were no big differences in apparent Young's modulus among gels populated by the different fibroblasts. We may see a small difference in apparent Young's modulus between healthy and Dupuytren gels (being the latest slightly stiffer) after 2 days of incubation. This is understandable since Dupuytren fibroblasts present more spread morphology than healthy fibroblasts and cell density is larger by a million cells, increasing cell-ECM contraction. However, after 2 weeks of incubation, gels' stiffness stabilizes, displaying no differences among the different fibroblasts.

We would have expected to see differences between gel stiffness when different types of fibroblasts were inserted; however, that is not the case in our results. A possible explanation may be that the number of cells inserted was not enough to produce a readable gel contraction and change in stiffness or the stiffness of the gel itself was low to activate cell's response. Besides, it could also be that the technology employed to characterize it (AFM) was not the most appropriate. AFM technique allows the use of cantilevers of different geometries and dimensions. We employed a spherical tip with a 5.5 μm radius, considering it a good compromise between spatial resolution and large scan size. Moreover, a large tip radius, like the one we use, needs to apply large forces to reach reasonable indentation depths. Even then, since our hydrogels have around 250 μm thickness, the AFM tip only records surface responses, which may not be sufficient to get a good value for the general gel stiffness.

Rheological properties of the gels were measured and the frequency dependence of the storage and loss modulus showed almost identical distribution. Loss modulus is almost 10-fold smaller than the storage modulus, indicating that these gels have properties close to pure elastic materials due to the low viscous contribution they have in comparison to cells. After 10 Hz, loss modulus distribution does not show same frequency dependence as cells. The more marked frequency dependence of loss modulus shown by cells is linked to the intrinsic viscous behavior of cells related to the presence of micro and macromolecules that cause friction, like proteins and organelles in the cell's cytosol that actually is really different to the composition of the artificial collagen hydrogels. The larger the molecule, the larger the viscous contribution (Kalwarczyk *et al.*, 2011). Loss tangent values are similar in all gels at the same incubation time but there is a slight increase over time, related to an increase in the liquid-like behavior, which can be related to an increase in cell number and/or spreading. This small change in gel's loss tangent towards more liquid-like behavior resembles cell interior, in which embedded cells mimic the micro and macromolecules in the cytosol. An increment in cell number, provides an increase in frictional elements, thus in viscosity. Nevertheless, loss tangent values of the gels are still smaller than the cell's values, indicating a more elastic/solid-like behavior. Similar loss tangent values were observed in PDMS gels (Deguchi *et al.*, 2015). Storage modulus' increase of the gels over time has been seen with a rather constant power law exponent. The almost constant values of power law exponent of the gels over time suggests that gel's rheological changes after two weeks of incubation may not be sufficient to procure substantial changes that are readable with our equipment.

The large difference in cell number inside each gel does not procure substantial mechanical changes. At the longest incubation time, apart from an increase in cell number inside the gels, an increase in cell deposition on the upper layer of the gel, presenting elongated morphologies similar to the 2D images, was observed. The accumulation of cells on the top of the gels may suggest a cells' tendency not to stay inside the collagen gel, migrating to the upper layer. It may appear that the fibroblast's nature leads to leaving the resting state they acquired inside the 3D gel towards a more contractile behavior in the 2D environment, behaving similarly to wound healing process.

As above mentioned, healthy and scar fibroblasts present more rounded shape than Dupuytren fibroblasts at short incubation times (2 days). Nonetheless, at longer incubation times all fibroblasts display similar morphological features showing membrane protrusions, resembling dendritic extensions (Grinnell, 2003). Fibroblasts exhibiting dendritic/bipolar morphologies resemble fibroblasts in tissue under resting conditions (Breathnach, 1978; Salomon, Saurat and Meda, 1988; Doljanski, 2004; Goldsmith *et al.*, 2004; Langevin *et al.*, 2005) while cells with well-defined stress fibers are typically observed in 2D conditions, like in petri dishes or during activated conditions such as wound repair and fibrosis (Eckes *et al.*, 1999; Tomasek *et al.*, 2002; Desmoulière, Chaponnier and Gabbiani, 2005). Those differences in cell dendritic protrusions and well-defined stress fibers can be observed in figure 5.6 and figure 5.11, representing fibroblasts in 2D and 3D collagen matrices, respectively. Furthermore, it was observed that fibroblasts stress is linked to the stiffness of the matrix, needing a certain matrix stiffness to develop stress fibers and later on differentiate into myofibroblast phenotype (Hinz, 2007). Our fibroblasts morphological features in soft 3D collagen gels suggests that they present a resting state as the stiffness of the gel is not enough to stimulate fibroblast activation and therefore myofibroblast differentiation. Moreover, our gels' mechanical properties (too soft) do not allow distinguishing between healthy and "pathological" Dupuytren fibroblasts' contractile properties either.

AFM measurements were combined with immunostaining for fibronectin. In natural conditions, fibroblasts secrete fibronectin along with collagen I and III. The absence of collagen I and collagen III in our data, even after 2 weeks of incubation, may suggest that the formation and secretion of those proteins by fibroblasts is produced on longer time scales. Different incubation times for both primary and secondary antibodies were applied, finally improving fibronectin signals using longer incubation time periods. Protocols similar to whole mount staining, which is used for thick tissue samples such as embryos, did not provide better results, as well as sirius red staining (employed to stain and distinguish collagen from the rest of the sample components). Fibroblasts are one of the most important cells that secrete fibronectin to the matrix and it is a key factor for wound healing. Fibronectin helps in the formation of a proper matrix for cell's migration and growth during the development of granulation tissue, connective tissue. Besides collagen deposition at the wounded area is developed with the help of fibronectin. Therefore, fibronectin secretion by fibroblasts before collagen deposition is in agreement with our results. We saw how fibronectin signal increases over incubation time, from no signal after 2 days of incubation to visible fibers after 2 weeks of incubation. Moreover, gels in which Dupuytren fibroblasts were embedded seem to present clearer fibronectin filaments over the other fibroblasts. This corroborates the pathological myofibroblast phenotype of Dupuytren fibroblasts that secrete more fibronectin to the matrix than the other two cell types. Changes in fibronectin expression were also observed in cancer and its increment was seen in lung carcinoma (Han, Khuri and Roman, 2006).

5.5 Materials and Methods

5.5.1 Collagen extraction

Tails of Sprague-Dawley rats (male, 350 g) were collected as a by-product from other experiments in the animal facilities of the School of Medicine (University of Barcelona) and tendons were extracted to obtain a type I collagen solution by following the protocol by Rajan and coworkers (Rajan *et al.*, 2006). Briefly, tendons were washed with 100 % acetone and 70 % isopropanol for five minutes each. Washed tendons were then dissolved in 0.02 M acetic acid and kept for 48-72 hours at 4°C under slow stirring until complete dissolution. Collagen fibers were triturated and kept frozen at -80°C. Finally, frozen collagen was lyophilized and kept at -80°C until used. 5.5 mg/ml collagen solution in 0.02 M acetic acid was employed.

5.5.2 Gel preparation

Collagen I from rat-tail was used to generate collagen gels of different stiffness. We called "soft" to collagen gels with a concentration of 5.5 mg/ml in 0.02 M acetic acid and "methacrylated" to the methacrylated collagen. Methacrylated collagen increases its stiffness with respect to the soft collagen up to 10%. Briefly, 5.5 mg/ml collagen was mixed with 1/9 of PBS 10x and 19 μL NaOH 1M. The solution was mixed and 6 % of methacrylic anhydride (Sigma), 9 μL of Irgacure initiator (Advanced Biomatrix) and 19 μL NaOH 1M was added. The solution was vortexed and a neutral pH around 7-8 should be obtained. Collagen solution (either soft collagen or methacrylated) was poured in a hydrophilic 24 mm square coverslip and covered with a hydrophobic 22 mm ø circular coverslip to generate a flat surface and to get a homogeneous gel height. The collagen solution between the coverslips was incubated for one hour at 37°C at 5 % CO_2 for polymerization and once the gel was formed; the top coverslip can be removed adding PBS to detach it easily. Methacrylated gels then were exposed to 10 minutes UV light to increase gel stiffness.

3D-gels with cells in it were prepared as follows: first, collagen gel solution was made: 5.5 mg/ml collagen was mixed with 1/9 of PBS 10x and 19 μL NaOH 1M. The solution was vortexed and a neutral pH around 7-8 should be obtained. Then $4 \cdot 10^5$ cells/ml were prepared and added to the collagen solution. 460 μL of collagen solution were mixed with 40 μL of cells solution. The final cells' concentration used was $8 \cdot 10^5$ cells/cm^3. Then, 250 μL of the mixed solution were poured in the 24 mm square coverslips and covered with the 22 mm ø coverslips to generate a homogenous flat surface for AFM experiments. The mixture was incubated for 1 hour at 37°C and 5 % CO_2. Finally, the top coverslip was released and the gels were immersed in cell culture medium and incubated until AFM experiments were performed.

5.5.3 Coverslips functionalization

24 mm square coverslips were functionalized to make them positively charged. Coverslips were washed with 100 % ethanol and exposed to ambient air until dried. Then, they were incubated with NaOH 0.1M and (N-[3(Trimethoxysilyl)propyl]ethylenediamine) (Sigma Merck) for 3 minutes each step. Coverslips were then washed three times with milliQ water for 10 minutes each step and incubated with 0.5 % glutaraldehyde for 30 minutes. Finally, they were washed three times with milliQ water for 10 minutes each step and exposed to ambient air until they were completely dried.

22 mm ø circular coverslips were functionalized to make them hydrophobic. Coverslips were washed with 100 % ethanol and dried. Then, they were covered with sigmacote solution (Sigma) for 1 minute and washed three times with milliQ water for 10 minutes each step. Finally, the coverslips were exposed to ambient air to dry.

5.5.4 Cell culture

Three types of primary fibroblasts from the palm of the same patient who suffered from Dupuytren's disease were used in this work: healthy fibroblasts from the dermis of the palm, scar fibroblasts from a wounded area, and Dupuytren fibroblasts from the palmar fascia. All cell types were cultured in DMEM medium (containing 4.5 g/L D-glucose, FG0435, Sigma) and incubated at 37°C in a humidified atmosphere of 95 % air and 5 % CO_2. Medium was supplemented with 10 % FBS (fetal bovine serum) (F7524, Sigma) and 2 % penicillin-streptomycin (P0781, Sigma). Prior cell seeding, 2D-collagen gels were incubated with medium for 30 minutes to promote serum protein absorption on the gels, hence, cell adhesion. Cells were seeded 48 hours prior to the AFM measurements. 3D-collagen gels were incubated 2 days, 1 week or 2 weeks prior to AFM experiments. Fibroblasts between passages 8-12 were used for all the experiments. The study was conducted in accordance with the Declaration of Helsinki, and approved by the local Ethics Committee (rztekammer Bremen, #336/2012). Patient was informed pre-operatively and had given its informed consent to anonymous tissue donation.

5.5.5 AFM experiments

AFM experiments were performed with a MFP3D AFM (Asylum Research, Santa Barbara, CA, USA) to measure mechanical properties of fibroblasts in 2D- and 3D-environment. An optical microscope was combined with the AFM to be able to control tips and samples (Zeiss Axiovert 135, Zeiss, Oberkochen). PFQNM cantilevers presenting three-sided pyramidal tips with 70 nm tip radius (Bruker, nominal spring constant 100 pN/nm and 45 kHz resonance frequency in air) were used to investigate cell properties in 2D-gels. MLCT-SPH-5UM (Bruker, nominal spring constant 150 pN/nm and 17 kHz resonance frequency in air) with 5.5 μm tip radii were employed to assess gel properties in 3D-environment (fibroblasts inside the gels). Samples were fixed to an aluminum holder with vacuum grease and mounted on the AFM stage with two magnets. The entire set-up was enclosed in a home built polymethylmethacrylate (PMMA) box in order to inject and maintain 5% CO_2 during experiments.

Apparent Young's modulus values were extracted from regular force curves and sweep frequency method was used to obtain cell rheological properties. For measuring cells seeded on 2D-collagen matrices, force map scan size was 5 μm and composed of 16 or 256 force curves (4 x 4 or 16 x 16 lines per frame). Typically, force curves were recorded at a scan rate of 2 Hz; corresponding to a maximum velocity of 20 μm/s. Indentation depths were always greater than 500 nm in order to average the stiffness over a large contact area. For 3D-gels measurements, force curves were acquired over a large area 20 x 20 μm and force maps were composed of 16 or 36 force curves (4 x 4 or 6 x 6 lines per frame). Force curves were recorded at a scan rate of 1 Hz, corresponding to a maximum probing velocity of 7.94 μm/s.

5.5.6 AFM data analysis

The data analysis software IGOR (Wavemetrics, Lake Oswego, OR, USA) was used to evaluate the mechanical properties of cells in terms of apparent Young's modulus (E). The Hertzian model for spherical tips was used to calculate the apparent Young's modulus for each force curve within a force map. The median and 25/75 percentiles and logarithmic histogram of apparent Young's modulus were considered as representative modulus of each force map. Sweep frequency data were fitted with the power law structural damping model. E^* data are separated into real (in phase) and imaginary (out of phase) parts. The real part represents the storage modulus and it is a measure of the elastic energy stored and recovered per cycle of oscillation. The imaginary part depicts the loss modulus and it accounts for the energy dissipated per cycle of sinusoidal deformation. We also calculate the loss tangent, which is an index of the solid-like (<1) or the liquid-like (>1) behavior of the cell. This model assumes a storage modulus that increases with frequency following a power law with exponent α, and a loss modulus that includes a term that is a fraction η of the storage modulus and a Newtonian viscous term.

5.5.7 Live/Dead staining

After 2 days, 1 week and 2 weeks of culture, cells were stained to assess cell viability within 3D collagen gels. Live-dead kits (ThermoFisher, R37601) were used by following manufacturer instructions. Calcein AM solution was transferred to BOBO-3 Iodid solution and mixed. All content was added to the 3D-gels with the same amount of cell culture medium. Samples were incubated for 15 minutes at room temperature and finally imaged. Calcein AM provides green color to alive cells and BOBO-3 Iodid red to dead cells. Nikon Eclipse Ti Inverted epifluorescence Microscope (Nikon Instruments Inc., Melville, New York) with a 20x objective lens was used to image the samples.

5.5.8 Cells staining for morphological analysis

Cells seeded on 2D-collagen gels and petri dishes were fixed with 4% paraformaldehyde for 30 minutes and permeabilized with 0.2% Triton X100 for 5 minutes. Samples were washed with PBS after each step and then incubated with 10% FBS for 30 minutes at room temperature. ActinRed (Invitrogen, ready probes) was used to label actin fibers and NucBlue (Invitrogen, ready probes) for nuclear staining, two drops of each solution was added to 1 mL PBS and then incubated for 30 minutes at room temperature. After three times washing with PBS, cells were finally stored in PBS at 4°C prior to image acquisition. Nikon Eclipse Ti Inverted epifluorescence Microscope (Nikon Instruments Inc., Melville, New York) with a 40x objective lens was used to observe cells and collect fluorescent images.
Eccentricity of the cells was computed by adjusting an ellipse to the polygon described generated by ImageJ software, as described in (Klinker *et al.*, 2017). Cell number inside each 3D collagen gels was obtained counting the number of nucleus in each z-stack layer using Image J software.

5.5.9 Gel immunostaining

3D-gels were stained for fibronectin to assess the secretion of ECM proteins by the different fibroblasts. Samples were fixed with 4% PFA for 30 minutes at room temperature. Samples were then blocked with PBS, 0.4 % Triton and 10 % donkey serum solution for one hour at room temperature. Primary antibody against fibronectin (mouse anti-fibronectin, 1:50, ThermoFisher, CSI 005-17-02) was incubated in a solution of PBS, 0.4 % Triton and 0.1 % donkey serum for 24h at room temperature. The samples were rinsed three times with the same solution. Hoechst 33342 (1:1000, A-21202 Invitrogen) was used to visualize cell nucleus and secondary antibody (donkey anti-mouse AlexaFlour 488, 1:1000, H3570 Invitrogen) was incubated in PBS and 0.4 % Triton for 2 h at 37°C. Three times rinsed with PBS were applied to eliminate unbound secondary antibodies. Olympus FluoVIEW 3000 RS confocal microscope with 10x and 20x objective lens was used to acquire images.

5.5.10 Statistical analysis

Differences between the apparent Young's modulus and rheological parameters of different cells or gels were determined with Wilcoxon signed-rank test and Cohen's d test using IGOR. P-values obtained from Wilcoxon signed-rank test, * indicating $p < 0.01$ and Cohen's d test with # indicating $0.2 < d < 0.5$ and ## indicating $d > 0.5$.

5.6 Conclusion

The modulation of the mechanical properties of collagen gels was possible thanks to the addition of methacrylic anhydride, a crosslinker that increases the number of crosslinks between collagen fibers leading to an increase of the gel's stiffness. Healthy and scar fibroblasts behaved similarly when changing the mechanical properties of the underlying support, suggesting that the scar fibroblasts' mechanical properties under these specific conditions resembled more those of healthy fibroblasts. Moreover, the apparent Young's modulus of these fibroblasts when seeded on soft collagen gels was similar or even higher than when seeded on hard Petri dishes. However, Dupuytren fibroblasts modified its stiffness to that of the substrate, supporting its myofibroblast phenotype. Furthermore, the morphology of fibroblasts in soft collagen gels closely resembled that in hard Petri dishes, suggesting that the morphological and mechanical properties of our fibroblasts are not only influenced by the substrate's stiffness but also by the biochemical composition. The different fibroblast types embedded in soft 3D-collagen gels did not produce large differences in gel mechanical properties; thus, gel tension. Dupuytren fibroblasts spread faster at shorter time periods; nevertheless, at longer time periods all fibroblasts presented similar morphology and contraction properties. The stiffness of the 3D collagen gels prepared was not sufficient to activate the contractile properties of fibroblasts; hence, cells did not differentiate to myofibroblasts; thus, the fibroblasts presented dendritic protrusions as if they were in resting state. This study corroborates the fact that myofibroblast differentiation is governed by changes in the stiffness of the surrounding environment and is facilitated by stiffer environments. Our study encompasses a wide range of cell response, from 2D to 3D environment, increasing the resemblance of tissue-like conditions, which is closer to the cell's natural environment. We believe that artificial hydrogels made of some representative ECM protein, such as collagen, are a good compromise to study cell behavior in 3D.

5.7 Author contributions

S.P-D. designed the experimental scheme and performed AFM measurements, data analysis, collagen gels preparation, cell's fluorescent images in 2D and 3D and manuscript preparation. H.S.F. helped obtaining collagen from rat-tails, preparing collagen gels and manuscript preparation. L.M.V. helped establishing gel's immunofluorescence protocol, analysis of gel’s immunofluorescence data and manuscript preparation. M.A. helped establishing gel’s immunofluorescence protocol, analysis of gel’s immunofluorescence data and manuscript preparation. J.O. helped obtaining collagen from rat-tail, collagen gel’s protocol and manuscript preparation and M.R. helped designing the experimental scheme, data analysis and manuscript preparation.

5.8 Acknowledgements

We would like to thank Cesare Covino for acquiring gel’s immunofluorescence images. We would like to thank Prof. Ursula Mirastschijski for providing tissue samples and Prof. Gazanfer Belge for stabilizing cell lines from primary cells. We would like to thank Nina Messerschmidt for the help in sample preparation. We would also like to thank the Biophysics and Bioengineering unit of the Medicine department at the University of Barcelona for providing rat-tails to obtain collagen. We would also like to thank Prof. Dorothea Brüggemann for the use of the epifluorescence microscope and Dr. Arundhati Joshi and Dr. Deepanjalee Dutta for the helpful discussions and suggestions.

5.9 Funding

This project has received funding from the European Union’s Horizon 2020 research and Innovation programme under the H2020-MSCA-ITN-2018 Grant Agreement No. 812772.

The authors acknowledge Euro-BioImaging (www.eurobioimaging.eu) for providing access to imaging technologies and services via the Italian Node (ALEMBIC, Milan, Italy).

5.10 Institutional Review Board Statement

The study was conducted in accordance with the Declaration of Helsinki, and approved by the local Ethics Committee (rztekammer Bremen, #336/2012.)

5. 11 Informed Consent Statement

Patient was informed pre-operatively and had given its informed consent to anonymous tissue donation.

5.12 Supporting information

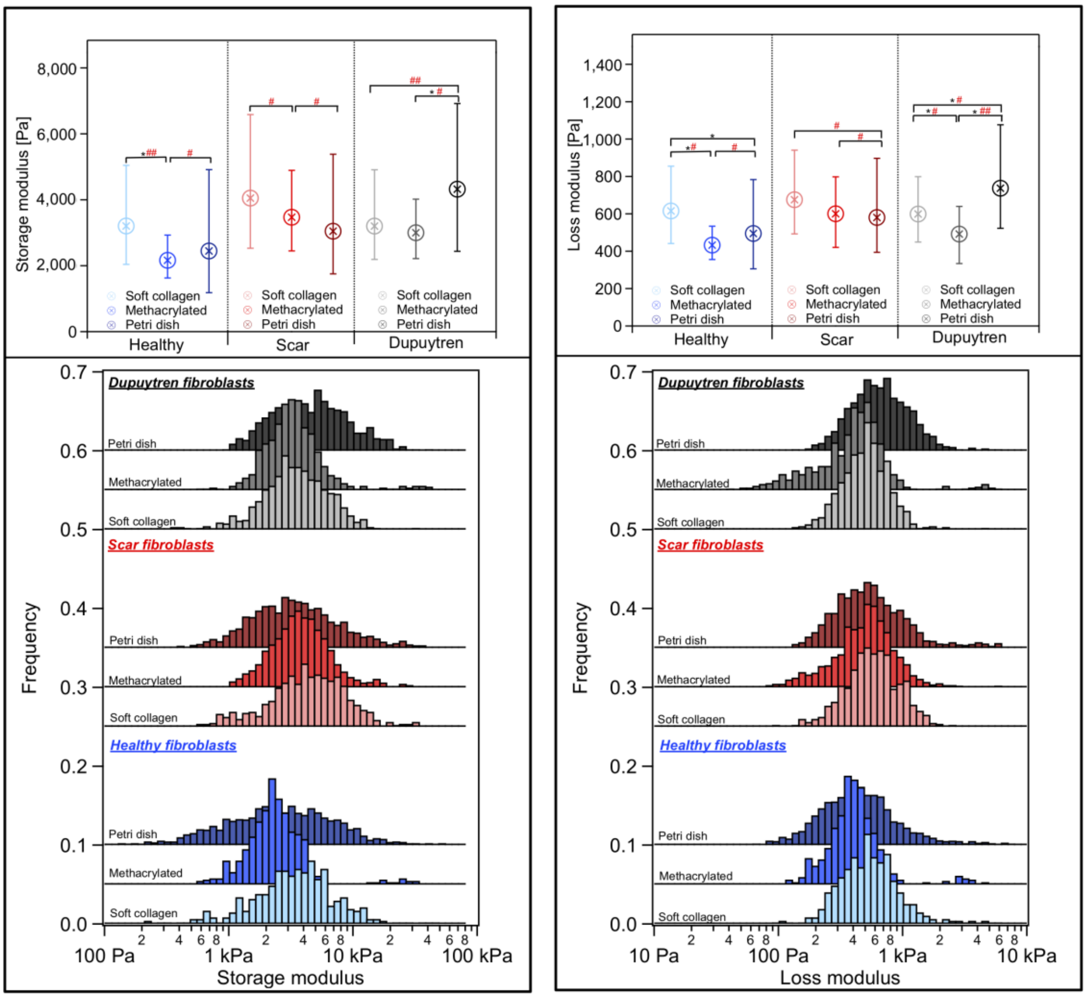

Figure S5.1 Box plot (median with 25/75 percentiles) and histogram distribution of storage and loss modulus at 1 Hz ($n = 50$). Data are sorted by cell type and within each group each color presents one type of substrate (from lightest to darkest: soft collagen to petri dish).

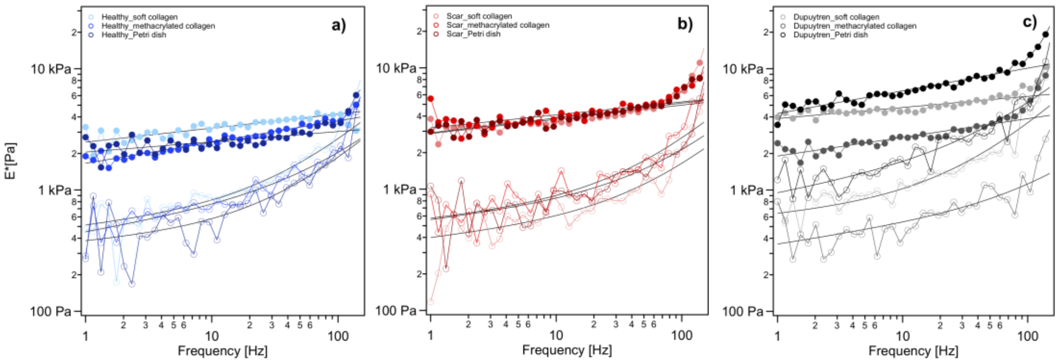

Figure S5.2 Frequency dependence of storage and loss modulus after hydrodynamic viscous drag correction. Close symbols represent the storage modulus and the open symbols the loss modulus. a) Healthy fibroblasts, b) scar fibroblasts and c) Dupuytren fibroblasts. From lightest to darkest color in each graph represents fibroblasts seeded on soft collagen to Petri dish (*n* = 50).

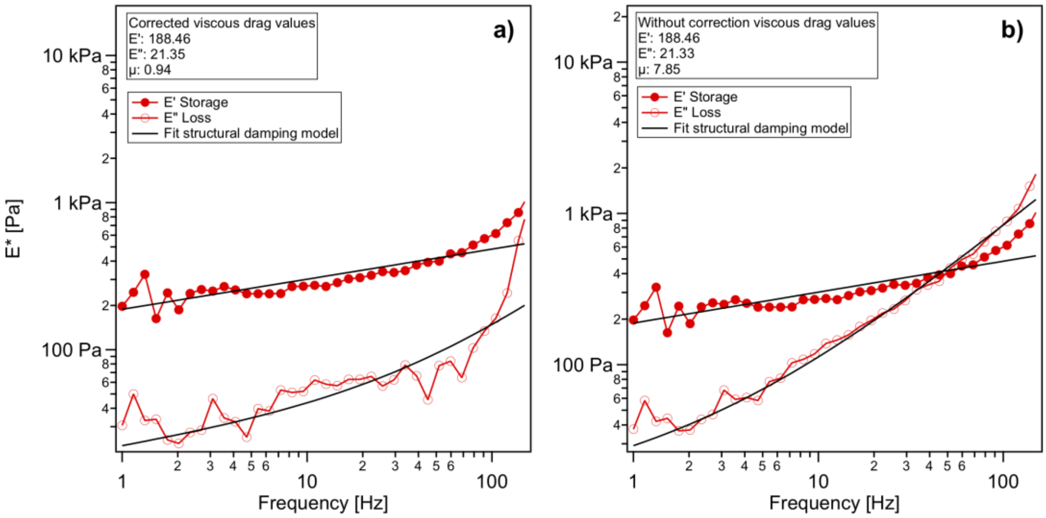

Figure S5.3 Representation of E* values over frequency, corrected for the viscous drag (a) and without correction (b).

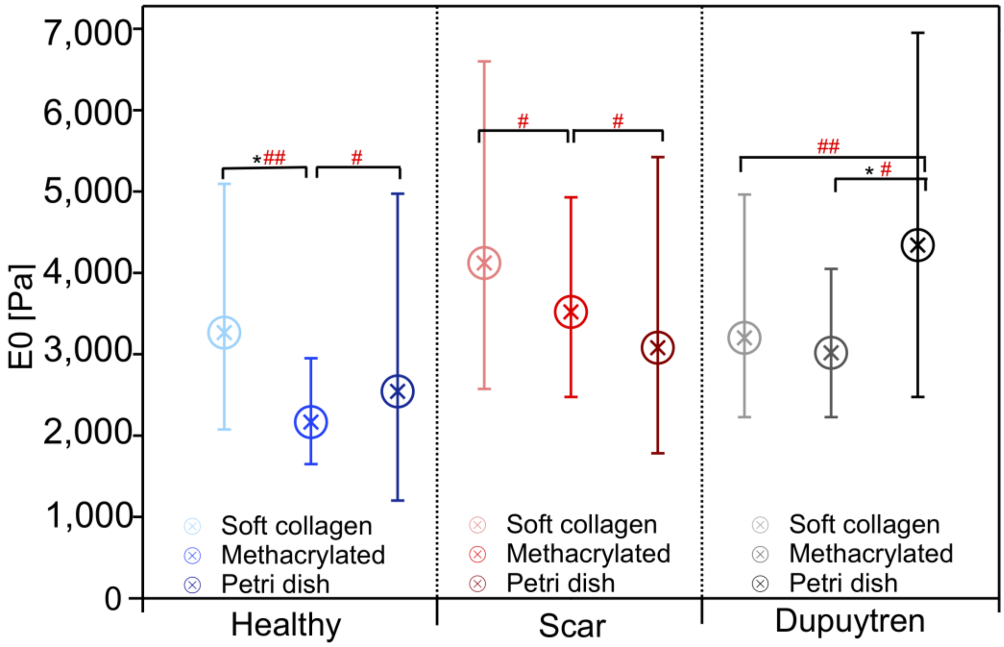

Figure S5.4 Box plot (median with 25/75 percentiles) of E_0 (*n* = 50). Data are sorted by cell type and within each group each color presents one type of substrate (from lightest to darkest: soft collagen to petri dish).

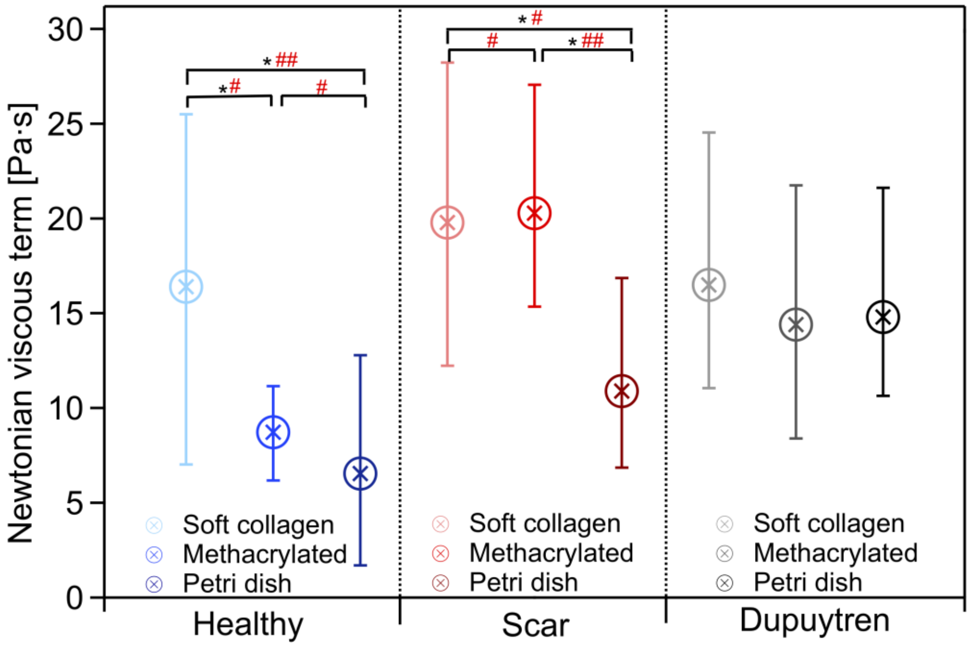

Figure S5.5 Box plot (median with 25/75 percentiles) of μ ($n = 50$). Data are sorted by cell type and within each group each color presents one type of substrate (from lightest to darkest: soft collagen to petri dish).

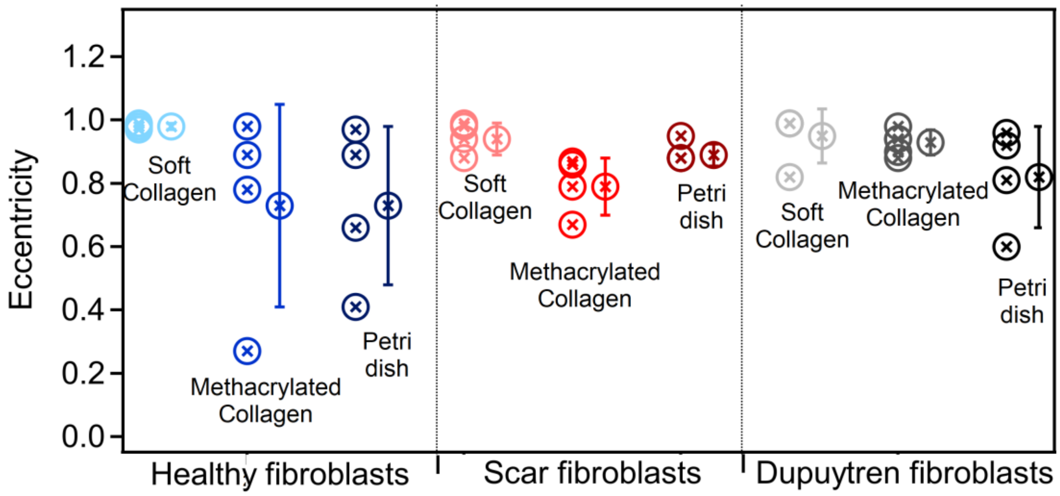

Figure S5.6 Quantification of cell eccentricity to characterize their morphology. Mean ± standard deviation; symbols with the same color next to the mean value correspond to the individual measurements. Data are sorted by cell type and within each group each color presents one type of substrate (from lightest to darkest: soft collagen to petri dish).

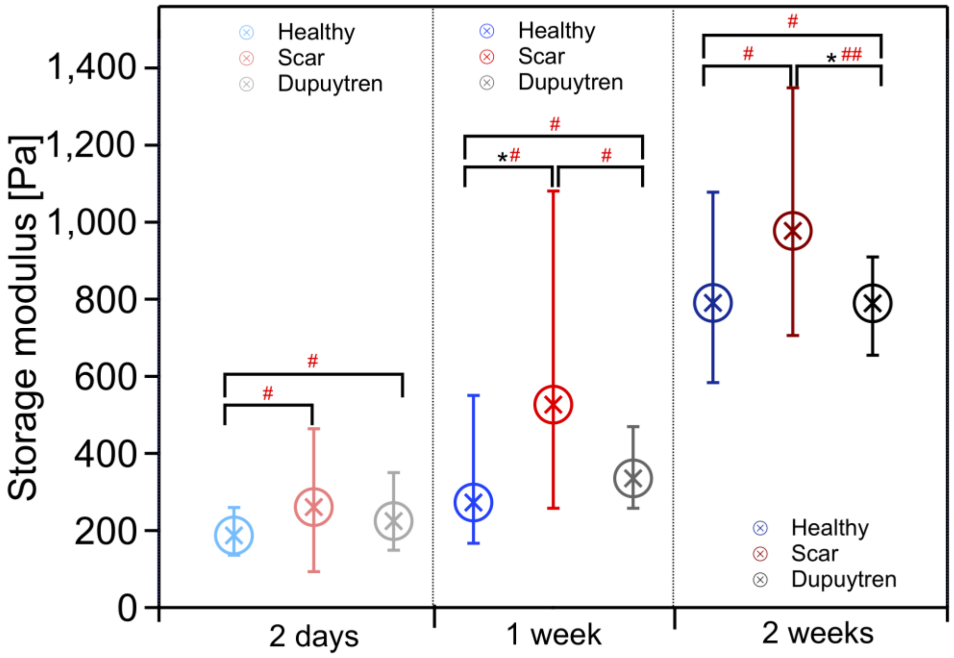

Figure S5.7 Box plot (median with 25/75 percentiles) of E', storage modulus at 1 Hz (*n* = 30). Within each group (incubation time) each color presents one type of fibroblasts (blue healthy, red scar and black Dupuytren fibroblasts).

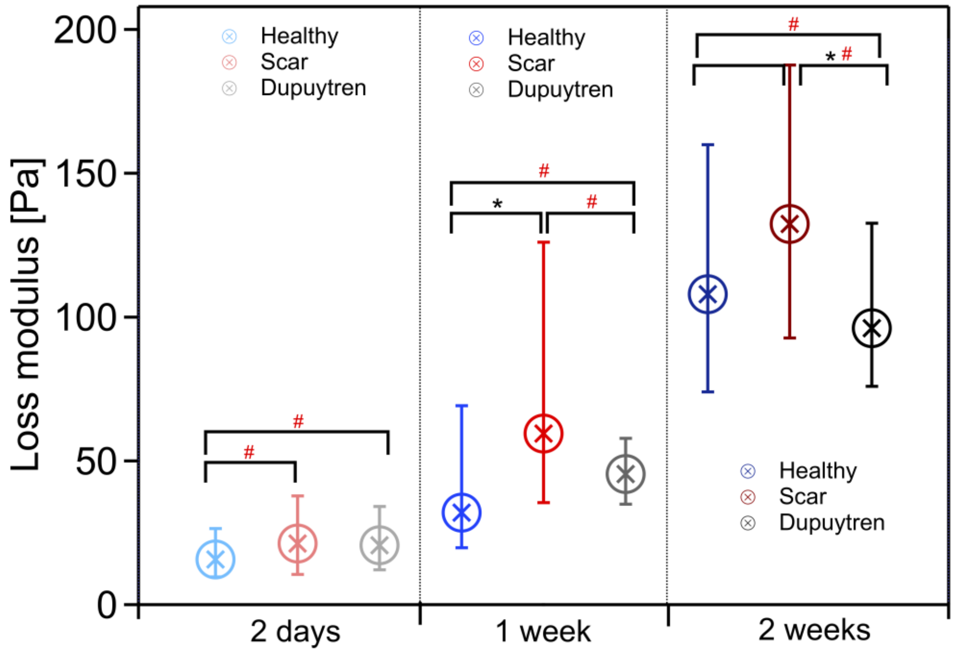

Figure S5.8 Box plot (median with 25/75 percentiles) of E", loss modulus at 1 Hz (*n* = 30). Within each group (incubation time) each color presents one type of fibroblasts (blue healthy, red scar and black Dupuytren fibroblasts).

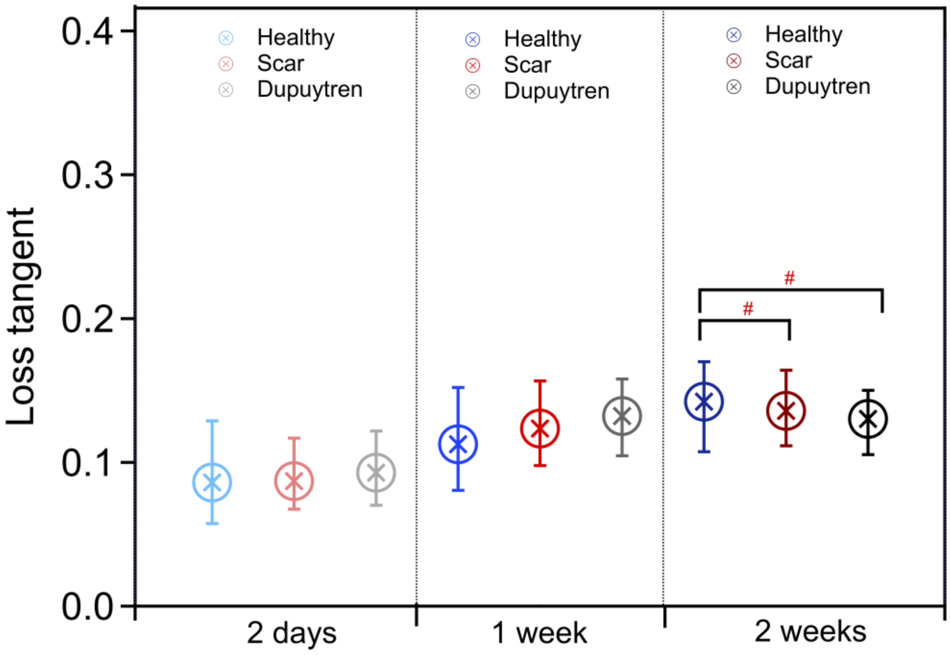

Figure S5.9 Box plot (median with 25/75 percentiles) of η, loss tangent at 1 Hz (n = 30). Within each group (incubation time) each color presents one type of fibroblasts (blue healthy, red scar and black Dupuytren fibroblasts).

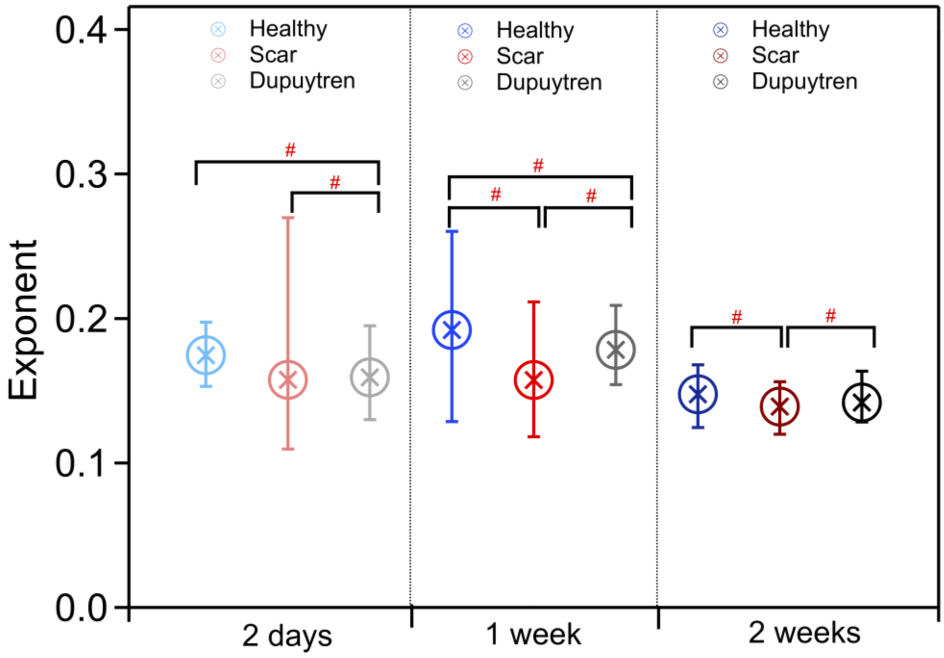

Figure S5.10 Box plot (median with 25/75 percentiles) of α, exponent (n = 30). Within each group (incubation time) each color presents one type of fibroblasts (blue healthy, red scar and black Dupuytren fibroblasts).

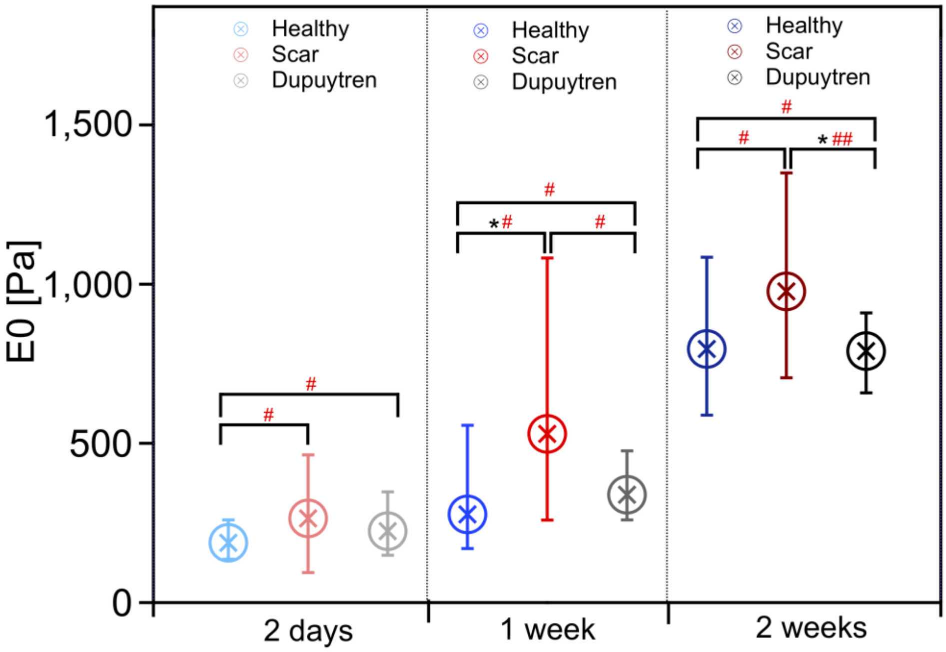

Figure S5.11 Box plot (median with 25/75 percentiles) of E_0 ($n = 30$). Within each group (incubation time) each color presents one type of fibroblasts (blue healthy, red scar and black Dupuytren fibroblasts).

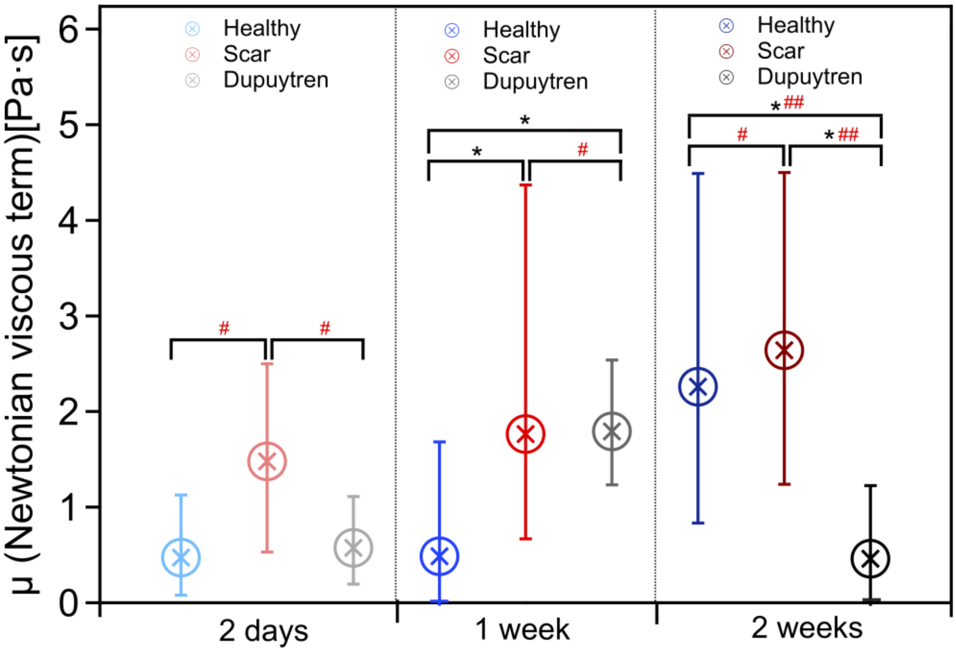

Figure S5.12 Box plot (median with 25/75 percentiles) of μ ($n = 30$). Within each group (incubation time) each color presents one type of fibroblasts (blue healthy, red scar and black Dupuytren fibroblasts).

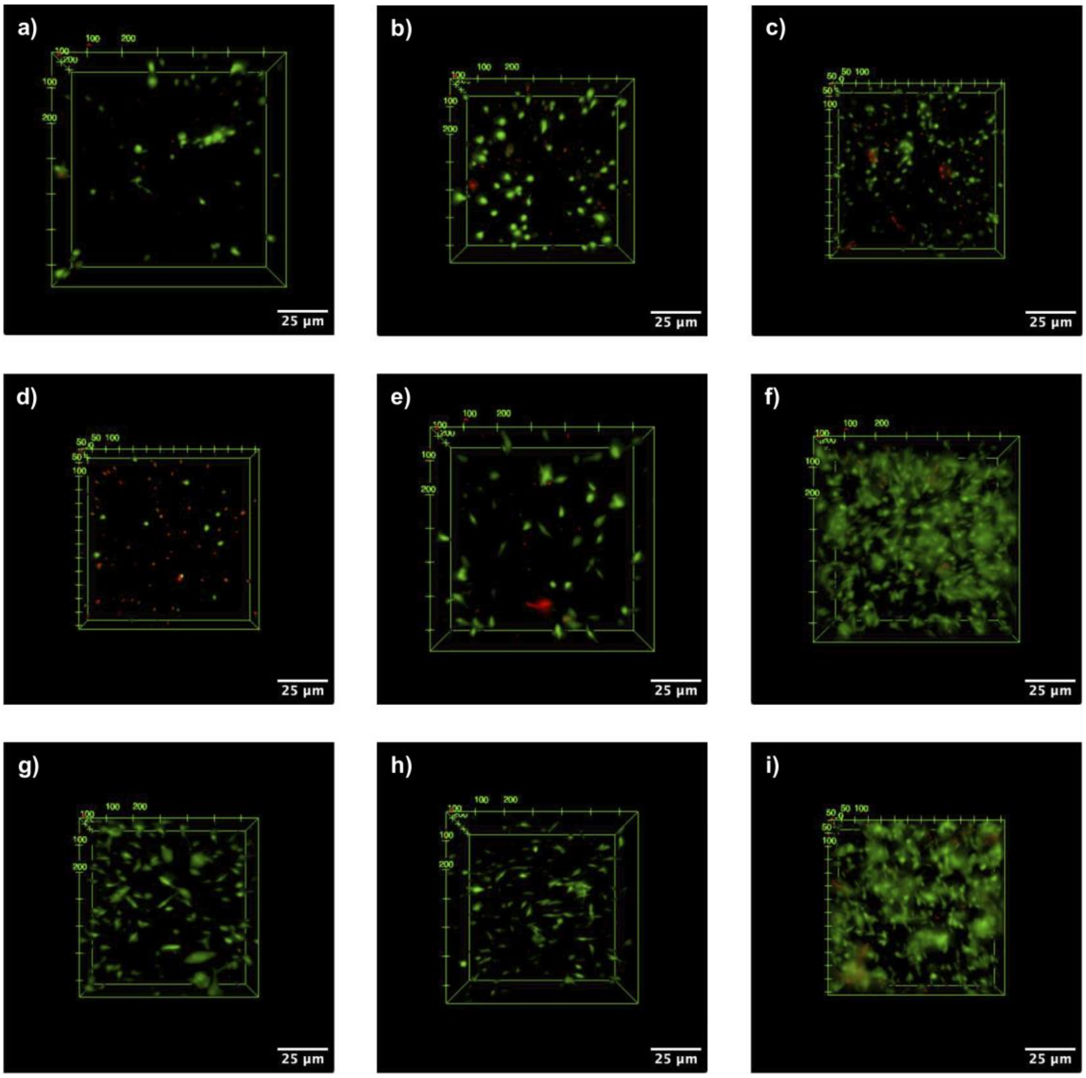

Figure S5.13 Live/dead staining of fibroblasts in all gel conditions. Alive cells are labelled in green and dead cells in red. 2 days incubation: a) healthy, b) scar and c) Dupuytren fibroblasts; 1 week incubation: d) healthy, e) scar and f) Dupuytren fibroblasts and 2 weeks incubation: g) healthy, h) scar and i) Dupuytren fibroblasts. Scale bar: 25 µm.

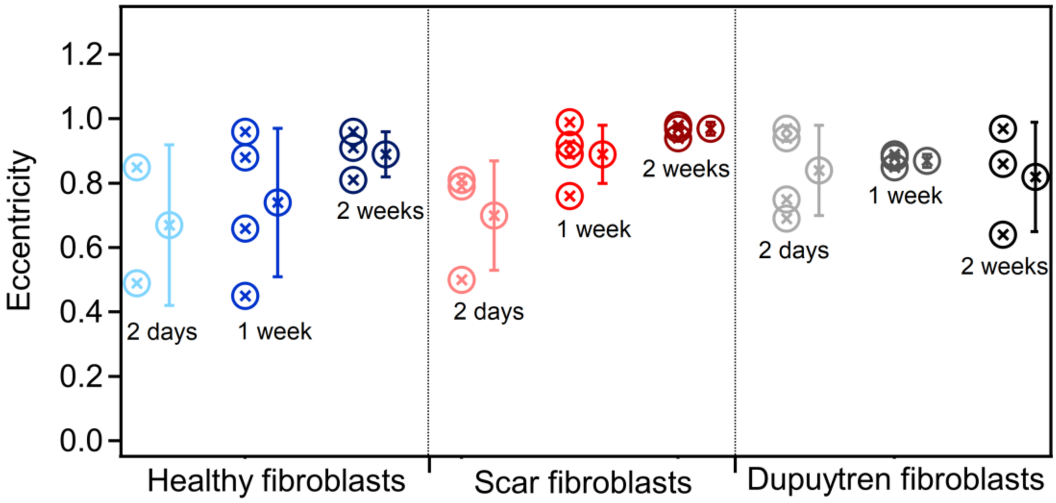

Figure S5.14 Quantification of cell eccentricity to characterize their morphology. Mean ± standard deviation; symbols with the same color next to the mean value correspond to the individual measurements.

Chapter 6

Conclusions and future perspectives

6.1 General conclusions about the research experiments

The general aim of this thesis was to study the differences between three primary fibroblasts from the Dupuytren's disease in different environments and conditions using mostly AFM supported by other techniques like immunofluorescence.

The three primary cell types were obtained from different tissue samples from the palm of the same patient who suffered from Dupuytren's disease. In previous studies in our laboratory, it has been identified the different nature of the three samples, showing healthy fibroblasts phenotype for the cells subtracted from dermal regions of the palm, ambiguous behavior of the cells subtracted from the scar tissue and myofibroblast phenotype for the cells obtained from the nodules of the palmar fascia. Knowing the differences between the cell types, different strategists were applied to learn more about the disease and to disentangle new scientific problems.

Cell mechanics have been used for many years to obtain information about cell characteristics linked to mechanical properties. Lekka et al. were the first to use it as a diagnostic tool to distinguish between healthy and cancerous cells, discovering the softer nature of cancerous cells on hard supports (glass and plastic cell culture dishes) (Lekka et al., 1999). Since then, cell mechanics has become a useful methodology to study many cell behavior at single cell level, such as diseased cells response under pharmacological treatments. As mentioned before, cell mechanics enables the design of a multitude of experiments to assess single cell response in different conditions, like cell's behavior in matrices of different mechanical properties as well as different biochemical composition, cells under pharmacological treatment, salt, pH and temperature variations, etc. However, in natural conditions cells are surrounded by neighboring cells and ECM. Therefore, cells mechanics in 2D environment will differ from those in 3D environment. In 3D, cells are subjected to space limitations (constraints) and cell-cell and cell-ECM interactions. Neighboring cells communicate and interact to each other developing characteristic cell behavior in tissue, which will be different at single cell level due to the lack of cells cross-communication. Thus, research experiments turning into tissue-like conditions can help to decipher hidden mechanisms in diseases.

In this line, this thesis evolves from single cell level experiments to more tissue-like conditions in an attempt to disentangle unknown characteristics of Dupuytren's disease.

6.1.1 Individual conclusions by chapter

Chapter 3: Comparison of rheological properties of healthy versus Dupuytren fibroblasts when treated with a cell contraction inhibitor by Atomic Force Microscope

1. Rheological properties of healthy, scar and Dupuytren fibroblasts were evaluated. There is an increasing gradient in stiffness from healthy to Dupuytren fibroblasts, corroborating the myofibroblast phenotype of pathological fibroblasts "Dupuytren fibroblasts" and normal fibroblast phenotype of healthy fibroblasts. Scar fibroblasts showing intermediate stiffness suggest behavior between fibroblast to myofibroblast transition, such as proto-myofibroblast. It is worth to mention that those properties were measured in stiff supports: "plastic cell culture dishes".

2. AFM sweep modulation methodology combined with structural damping model was employed to extract the elastic and viscous properties of individual cells. Sweep frequency modulation is based on oscillatory testing of rheological properties of cells at different frequencies. Storage and loss modulus over two frequency decades at low amplitude were extracted showing a similar frequency dependence up to 10 Hz and then the loss modulus frequency dependence increases at higher frequencies.

3. The cell cytoskeleton inhibitor ML-7 was used at different concentrations to evaluate cell reactions. Since ML-7 is a MLCK inhibitor, it disrupts actin-myosin network and cell contractile activity. Healthy and scar fibroblasts were more resistant than Dupuytren fibroblasts to the inhibition and this effect was even clearer at higher concentrations. There were a fair percentage of cells that rounded up and softened when the inhibitor was added. However, after some time they started to recover their mechanical properties and morphology. ML-7 could be a potential pharmacological treatment for Dupuytren's disease inhibiting myofibroblasts survival.

Chapter 4: Rheological comparison between control versus Dupuytren fibroblasts when plated in circular micropatterns using Atomic Force Microscopy

1. Fibroblasts were plated on circular micropatterns of different diameters (25, 35 and 45 μm) and their mechanical properties were evaluated. Two different coatings were tested and fibronectin stimulated better cell attachment to the micropatterns than collagen I.

2. Fibroblasts showed differences in mechanical properties when plated on different diameter micropatterns. Dupuytren fibroblasts maintained their stiffness regardless of pattern diameter; however, the apparent Young's modulus of healthy "control" fibroblasts increased when increasing circular diameter. Scar fibroblasts again showed intermediate behavior, presenting an increase in stiffness from the small to the middle circle and constant mechanics from middle to big circle diameter. Healthy "control" fibroblasts increase in stiffness comes together with a decrease in loss tangent, which is related to a more solid-like behavior.

3. Cell mechanical properties were correlated with immunofluorescence, in which actin, vimentin and cell nucleus were stained. In the case of healthy "control" fibroblasts a visible cytoskeleton development when increasing the pattern diameter, presenting randomly distributed fibers when plated in the small circle and radial and concentric filaments when plated in the middle and big circles. An accumulation of more orientated actin fibers was observed as well. Scar and Dupuytren fibroblasts presented more accumulation of actin fibers with a better organization since the beginning (small circle). The actin fibers organization and development were correlated with mechanical properties, suggesting that healthy "control" fibroblasts mimicked a transition towards myofibroblasts phenotype due to the increment in stiffness and cytoskeleton development with pattern diameter.

Chapter 5: Dupuytren fibroblasts response in 2D and 3D environment

1. Fibroblasts were seeded in two collagen matrices of different stiffness (0.2 and 2 kPa, respectively) and plastic cell culture dishes as a stiff substrate. Mechanical properties of fibroblasts were evaluated on the different substrates.

2. Healthy and scar fibroblasts maintained their apparent Young's modulus regardless substrate stiffness; however, Dupuytren fibroblasts modify their mechanical properties to the stiffness of the underlying support. This behavior of Dupuytren fibroblasts is typical of myofibroblast phenotype as they increase their stiffness when the surrounding environment also changes due to the cell-ECM interplay through focal adhesions. Actin fibers labeling showed elongated cell morphology of Dupuytren and scar fibroblasts when seeded in soft collagen, while they presented spread shape when the stiffness of the substrate increases. Changes in cell morphology may be influenced by matrix fibers alignment.

3. Rheological properties of the cells in different conditions showed a slightly decrease in loss tangent from soft collagen to Petri dish substrates of Dupuytren fibroblasts referring to a more solid-like behavior.

4. Fibroblasts were embedded in 3D-collagen gels and mechanical properties of the gels were measured over time (2 days, 1 week and 2 weeks of cell incubation). A general increase in gel stiffness was observed over time regardless fibroblast type. Gels measurements after 2 days of Dupuytren fibroblasts incubation presented a slightly increase in apparent Young's modulus with respect to the other two cell types. Actin labeling corroborates that this increase in gel stiffness with Dupuytren fibroblasts inside was due to a more spread morphology in comparison to the other two types.

5. Gels staining for fibronectin and collagen III showed an increase in the secretion and deposition of fibronectin over time and more marked in gels in which Dupuytren fibroblasts were inserted.

These experiments and findings corroborate the myofibroblast phenotype of Dupuytren fibroblasts that can be modulated by tuning the mechanical properties of the surrounding environment. Cytoskeleton inhibitors are a good strategy to revert myofibroblast differentiation and more specifically finding a proper α-SMA inhibitor. 3D-environment serves to investigate cell behavior under tissue-like conditions, which is closer to nature cell's environment.

6.2 Future perspectives

Dupuytren's disease, like all fibrotic diseases, shows the accumulation of myofibroblasts in the damaged area. Specifically, in Dupuytren's disease myofibroblasts accumulate in the nodules and cord in the palmar fascia. Different strategies have been applied to revert myofibroblast differentiation, using cytokines such as IFN-γ, TNF-α, interleukins, etc; however, many of them just work for TGFβ-1 induced myofibroblasts but not with already differentiated myofibroblasts. Those inhibitors are focused on the disruption of α-SMA fibers; nevertheless, new directions focusing on other myofibroblast's features may help in reverting their differentiation. Myofibroblasts develop during wound healing have the task to close the wound. Previous studies suggested that myofibroblast activation could be produced by cytokine liberation from blood-borne cells and/or changes in ECM stiffness. Therefore, myofibroblasts are very sensitive to changes in their environment, modifying and modulating their mechanical properties to those of the environment. These ECM changes are transmitted through focal adhesion complexes, thus inhibitors targeting the formation of supermature focal adhesion complexes may destabilize cell-ECM interplay. Thus, they will also influence in the strength of the cell-substrate attachment.

Due to the variety of myofibroblast's origin, there may be differences between myofibroblasts coming from bone-marrow cells and any other cell type, like dermal fibroblasts. Combining together differentiated myofibroblasts with non-differentiated cells (but susceptible to differentiate), like smooth muscle cells, cardiomyocytes, fibroblasts or any other cell type that differentiate into myofibroblasts may help in the understanding of the transition. Another approach would be communicating blood-borne cells with cells susceptible of myofibroblasts differentiation as well as differentiated myofibroblasts in order to identify any substance that actives the transition. In this sense, the differentiation process could be monitored and controlled. For this type of experiments, a microfluidic device, in which blood-borne cells could be in one channel and "myofibroblasts" in the adjacent channel with a barrier open to diffusion, so that cells could "communicate" with each other.

In the early days, Dupuytren's disease was called Viking disease because most of the documented cases came from Nordic areas. It is conceivable that climate may also influence in the development of the disease. Climate hypothesis may come together with a deficiency of solar light and vitamin D levels that may also influence in the progression or development of the disease. In this context, changes in the mechanical properties of myofibroblasts related to climate variation may also be worth of study (temperature, light, vitamins access…).

Nowadays, there is wide variety of models to describe cell mechanical behavior, such as linear viscoelasticity, tensegrity, poroelasticity, soft glassy rheology models, etc. Although they are well spread and used for describing cell mechanics, they tend to describe only few characteristics of cell behavior. None of them encompass all complex individual cell responses and mechanisms. Cells are complex heterogeneous materials. Thus, it is hard to develop a model, which embraces all cell events. Nonetheless, when using one of the previous models, cell behavior is verily described as they focus on one or few mechanisms. Therefore, new models that include many cellular events are needed in order to come closer to the truly cell behavior.

The study of cell mechanics at single cell level has been used to decipher many biological questions, like cancer cells being softer than healthy counterparts in hard substrates or the static mechanical properties of cancer cells when modulating the stiffness of the underlying support. In addition, metastatic cells' invasive behavior was corroborated when using soft matrices and migration properties were observed when forced to move into constraint channels. Restricted cancer cells were found to be softer than free cells (Rianna et al., 2020). However, in natural conditions cells are not alone, but surrounded by neighboring cells and ECM. This environment is far from 2D laboratory cell mechanical experiments, which may probably lead to different cell responses. In tissue, cells are forced to acquire a specific shape due to the limited available space; therefore, they are subjected to complex physical constraints. Moreover, ECM biochemical and biomechanical composition differs a lot from normal substrates employed for cell mechanical experiments. There is a recent tendency to perform experiments employing artificial and natural gels and matrices made of some ECM protein, such as collagen, hyaluronic acid, fibronectin, etc. Although 2D-gels simulating ECM stiffness is an improvement, 3D-gels resemble much more tissue-like conditions. The use of 3D-gels made of one or two ECM proteins helps to investigate cell behavior in natural conditions; however, the use of natural ECM will open a new door to study cell response in tissue-like conditions, which is closer to actual natural cell environment. To summarize, we believe that 3D-matrices resembling as close as possible ECM properties is the way to continue investigating the mechanical properties of cells.

List of publications

1. Atomic force microscopy for cell mechanics and diseases. [Review Article] ***Pérez-Domínguez S.**, *Kulkarni S. G., Rianna C., Radmacher M. *Neuroforum,* 26:2 (**2020**). doi.org/10.1515/nf-2020-0001. *Equally contributed.

2. Rheological comparison between control and Dupuytren fibroblasts when plated in circular micropatterns using atomic force microscopy. [Research Article] **Pérez-Domínguez S.**, Werkmeister E., Marini M. L., Dupres V., Janel S., Lafont F., Radmacher M. *Frontiers in Physics,* 10:1052203 (**2022**). doi:10.3389/fphy.2022.1052203.

3. Comparison of rheological properties of healthy versus Dupuytren fibroblasts when treated with a cell contraction inhibitor by Atomic Force Microscope. [Research Article] **Pérez-Domínguez S**., López-Alonso J., Lafont F., Radmacher M. *International Journal of Molecular Sciences*, 24:2043 (**2023**). doi:10.3390/ijms24032043.

Submitted manuscripts

1. Characterizing the viscoelastic properties of different fibroblasts in 2D and 3D collagen gels. [Research Article] **Pérez-Domínguez S**., Sanz-Fraile H., Martínez-Vidal L., Alfano M., Otero J., Radmacher M. *bioRxiv,* (**2023**). doi: 10.1101/2023.12.15.571880 (accepted during thesis corrections after thesis colloquium).

2. Influence of cantilever tip geometry and contact model on AFM elasticity measurement of cells. [Research Article] *Kulkarni S. G., ***Pérez-Domínguez S**., Radmacher M. *Journal of Molecular Recognition,* (**2023**). *Equally contributed (accepted during thesis corrections after thesis colloquium; doi: 10.1002/jmr.3018).

Manuscripts in preparation

1. Sweep modulation microrheological approach to study cell viscoelastic behaviour. [Research Article] ***Pérez-Domínguez S**., *Kulkarni S., Rianna C., Viji Babu P. K., Radmacher M. *Physical Review E.* (**2023**). *Equally contributed

2. Reliable, standardized measurements for cell mechanical properties. [Research Article] **Pérez-Domínguez S**., Kulkarni S. G., Gnanachandran K., Lorenz E., Holuigue H. *et al., Nanoletters*. (**2023**). (submitted and accepted during thesis corrections after thesis colloquium; doi: 10.1039/D3NR02034G)

Bibliography

Abdelrahman, I., Elmasry, M., Steinvall, I. *et al.* (2020) 'Needle Fasciotomy or Collagenase Injection in the Treatment of Dupuytren's Contracture', *Plast. Reconst.,* 8(1), p. e2606. doi: 10.1097/gox.0000000000002606.

Aberle, H., Schwartz, H. and Kemler, R. (1996) 'Cadherin-catenin complex: Protein interactions and their implications for cadherin function', *J. Cell. Biochem.*, 61, pp. 514–523. doi: 10.1002/(SICI)1097-4644(19960616)61:4<514::AID-JCB4>3.0.CO;2-R.

Abidine, Y., Constantinescu, A., Laurent, V. M. *et al.* (2018) 'Mechanosensitivity of Cancer Cells in Contact with Soft Substrates Using AFM', *Biophys. J.*, 114, pp. 1165–1175. doi: 10.1016/j.bpj.2018.01.005.

Alberts, B., Bray, D., Lewis, J. *et al.* (1994) 'Molecular biology of the cell', (3rd ed.) *Garland Publishing, New York and London. Biochem. Educ.*, 22, pp. 1361. doi: 10.1016/0307-4412(94)90059-0.

Alcaraz, J., Buscemi, L., Puig-de-Morales, M. *et al.* (2002) 'Correction of microrheological measurements of soft samples with atomic force microscopy for the hydrodynamic drag on the cantilever', *Langmuir*, 18(3), pp. 716–721. doi: 10.1021/la0110850.

Alcaraz, J., Buscemi, L., Grabulosa, M. *et al.* (2003) 'Microrheology of human lung epithelial cells measured by atomic force microscopy', *Biophys. J.*, 84(3), pp. 2071–2079. doi: 10.1016/S0006-3495(03)75014-0.

Ali, M. Y., Chuang, C. Y. and Saif, M. T. A. (2014) 'Reprogramming cellular phenotype by soft collagen gels', *Soft Matter.*, 10(44), pp. 8829–8837. doi: 10.1039/c4sm01602e.

Alldritt, B., Urtev, F., Oinonen, N. *et al.* (2022) 'Automated tip functionalization via machine learning in scanning probe microscopy', *Comput. Phys. Commun.*, 273, p. 108258. doi: 10.1016/j.cpc.2021.108258.

Arnoldi, R., Chaponnier, C., Gabbiani, G. *et al.* (2012) 'Heterogeneity of Smooth Muscle', *Muscle,* 2. doi: 10.1016/B978-0-12-381510-1.00088-0.

Aumailley, M. and Gayraud, B. (1998a) 'Structure and biological activity of the extracellular matrix', *J. Mol. Med.*, 76(3–4), pp. 253–265. doi: 10.1007/s001090050215.

Aumailley, M. and Smyth, N. (1998b) 'The role of laminins in basement membrane function', *J. Anat.*, 193, pp. 1–21. doi: 10.1017/S0021878298003720.

Azioune, A., Carpi, N., Tseng, Q. *et al.* (2010) 'Protein Micropatterns. A Direct Printing Protocol Using Deep UVs.', *Methods Cell Biol.*, 97, pp. 133–146. doi:

10.1016/S0091-679X(10)97008-8.

Badois, F. J., Lermusiaux, J. L., Massé, C. (1993) ‘Non-surgical treatment of Dupuytren disease using needle fasciotomy’, *Rev. Rhum. Ed. Fr.*, 60(11), pp. 808-813.

Baum, J. and Duffy, H. S. (2011) ‘Fibroblasts and myofibroblasts: What are we talking about?’, *J. Cardiovasc. Pharmacol.*, 57, pp. 376–379. doi: 10.1097/FJC.0b013e3182116e39.

Bausch, A. R., Hellerer, U., Essler, M. *et al.* (2001) ‘Rapid stiffening of integrin receptor-actin linkages in endothelial cells stimulated with thrombin: A magnetic bead microrheology study’, *Biophys. J.*, 80, pp. 2649–2657. doi: 10.1016/S0006-3495(01)76234-0.

Bayat, A., Watson, J. S., Stanley, J. K. *et al.* (2002) ‘Genetic susceptibility in Dupuytren’s disease’, *J. Bone Jt. Surg. [Br]*, 84(B), pp. 211–215. doi: 10.1302/0301-620X.84B2.12083.

Becker, K., Siegert, S., Toliat, M. R. *et al.* (2016) ‘Meta-analysis of genome-wide association studies and network analysis-based integration with gene expression data identify new suggestive loci and unravel a Wnt-centric network associated with Dupuytren’s disease’, *PLoS ONE*, 11(7), p. e0158101. doi: 10.1371/journal.pone.0158101.

Benjamin, M. (2010) ‘The structure of tendons and ligaments’, *Regenerative Medicine and Biomaterials for the Repair of Connective Tissues*, pp. 351–374. doi: 10.1533/9781845697792.2.351.

Bian, K., Gerber, C., Heinrich, A. J. *et al.* (2021) ‘Scanning probe microscopy’, *Nat. Rev. Methods Primers*, 1(36). doi: 10.1038/s43586-021-00033-2.

Bilodeau, G. (1992) ‘Regular pyramid punch problem’, *J. Appl. Mech.*, 59, pp. 519-523. doi: 10.1115/1.2893754

Binning, G., Rohrer, H., Gerber, C. *et al.* (1982) ‘Surface Studies by Scanning Tunneling Microscopy’, *Physical Review Letters*, 49(1), pp. 57–61.

Binning, G., Quate, C. F. and Gerber, C. (1986) ‘Atomic Force Microscope’, *Phys. Rev. Lett.*, 56(9), pp. 930–933.

Bisson, M. A., Beckett, K. S., McGrouther, D. A. *et al.* (2009) ‘Transforming Growth Factor-β1 Stimulation Enhances Dupuytren’s Fibroblast Contraction in Response to Uniaxial Mechanical Load Within a 3-Dimensional Collagen Gel’, *J. Hand Surg.*., 34A, pp. 1102–1110. doi: 10.1016/j.jhsa.2009.02.008.

Bochaton-Piallat, M. L., Gabbiani, G. and Hinz, B. (2016) ‘The myofibroblast in wound healing and fibrosis: Answered and unanswered questions’, *F1000Research*, 5(752), pp. 1–8. doi: 10.12688/f1000research.8190.1.

Bohnet, S., Ananthakrishnan, R., Mogilner, A. *et al.* (2006) ‘Weak force stalls protrusion at the leading edge of the lamellipodium’, *Biophys. J.*, 90, pp. 1810–1820. doi: 10.1529/biophysj.105.064600.

Bonfanti, A., Kaplan, J. L., Charras, G. *et al.* (2020) ‘Fractional viscoelastic models for power-law materials’, *Soft Matter.*, 16(26), pp. 6002–6020. doi: 10.1039/d0sm00354a.

Borghi, N., Sorokina, M., Shcherbakova, O. G. *et al.* (2012) ‘E-cadherin is under constitutive actomyosin-generated tension that is increased at cell-cell contacts upon externally applied stretch’, *PNAS*, 109(31), pp. 12568–12573. doi: 10.1073/pnas.1204390109.

Bosman, F. T. and Stamenkovic, I. (2003) ‘Functional structure and composition of the extracellular matrix’, *J. Pathol.*, 200, pp. 423–428. doi: 10.1002/path.1437.

Boyer, H. E. (1987) ‘Atlas of Stress-strain Curves’. *ASM International, Metals Park, USA,* 630.

Brás, M. M., Cruz, T. B., Maia, A. E. *et al.* (2022) ‘Mechanical Properties of Colorectal Cancer Cells Determined by Dynamic Atomic Force Microscopy: A Novel Biomarker’, *Cancers*, 14(5053). doi: 10.3390/cancers14205053.

Breathnach, A. S. (1978) ‘Development and differentiation of dermal cells in man’, *J. Invest. Dermatol.*, 71, pp. 2–8. doi: 10.1111/1523-1747.ep12543601.

Brock, A. Chang, E., Ho, C-C. *et al.* (2003) ‘Geometric determinants of directional cell motility revealed using microcontact printing’, *Langmuir*, 19(5), pp. 1611–1617. doi: 10.1021/la026394k.

Broekstra, D. C., Groen, H., Molenkamp, S. *et al.* (2018) ‘A Systematic Review and Meta-Analysis on the Strength and Consistency of the Associations between Dupuytren Disease and Diabetes Mellitus, Liver Disease, and Epilepsy’, *Plast. Reconst.*, 141, pp. 367e-379e. doi: 10.1097/PRS.0000000000004120.

Brown, L. F., Lanir, N., McDonagh, J. *et al.* (1993) ‘Fibroblast migration in fibrin gel matrices’, *Am. J. Pathol.*, 142(1), pp. 273–283.

Burridge, K. and Chrzanowska-Wodnicka, M. (1996) ‘Focal adhesions, contractility, and signaling’, *Annu. Rev. Cell Dev. Biol.*, 12, pp. 463–519. doi: 10.1146/annurev.cellbio.12.1.463.

Butt, H. J. and Jaschke, M. (1995) ‘Calculation of thermal noise in atomic force microscopy’, *Nanotechnology*, 6(1), pp. 1–7. doi: 10.1088/0957-4484/6/1/001.

Camelliti, P., Borg, T. K. and Kohl, P. (2005) ‘Structural and functional characterisation of cardiac fibroblasts’, *Cardiovasc. Res.*, 65, pp. 40–51. doi: 10.1016/j.cardiores.2004.08.020.

Carl, P. and Schillers, H. (2008) ‘Elasticity measurement of living cells with an atomic force microscope: Data acquisition and processing’, *Pflugers Arch. Eur. J. Phy.*, 457(2), pp. 551–559. doi: 10.1007/s00424-008-0524-3.

Carlson, M. A. and Longaker, M. T. (2004) ‘The fibroblast-populated collagen matrix as a model of wound healing: A review of the evidence’, *Wound Repair Regen.*, 12, pp. 134–147. doi: 10.1111/j.1067-1927.2004.012208.x.

Chan, C. J., Whyte, G., Boyde, L. *et al.* (2014) ‘Impact of heating on passive and active biomechanics of suspended cells’, *Interface Focus*, 4(20130069). doi: 10.1098/rsfs.2013.0069.

Chen, C. S., Mrksich, M., Huang, S. *et al.* (1997) ‘Geometric Control of Cell Life and Death’, *Science*, 276 (5317), pp. 425–1428. doi: 10.1126/science.276.5317.1425.

Cheng, X., Wang, X., Wan, Y. *et al.* (2015) ‘Myosin light chain kinase inhibitor ML7 improves vascular endothelial dysfunction via tight junction regulation in a rabbit model of atherosclerosis’, *Mol. Med. Rep.*, 12(3), pp. 4109–4116. doi: 10.3892/mmr.2015.3973.

Cheung, D. T., Nimni, M. E. (1982) ‘Mechanicm of crosslinking of proteins by glutaraldehyde II. Reaction with monomeric and polymeric collagen’, *Connect. Tissue Res.*, 10, pp. 201-216. doi: 10.3109/03008208209034419.

Choi, C. K., Vicente-Manzanares, M., Zareno, J. *et al.* (2008) ‘Actin and α-actinin orchestrate the assembly and maturation of nascent adhesions in a myosin II motor-independent manner’, *Nat. Cell Biol.*, 10(9), pp. 1039–1050. doi: 10.1038/ncb1763.

Chopra, A., Tabdanov, E., Patel, H., *et al.* (2011) ‘Cardiac myocyte remodeling mediated by N-cadherin-dependent mechanosensing’, *Am J. Physiol. Heart Circ. Physiol.*, 300(4), pp. 1252–1266. doi: 10.1152/ajpheart.00515.2010.

Choquet, D., Felsenfeld, D. P. and Sheetz, M. P. (1997) ‘Extracellular matrix rigidity causes strengthening of integrin- cytoskeleton linkages’, *Cell.*, 88(1), pp. 39–48. doi: 10.1016/S0092-8674(00)81856-5.

Chowdhury, T. T., Bader, D. L., Shelton, J. C., *et al.* (2003) ‘Temporal regulation of chondrocyte metabolism in agarose constructs subjected to dynamic compression’, *Arch. Biochem. Biophys.*, 417, pp. 105–111. doi: 10.1016/S0003-9861(03)00340-0.

Christensen, R. M. (1982) ‘Theory of viscoelasticity’, *Academic Press. Inc.*

Chu, Y. S., Thomas, W. A., Eder, O. *et al.* (2004) ‘Force measurements in E-cadherin-mediated cell doublets reveal rapid adhesion strengthened by actin cytoskeleton remodeling through Rac and Cdc42’, *J. Cell Biol.*, 167(6), pp. 1183–1194. doi: 10.1083/jcb.200403043.

Cleveland, J. P., Manne, S., Bocek, D. *et al.* (1993) ‘A nondestructive method for determining the spring constant of cantilevers for scanning force microscopy’, *Rev. Sci. Instrum.*, 64, pp. 403–405. doi: 10.1063/1.1144209.

Colombo, E., Calcaterra, F., Cappelletti, M. *et al.* (2013) ‘Comparison of Fibronectin and Collagen in Supporting the Isolation and Expansion of Endothelial Progenitor Cells from Human Adult Peripheral Blood', *PLoS ONE*, 8(6), p. e66734. doi: 10.1371/journal.pone.0066734.

Cooper, G. (2000) 'The Cell: A molecular approach. 2nd edition. Actin, myosin and cell movement', *Sunderland (MA): Sinauer Associates*. doi: 10.1111/1440-1681.12162.

Coué, M., Brenner, S. L., Spector, I. *et al.* (1987) 'Inhibition of actin polymerization by latrunculin A', *FEBS Letters*, 213(2), pp. 316–318. doi: 10.1016/0014-5793(87)81513-2.

Court, M., Malier, M. and Millet, A. (2019) '3D type I collagen environment leads up to a reassessment of the classification of human macrophage polarizations', *Biomaterials*, 208, pp. 98–109. doi: 10.1016/j.biomaterials.2019.04.018.

Courtney, T. H. (2005) 'Mechanical behavior of materials', *(2nd ed.) Waveland Press, Inc.*

Critchley, D. R. (2000) 'Focal adhesions - The cytoskeletal connection', *Curr. Opin. Cell Biol.*, 12, pp. 133–139. doi: 10.1016/S0955-0674(99)00067-8.

Darling, E. M., Zauscher, S., Block J. A. *et al.* (2007) 'A thin-layer model for viscoelastic, stress-relaxation testing of cells using atomic force microscopy: Do cell properties reflect metastatic potential?', *Biophys. J.*, 92, pp. 1784–1791. doi: 10.1529/biophysj.106.083097.

Deguchi, S., Hotta, J., Yokoyama, S. *et al.* (2015) 'Viscoelastic and optical properties of four different PDMS polymers', *J. Micromech. Microeng.*, 25(9). doi: 10.1088/0960-1317/25/9/097002.

Deng, L., Trepat, X., Butler, J. P. *et al.* (2006) 'Fast and slow dynamics of the cytoskeleton', *Nat. Mater.*, 5(8), pp. 636–640. doi: 10.1038/nmat1685.

Desai, S. S. and Hentz, V. R. (2011) 'The treatment of Dupuytren disease', *J. Hand Surg.*, 36A, pp. 936–942. doi: 10.1016/j.jhsa.2011.03.002.

Descatha, A. *et al.* (2012) 'Heavy manual work, exposure to vibration and Dupuytren's disease? Results of a surveillance program for musculoskeletal disorders', *Occup. Environ. Med.*, 69, pp. 296–299. doi: 10.1136/oemed-2011-100319.

Desmoulière, A., Geinoz, A., Gabbiani, F. *et al.* (1993) 'Transforming growth factor-β1 induces α-smooth muscle actin expression in granulation tissue myofibroblasts and in quiescent and growing cultured fibroblasts', *J. Cell Biol.*, 122(1), pp. 103–111. doi: 10.1083/jcb.122.1.103.

Desmoulière, A., Chaponnier, C. and Gabbiani, G. (2005) 'Tissue repair, contraction, and the myofibroblast', *Wound Repair Regen.*, 13(1), pp. 7–12. doi: 10.1111/j.1067-1927.2005.130102.x.

Desmoulière, A. and Gabbiani, G. (1995) ‘Smooth Muscle Cell and Fibroblast Biological and Functional Features: Similarities and Differences’, *Vascular Smooth Muscle Cell*, pp. 329–359. doi: 10.1016/b978-012632310-8/50015-2.

De Sousa, J. S., Freire, R. S., Sousa, F. D. *et al.* (2020) ‘Double power-law viscoelastic relaxation of living cells encodes motility trends’, *Sci. Rep.*, 10(1), pp. 1–9. doi: 10.1038/s41598-020-61631-w.

Dick, M. K., Miao, J. H., Limaiem, F. (2022) ‘Histology, Fibroblast’, *Treasure Island*. https://www.ncbi.nlm.nih.gov/books/NBK541065/.

Ding, J., Li, Z., Liang, L. *et al.* (2020) ‘Myosin light chain kinase inhibitor ML7 improves vascular endothelial dysfunction and permeability via the mitogen-activated protein kinase pathway in a rabbit model of atherosclerosis’, *Biomed. Pharmacother.*, 128(110258), pp. 1–8. doi: 10.1016/j.biopha.2020.110258.

Doljanski, F. (2004) ‘The sculpturing role of fibroblast-like cells in morphogenesis’, *Perspect. Biol. Med.*, 47(3), pp. 339–356. doi: 10.1353/pbm.2004.0048.

Dooley, S., Said, H. M., Gressner, A. M. *et al.* (2006) ‘Y-box protein-1 is the crucial mediator of antifibrotic interferon-γ effects’, *J. Biol. Chem.*, 281(3), pp. 1784–1795. doi: 10.1074/jbc.M510215200.

Drzewiecki, K. E., Parmar, A. S., Gaudet, I. D. *et al.* (2014) ‘Methacrylation Induces Rapid, Temperature-Dependent, Reversible Self-Assembly of Type - I Collagen’, *Langmuir*, 30, pp. 11204–11211. doi: doi.org/10.1021/la502418s.

Dugina, V., Fontao, L., Chaponnier, C. *et al.* (2001) ‘Focal adhesion features during myofibroblastic differentiation are controlled by intracellular and extracellular factors’, *J. Cell Sci.*, 114, pp. 3285–3296. doi: 10.1242/jcs.114.18.3285.

Dupuytren, B. (1833) ‘Clinical Lectures on Surgery’, *Lancet.*
Duval, K., Grover, H., Han, L-H. *et al.* (2017) ‘Modeling physiological events in 2D vs. 3D cell culture’, *Physiology*, 32(4), pp. 266–277. doi: 10.1152/physiol.00036.2016.

Dyba, M. and Hell, S. W. (2003) ‘Photostability of a fluorescent marker under pulsed excited-state depletion through stimulated emission’, *Appl. Opt.*, 42(25). doi: 10.1364/ao.42.005123.

Ebner, A., Widling, L., Zhu, R. *et al.* (2008) ‘Functionalization of probe tips and supports for single-molecule recognition force microscopy’, *Top. Curr. Chem.*, doi: 10.1007/128_2007_24.

Eckes, B., Kessier, D., Aumailley, M. *et al.* (1999) ‘Interactions of fibroblasts with the extracellular matrix: Implications for the understanding of fibrosis’, *Semin. Immunopathol.*, 21(4), pp. 415–429. doi: 10.1007/BF00870303.

Engel, A. and Müller, D. J. (2000) ‘Observing single biomolecules at work with the atomic force microscope', *Nature America Inc.*, 7(9), pp. 715–718.

Engler, A. J., Sen, S., Sweeney, H. L. et al. (2006) 'Matrix elasticity directs stem cell lineage', *Cell*, 126(4), pp. 677-689. doi: 10.1016/j.cell.2006.06.044.

Erlebacher, A., Filvaroff, E. H., Gitelman, S. E. *et al.* (1995) 'Toward a molecular understanding of skeletal development', *Cell*, 80, pp. 371–378. doi: 10.1016/0092-8674(95)90487-5.

Eyre, D. R. (2004) 'Collagens and cartilage matrix homeostasis', *Clin. Orthop. Relat. Res.*, 427, pp. S118-S122. doi: 10.1097/01.blo.0000144855.48640.b9

Fabry, B., Maksym, G. N., Butler, J. P. *et al.* (2001) 'Scaling the microrheology of living cells', *Phys. Rev. Lett.*, 87(14), pp. 1–4. doi: 10.1103/PhysRevLett.87.148102.

Fabry, B., Maksym, G. N., Butler, J. P. *et al.* (2003) 'Time scale and other invariants of integrative mechanical behavior in living cells', *Phys. Rev. E,* 68(041914), pp. 1–18. doi: 10.1103/PhysRevE.68.041914.

Fancey, K. S. (2005) 'A mechanical model for creep, recovery and stress relaxation in polymeric materials', *J. Mater. Sci.*, 40, pp. 4827–4831. doi: 10.1007/s10853-005-2020-x.

Ferry, J. D. (1980) 'Viscoelastic properties of polymer*s*', *John Wiley & Sons, Inc.*

Fink, J., Théry, M., Azioune, A., Dupont, R., Chatelain, F., Bornens, M., and Piel, M. (2007). 'Comparative study and improvement of current cell micro-patterning techniques', *Lab Chip*, 7(6), 672–680. doi: 10.1039/B618545B.

Fletcher, D. A. and Mullins, R. D. (2010) 'Cell mechanics and the cytoskeleton', *Nature*, 463, pp. 485–492. doi: 10.1038/nature08908.

Flormann, D. A. D., Anton, C., Pohland, M. O. *et al.* (2021) 'Oscillatory Microrheology, Creep Compliance and Stress Relaxation of Biological Cells Reveal Strong Correlations as Probed by Atomic Force Microscopy', *Front. Phys.*, 9(711860). doi: 10.3389/fphy.2021.711860.

Forbes, S. J., Russo, F. P., Rey, V. *et al.* (2004) 'A significant proportion of myofibroblasts are of bone marrow origin in human liver fibrosis', *Gastroenterology*, 126(4), pp. 955-963. doi: 10.1053/j.gastro.2004.02.025.

Francis-Sedlak, M. E., Uriel, S., Larson, J. C. *et al.* (2009) 'Characterization of type I collagen gels modified by glycation', *Biomaterials*, 30, pp. 1851-1856. doi: 10.1016/j.biomaterials.2008.12.014.

Franck, C., Maskarinec, S. A., Tirrell, D. A. *et al.* (2011) 'Three-dimensional traction force microscopy: A new tool for quantifying cell-matrix interactions', *PLoS ONE*, 6(3), p. e17833. doi: 10.1371/journal.pone.0017833.

Fratzl, P. (2008) 'Collagen: Structure and mechanics', in *(eds) Collagen. Springer,* *Boston, MA*. doi: 10.1007/978-0-387-73906-9_1.

Fredberg, J. J. and Stamenovic, D. (1989) 'On the imperfect elasticity of lung tissue', *J. Appl. Physiol.*, 67(6), pp. 2408–2419. doi: 10.1152/jappl.1989.67.6.2408.

Fu, J., Wang, Y-K., Yang, M. T. *et al.* (2010) 'Mechanical regulation of cell function with geometrically modulated elastomeric substrates', *Nat. Methods*, 7(9), pp. 733–736. doi: 10.1038/nmeth.1487.

Fudge, D. S., Gardner, K. H., Forsyth, V. T. *et al.* (2003) 'The mechanical properties of hydrated intermediate filaments: Insights from hagfish slime threads', *Biophys. J.*, 85(3), pp. 2015–2027. doi: 10.1016/S0006-3495(03)74629-3.

Gabbiani, G., Hirschel, B. J., Ryan, G. B. *et al.* (1972) 'Granulation Tissue as a Contractile Organ', *J. Exp. Med.*, 135, pp. 719–734.

Gabrielli, A., Avvedimento, E. and Krieg, T. (2009) 'Scleroderma', *New Engl. J. Med.*, 360, pp. 1989–2003. doi: 10.1177/1461444810365020.

Gallant, N. D., Michael, K. E. and García, A. J. (2005) 'Cell adhesion stregthening: contributions of adhesive area, integrin binding, and focal adhesion assembly', *Mol. Biol. Cell*, 16, pp. 4329–4340. doi: 10.1091/mbc.e05-02-0170.

Gaudet, I. D. and Shreiber, D. I. (2012) 'Characterization of methacrylated Type-I collagen as a dynamic, photoactive hydrogel', *Biointerphases*, 7(25), pp. 1–9. doi: 10.1007/s13758-012-0025-y.

Gavara, N. (2016) 'A beginner's guide to atomic force microscopy probing for cell mechanics', *Microsc. Res. Tech.*, pp. 1–10. doi: 10.1002/jemt.22776.

Gerum, R., Mirzahossein, E., Eroles, M. *et al.* (2022) 'Viscoelastic properties of suspended cells measured with shear flow deformation cytometry', *eLife*, 11(e78823). doi: 10.7554/eLife.78823.

Goffin, J. M., Pitet, P., Csucs, G. *et al.* (2006) 'Focal adhesion size controls tension-dependent recruitment of α-smooth muscle actin to stress fibers', *J. Cell Biol.*, 172(2), pp. 259–268. doi: 10.1083/jcb.200506179.

Goldsmith, E. C., Hoffman, A., Morales, M. *et al.* (2004) 'Organization of fibroblasts in the heart', *Dev. Dyn.*, 230(4), pp. 787–794. doi: 10.1002/dvdy.20095.

Grinnell, F. (1994) 'Fibroblasts, Myofibroblasts, and Wound Contraction.', *J. Cell Biol.*, 124(4), pp. 401–404. Available at: http://www.ncbi.nlm.nih.gov/pubmed/2119916.

Grinnell, F. (2003) 'Fibroblast biology in three-dimensional collagen matrices', *Trends Cell Biol.*, 13(5), pp. 264–269. doi: 10.1016/S0962-8924(03)00057-6.

Gu, L., Zhu, Y-J., Guo, Z-J. *et al.* (2004) 'Effect of IFN-γ and dexamethasone on TGF-β1-induced human fetal lung fibroblast-myofibroblast differentiation', *Acta*

Pharmacol. Sin., 25(11), pp. 1479–1488.

Gu, L. Z., Hu, W-Y., Antic, N. *et al.* (2006) ‘Inhibiting myosin light chain kinase retards the growth of mammary and prostate cancer cells’, *Eur. J. Cancer*, 42(7), pp. 948–957. doi: 10.1016/j.ejca.2005.12.017.

Guck, J., Ananthakrishnan, R., Mahmood, H. *et al.* (2001) ‘The optical stretcher: A novel laser tool to micromanipulate cells’, *Biophys. J.*, 81, pp. 767–784. doi: 10.1016/S0006-3495(01)75740-2.

Guyot, C., Lepreux, S., Combe, C. *et al.* (2006) ‘Hepatic fibrosis and cirrhosis: The (myo)fibroblastic cell subpopulations involved’, *Int. J. Biochem. Cell Biol.*, 38, pp. 135–151. doi: 10.1016/j.biocel.2005.08.021.

Hadeed, J. G., Bond, J. E., Selim, M. A., *et al.* (2011) ‘Calcium-dependent signaling in Dupuytren’s disease’, *Hand*, 6, pp. 159–164. doi: 10.1007/s11552-010-9314-4.

Hale, C. M., Sun, S. X. and Wirtz, D. (2009) ‘Resolving the role of actoymyosin contractility in cell microrheology’, *PLoS ONE*, 4(9), p. e7054. doi: 10.1371/journal.pone.0007054.

Han, S. W., Khuri, F. R. and Roman, J. (2006) ‘Fibronectin stimulates non-small cell lung carcinoma cell growth through activation of Akt/mammalian target of rapamycin/S6 kinase and inactivation of LKB1/AMP-activated protein kinase signal pathways’, *Cancer Res.*, 66(1), pp. 315–323. doi: 10.1158/0008-5472.CAN-05-2367.

Hart, M. G. and Hooper, G. (2005) ‘Clinical associations of Dupuytren’s disease’, *Postgrad. Med. J.*, 81, pp. 425–428. doi: 10.1136/pgmj.2004.027425.

Hazan, R. B., Qiao, R., Keren, R. *et al.* (2004) ‘Cadherin switch in tumor progression’, *Ann. N. Y. Acad. Sci.*, 1014, pp. 155–163. doi: 10.1196/annals.1294.016.

Hearn, E. J. (1997) *Mech. mater.*. doi: 10.1016/B978-0-7506-3265-2.X5000-2.

Hecht, F. M., Rheinlaender, J., Schierbaum, N., *et al.* (2015) ‘Imaging viscoelastic properties of live cells by AFM: Power-law rheology on the nanoscale’, *Soft Matter*, 11(23), pp. 4584–4591. doi: 10.1039/c4sm02718c.

Heffernan, J. M., Overstreet, D. J., Le, L. D. *et al.* (2015) ‘Bioengineered Scaffolds for 3D Analysis of Glioblastoma Proliferation and Invasion’, *Ann. Biomed. Eng.*, 43(8), pp. 1965–1977. doi: 10.1007/s10439-014-1223-1.

Hermanowicz, P., Sarna, M., Burda, K. *et al.* (2014) ‘AtomicJ: An open source software for analysis of force curves’, *Rev. Sci. Instrum.*, 85. doi: 10.1063/1.4881683.

Hertz, H. (1881) ‘Über die Berührung fester elastischer Körper’, *J. Reine Angew. Mathematik.*, 92, pp. 156–171. doi: 10.1515/crll.1882.92.156.

Higashi, K. *et al.* (2003) ‘Interferon-γ Interferes with Transforming Growth Factor-β

Signaling through Direct Interaction of YB-1 with Smad3', *J. Biol. Chem.*, 278(44), pp. 43470–43479. doi: 10.1074/jbc.M302339200.

Hildebrandt, J. (1969) 'Comparison of Mathematical Models For Cat Lung And Viscoelastic Balloon Derived By Laplace Transform Methods From Pressure-Volume Data', *Bull. Math. Biophys.*, 31, pp. 651–667. doi: 10.1007/BF02477779.

Hinz, B., Celetta, G., Tomasek, J. J. *et al.* (2001) 'Alpha-smooth muscle actin expression upregulates fibroblast contractile activity', *Mol. Biol. Cell*, 12(9), pp. 2730–2741. doi: 10.1091/mbc.12.9.2730.

Hinz, B., Dugina, V., Ballestrem, C. *et al.* (2003) 'A-Smooth Muscle Actin Is Crucial for Focal Adhesion Maturation in Myofibroblasts', *Mol. Biol. Cell*, 14(6), pp. 2508–2519. doi: 10.1091/mbc.E02-11-0729.

Hinz, B. (2007) 'Formation and function of the myofibroblast during tissue repair', *J. Invest. Dermatol.*, 127(3), pp. 526–537. doi: 10.1038/sj.jid.5700613.

Hinz, B. (2010) 'The myofibroblast: Paradigm for a mechanically active cell', *J. Biomech.*, 43, pp. 146–155. doi: 10.1016/j.jbiomech.2009.09.020.

Hinz, B. (2015a) 'Myofibroblasts', *Exp. Eye Res.*, 142, pp. 56–70. doi: 10.1016/j.exer.2015.07.009.

Hinz, B. (2015b) 'The extracellular matrix and transforming growth factor-β1: Tale of a strained relationship', *Matrix Biol.*, 47, pp. 54–65. doi: 10.1016/j.matbio.2015.05.006.

Hinz, B. (2016) 'Myofibroblasts', *Exp. Eye Res.*, 142, pp. 56–70. doi: 10.1016/j.exer.2015.07.009.

Hiratsuka, S., Mizutani, Y., Tsuchiya, M. *et al.* (2009) 'The number distribution of complex shear modulus of single cells measured by atomic force microscopy', *Ultramicroscopy.*, 109, pp. 937–941. doi: 10.1016/j.ultramic.2009.03.008.

Ho, Y. Y., Lagares, D., Tager, A. M. *et al.* (2014) 'Fibrosis - A lethal component of systemic sclerosis', *Nat. Rev. Rheumatol.*,10, pp. 390–402. doi: 10.1038/nrrheum.2014.53.

Hochmuth, R. M., Shao, J-Y., Dai, J. *et al.* (1996) 'Deformation and flow of membrane into tethers extracted from neuronal growth cones', *Biophys. J.*, 70, pp. 358–369. doi: 10.1016/S0006-3495(96)79577-2.

Hoffman, B. D. and Crocker, J. C. (2009) 'Cell Mechanics: Dissecting the Physical Responses of Cells to Force', *Annu. Rev. Biomed. Eng.*, 11(1), pp. 259–288. doi: 10.1146/annurev.bioeng.10.061807.160511.
Hulmes, D. J. (1992) 'The collagen superfamily: diverse structures and assemblies', *Essays Biochem.*, 27, pp. 49-67. PMID: 1425603.

Hurst, L. C., Badalamente, M. A., Hentz, V. R. *et al.* (2009) 'Injectable Collagenase clostridium histolyticum for Dupuytren's contracture', *N. Engl. J. Med.*, 361, pp. 968–79. doi: 10.1517/14712598.2010.510509.

Hynes, R. O. (1992) 'Integrins: Versatility, modulation, and signaling in cell adhesion', *Cell*, 69, pp. 11–25. doi: 10.1016/0092-8674(92)90115-S.

Ignatova, Z., Gierash, L. M. (2007) 'Effects of osmolytes on protein folding and aggregation in cells', *Methods Enzymol.*, 428, pp. 355-372. doi: 10.1016/S0076-6879(07)28021-8.

Illanes, A. (1999) 'Stability of biocatalysts', *Electron. J. Biotechnol.*, 2(1). doi: 10.2225/vol2-issue1-fulltext-2.

Ingber, D. E. (1993) 'Cellular tensegrity: Defining new rules of biological design that govern the cytoskeleton', *J. Cell Sci.*, 104, pp. 613–627. doi: 10.1242/jcs.104.3.613.

Malvern Instruments, (2016) 'Rheology and viscosity: A Basic Introduction to Rheology', *Whitepaper (Spectris plc)*. Available at: https://cdn.technologynetworks.com/TN/Resources/PDF/WP160620BasicIntroRheology.pdf.

Isambert, H. and Maggs, A. C. (1996) 'Dynamics and rheology of actin solutions', *Macromolecules*, 29, pp. 1036–1040. doi: 10.1021/ma946418x.

Isemura, M., Mita, T., Satoh, K. *et al.* (1991) 'Myosin light chain kinase inhibitors ML-7 and ML-9 inhibit mouse lung carcinoma cell attachment to the fibronectin substratum', *Cell Biol. Int. Rep.*, 15(10), pp. 965–972. doi: 10.1016/0309-1651(91)90146-A.

James, J., Goluch, E. D., Hu, H. *et al.* (2008) 'Subcellular curvature at the perimeter of micropatterned cells influences lamellipodial distribution and cell polarity', *Cell Motil. Cytoskelet.*, 65(11), pp. 841–852. doi: 10.1002/cm.20305.

Jamora, C. and Fuchs, E. (2002) 'Intercellular adhesion, signalling and the cytoskeleton', *Nat. Cell Biol.*, 4, pp. 101–108. doi: 10.1038/ncb0402-e101.

Janmey, P. A. and Miller, R. T. (2011) 'Mechanisms of mechanical signaling in development and disease', *J. Cell Sci.*, 124(1), pp. 9–18. doi: 10.1242/jcs.071001.

Janmey, P. A. and Schliwa, M. (2008) 'Quick guide Rheology', *Curr. Biol.*, 18(15), pp. R639–R641.

Jastrzebski, Z. D. (1960) 'Nature and properties of engineering materials', *J. Appl. Polym. Sci.*, 571. doi: 10.1002/app.1960.070041224.

Jensen, C. and Teng, Y. (2020) 'Is It Time to Start Transitioning From 2D to 3D Cell Culture?', *Front. Mol. Biosci.*, 7(33), pp. 1–15. doi: 10.3389/fmolb.2020.00033.

Jockusch, B. M., Bubeck, P. Giehl, K. *et al.* (1995) 'The molecular architecture of focal adhesions', *Annu. Rev. Cell Dev. Biol.*, 11, pp. 379–416.

Jóźwiak, B., Orczykowska, M. and Dziubiński, M. (2015) ‘Fractional generalizations of Maxwell and Kelvin-Voigt models for biopolymer characterization’, *PLoS ONE*, 10(11), pp. 1–19. doi: 10.1371/journal.pone.0143090.

Kalwarczyk, T., Ziębacz, N., Bielejewska, A. *et al.* (2011) ‘Comparative analysis of viscosity of complex liquids and cytoplasm of mammalian cells at the nanoscale’, *Nano Letters*, 11(5), pp. 2157–2163. doi: 10.1021/nl2008218.

Kanangat, S., Postlethwaite, A. E., Higgins, G. C. *et al.* (2006) ‘Novel functions of intracellular IL-1ra in human dermal fibroblasts: Implications in the pathogenesis of fibrosis’, *J. Invest. Dermatol.*, 126, pp. 756–765. doi: 10.1038/sj.jid.5700097.

Kaneko, K., Satoh, K., Masamune, A. *et al.* (2002) ‘Myosin light chain kinase inhibitors can block invasion and adhesion of human pancreatic cancer cell lines’, *Pancreas*, 24(1), pp. 34–41. doi: 10.1097/00006676-200201000-00005.

Kasza, K. E., Rowat, A. C., Liu, J. *et al.* (2007) ‘The cell as a material’, *Curr. Opin. Cell Biol.*, 19(1), pp. 101–107. doi: 10.1016/j.ceb.2006.12.002.

Kaufman, L. J., Brangwynne, C. P., Kasza, K. E. *et al.* (2005) ‘Glioma expansion in collagen I matrices: Analyzing collagen concentration-dependent growth and motility patterns’, *Biophys. J.*, 89, pp. 635–650. doi: 10.1529/biophysj.105.061994.

Khan, M. K., Wang, Q. Y. and Fitzpatrick, M. E. (2016) Atomic Force Microscopy (AFM) for Materials Characterization, ‘Materials Characterization Using Nondestructive Evaluation (NDE)’ *Methods.*, doi: 10.1016/B978-0-08-100040-3.00001-8.

Kilinc, D. and Lee, G. U. (2014) ‘Advances in magnetic tweezers for single molecule and cell biophysics’, *Integr. Biol.*, 6, p. 27. doi: 10.1039/c3ib40185e.

Kirmizis, D. and Logothetidis, S. (2010) ‘Atomic force microscopy probing in the measurement of cell mechanics’, *Int. J. Nanomed.*, 5, pp. 137–145. doi: 10.2147/ijn.s5787.

Klar, T. A., Jakobs, S., Dyba, M. *et al.* (2000) ‘Fluorescence microscopy with diffraction resolution barrier broken by stimulated emission’, *PNAS*, 97(15), pp. 8206–8210. doi: 10.1073/pnas.97.15.8206.

Kleinman, H. K., Klebe, R. J., Martin, G. R. (1981) ‘Role of collagenous matrices in the adhesion and growth of cells’, *J. Cell. Biol.*, 88(3), pp. 473-485. doi: 10.1083/jcb.88.3.473.

Kleinman, H. K., Luckenbill-Edds, L., Cannon, F. W. et al. (1987) ‘Use of extracellular matrix components for cell culture’, *Anal. Biochem.*, 166(1), pp. 1-13. doi: 10.1061/0003-2697(87)90538-0.

Klingberg, F., Chow, M. L., Koehler, A. *et al.* (2014) ‘Prestress in the extracellular matrix sensitizes latent TGF-β1 for activation’, *J. Cell Biol.*, 207(2), pp. 283–297. doi: 10.1083/jcb.201402006.

Klinker, M. W., Marklein, R. A., Surdo, J. L. *et al.* (2017) 'Morphological features of IFN-γ-stimulated mesenchymal stromal cells predict overall immunosuppressive capacity', *PNAS*, 114(13), pp. E2598–E2607. doi: 10.1073/pnas.1617933114.

Kloen, P., Jennings C. L., Gebhardt, M. C. *et al.* (1995) 'Transforming growth factor-β: Possible roles in Dupuytren's contracture', *J. of Hand Surg.*, 20A(1), pp. 101–108. doi: 10.1016/S0363-5023(05)80067-X.

Klymenko, O., Wiltowska-Zuber, J., Lekka, M. *et al.* (2009) 'Energy dissipation in the AFM elasticity measurements', *Acta Phys. Pol. A*, 115(2), pp. 548–551. doi: 10.12693/APhysPolA.115.548.

Knust, E. and Bossinger, O. (2002) 'Composition and formation of intercellular junctions in epithelial cells', *Science*, 298, pp. 1955–1959. doi: 10.1126/science.1072161.

Kollmannsberger, P. and Fabry, B. (2011) 'Linear and Nonlinear Rheology of Living Cells', *Annu. Rev. Mater. Res.*, 41(1), pp. 75–97. doi: 10.1146/annurev-matsci-062910-100351.

Kono, T., Tanii, T., Furukawa, M. *et al.* (1990) 'Cell cycle analysis of human dermal fibroblasts cultured on or in hydrated type I collagen lattices', *Arch. Dermatol. Res.*, 282, pp. 258–262. doi: 10.1007/BF00371646.

Kovács, M., Tóth, J., Hetényi, C. *et al.* (2004) 'Mechanism of blebbistatin inhibition of myosin II', *J. Biol. Chem.*, 279(34), pp. 35557–35563. doi: 10.1074/jbc.M405319200.

Kraning-Rush, C. M., Califano, J. P. and Reinhart-King, C. A. (2012) 'Cellular traction stresses increase with increasing metastatic potential', *PLoS ONE*, 7(2), p. e32572. doi: 10.1371/journal.pone.0032572.

Kuddus, M. (2019) 'Introduction to food enzymes', *Enzymes Food Biotechnol.*, doi: 10.1016/B978-0-12-813280-7.00001-3.

Kwon, Y.S., Lim, E. S., Kim, H. M. et al. (2015) 'Genipin, a crosslinking agent, promotes odontogenic differentiation of human dental pulp cells', *J. Endodontics*, 41, pp. 501-507. doi: 10.1016/j.joen.2014.12.002.

Labat-Robert, J., Bihari-Varga, M. and Robert, L. (1990) 'Extracellular matrix', *FEBS Letters*, 268(2), pp. 386–393.

Lacouture, M. E., Schaffer, J. L. and Klickstein, L. B. (2002) 'A comparison of type I collagen, fibronectin, and vitronectin in supporting adhesion of mechanically strained osteoblasts', *J. Bone Miner. Res.*, 17(3), pp. 481–492. doi: 10.1359/jbmr.2002.17.3.481.

Lane Smith, R., Trindade, M. C. D., Ikenoue, T. *et al.* (2000) 'Effects of shear stress on articular chondrocyte metabolism', *Biorheology*, 37(1-2), pp. 95-107.

Langevin, H. M., Bouffard, N., Badger, G. *et al.* (2005) 'Dynamic fibroblast cytoskeletal response to subcutaneous tissue stretch ex vivo and in vivo', *Am. J. Physiol. Cell Physiol.*, 288(3 57-3), pp. 747–756. doi: 10.1152/ajpcell.00420.2004.

Lee, C. H., Singla, A. and Lee, Y. (2001) 'Biomedical applications of collagen', *Int. J. Pharm.,* 221, pp. 1–22. doi: 10.1016/S0378-5173(01)00691-3.

Lehenkari, P. P. and Horton, M. A. (1999) 'Single integrin molecule adhesion forces in intact cells measured by atomic force microscopy', *Biochem. Biophys. Res. Commun.*, 259(3), pp. 645–650. doi: 10.1006/bbrc.1999.0827.

Lekka, M., Laidler, P., Gil, D. *et al.* (1999) 'Elasticity of normal and cancerous human bladder cells studied by scanning force microscopy', *Eur. Biophys. J.*, 28, pp. 312–316. doi: 10.1007/s002490050213.

Lekka, M. (2016) 'Discrimination Between Normal and Cancerous Cells Using AFM', *BioNanoSci.*, 6, pp. 65–80. doi: 10.1007/s12668-016-0191-3.

Li, Y., Asadi, A., Monroe, M. R. *et al.* (2009) 'pH effects on collagen fibrillogenesis in vitro: electrostatic interactions and phosphate binding', *Mater. Sic. Eng. C*, 29, pp. 1643-1649. doi: 10.1016/j.msec.2009.01.001.

Link, P. A., Pouliot, R. A., Mikhaiel, N. *et al.* (2017) 'Tunable hydrogels from pulmonary extracellular matrix for 3D cell culture', *J. Vis. Exp.*, 2017(119), pp. 1–9. doi: 10.3791/55094.

Liu, Y., Liu, B., Kong, J. (2005) 'Controlled switchable surface', *Chemistry Eur. J.* 11(9), pp. 2622–2631. doi: 10.1002/chem.200400931.

Lowin, T., Anssar, T. M., Bäuml, M. *et al.* (2020) 'Positive and negative cooperativity of TNF and Interferon-γ in regulating synovial fibroblast function and B cell survival in fibroblast/B cell co-cultures', *Sci. Rep.*, 10(780), pp. 1–14. doi: 10.1038/s41598-020-57772-7.

Lu, L., Oswald, S. J., Ngu, H. *et al.* (2008) 'Mechanical properties of actin stress fibers in living cells', *Biophys. J.*, 95, pp. 6060–6071. doi: 10.1529/biophysj.108.133462.

Lu, P., Takai, K., Weaver, V. M. et al. (2011) 'Extracellular matrix degradation and remodeling in development and disease', *Cold Spring Harb Perspec. Biol.*, 3(a005058). doi: 10.1101/cshperspect.a005058.

Lyapunova, E., Nikituk, A., Bayandin, Y. *et al.* (2016) 'Passive microrheology of normal and cancer cells after ML7 treatment by atomic force microscopy', *AIP Conf. Proc.*, 1760. doi: 10.1063/1.4960265.

Ma, C., Qu, T., Chang, B. et al. (2018) '3D maskless micropatterning for regeneration of highly organized tubular tissue', *Adv. Healthc. Mater.*, 7(3). doi: 10.1002/adhm.201700738.

Mahaffy, R. E., Shih, C. K., MacKintosh, F. C. *et al.* (2000) ‘Scanning probe-based frequency-dependent microrheology of polymer gels and biological cells’, *Phys. Rev. Lett.*, 85(4), pp. 880–883. doi: 10.1103/PhysRevLett.85.880.

Makris, N. and Constantinou, M. C. (1991) ‘Fractional-derivative Maxwell model for viscous dampers’, *J. Struct. Eng.*, 117(9), pp. 2708–2724.

Maksym, G. N., Fabry, B., Butler, J. P. *et al.* (2000) ‘Mechanical properties of cultures human airway smooth muscle cells from 0.05 to 0.4 Hz’, *J. Appl. Physiol.*, 89, pp. 1619–1632. doi: 10.1152/jappl.2000.89.4.1619.

Malmström, J., Lindberg, H., Lindberg, C. *et al.* (2004) ‘Transforming growth factor-β1 specificically induce proteins involved in the myofibroblast contractile apparatus’, *Mol. Cell. Proteomics*, 3(5), pp. 466–477. doi: 10.1074/mcp.M300108-MCP200.

Mandadapu, K. K., Govindjee, S. and Mofrad, M. R. K. (2008) ‘On the cytoskeleton and soft glassy rheology’, *J. Biomech.*, 41, pp. 1467–1478. doi: 10.1016/j.jbiomech.2008.02.014.

Mandal, S. S. (2020) ‘Force Spectroscopy on Single Molecules of Life’, *ACS Omega*, 5, pp. 11271–11278. doi: 10.1021/acsomega.0c00814.

Marenzana, M., Wilson-Jones, N., Mudera, V. *et al.* (2006) ‘The origins and regulation of tissue tension: Identification of collagen tension-fixation process in vitro’, *Exp. Cell Res.*, 312, pp. 423–433. doi: 10.1016/j.yexcr.2005.11.005.

Martens, J. C. and Radmacher, M. (2008) ‘Softening of the actin cytoskeleton by inhibition of myosin II’, *Pflug. Arch. Eur. J. Physiology*, 456(1), pp. 95–100. doi: 10.1007/s00424-007-0419-8.

Matte, B. F., Kumar, A., Placone, J. K. *et al.* (2019) ‘Matrix stiffness mechanically conditions EMT and migratory behavior of oral squamous cell carcinoma’, *J. Cell Sci.*, 132(1). doi: 10.1242/jcs.224360.

Mazia, D., Schatten, G. and Sale, W. (1975) ‘Adhesion of cells to surfaces coated with polylysine. Applications to electron microscopy’, *J. Cell Biol.*, 66(1), pp. 198-200. doi: 10.1083/jcb.66.1.198.

McCoy, M. G., Seo B. R., Choi, S. et al. (2016) ‘Collagen I hydrogel microstructure and composition conjointly regulate vascular network formation’, *Acta Biomater.*, 44, pp. 200-208. doi: 10.1016/j.actbio.2016.08.028.

McKenzie, A. J., Hicks, S. R., Svec, K. V. *et al.* (2018) ‘The mechanical microenvironment regulates ovarian cancer cell morphology, migration, and spheroid disaggregation’, *Sci. Rep.*, 8(7228), pp. 1–20. doi: 10.1038/s41598-018-25589-0.

Mecham, R. O. (2012) ‘Overview of extracellular matrix’, *Curr. Protoc. Cell Biol.*, 57(10.1.1-10.1.16). doi: 10.1002/0471143030.cb1001s57.

Mederacke, I. *et al.* (2013) ‘Fate tracing reveals hepatic stellate cells as dominant contributors to liver fibrosis independent of its aetiology', *Nat. Commun.*, 4(2823). doi: 10.1038/ncomms3823.

Meyer, E. (1992) 'Atomic force microscopy', *Prog. Surf. Sci.*, 41(1), pp. 3–49. doi: https://doi.org/10.1016/0079-6816(92)90009-7.

Meyers, M. A., Chen, P-Y., Lin, A. Y-M. *et al.* (2008) 'Biological materials: Structure and mechanical properties', *Prog. Mater. Sci.*, 53(1), pp. 1–206. doi: 10.1016/j.pmatsci.2007.05.002.

Meyvis, T. K. L., Stubbe, B. G., Van Steenbergen, M. J. *et al.* (2002) 'A comparison between the use of dynamic mechanical analysis and oscillatory shear rheometry for the characterisation of hydrogels', *Int. J. Pharm.*, 244, pp. 163–168. doi: 10.1016/S0378-5173(02)00328-9.

Mi, Y., Chan, Y., Trau, D. *et al.* (2006) 'Micromolding of PDMS scaffolds and microwells for tissue culture and cell patterning: A new method of microfabrication by the self-assembled micropatterns of diblock copolymer micelles', *Polymer*, 47, pp. 5124–5130. doi: 10.1016/j.polymer.2006.04.063.

Mietke, A., Otto, O., Girardo, S. *et al.* (2015) 'Extracting Cell Stiffness from Real-Time Deformability Cytometry: Theory and Experiment', *Biophys. J.*, 109(10), pp. 2023–2036. doi: 10.1016/j.bpj.2015.09.006.

Moeendarbary, E. and Harris, A. R. (2014) 'Cell mechanics: Principles, practices, and prospects', *Wiley Interdiscip. Rev. Syst. Biol. Med.*, 6(5), pp. 371–388. doi: 10.1002/wsbm.1275.

Morelli, I., Fraschini, G. and Banfi, A. E. (2017) 'Dupuytren's disease: Predicting factors and associated conditions. A single center questionnaire-based case- control study', *Arch. Bone Jt. Surg.*, 5(6), pp. 384–391. doi: 10.22038/abjs.2017.21022.1542.

Moreno-Flores, S., Benitez, R., de Vivanco, M. *et al.* (2010) 'Stress relaxation and creep on living cells with the atomic force microscope: A means to calculate elastic moduli and viscosities of cell components', *Nanotechnology*, 21(445101). doi: 10.1088/0957-4484/21/44/445101.

Mostafavi-Pour, Z., Askari, J. A., Parkinson, S. J. *et al.* (2003) 'Integrin-specific signaling pathways controlling focal adhesion formation and cell migration', *J. Cell Biol.*, 161(1), pp. 155–167. doi: 10.1083/jcb.200210176.

Müller, T., Schumann, C. and Kraegeloh, A. (2012) 'STED microscopy and its applications: New insights into cellular processes on the nanoscale', *ChemPhysChem*, 13, pp. 1986–2000. doi: 10.1002/cphc.201100986.

Murata, H. (2012) 'Rheology - Theory and Application to Biomaterials', *Polymerization*. doi: 10.5772/48393.

Nakanishi, J., Takarada, T., Yamaguchi, K. *et al.* (2008) 'Recent advances in cell micropatterning techniques for bioanalytical and biomedical sciences', *Anal. Sci.*, 24, pp. 67–72. doi: 10.2116/analsci.24.67.

Neuman, K. C. and Nagy, A. (2008) ‘Single-molecule force spectroscopy: Optical tweezers, magnetic tweezers and atomic force microscopy’, *Nat. Methods*, 5(6), pp. 491–505. doi: 10.1038/nmeth.1218.

Nguyen, S. T., Dormieux, L., Le Pape, Y. *et al.* (2011) ‘A Burger Model for the Effective Behavior of a Microcracked Viscoelastic Solid’, *Int. J. Damage Mech.*, 20(8), pp. 1116–1129. doi: 10.1177/1056789510395554.

Nguyen, T. U., Watkins, K. E. and Kishore, V. (2019) ‘Photochemically crosslinked cell-laden methacrylated collagen hydrogels with high cell viability and functionality’, *J. Biomed. Mater. Res. Part A*, 107A, pp. 1541–1550. doi: 10.1002/jbm.a.36668.

Nichol, J. W., Koshy, S. T., Bae, H. *et al.* (2010) ‘Cell-laden microengineered gelatin methacrylate hydrogels’, *Biomaterials*. Elsevier Ltd, 31(21), pp. 5536–5544. doi: 10.1016/j.biomaterials.2010.03.064.

Nwoke, O. N., Okokpujie, I. P. and Ekenyem, S. C. (2017) ‘Investigation of Creep Responses of Selected Engineering Materials’, *JOSEDET*, 1(1), pp. 1–15.

Okada, H., Kikuta, T., Kobayashi, T. *et al.* (2005) ‘Connective tissue growth factor expressed in tubular epithelium plays a pivotal role in renal fibrogenesis’, *J. Am. Soc. Nephrol.*, 16, pp. 133–143. doi: 10.1681/ASN.2004040339.

Olde Damink, L. H. H., Dijkstra, P. J., Van Luyn, M. J. A., *et al.* (1995) ‘Crosslinking of dermal sheep collagen using hexamethylene diisocyanate’, *J. Mater. Sci. Mater. Med.*, 6, pp. 429-434. doi: 10.1007/BF00120286.

Otto, O., Rosendahl, P., Mietke, A. *et al.* (2015) ‘Real-time deformability cytometry: On-the-fly cell mechanical phenotyping’, *Nat. Methods*, 12, pp. 199–202. doi: 10.1038/nmeth.3281.

Pajic-Lijakovic, I. and Milivojevic, M. (2019) ‘Jamming state transition and collective cell migration’, *J. Biol. Eng.*, 13(73), pp. 1–13. doi: 10.1186/s13036-019-0201-4.

Pajic-Lijakovic, I. and Milivojevic, M. (2022) ‘The role of viscoelasticity in long time cell rearrangement’, *Prog. Biophys. Mol. Biol.*, 173, pp. 60–71. doi: 10.1016/j.pbiomolbio.2022.05.005.

Papanicolaou, G. C. and Zaoutsos, S. P. (2010) ‘Viscoelastic constitutive modeling of creep and stress relaxation in polymers and polymer matrix composites’, *Creep and Fatigue in Polymer Matrix Composites*, pp. 3-47. doi: 10.1533/9780857090430.1.3.

Parker, K. K., Brock, A. L., Brangwynne, C. *et al.* (2002) ‘Directional control of lamellipodia extension by constraining cell shape and orienting cell tractional forces’, *FASEB J.*, 16(10), pp. 1195–1204. doi: 10.1096/fj.02-0038com.

Passeri, D., Dong, C., Reggente, M. *et al.* (2014) 'Magnetic force microscopy', *BioMatter*, 4(1). doi: 10.4161/biom.29507.

Pegoraro, A. F., Janmey, P. and Weitz, D. A. (2017) 'Mechanical properties of the cytoskeleton and cells', *Cold Spring Harb. Perspect. Biol.*, 9(a022038). doi: 10.1101/cshperspect.a022038.

Pelleg, J. (2013) 'Solid mechanics and its applications: Mechanical properties of materials', *Springer Dordrecht*, 190. doi: 10.1007/978-94-007-4342-7.

Pérez-Domínguez, S., Kulkarni, S. G., Rianna, C. *et al.* (2020) 'Atomic force microscopy for cell mechanics and diseases', *Neuroforum*, pp. 1–9.

Pérez-Domínguez, S., Caballero-Mancebo, S., Marcuello, C., *et al.* (2022) 'Nanomechanical Study of Enzyme: Coenzyme Complexes: Bipartite Sites in Plastidic Ferredoxin-NADP+ Reductase for the Interaction with NADP+', *Antioxidants*, 11(3), pp. 1–21. doi: 10.3390/antiox11030537.

Pérez-Domínguez, S., Werkmeister, E., Marini, M. L. *et al.* (2022) 'Rheological comparison between control and Dupuytren fibroblasts when plated in circular micropatterns using atomic force microscopy', *Front. Phys.*, 10(1052203), pp. 1–14. doi: 10.3389/fphy.2022.1052203.

Petridou, S., Maltseva, O., Spanakis, S. *et al.* (2000) 'TGF-β receptor Expression and Smad2 Localization Are Cell Density Dependent in Fibroblasts', *Invest Ophthalmol Vis Sci.*, 41, pp. 89–95.

Pittenger, M. F. *et al.* (1999) 'Multilineage potential of adult human mesenchymal stem cells', *Science*, 284, pp. 143–147. doi: 10.1126/science.284.5411.143.

Pittet, P., Lee, K., Kulik, A. J., *et al.* (2008) 'Fibrogenic fibroblasts increase intercellular adhesion strength by reinforcing individual OB-cadherin bonds', *J. Cell Sci.*, 121(6), pp. 877–886. doi: 10.1242/jcs.024877.

Plikus, M. V., Wang, X., Sinha, S. *et al.* (2021) 'Fibroblasts: Origins, definitions, and functions in health and disease', *Cell*, 184(15), pp. 3852–3872. doi: 10.1016/j.cell.2021.06.024.

Preissner, K. T. (1991) 'Structure and biological role of vitronectin', *Annu. Rev. Cell. Biol.*, 7(1), pp. 275-310. doi: 10.1146/annurev.cb.07.110191.001423.

Puech, P. H., Poole, K., Knebel, D. *et al.* (2006) 'A new technical approach to quantify cell-cell adhesion forces by AFM', *Ultramicroscopy*, 106, pp. 637–644. doi: 10.1016/j.ultramic.2005.08.003.

Radmacher, M. (1997) 'Measuring the Elastic Properties of Biological Samples with the AFM', *IEEE Eng. Med. Biol.*, 16, pp. 47–57. doi: 10.1109/51.582176.

Radmacher, M. (2002) 'Measuring the elastic properties of living cells', *Methods Cell Biol.*, 68. doi: 10.1016/s0091-679x(02)68005-7.

Radmacher, M., Tillmann, R. W. and Gaub, H. . (1993) ‘Imaging viscoelasticity by force modulation’, *Biophys. J.*, 64, pp. 735–742. doi: 10.1016/S0006-3495(93)81433-4.

Rajan, N., Habermehl, J., Coté, M-F. *et al.* (2006) ‘Preparation of ready-to-use, storable and reconstituted type I collagen from rat tail tendon for tissue engineering applications’, *Nat. Protoc.*, 1(6), pp. 2753–2758. doi: 10.1038/nprot.2006.430.

Rebêlo, L. M., de Sousa, J. S., Mendes Filho, J. *et al.* (2014) ‘Microrheology of cells with magnetic force modulation atomic force microscopy’, *Soft Matter*, 10, pp. 2141–2149. doi: 10.1039/c3sm52045e.

Rehfeldt, F., Engler, A. J., Eckhardt, A. *et al.* (2007) ‘Cell responses to the mechanochemical microenvironment-Implications for regenerative medicine and drug delivery’, *Adv. Drug Deliv. Rev.*, 59, pp. 1329–1339. doi: 10.1016/j.addr.2007.08.007.

Rhee, S. and Grinnell, F. (2007) ‘Fibroblast mechanics in 3D collagen matrices’, *Adv. Drug Deliv. Rev.*, 59, pp. 1299–1305. doi: 10.1016/j.addr.2007.08.006.

Rianna, C., Rossano, L., Kollarigowda, R. H., et al. (2016a) ‘Spatio-Temporal control of dynamic topographic patterns on azopolymers for cell culture applications’, *Adv. Funct. Mater.*, 26, pp. 7572-7580. doi: 10.1002/adfm.201602577.

Rianna, C. and Radmacher, M. (2016b) ‘Cell mechanics as a marker for diseases: Biomedical applications of AFM’, *AIP Conf. Proc.*, 1760(020057). doi: 10.1063/1.4960276.

Rianna, C. and Radmacher, M. (2017a) ‘Comparison of viscoelastic properties of cancer and normal thyroid cells on different stiffness substrates’, *Eur. Biophys. J.*, 46, pp. 309-324. doi: 10.1007/s00249-016-1168-4.

Rianna, C. and Radmacher, M. (2017b) ‘Influence of microenvironment topography and stiffness on the mechanics and motility of normal and cancer renal cells’, *Nanoscale.*, 9, pp. 11222–11230. doi: 10.1039/c7nr02940c.

Rianna, C., Radmacher, M. and Kumar, S. (2020) ‘Direct evidence that tumor cells soften when navigating confined spaces’, *Mol. Biol. Cell*, 31(16), pp. 1726–1734. doi: 10.1091/mbc.E19-10-0588.

Rico, F., Roca-Cusachs, P., Gavara, N. *et al.* (2005) ‘Probing mechanical properties of living cells by atomic force microscopy with blunted pyramidal cantilever tips’, *Phys. Rev. E*, 72(021914). doi: 10.1103/PhysRevE.72.021914.

Rico, F., Gonzalez, L., Casuso, I. *et al.* (2013) ‘High-speed force spectroscopy unfolds titin at the velocity of molecular dynamics simulations’, *Science*, 342(6159), pp. 741–743. doi: 10.1126/science.1239764.

Rico, F., Russek, A., González, L. *et al.* (2019) ‘Heterogeneous and rate-dependent streptavidin–biotin unbinding revealed by high-speed force spectroscopy and atomistic simulations', *PNAS*, 116(14), pp. 6594–6601. doi: 10.1073/pnas.1816909116.

Rigato, A., Rico, F., Eghiaian, F. *et al.* (2015) 'Atomic Force Microscopy Mechanical Mapping of Micropatterned Cells Shows Adhesion Geometry-Dependent Mechanical Response on Local and Global Scales', *ACS Nano*, 9(6), pp. 5846–5856. doi: 10.1021/acsnano.5b00430.

Rigato, A., Miyagi, A., Scheuring, S. *et al.* (2017) 'High-frequency microrheology reveals cytoskeleton dynamics in living cells', *Nat. Phys.*, 13(8), pp. 771–775. doi: 10.1038/NPHYS4104.

Rittweger, E., Han, K. Y., Irvine, S. E. *et al.* (2009) 'STED microscopy reveals crystal colour centres with nanometric resolution', *Nat. Photon.,* 3, pp. 144–147. doi: 10.1038/nphoton.2009.2.

Rockey, D. C., Bell, P. D. and Hill, J. A. (2015) 'Fibrosis — A Common Pathway to Organ Injury and Failure', *N. Engl. J. Med.*, 372, pp. 1138–1149. doi: 10.1056/nejmra1300575.

Rodriguez, M. L. and Sniadecki, N. J. (2014) 'Computational modeling of cell mechanics, Computational Modelling of Biomechanics and Biotribology in the Musculoskeletal System', *Biomater. Tissues,* pp. 93-140. doi: 10.1533/9780857096739.2.93.

Rosenbloom, J., Castro, S. V. and Jimenez, S. A. (2010) 'Narrative Review: Fibrotic Diseases: Cellular and Molecular Mechanisms and Novel Therapies', *Ann. Intern. Med.*, 152, p. 159. doi: 10.7326/0003-4819-152-3-201002020-00007.

Rosendahl, P., Plak, K., Jacobi, A. *et al.* (2018) 'Real-time fluorescence and deformability cytometry', *Nat. Methods*, 15(5), pp. 355–358. doi: 10.1038/nmeth.4639.

Rother, J., Nöding, H., Mey, I. *et al.* (2014) 'Atomic force microscopy-based microrheology reveals significant differences in the viscoelastic response between malign and benign cell lines', *Open Biol.*, 4(140046). doi: 10.1098/rsob.140046.

Rotsch, C. and Radmacher, M. (2000) 'Drug-induced changes of cytoskeletal structure and mechanics in fibroblasts: An atomic force microscopy study', *Biophys. J.*, 78, pp. 520–535. doi: 10.1016/S0006-3495(00)76614-8.

Sader, J. E., Larson, I., Mulvaney, P. *et al.* (1995) 'Method for the calibration of atomic force microscope cantilevers', *Rev. Sci. Instrum.*, 66(7), pp. 3789–3798. doi: 10.1063/1.1145439.

Salomon, D., Saurat, J. H. and Meda, P. (1988) 'Cell-to-cell communication within intact human skin', *J. Clin. Investig.*, 82, pp. 248–254. doi: 10.1172/JCI113578.

Sarber, R., Hull, B., Merrill, C. *et al.* (1981) 'Regulation of proliferation of fibroblasts of low and high population doubling levels grown in collagen lattices', *Mech. Ageing*

Dev., 17, pp. 107–117. doi: 10.1016/0047-6374(81)90077-4.

Sarrigiannidis, S. O., Rey, J. M., Dobre, O. et al. (2021) ‘A tough act to follow: collagen hydrogel modifications to improve mechanical and growth factor loading capabilities’, *Mater. Today Bio*, 10(100098). doi: 10.1016/j.mtbio.2021.100098.

Sayadi, L. R., Alhunayan, D., Sarantopoulos, N. *et al.* (2019) ‘The Molecular Pathogenesis of Dupuytren Disease’, *Ann. Plast. Surg.*, 83(5), pp. 594–600. doi: 10.1097/SAP.0000000000001918.

Schäfer, A. and Radmacher, M. (2005) ‘Influence of myosin II activity on stiffness of fibroblast cells’, *Acta Biomater.*, 1, pp. 273–280. doi: 10.1016/j.actbio.2005.02.004.

Schmidt, B. M. W. and Schmieder, R. E. (2003) ‘Aldosterone-induced cardiac damage: Focus on blood pressure independent effects’, *Am. J. Hypertens.*, 16(1), pp. 80–86. doi: 10.1016/S0895-7061(02)03199-0.

Sengupta, P., Ruano, M. J., Tebar, F. *et al.* (2007) ‘Membrane-permeable calmodulin inhibitors (e.g. W-7/W-13) bind to membranes, changing the electrostatic surface potential’, *J. Biol. Chem.*, 282(11), pp. 8474–8486. doi: 10.1074/jbc.M607211200.

Seo, B. R., Chen, X., Ling, L. *et al.* (2020) ‘Collagen microarchitecture mechanically controls myofibroblast differentiation’, *Proc. Natl. Acad. Sci. U.S.A.*, 117, pp. 11387-11398. doi: 10.1073/pnas.1919394117.

Serini, G., Bochaton-Piallat, M-L., Ropraz, P. *et al.* (1998) ‘The fibronectin domain ED-A is crucial for myofibroblastic phenotype induction by transforming growth factor-β1’, *J. Cell Biol.*, 142(3), pp. 873–881. doi: 10.1083/jcb.142.3.873.

Shao, Z., Mou, J., Czajkowsky, D. M. *et al.* (1996) ‘Biological atomic force microscopy: What is achieved and what is needed’, *Adv. Phys.*, 45(1), pp. 1–86. doi: 10.1080/00018739600101467.

Shaw, R. B., Chong, A. K. S., Zhang, A. *et al.* (2007) ‘Dupuytren’s disease: History, diagnosis, and treatment’, *Plast. Reconstr. Surg.*, 120(3), pp. 44–54. doi: 10.1097/01.prs.0000278455.63546.03.

Shephard, P., Martin, G., Smola-Hess, S. *et al.* (2004) ‘Myofibroblast differentiation is induced in keratinocyte-fibroblast co-cultures and is antagonistically regulated by endogenous transforming growth factor-β, and interleukin-1’, *Am. J. Pathol.*, 164(6), pp. 2055–2066. doi: 10.1016/S0002-9440(10)63764-9.

Sheu, M. T., Huang, J-C., Yeh, G-C. *et al.* (2001) ‘Characterization of collagen gel solutions and collagen matrices for cell culture’, *Biomaterials*, 22, pp. 1713–1719. doi: 10.1016/S0142-9612(00)00315-X.

Shi, J., Takahashi, S., Jin, X-H. *et al.* (2007) ‘Myosin light chain kinase-independent inhibition by ML-9 of murine TRPC6 channels expressed in HEK293 cells’, *Br. J. Pharmacol.*, 152, pp. 122–131. doi: 10.1038/sj.bjp.0707368.

Shoelson, B., Dimitriadis, E. K., Cai, H. *et al.* (2004) 'Evidence and implications of inhomogeneity in tectorial membrane elasticity', *Biophys. J.*, 87, pp. 2768–2777. doi: 10.1529/biophysj.104.040774.

Shoulders, M. D. and Raines, R. T. (2009) 'Collagen structure and stability', *Ann. Rev. Biochem.*, 78, pp. 929–958. doi: 10.1146/annurev.biochem.77.032207.120833.

Silver, F. H. (1981) 'Type I collagen fibrillogenesis in vitro. Additional evidence for the assembly mechanism', *J. Biol. Chem.*, 256(10), pp. 4973-4977. doi: 10.1016/S0021-9258(19)69353-1.

Singh, P., Reimer, C. L., Peters, J. H. *et al.* (2004) 'The spatial and temporal expression patterns of integrin α9β1 and one of its ligands, the EIIIA segment of fibronectin, in cutaneous wound healing', *J. Invest. Dermatol.*, 123, pp. 1176–1181. doi: 10.1111/j.0022-202X.2004.23485.x.

Siwik, D. A., Chang, D. L. F. and Colucci, W. S. (2000) 'Interleukin-1 β and tumor necrosis factor-α decrease collagen synthesis and increase matrix metalloproteinase activity in cardiac fibroblasts in vitro', *Cir. Res.*, 86(12), pp. 1259–1265. doi: 10.1161/01.RES.86.12.1259.

Sneddon, I. N. (1965) 'The relation between load and penetration in the axisymmetric boussinesq problem for a punch of arbitrary profile', *Int. J. Engng. Sci.*, 3, pp. 47–57. doi: 10.1016/0020-7225(65)90019-4.

Sollich, P., Lequeux, F., Hébraud, P. *et al.* (1997) 'Rheology of soft glassy materials', *Phys. Rev. Lett.*, 78(10), pp. 2020–2023. doi: 10.1103/PhysRevLett.78.2020.

Sollich, P. (1998) 'Rheological constitutive equation for a model of soft glassy materials', *Phys. Rev. E*, 58(1), pp. 738–759. doi: 10.1103/PhysRevE.58.738.

Song, W., Lu, H., Kawazoe, N. *et al.* (2011) 'Adipogenic differentiation of individual mesenchymal stem cell on different geometric micropatterns', *Langmuir*, 27(10), pp. 6155–6162. doi: 10.1021/la200487w.

Song, W., Kawazoe, N. and Chen, G. (2011) 'Dependence of spreading and differentiation of mesenchymal stem cells on micropatterned surface area', *J. Nanomater.*, pp. 1–9. doi: 10.1155/2011/265251.

Stamenovic, D., Wang, N. and Ingber, D. E. (2006) 'Cellular tensegrity models and cell-substrate interactions', *Principales Cell. Eng.*, doi: 10.1016/B978-0-12-369392-1.50005-X.

Strelow, J., Dewe, W., Iversen, P. W. *et al.* (2012) 'Mechanism of Action Assays for Enzymes', *Eli Lilly & Company and the National Center for Advancing Translational Sciences; 2004*.

Style, R. W., Boltyanskiy, R., German, G. K. *et al.* (2014) 'Traction force microscopy in physics and biology', *Soft Matter*, 10, p. 4047. doi: 10.1039/c4sm00264d.

Sumbul, F., Marchesi, A. and Rico, F. (2018) 'History, rare, and multiple events of mechanical unfolding of repeat proteins', *J. Chem. Phys.*, 148(12). doi: 10.1063/1.5013259.

Sundararaghavan, H. G., Monteiro, G. A., Lapin, N. A. *et al.* (2008) 'Genipin-induced changes in collagen gels: Correlation of mechanical properties to fluorescence', *J. Biomed. Mater. Res. Part A*, 87(2), pp. 308–320. doi: 10.1002/jbm.a.31715.

Tamariz, E. and Grinnell, F. (2002) 'Modulation of Fibroblast Morphology and Adhesion during Collagen Matrix Remodeling', *Mol. Biol. Cell*, 13, pp. 3915–3929. doi: 10.1091/mbc.E02.

Tan, I. and Leung, T. (2009) 'Myosin light chain kinases: Division of work in cell migration', *Cell Adh. Migr.*, 3(3), pp. 256–258. doi: 10.4161/cam.3.3.8212.

Tanaka, K., Sano, K., Nakano, T. *et al.* (2007) 'Suppression of α smooth muscle actin expression by IFN-γ in established myofibroblast cell lines', *J. Interferon Cytokine Res.*, 27(10), pp. 835–839. doi: 10.1089/jir.2007.0028.

Tanaka, K., Sano, K., Tanaka, K. *et al.* (2001) 'Demonstration of downregulation of α-smooth muscle actin in interferon-γ-treated myofibroblast by a novel cell-capture enzyme immunoassay', *International Immunopharmacology*, 1, pp. 769–775. doi: 10.1016/S1567-5769(01)00011-X.

Tanaka, K., Sano, K., Yuba, K. *et al.* (2003) 'Inhibition of induction of myofibroblasts by interferon γ in a human fibroblast cell line', *Int. Immunopharmacol.*, 3, pp. 1273–1280. doi: 10.1016/S1567-5769(03)00102-4.

Théry, M., Pépin, A., Dressaire, E. *et al.* (2006) 'Cell distribution of stress fibres in response to the geometry of the adhesive environment', *Cell Motil. Cytoskelet.*, 63(6), pp. 341–355. doi: 10.1002/cm.20126.

Théry, M. (2010) 'Micropatterning as a Tool to Decipher Cell Morphogenesis and Functions', *J. Cell Sci.*, 123, pp. 4201–4213. doi: 10.1242/jcs.075150.

Tojkander, S., Gateva, G. and Lappalainen, P. (2012) 'Actin stress fibers - Assembly, dynamics and biological roles', *J. Cell Sci.*, 125, pp. 1855–1864. doi: 10.1242/jcs.098087.

Tomasek, J. J., Gabbiani, G., Hinz, B. *et al.* (2002) 'Myofibroblasts and mechanoregulation of connective tissue remodelling', *Nat. Rev. Mol. Cell Biol.*, 3(5), pp. 349–363. doi: 10.1038/nrm809.

Trappmann, B. and Chen, C. S. (2013) 'How cells sense extracellular matrix stiffness: A material's perspective', *Curr. Opinion Biotechnol.*, 24(5), pp. 948–953. doi: 10.1016/j.copbio.2013.03.020.

Ulrich, T. A., De Juan Pardo, E. M. and Kumar, S. (2009) 'The mechanical rigidity of the extracellular matrix regulates the structure, motility, and proliferation of glioma cells', *Cancer Res.*, 69(10), pp. 4167–4174. doi: 10.1158/0008-5472.CAN-08-4859.

Van Dongen, S. F. M.; Maiuri, P.; Marie, E. *et al.* (2013) ‘Triggering Cell Adhesion, Migration or Shape Change with a Dynamic Surface Coating’, *Adv. Mater.*, 25, pp. 1687– 1691. doi: 10.1002/adma.201204474.

Van Rijssen, A. L., Gerbrandy, F. S. J., Linden, H. T. *et al.* (2006) ‘A Comparison of the Direct Outcomes of Percutaneous Needle Fasciotomy and Limited Fasciectomy for Dupuytren’s Disease: A 6-Week Follow-Up Study’, *J. Hand Surg.*, 31(5), pp. 717–725. doi: 10.1016/j.jhsa.2006.02.021.

Varga, J. and Abraham, D. (2007) ‘Systemic sclerosis: A prototypic multisystem fibrotic disorder’, *J. Clin. Investig.*, 117(3), pp. 557–567. doi: 10.1172/JCI31139.

Vaughan, M. B., Xu, G., Morris, T. L. *et al.* (2019) ‘Predictable fibroblast tension generation by measuring compaction of anchored collagen matrices using microscopy and optical coherence tomography’, *Cell Adh. Migr.*, 13(1), pp. 302–313. doi: 10.1080/19336918.2019.1644855.

Vicens-Zygmunt, V., Estany, S., Colom, A. *et al.* (2015) ‘Fibroblast viability and phenotypic changes within glycated stiffened three-dimensional collagen matrices’, *Respir. Res.*, 16(82), pp. 1–15. doi: 10.1186/s12931-015-0237-z.

Viji Babu, P. K., Rianna, C., Belge, G. *et al.* (2018) ‘Mechanical and migratory properties of normal, scar, and Dupuytren’s fibroblasts’, *J. Mol. Recognit.*, 31(9), pp. 1–11. doi: 10.1002/jmr.2719.

Viji Babu, P. K., Rianna, C., Mirastschijski, U. *et al.* (2019) ‘Nano-mechanical mapping of interdependent cell and ECM mechanics by AFM force spectroscopy’, *Sci. Rep.*, 9(1), p. 12317. doi: 10.1038/s41598-019-48566-7.

Viji Babu, P. K., Mirastschijski, U., Belge, G. *et al.* (2021) ‘Homophilic and heterophilic cadherin bond rupture forces in homo- or hetero-cellular systems measured by AFM based SCFS’, *Eur. Biophys. J.*, (0123456789). doi: 10.1101/2020.02.11.943597.

Vinckier, A. and Semenza, G. (1998) ‘Measuring elasticity of biological materials by atomic force microscopy’, *FEBS Letters*, 430, pp. 12–16. doi: 10.1016/S0014-5793(98)00592-4.

Vlassov, S., Antsov, M., Sosnin, I. *et al.* (2018) ‘Adhesion and mechanical properties of PDMS-based materials probed with AFM: a review’, *Rev. Adv. Mater. Sci.*, 56, pp. 62–78. doi: 10.1515/rams-2018-0038.

Vogel, S., Ullm, F., Müller, C. D. *et al.* (2020) ‘Remodeling of Three-Dimensional Collagen I Matrices by Human Bone Marrow Stromal Cells during Osteogenic Differentiation in Vitro’, *ACS Appl. Bio Mater.*, 3(10), pp. 6967–6978. doi: 10.1021/acsabm.0c00856.

Wang, X., Nakamoto, T., Dulinska-Molak, I. *et al.* (2016) ‘Regulating the stemness of mesenchymal stem cells by tuning micropattern features’, *J. Mater. Chem. B*, 4(1), pp. 37–45. doi: 10.1039/c5tb02215k.

Warwick, D., Thomas, A. and Bayat, A. (2012) ‘Dupuytren’s disease: overview of a common connective tissue disease with a focus on emerging treatment options’, *Int. J. Clin. Rheumat.*, 7(3), pp. 309–323.

Watkins, S. and Sontheimer, H. (2011) ‘Hydrodynamic cellular volume changes enable glioma cell invasion’, *J Neurosci.*, 31(47), pp. 17250–17259. doi: 10.1523/JNEUROSCI.3938-11.2011.

Weadock, K., Olson, R. M., Silver F. H. (1983) ‘Evaluation of collagen crosslinking techniques’, *Biomater. Med. Devices Artif. Organs*, 11, pp. 293-318. doi: 10.3109/10731198309118815.

Wehrle-Haller, B. (2012) ‘Structure and function of focal adhesions’, *Curr. Opinion Cell Biol.*, 24, pp. 116–124. doi: 10.1016/j.ceb.2011.11.001.

Wendling, S., Oddou, C. and Isabey, D. (1999) ‘Stiffening response of a cellular tensegrity model’, *J. Theor. Biol.*, 196, pp. 309–325. doi: 10.1006/jtbi.1998.0841.

Wheelock, M. J. and Johnson, K. R. (2003) ‘Cadherin-mediated cellular signaling’, *Curr. Opinion Cell Biol.*, 15, pp. 509–514. doi: 10.1016/S0955-0674(03)00101-7.

Wirtz, D. (2009) ‘Particle-tracking microrheology of living cells: Principles and applications’, *Annu. Rev. Biophys.*, 38, pp. 301–326. doi: 10.1146/annurev.biophys.050708.133724.

Witkowska-Zimny, M., Walenko, K., Wrobel, E. *et al.* (2013) ‘Effect of substrate stiffness on the osteogenic differentiation of bone marrow stem cells and bone-derived cells’, *Cell Biol. Inter.*, 37, pp. 608–616. doi: 10.1002/cbin.10078.

Wood, G. C., Keech, M. K. (1960) ‘The formation of fibrils from collagen solutions 1. The effect of experimental conditions: kinetic and electron-microscope studies’,*Biochem. J.*, 75, pp. 588-598. doi: 10.1042/bj0750588.

Wu, H. W., Kuhn, T. and Moy, V. T. (1998) ‘Mechanical properties of L929 cells measured by atomic force microscopy: Effects of anticytoskeletal drugs and membrane crosslinking’, *Scanning*, 20, pp. 389–397. doi: 10.1002/sca.1998.4950200504.

Wu, P. H., Aroush, D. R-B., Asnacios, A. *et al.* (2018) ‘A comparison of methods to assess cell mechanical properties’, *Nat. Methods*. Springer US, 15(7). doi: 10.1038/s41592-018-0015-1.

Wynn, T. (2008) ‘Cellular and molecular mechanisms of fibrosis’, *J. Pathol.*, 214, pp. 199–210. doi: 10.1002/path.2277.

Wynn, T. A. and Ramalingam, T. R. (2012) ‘Mechanisms of fibrosis: Therapeutic translation for fibrotic disease’, *Nat. Med.*, 18(7), pp. 1028–1040. doi: 10.1038/nm.2807.

Xie, J., Bao, M., Bruekers, S. M. C. *et al.* (2017) 'Collagen Gels with Different Fibrillar Microarchitectures Elicit Different Cellular Responses', *ACS Appl. Mater. Interfaces*, 9(23), pp. 19630–19637. doi: 10.1021/acsami.7b03883.

Xiong, Y., Wang, C., Shi, L. *et al.* (2017) 'Myosin light chain kinase: A potential target for treatment of inflammatory diseases', *Front. Pharmacol.*, 8, pp. 1–7. doi: 10.3389/fphar.2017.00292.

Yamaguchi, H. and Condeelis, J. (2007) 'Regulation of the actin cytoskeleton in cancer cell migration and invasion', *Biochim. Biophys. Acta*, 1773, pp. 642–652. doi: 10.1016/j.bbamcr.2006.07.001.

Yang, L., Bataller, R., Dulyx, J. *et al.* (2005) 'Attenuated hepatic inflammation and fibrosis in angiotensin type 1a receptor deficient mice', *J. Hepatol.*, 43, pp. 317–323. doi: 10.1016/j.jhep.2005.02.034.

Yango, A., Schäpe, J., Rianna, C. *et al.* (2016) 'Measuring the viscoelastic creep of soft samples by step response AFM', *Soft Matter*, 12(40), pp. 8297–8306. doi: 10.1039/c6sm00801a.

Yap, A. S. and Kovacs, E. M. (2003) 'Direct cadherin-activated cell signaling: A view from the plasma membrane', *J. Cell Biol.*, 160(1), pp. 11–16. doi: 10.1083/jcb.200208156.

Yeung, T., Georges, P. C., Flanagan, L. A. *et al.* (2005) 'Effects of substrate stiffness on cell morphology, cytoskeletal structure, and adhesion', *Cell Motil. Cytoskelet.*, 60, pp. 24–34. doi: 10.1002/cm.20041.

Yilbas, B. S., Al-Sharafi, A. and Ali, H. (2019) 'Chapter 3- Surfaces for self-cleaning', *Self-Clean. Surf. Water Drop. Mobil.*, pp. 45-98. doi: 10.1016/B978-0-12-814776-4.00003-3.

Zemła, J. *et al.* (2020) 'Indenting soft samples (hydrogels and cells) with cantilevers possessing various shapes of probing tip', *Eur. Biophys. J.*, 49, pp. 485–495. doi: 10.1007/s00249-020-01456-7.

Zhang, H. and Liu, K. K. (2008) 'Optical tweezers for single cells', *J. R. Soc. Interface*, 5, pp. 671–690. doi: 10.1098/rsif.2008.0052.

Zhang, X., Chen, X., Yang, T. *et al.* (2014) 'The effects of different crossing-linking conditions of genipin on type I collagen scaffolds: an in vitro evaluation', *Cell and Tissue Bank*, 15, pp. 531–541. doi: 10.1007/s10561-014-9423-3.

Zhu, J. (2010) 'Bioactiive modification of poly(ethylene glycol) hydrogels for tissue engineering', *Biomaterials*, 31, pp. 4639-4656. doi: 10.1016/j.biomaterials.2010.02.044.